ULTRAFAST COHERENT STUDIES OF EXCITONS AND EXCITONIC COMPLEXES IN DOPED AND UNDOPED GaAs QUANTUM WELLS

by

ALEXANDER ANTHONY BUSCH

B.Eng., McMaster University, 1992
M.A.Sc., University of British Columbia, 1994

A THESIS SUBMITTED IN PARTIAL FULFILMENT OF
THE REQUIREMENTS FOR THE DEGREE OF

DOCTOR OF PHILOSOPHY

in

THE FACULTY OF GRADUATE STUDIES

(Department of Physics & Astronomy)

We accept this thesis as conforming
to the required standard

THE UNIVERSITY OF BRITISH COLUMBIA

April 2003

Department of Physics

The University of British Columbia

Vancouver, Canada

Date 17 APRIL 2003

Abstract

This thesis reports a systematic study of near-band edge linear and nonlinear optical properties of doped and undoped semiconductor multiple quantum well samples, aimed at quantifying and separating the numerous contributions to the overall material response from photon excitation. Information obtained from *both* linear absorption and nonlinear, degenerate four-wave-mixing experiments is compared with elaborate numerical simulations. Accurate measures of 1S-2S binding energies and dephasing rates as a function of temperature from 5 to 40 K is established. The biexciton binding energy and dephasing rate over the temperature range 5 to 40 K is measured and, by comparison with theories reported in the literature, it is found that localization effects have a significant influence on the biexciton binding energy in 5 nm quantum wells. The first systematic attempt to quantitatively account for the continuum contribution to nonlinear response by fitting a series of spectra obtained at various input laser pulse detunings was conducted. Unique evidence for coherent beating between multi-exciton/free electron complexes in lightly doped material was also found.

Contents

List of Tables

List of Figures

Acknowledgements

There are several people whose assistance and efforts contributed to this work. First, I would like to acknowledge my supervisor, Dr. Jeff Young. He assisted not only in providing theoretical understanding and motivation for this work, but also in providing guidance and advice throughout the experimental and analysis stages of this work.

For earlier work, I would like to acknowledge Dr. Simon Brown, who processed the samples and conducted the early linear absorption studies on them, as well as Rong Zhu, for his work on early versions of the experimental system. Thanks also to Dr. Paul Paddon, both for his work on the experimental system after Rong had finished and for the many useful conversations we have had about the research results.

Dr. Jennifer Watson, who took up the work where Paul and Rong left off, deserves special mention. She greatly improved the experimental data collection system (hardware, software, and experimental procedures), as well as providing much of the early experimental data on the samples. Many of the experiments were done in conjunction with Jennifer, and the opportunity of working with her on this research was rewarding.

Murray McCutcheon assisted me with some of the last experiments – his help was appreciated. Thanks are also due to Alison Corrall, who spent many hours learning to fit the data, thereby helping to flush out the remaining bugs in the simulation software. Also of mention are the many conversations I have had during the course of this research with Vighen Pacradouni, Francois Sfigakis, and Jody Mandeville, they were all very helpful as a sounding board for ideas. Jody and Vighen deserve special mention for allowing me to pretend that I wasn't just talking to myself!

Others who deserve special mention are my family members and Aloys Schmalz, all of whom helped me keep (somewhat) sane during this process. A special mention also goes to Elana Brief, who helped me track down a last minute reference in record time.

Chapter 1

Introduction & Motivation

The Coulomb interaction between photo-excited electrons and holes in III-V semiconductors and semiconductor heterostructures is known to be an important factor that influences the shape and energy of optical absorption spectra near the fundamental absorption edge of these materials. The effects range over at least several meV and are particularly evident in the absorption spectra of quantum wells and wires (planar and linear heterostructures respectively). However, despite much work, a full quantitative understanding of these Coulomb effects has been elusive.

Part of the difficulty in making quantitative progress on understanding these Coulomb effects, especially in quantum wells, is due to the competing influence of intrinsic dephasing mechanisms and geometric imperfections. Random geometric imperfections in narrow quantum wells can, for example, generate additional localization. Since these effects will also be present in any devices made from these structures, it is important to understand and quantify their influence on the optical properties.

In operation, practical devices often contain a relatively high density of electrons and/or holes in the optically active region. This background of free particles modifies the bare electron-hole Coulomb interaction (many-body physics) and it is important to be able to understand and model these effects. These interactions are especially important in narrow semiconductor quantum wells (QW) where the effects of Coulomb interactions can be quite pronounced — even at room temperature where most practical devices, such as semiconductor lasers, operate.
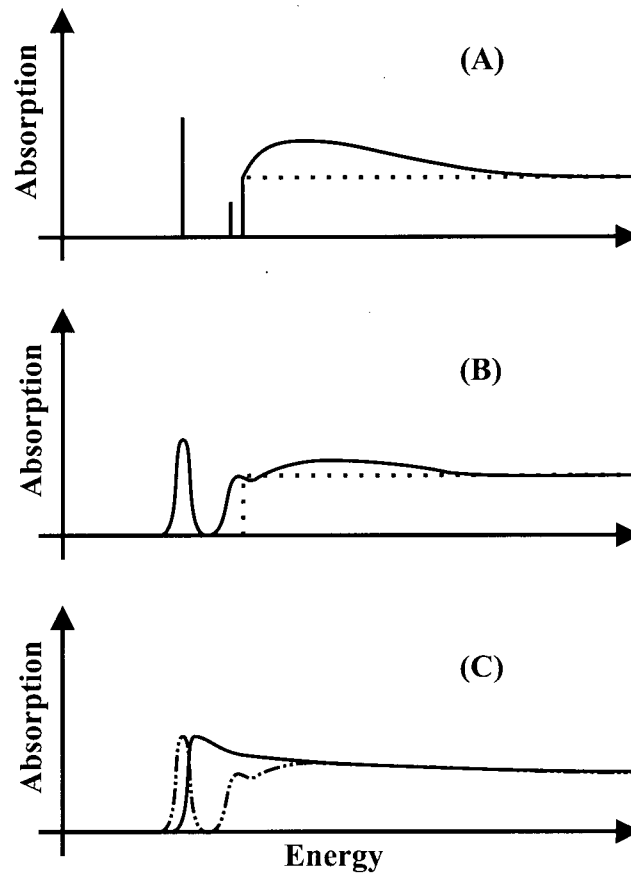
Figure 1.1: Schematic illustrations of the effects of Coulomb interactions on linear absorption in a 2-D quantum well. (A) Without (dashed line) and with (solid lines) Coulomb interactions. (B) The solid line shows the added effects of intrinsic dephasing mechanisms, and the dashed line corresponds to that shown in (A). (C) The solid line shows the effects of having excess carriers in the well, with the dash-dotted line corresponding to the solid line in (B).

Figure 1.1 schematically illustrates the effect of the electron-hole Coulomb interaction on the linear absorption spectrum near the band edge of an ideal 2-dimensional (2D) quantum well. In (A), the dashed line shows how the absence of Coulomb effects would lead to a sharp continuum transition (band edge) in the absorption spectra. When Coulomb interactions between electrons and holes are considered, the shape of the continuum absorption is altered (called the Sommerfeld enhancement) and a series of hydrogen-like transitions appear below the continuum edge, corresponding to bound

electron-hole (exciton) states [1].

Dephasing mechanisms such as electron-hole recombination and carrier-phonon scattering broaden the transitions [1,2]. Geometric imperfections also broaden the transitions and could also cause additional localization in some regions of the quantum well. This is illustrated in part (B) of Figure 1.1. Inhomogeneous broadening caused, for example, by geometric variations inside and between quantum wells, widens these features further. The combination of these broadening mechanisms tends to obscure the individual transitions, making quantitative determination of the exact energy position of the excited excitonic states and continuum difficult.

In addition to the single exciton states, two-exciton bound states (biexcitons) can also form in these materials at intermediate optical excitation densities [1,2]. The energy required to create these states is slightly less than that required to create two free, single exciton states. The optical emission from a biexciton state creates a photon and 1S exciton, with the emitted photon at slightly lower energy than the 1S exciton energy. The presence of inhomogeneous broadening blends the emission from these two states, obscuring evidence of the biexciton transition.

Figure 1.1 (C) illustrates the effect of excess free carriers in a doped 2-D quantum well. Qualitatively, one would expect these carriers to screen the single electron-hole interaction, decreasing the binding energy and reducing the oscillator strength. Rigorous theoretical treatments suggest that the absorption edge of doped quantum wells takes the form of a Fermi edge (power law) singularity, similar to what is observed in the X-ray absorption spectra of metals [3,4]. However, the doped quantum well system is different from metals, and interesting new features are predicted. For example, the main absorption threshold has been associated with the excitation of a negatively charged exciton, or trion, even at low doping densities [4–6].

1.1 Experimental Probes

Both experimental and theoretical developments are needed to attempt to separate and quantify the effects discussed above. Experimentally, two optical probes are used in this work to study the properties of the electrons and holes in multiple quantum well samples. These two techniques are linear absorption and a nonlinear, third-order, coherent polarization mixing process called four-wave-mixing (FWM).

1.1.1 Linear Absorption

Linear absorption is relatively easy to implement, for example by measuring the normalized transmission through a sample. This technique can be used to estimate the binding energies of excitons [7], and places an upper limit on the intrinsic dephasing rate [8]. Extensive experimental and theoretical results have been reported on undoped quantum heterostructures [7, 9–15]. The accuracy of the parameters extracted directly from absorption spectra are often limited by inhomogeneous broadening of the bandedge features.

Inhomogeneous broadening is particularly problematic in quantum wells with widths below about 8 nm, in which just a half a monolayer variation in thickness can lead to energy shifts on the order of the exciton binding energies [16, 17]. This broadening interferes with the accurate determination of binding energies, continuum edge energies, and excited state energies. It also completely masks the intrinsic dephasing rates, which can be below a single meV.

Linear absorption spectra from n-doped quantum wells were first observed and reported by Skolnick, Rorison, Nash, et. al. in 1987 [18]. They reported evidence of strong enhancement of the luminescence spectra close to the Fermi-edge in the doped quantum well, arguing that localized holes were necessary for its presence. The absorption edge's asymmetrically broadened power law dependence (or, Fermi-edge singularity) for excitons in semiconductors had been previously predicted [3]. Further observations, however, showed that there was evidence for the presence of doubly occupied states (charged exci-

tons, or trions) when excess electrons were present in the wells, and that the onset of the Fermi-edge singularity corresponded to the presence of these charged excitonic states, a state not included in the previous theories, even in the presence of a dense 2-D electron gas (for example, see Finkelstein [19], Shields [20], and Buhmann [21]).

Works by Hawrylak [22] and Brum [4] attempted to remedy this theoretically, by modelling the transition from the excitonic to the Fermi-edge state, including the doubly occupied state and electron-electron interactions missing from previous theoretical treatments. This work is summarized by Brown, et. al. [5,6], who observed absorption and luminescence from a series of doped and undoped quantum wells, narrower than those in the above works. These narrow wells allowed a clear separation of the light and heavy hole absorption peaks and allowed them to estimate the power law exponents as a function of Fermi-energy, comparing them to the theoretical predictions. In addition, Brown [6] provided evidence that localization may not be required for the presence of the Fermi-edge singularity to be observed, showing that more work was necessary on both the theoretical and experimental levels.

Although providing more information about the Fermi-edge singularity and its transition with increased excess electron doping, the amount of information that was extractable was, however, limited by the inhomogeneous broadening in these samples. This did not allow for clear experimental evidence of both neutral and charged-excitons that were theoretically predicted. To get around these problems, associated with inhomogeneous broadening, nonlinear optical spectroscopy can sometimes be used to access the intrinsic material properties, even in the presence of significant inhomogeneous broadening, as described below.

1.1.2 Four-Wave Mixing

One technique that can minimize effects due to inhomogeneous broadening is nonlinear, third-order, four-wave mixing (FWM). It separates inhomogeneous effects from intrinsic effects in much the same way that spin-echo techniques achieve this goal in nuclear
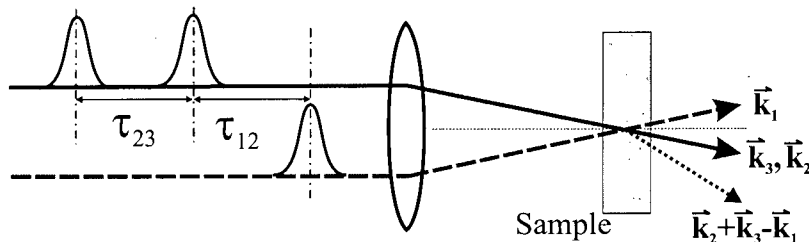
Figure 1.2: Schematic illustration of four-wave mixing. For this work the two pulse four-wave mixing geometry is used, where $\tau_{23} = 0$.

magnetic resonance [23]. Conceptually, FWM can be best understood by assuming a three-pulse excitation scheme, as illustrated schematically in Figure 1.2. Two relatively strong "pump" beams are used to produce a transient refractive index grating in the system of interest. A relatively weak third beam is then used to probe the decay of the transient grating, via diffraction.

More specifically, the first pulse incident on the sample (1) sets up a coherent polarization in the sample which immediately starts to evolve according to Schrodinger's equation, while decaying due to dephasing collision processes. A second beam (2) hits the sample after the first one, setting up another polarization wave that interacts with what remains of the polarization excited by the first pulse, thus forming a polarization grating. This effectively modulates the refractive index of the material in a periodic manner, where the strength of the grating depends on the evolution of the polarization waves excited by the first two pulses. In general, this evolution can be probed by diffracting a third beam from the transient grating, while varying the relative arrival times of all three pulses. It is the diffraction of the third pulse that provides the FWM signal.

Several optical geometries can be used to obtain useful FWM signals. The one in Figure 1.2 corresponds closely to the one used in the present work, where a "two-pulse" geometry is used. In this case, the second pulse also acts as the third pulse (that is, the angle and delay between the second and third pulses is zero). This is a popular scattering configuration [24–26] that provides background free diffraction signals using a single (variable) delay line.
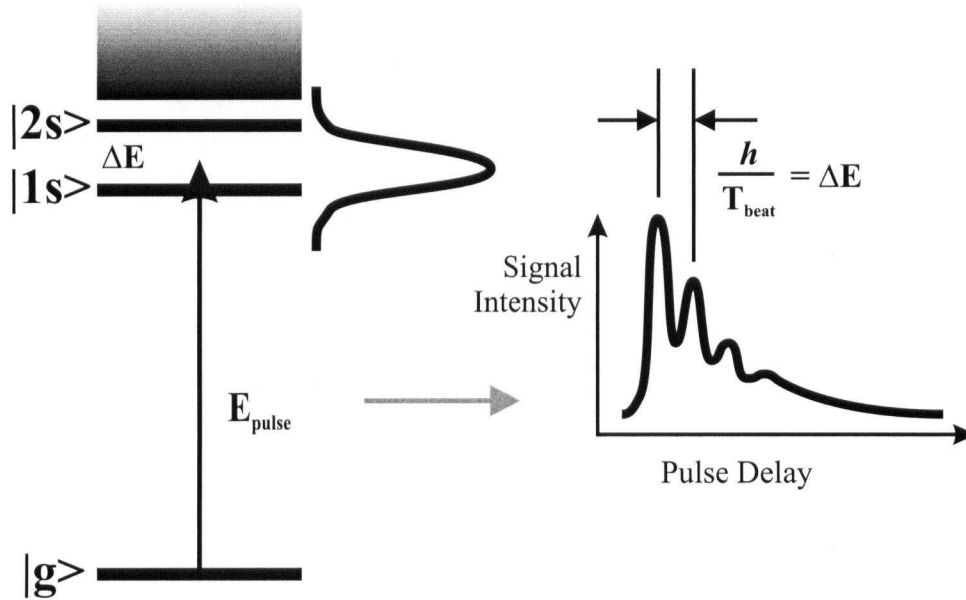
Figure 1.3: Schematic illustration of a four-wave mixing signal. On the left is a system of levels; for example, it could be exciton 1s, 2s, ... levels, along with the continuum states. The laser pulse overlapping the two levels is also illustrated. On the right, an illustration of the expected FWM signal resulting from the interaction of the pulse with two energy levels.

A variety of pulse durations, typically from 25 fs to several ps, have been used to study semiconductor heterostructures [26–28]. The pulse duration limits the minimum dephasing rates that can be measured using this time-domain technique. If the system under study consists of a single, isolated state, the FWM decay rate can be used to deduce the homogeneous dephasing rate of that level as a function of temperature and other system parameters. When more than one energy level can be coherently driven by the finite bandwidth of the excitation pulses , the resultant FWM signal will oscillate as it decays. The period of the beat signal is equal to the energy separation between the two levels. This is illustrated schematically in Figure 1.3, where the expected FWM signal resulting from the spectral overlap of a pulse with two single-particle states (labelled 1S & 2S) in the system is illustrated. Measuring these beats provides an accurate estimate of the energy separations in a system, even in the presence of substantial inhomogeneous broadening.

The FWM technique described above can be applied to a wide variety of material systems as long as the excitation pulses can be tuned in the relevant energy range and have pulse widths appropriate to the processes being studied. By varying the input pulse central frequencies, intensity, and polarization of the input laser pulses, the FWM technique can provide a wealth of information about the nature of the particles present in the system not available through the linear absorption studies.

Early theoretical developments of the FWM technique, based on the simplifying assumption of delta-function excitation pulses, were used to explain the coherent beating observed between the light and heavy hole exciton states in relatively wide, undoped quantum wells [24, 25]. Although excited excitonic states were also observed using this technique [28–31], no attempts were made to quantitatively extract data from these observations. When evidence of biexciton states (two bound excitons) was found, these theoretical developments were extended to include the treatment of biexcitons [26, 32]. Biexciton studies [26, 32] measured the binding energies of the biexciton and dephasing rates of the exciton and biexciton states as a function of input pulse detuning [26] and temperature [33]. An important feature to come out of these studies was that localization effects could dramatically increase the binding energy of these weakly bound states [17, 34, 35], increasing them by up to about 2× what was expected without localization effects being present.

Although much work has been done using the FWM technique to experimentally investigate light hole – heavy hole beating and to identify and characterize biexciton binding in semiconductors, little has been done in quantum wells as narrow as those in this work. In addition few studies have looked at narrow, doped quantum wells, where charged excitons are expected to be the dominant mechanism [5]. Of those that have experimentally looked at these systems with the coherent FWM technique [36–38], the main observation was an inhibition of the scattering rate near the Fermi energy in a relatively highly doped sample. No studies comparable to those conducted here on a lightly doped sample have been reported. To our knowledge, there have also been no

attempts such as the one in this work to conduct extensive, quantitative experiments with an integrated theoretical approach, to extract both linear and nonlinear material parameters simultaneously from the data.

1.2 Material Structure

The material structures used in this study consisted of high quality samples of 50–5 nm gallium arsenide (GaAs) multiple quantum wells with aluminium gallium arsenide ($Al_{0.3}Ga_{0.7}As$) barrier layers, with a variety of excess electron dopings in the wells. The materials used for this study are of interest partially for their use in optoelectronic structures such as semiconductor lasers: with transitions in the 800 nm range, they can be used in very short reach fiber optic transmission applications. As well, they form parts of more complex trinary and quaternary alloys, such as InGaAsP (used in longer reach fiber optic transmission systems). Since GaAs/AlGaAs quantum wells have been grown for a longer time, they are available with higher quality than their more complex siblings. This allows for the study of a 'purer' system, freer from impurities than that available from more complex material systems. These same experimental techniques can, however, be applied to a wide variety of semiconductor material systems.

The GaAs quantum well energy structure is illustrated schematically in Figure 1.4, as a function of the in-plane, 2-dimensional, crystal momentum. Only the most relevant levels have been illustrated in the figure. GaAs is a direct gap semiconductor, meaning that the bottom of the conduction band and top of the uppermost valence band coincide, and electrons in the top of the valence band can be directly excited by photons into the bottom of the conduction band.

Although in bulk GaAs the heavy and light hole bands are degenerate at $\vec{k} = 0$, they split apart in the presence of the barriers forming the quantum well. The interaction of the particle wavefunctions with the walls of the well depends, in the effective mass approximation, on the effective mass of the particles in the crystal. Since particles in the two illustrated valence bands have different effective masses, the presence of the
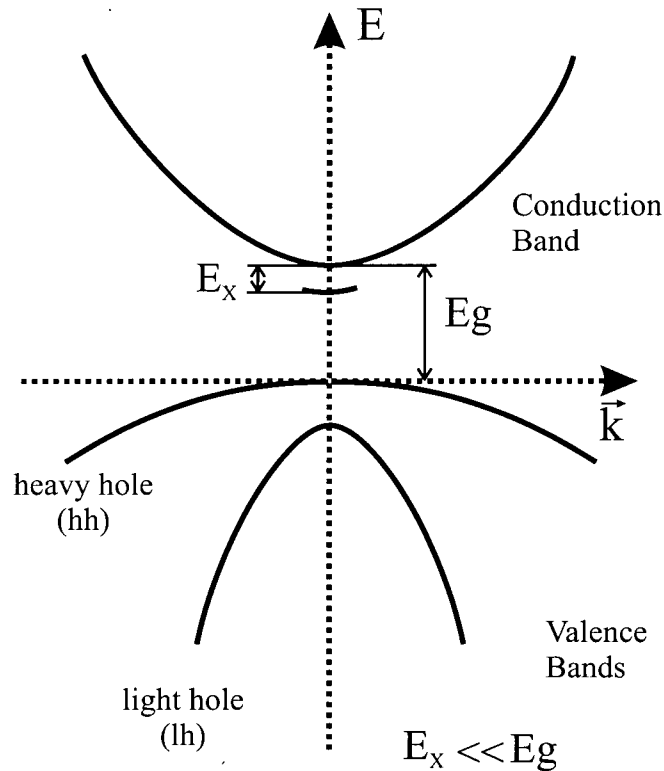
Figure 1.4: Schematic illustration of the energy band structure of a GaAs Quantum Well (QW), where E_g is the bandgap energy and E_X is the exciton binding energy. For simplicity, only the three bands relevant to this work are shown (the heavy and light hole valence bands and the conduction band).

quantum well causes these two levels to shift by different amounts, with the split in energy between the two bands becoming greater as the wells become narrower [39, pages 83-89]. The electrons and holes form hydrogenic-like particles each consisting of an electron and a hole, called excitons. For a 5 nm quantum well, the binding energy of these states is about 16 meV, approximately 1% of the energy gap in the material. As well as the ground state, or 1S exciton, excited excitonic states also exist close to the continuum, labelled 2S, 3S, etc. Two-particle states also exist, formed from two excitons, called biexcitons. Nonlinear FWM signals have, in the past, been used to accurately measure the energy separations and dephasing rates between single-particle light and heavy hole states (in wider quantum well samples), and to study double-particle biexciton states [24–27,32,33].

However, few, if any, studies been done on the narrow, 5 nm, wells used in the present study.

An advantage of the narrow wells is that the separation between light and heavy hole transitions in the GaAs quantum wells is larger and the heavy hole states can be excited independently of the light hole states. This allows determinations of the properties of the excited species under a wider range of input excitation conditions than has been observed in many other studies. In addition, the presence of the excited 2S excitonic state can also be more easily probed. Although observed in previous FWM works [28–31], no attempt has been made to quantitatively measure the properties of the 2S excitonic state. Studies of doped samples have also been reported using the FWM technique [36, 37], although relatively few studies have been published in comparison to those of undoped samples.

1.3 Electromagnetic Models

To properly interpret the experimental data, they must be placed inside a theoretical framework of the systems present in the quantum wells. Ideally, a consistent model would be used to extract information from all orders in the polarization (linear and nonlinear). Typically, this is accomplished within a common framework based on the use of Lorentzian lineshapes, which lead to exponential (or Markovian) decays of both populations (called T_1 times) and coherent signals (called T_2, or dephasing times) [1, 2, 8, 40]. Several models have been developed based on exciting electric fields that are delta-functions in time, for both one-particle states (excitons, including the light-heavy hole beating studies) and two-particle (biexciton) states [24, 25]. These are further simplified in some studies in an attempt to more easily extract parameters from the data, into models that are, essentially, reduced to exponentially decaying oscillations [26]. Although fast to evaluate numerically, these simplified models are inherently inaccurate at short times (within a few pulse-widths of the exciting light pulses). This is due to their exclusion of the exciting field pulse shape, giving inaccurate results when applied to quickly decaying levels.

Another feature lacking from these models is the inclusion of continuum states. Although this can be done by including a large set of closely spaced levels [41–43], a more elegant approach would be preferred, one that could be used consistently in both linear and nonlinear models. For doped samples, the prediction of a power law singularity in the linear absorption data [3] also needs to be taken into account in the model. Chapter 2 describes a model that addresses these issues, including the actual input pulse excitation conditions (pulse shape, polarization, intensity, central frequency) and the power law (Fermi-edge) singularity, which also allows for the inclusion of both discrete and continuum states in the same theoretical framework.

1.4 Thesis Outline

In the rest of this thesis, a report of a systematic study of near-edge linear and nonlinear optical properties of doped and undoped multiple quantum well samples is made, aimed at quantifying and separating the numerous contributions of the material response to photon excitation.

The next chapter outlines extensions to the standard optical model [8] to include continuum states through a general power law singularity, which allows quantitative comparisons to be made with experimental data. A summary of the effects predicted from this theoretical model is given in the latter part of the chapter.

The experimental equipment assembled for study of the quantum wells is discussed in Chapter 3, including a description of the four-wave mixing apparatus and the low temperature system assembled to study these samples over temperatures in the range 5-150 K.

The experimental results are discussed qualitatively in Chapter 4, followed by a quantitative analysis of the experimental data in Chapter 5. Among the highlights of this comparison are the (to our knowledge), first established accurate FWM measurements of 1S-2S exciton energy separation and the 2S exciton dephasing rates as a function of both temperature (from 5 to 40 K) and input pulse detuning. Biexciton binding energies and

dephasing rates are also compared over the same experimental conditions and compared with those reported in the literature, leading to the conclusion that localization effects have a significant influence on the biexciton binding energy in 5 nm quantum wells. A systematic attempt was also made to quantitatively account for the continuum contribution to nonlinear response by fitting a series of spectra obtained at various input pulse detunings, and evidence was found for coherent beating between multi-exciton/free electron complexes in lightly doped material (where the dominant mechanism is predicted to be due to charged exciton species [4–6]).

Chapter 2

Theory

The objective of the modelling done in this work was to develop realistic but practical simulations of the linear absorption and degenerate four wave mixing (DFWM) experimental results obtained from intrinsic and electron-doped 2-D multiple quantum well samples. Since considerable emphasis was placed on quantitatively fitting many spectra, the simulations had to include the finite bandwidth of the pulses used to excite the samples, and they had to run in a reasonable amount of time. It was therefore decided to work directly with the first- and third-order Maxwell equations in which the material response to the optical excitation is described in terms of the linear, $\overleftrightarrow{\chi}^{(1)}$, and nonlinear, $\overleftrightarrow{\chi}^{(3)}$, susceptibilities. Microscopic expressions for $\overleftrightarrow{\chi}^{(1)}$ and $\overleftrightarrow{\chi}^{(3)}$ in terms of the dipole moments, energies, and dephasing rates of near-band edge excitations, including the effects of inhomogeneous broadening, were used to extract these physical parameters from the fitting procedure.

This approach differs from the more general (and more complicated) solution of the full semiconductor optical Bloch equations [33, 42–46] in that it only includes first and third order effects, and it parameterizes the material response rather than self-consistently evaluating it as the system evolves. Based on the results reported in the following chapters, the main deficiency in the simplified treatment is the way it treats high-energy states that exist well above the band edge. Otherwise it describes well a wide range of linear absorption and DFWM results on both doped and undoped multiple quantum well samples.

An outline of this chapter is as follows: the theoretical approach taken to simulate the linear absorption and four-wave mixing data will be described, starting with the general expressions for the polarization ($\vec{\mathbf{P}}^{(n)}$) and susceptibility ($\overleftrightarrow{\mathbf{X}}^{(n)}$). These expressions are then modified to include power law exponents, in order to facilitate the treatment of continuum-like line shapes. The equivalent time-domain response functions are then discussed, along with the inclusion of inhomogeneous broadening. The susceptibility $\overleftrightarrow{\mathbf{X}}^{(1)}$ is then related to the linear absorption coefficient, which is the parameter that is measured experimentally. The $\overleftrightarrow{\mathbf{X}}^{(3)}$ terms that contribute to the resonant, two-pulse, degenerate four-wave mixing (DFWM) process are then discussed, starting with an overview of the FWM process.

A summary of the main features identified by applying these models to estimate the linear absorption and DFWM of our samples are presented in the later half of the chapter, starting in Section 2.6 on page 44. Supplementary material and formulae relevant to several specific pulse-shapes can be found in Appendix A, along with more detail on the numerical approach taken to evaluate some of the expressions derived in this chapter. Formulae describing the pulse shapes and the second harmonic generation process used in the pulse autocorrelation measurements can be found in Chapter 3 and Appendix B.

2.1 Basic Nonlinear Response Formalism

General formulae for the nth order susceptibility, $\overleftrightarrow{\mathbf{X}}^{(n)}$, and polarization, $\vec{\mathbf{P}}^{(n)}$, of materials are derived in nonlinear optics texts such as Butcher & Cotter [8], or Boyd [40]. The formulae expressed here generally follow the notation outlined in Butcher & Cotter. The expression for the nth order local polarization in the time domain, $\vec{\mathbf{P}}^{(n)}(t; \vec{\mathbf{r}})$, is given by

$$P_{\beta_0}^{(n)}(t; \vec{\mathbf{r}}) = \epsilon_o \int\limits_{-\infty}^{+\infty} d\omega_1 \cdots \int\limits_{-\infty}^{+\infty} d\omega_n \, \chi_{\beta_0\beta_1\ldots\beta_n}^{(n)}(-\omega_\Sigma; \omega_1, \ldots, \omega_n; \vec{\mathbf{r}})$$

$$\times \quad E^{\beta_1}(\omega_1; \vec{\mathbf{r}}) \cdots E^{\beta_n}(\omega_n; \vec{\mathbf{r}}) \exp\left\{-i\omega_\Sigma t\right\} \quad (2.1)$$

where $\omega_\Sigma = \omega_1 + \omega_2 + \cdots + \omega_n = \sum_{j=1}^{n} \omega_j$ and the β_j indices refer to the coordinate system (we use cartesian coordinates x, y, & z). The standard tensor notation that repeated indices are to be summed over is also followed [in Equation (2.1), this means summing over, or collapsing, the indices $\beta_1, \ldots, \beta_n$]. The electric field components are taken to have the form

$$\vec{\mathbf{E}}(t; \vec{\mathbf{r}}) = \frac{1}{2} \sum_a \left[\vec{\mathbf{E}}_a(t; \vec{\mathbf{r}}) + \vec{\mathbf{E}}_a^*(t; \vec{\mathbf{r}}) \right] , \qquad (2.2)$$

where

$$\vec{\mathbf{E}}_a(t; \vec{\mathbf{r}}) = \hat{e}_a E_a \left(t - \tau_a - (1/\vec{\mathbf{v}}_{g,a}) \cdot \vec{\mathbf{r}}_a \right) e^{-i\omega_a^p \left(t - \tau_a - (1/\vec{\mathbf{v}}_{g,a}) \cdot \vec{\mathbf{r}}_a \right)} , \qquad (2.3)$$

because of the pulsed nature of the fields used in this work. The delay time for the ath pulse is τ_a, the pulse central frequency is ω_a^p, the pulse envelope in the time domain is $E_a(t)$, and $\hat{e}_a$ is the normalized, complex polarization vector of the pulse.

The group velocity in Equation (2.3) is defined as

$$\vec{\mathbf{v}}_g = \left. \frac{\partial \omega}{\partial \vec{\mathbf{k}}} \right|_{\omega_p} , \qquad (2.4)$$

where the propagation vector, $\vec{\mathbf{k}}$, is given by

$$\vec{\mathbf{k}}(\omega) = \frac{\omega}{c} \vec{\mathbf{n}}(\omega) . \qquad (2.5)$$

Substituting Equations (2.3), (2.4), (2.5) into Equation (2.2) and taking the Fourier transform gives the general expression for the frequency dependent electric fields appearing in the polarization equation (2.1),

$$\begin{aligned}
\vec{\mathbf{E}}(\omega; \vec{\mathbf{r}}) &= \frac{1}{2} \sum_a \left[\vec{\mathbf{E}}_a(\omega; \vec{\mathbf{r}}) + \vec{\mathbf{E}}_a^*(\omega; \vec{\mathbf{r}}) \right] \\
&= \frac{1}{2} \sum_a \left[\hat{e}_a E_a \left(\omega - \omega_a^p; \vec{\mathbf{r}}_a \right) e^{+i \left(\omega \tau_a + \vec{\mathbf{k}}_a(\omega) \cdot \vec{\mathbf{r}}_a \right)} \right. \\
&\qquad \left. + \hat{e}_a^* E_a^* \left(\omega + \omega_a^p; \vec{\mathbf{r}}_a \right) e^{-i \left(\omega \tau_a + \vec{\mathbf{k}}_a(\omega) \cdot \vec{\mathbf{r}}_a \right)} \right] ,
\end{aligned} \qquad (2.6)$$

where $E_a(\omega; \vec{\mathbf{r}})$ is the pulse envelope profile in the frequency domain.

Applying the Fourier transform definition (see List of Symbols, page 156) to $\overrightarrow{\mathbf{P}}^{(n)}$ from Equation (2.1), the frequency domain polarization is

$$P_{\beta_0}^{(n)}(\omega; \overrightarrow{\mathbf{r}}) = \epsilon_o \int\limits_{-\infty}^{+\infty} d\omega_1 \cdots \int\limits_{-\infty}^{+\infty} d\omega_n \, \chi_{\beta_0\beta_1\ldots\beta_n}^{(n)}(-\omega_\Sigma; \omega_1, \ldots, \omega_n; \overrightarrow{\mathbf{r}})$$

$$\times \quad E^{\beta_1}(\omega_1; \overrightarrow{\mathbf{r}}) \cdots E^{\beta_n}(\omega_n; \overrightarrow{\mathbf{r}})\delta(\omega - \omega_\Sigma) \ . \quad (2.7)$$

If the electric field sum in Equations (2.2) & (2.6) contains m components (and their complex conjugates) then there will be, in general, $(2m)^n$ terms in $\overrightarrow{\mathbf{P}}^{(n)}$ from the field terms alone. The distinguishable characteristic of these terms comes from the spatial dependence of the field components $(\exp\{\pm i\overrightarrow{\mathbf{k}}_a \cdot \overrightarrow{\mathbf{r}}\})$.

The general, non-resonant nth order susceptibility expression is given by

$$\chi_{\beta_0\beta_1\beta_2\ldots\beta_n}^{(n)}\left(-\omega_\Sigma; \omega_1, \omega_2, \cdots, \omega_n; \overrightarrow{\mathbf{r}}\right) = \frac{N}{\epsilon_o \, n! \, \hbar^n \left(\sqrt{2\pi}\right)^{n-1}} \, \mathsf{S_T} \sum_x \rho_o(x)$$

$$\times \left\{ \frac{\mu_{xJ_1}^{\beta_0} \, \mu_{J_1 J_2}^{\beta_1} \, \mu_{J_2 J_3}^{\beta_2} \, \mu_{J_3 J_4}^{\beta_3} \cdots \mu_{J_{n-1} J_n}^{\beta_{n-1}} \, \mu_{J_n x}^{\beta_n}}{\left(\omega_{J_1 x} - \omega_1 - \omega_2 - \cdots - \omega_n\right)\left(\omega_{J_2 x} - \omega_2 - \cdots - \omega_n\right)\cdots\left(\omega_{J_n x} - \omega_n\right)} \right\} , \quad (2.8)$$

where N is the number density of particles (cm^{-3}) and $\rho_o(x)$ is thermal equilibrium fraction of the total population in state x $(\sum_x \rho_o(x) = 1)$. The x index sums over all the states of the system. The indices J_i can, in general, take on values representing all the states of the system. The overall permutation symmetry operator, $\mathsf{S_T}$, is only valid away from system resonances, where dephasing can be ignored and the susceptibility varies slowly. It provides a convenient way to compactly write the susceptibility. The operator $\mathsf{S_T}$ indicates that to expand the expression to its full $(n + 1)!$ terms the pairs $(\beta_0, -\omega_\Sigma)$, (β_1, ω_1), ..., (β_n, ω_n) are to be permuted (exchange places) through the expression.

The term $\mu_{J_i J_f}^{\beta_j}$ represents the dipole moment matrix element connecting the two

states i and f

$$\mu_{J_i J_f}^{\beta_j} = \langle\, \psi_f \mid q\, r^{\beta_j} \mid \psi_i \,\rangle = \int\limits_{-\infty}^{+\infty} dr^{\beta_j}\; \psi_f^*(\overrightarrow{\mathbf{r}})\, r^{\beta_j}\, \psi_i(\overrightarrow{\mathbf{r}})$$

$$= \langle\, \psi_i \mid q\, r^{\beta_j} \mid \psi_f \,\rangle^* = \left\{ \int\limits_{-\infty}^{+\infty} dr^{\beta_j}\; \psi_i^*(\overrightarrow{\mathbf{r}})\, r^{\beta_j}\, \psi_f(\overrightarrow{\mathbf{r}}) \right\}^* \qquad (2.9)$$

$$= \mu_{J_f J_i}^{*\,\beta_j} \,,$$

where q is the electron charge. The last two lines show that the absorption and emission dipole moment matrix elements connecting two states are complex conjugates of each other in the electric-dipole approximation. The full dipole interaction between the electric field and the material, proportional to $\langle\, \psi_f \mid q\hat{\boldsymbol{e}}\cdot\overrightarrow{\mathbf{r}} \mid \psi_i \,\rangle$, is evaluated by summing over the vector components β_j in Equation (2.9). These terms lead to what are usually referred to as 'dipole selection rules'.

Close to transitions, or resonances, one or more of the portions of the denominator of some of the terms in Equation (2.8) approach zero, so these 'resonant' terms will dominate the susceptibility. In this region, the resonant terms need to be identified and the equation needs to be modified to include dephasing processes.

2.1.1 Resonant terms and Inclusion of Dephasing

The selection of resonant terms and inclusion of dephasing in the susceptibility expressions is outlined in this section. Resonant terms are those for which the driving frequencies of the laser fields cause the denominator in some of the terms of the susceptibility in Equation (2.8) to go to zero. For third order polarization in semiconductor quantum wells, for example, 8 of the 24 terms in Equation (2.8) are resonant when the laser is tuned near the energy of the bandgap in the quantum well.

The resonant terms are identified by expanding the expression in Equation (2.8) into its $(n+1)!$ terms and searching for the terms where the denominator goes to zero. This must be done for each set of energy levels, $\omega_{J_i x}$, that can be expected in the system under

consideration. Resonant terms are those for which **all** the terms in the denominator are zero under this procedure.

Dephasing, also referred to as *homogeneous* broadening, is included phenomenologically using a single damping parameter, $\Gamma_{J_i x}$, for each transition. The inclusion of this broadening mechanism in the denominator terms of the susceptibility leads to an exponential decay of the polarization in time. The $\Gamma_{J_i x}$ terms represent the influence of coherence-destroying processes such as phonon scattering and collisions with other particles.

As was mentioned when the nth order susceptibility, $\overleftrightarrow{\boldsymbol{\chi}}^{(n)}$, was defined in Equation (2.8), the overall permutation symmetry operator $\mathsf{S_T}$ only applies away from resonance, where dephasing can be neglected. In our work we only include resonant contributions to $\overleftrightarrow{\boldsymbol{\chi}}^{(n)}$ that can be identified after expanding the expression for $\overleftrightarrow{\boldsymbol{\chi}}^{(n)}$ (Equation (2.8)) by permuting the pair $(\beta_0, -\omega_\Sigma)$ with each of the (β_i, ω_i) pairs in turn. The dephasing terms, $\Gamma_{J_i x}$, are then inserted in the denominators with the same sign as all the ω_i terms. This ensures that they lead to physically realistic, exponential decays in the time domain. This permutation process generates $(n+1)$ terms in the $\overleftrightarrow{\boldsymbol{\chi}}^{(n)}$ expansion

$$
\chi^{(n)}_{\beta_0\beta_1\beta_2...\beta_n}\left(-\omega_\Sigma;\omega_1,\omega_2,\cdots,\omega_n;\overrightarrow{\mathbf{r}}\right) = \frac{N}{\epsilon_o\, n!\, \hbar^n \left(\sqrt{2\pi}\right)^{n-1}}\, \mathsf{S}\sum_x \rho_o(x) \times \Bigg\{
$$

$$
\frac{\mu^{\beta_0}_{xJ_1}\, \mu^{\beta_1}_{J_1J_2}\, \mu^{\beta_2}_{J_2J_3}\, \mu^{\beta_3}_{J_3J_4}\cdots\mu^{\beta_{n-1}}_{J_{n-1}J_n}\, \mu^{\beta_n}_{J_n x}}{\left(\omega_{J_1 x}-\omega_1-\cdots-\omega_n-i\Gamma_{J_1 x}\right)\left(\omega_{J_2 x}-\omega_2-\cdots-\omega_n-i\Gamma_{J_2 x}\right)\cdots\left(\omega_{J_n x}-\omega_n-i\Gamma_{J_n x}\right)}
$$

$$
+\ \frac{\mu^{\beta_1}_{xJ_1}\, \mu^{\beta_0}_{J_1J_2}\, \mu^{\beta_2}_{J_2J_3}\, \mu^{\beta_3}_{J_3J_4}\cdots\mu^{\beta_{n-1}}_{J_{n-1}J_n}\, \mu^{\beta_n}_{J_n x}}{\left(\omega_{J_1 x}+\omega_1+i\Gamma_{J_1 x}\right)\left(\omega_{J_2 x}-\omega_2-\cdots-\omega_n-i\Gamma_{J_2 x}\right)\cdots\left(\omega_{J_n x}-\omega_n-i\Gamma_{J_n x}\right)}
$$

$$
+\ \frac{\mu^{\beta_2}_{xJ_1}\, \mu^{\beta_1}_{J_1J_2}\, \mu^{\beta_0}_{J_2J_3}\, \mu^{\beta_3}_{J_3J_4}\cdots\mu^{\beta_{n-1}}_{J_{n-1}J_n}\, \mu^{\beta_n}_{J_n x}}{\left(\omega_{J_1 x}+\omega_2+i\Gamma_{J_1 x}\right)\left(\omega_{J_2 x}+\omega_1+\omega_2+i\Gamma_{J_2 x}\right)\cdots\left(\omega_{J_n x}-\omega_n-i\Gamma_{J_n x}\right)}
$$

$$
\vdots
$$

$$
+\ \frac{\mu^{\beta_n}_{xJ_1}\, \mu^{\beta_1}_{J_1J_2}\, \mu^{\beta_2}_{J_2J_3}\, \mu^{\beta_3}_{J_3J_4}\cdots\mu^{\beta_{n-1}}_{J_{n-1}J_n}\, \mu^{\beta_0}_{J_n x}}{\left(\omega_{J_1 x}+\omega_n+i\Gamma_{J_1 x}\right)\left(\omega_{J_2 x}+\omega_1+\omega_n+i\Gamma_{J_2 x}\right)\cdots\left(\omega_{J_n x}+\omega_1+\cdots+\omega_n+i\Gamma_{J_n x}\right)}\Bigg\},
$$

$$
(2.10)
$$

where the permutation symmetry operator, S, indicates that the full expression for the

susceptibility is obtained by permuting the pairs (β_1, ω_1), (β_2, ω_2), ..., (β_n, ω_n). This generates $n!$ terms for each of the $(n+1)$ terms from the expansion of the overall permutation symmetry operator. Since the signs in front of the dephasing components are the same for the $n!$ terms in each of the $(n+1)$ terms in Equation (2.10), the appropriate resonant terms, including dephasing, can be extracted from the expression by comparing them with the previously identified resonant terms.

An example of the full 24 term expansion for $\overleftrightarrow{\chi}^{(3)}$ including the dephasing components is given in Appendix A (Table A.2, page 171), along with a table identifying the resonant terms. Also included is an algorithm for determining which terms in $\overleftrightarrow{\chi}^{(n)}$ are resonant, along with the sign of the dephasing components for each term in the denominator.

2.1.2 The Power Law Exponent

The expression for the nth order susceptibility presented so far was originally derived for systems with discrete transitions. In semiconductors there are discrete "excitonic" transitions only below the "continuum" edge, and only strictly in pure material. When exciting with short pulses and/or when studying samples with mobile free carriers present, one is not typically dealing with only discrete transitions.

From a modelling or theoretical perspective we can overcome this, in principle, by including a dense set of discrete transitions, with frequency dependent dipole moments, to represent the "continuum", or non-Lorentzian lineshapes. This approach works well for Gaussian-shaped distributions, and is in fact exactly how inhomogeneous broadening is included (see the discussion in Section 2.2, page 24). This is, however, more difficult for the continuum.

In approaches that solve the full semiconductor optical Bloch equations, the continuum is dealt with by including a set of closely-spaced Lorentzian levels, associated with different $\mathbf{k}$ (momentum) states [41–43]. The oscillator strength is allowed to vary with $\mathbf{k}$, typically using a phenomenological cutoff function in $\mathbf{k}$. With the significant amount of fitting we wished to accomplish with our model, avoiding the inclusion of a large number

of continuum states with variable oscillator strengths and dephasing rates was desirable. Since a power law response function was adopted to describe the transitions in the doped samples, we chose to approximate the continuum response with a power law response function that, effectively, provides a form of energy-dependent oscillator strength in the continuum.

This approach was motivated by theoretical treatments suggesting that the "Fermi-edge singularity" observed in the core level X-ray absorption spectra of metals is also present in doped semiconductors [3], leading to the prediction of a power law-like absorption edge. A recent review of this is given by Brum and Hawrylak [4], who report fitting the linear absorption excitonic edge of the n-doped Multiple Quantum Well (MQW) samples described in Chapter 3 to a power law function of the form

$$A(\omega) \approx (\omega - \omega_o)^{-\alpha} \tag{2.11}$$

with the power law exponent, α, approaching 0 as doping increases. This reflects the experimental observation that the absorption peak broadens asymmetrically as the density of excess carriers in the conduction band increases, evolving towards a step-like 2–D single particle continuum lineshape. Here we adopt this power law response function as a simple means of describing the linear and nonlinear response of realistic quantum well systems.

The power law exponent behaviour is inserted in a consistent manner for both linear and nonlinear susceptibilities, by simply adding the exponent to the denominator terms in the susceptibility expression. For the linear susceptibility, this gives the result that

$$\chi^{(1)}_{\beta_0\beta_1}\left(-\omega_\Sigma;\omega_1;\vec{r}\right) = \frac{N}{\epsilon_o\hbar}\sum_x \rho_o(x)\left\{\frac{\mu^{\beta_0}_{xJ_1}\mu^{\beta_1}_{J_1x}}{(\omega_{J_1x}-\omega_1)^{\alpha_{J_1x}}} + \frac{\mu^{\beta_1}_{xJ_1}\mu^{\beta_0}_{J_1x}}{(\omega_{J_1x}+\omega_1)^{\alpha_{J_1x}}}\right\}. \tag{2.12}$$

Extending the general susceptibility expression to include the power law exponent

gives

$$\chi^{(n)}_{\beta_0\beta_1\beta_2...\beta_n}\left(-\omega_\Sigma;\omega_1,\omega_2,\cdots,\omega_n;\overrightarrow{\mathbf{r}}\right) = \frac{N}{\epsilon_o\,n!\,\hbar^n\left(\sqrt{2\pi}\right)^{n-1}}\,\mathsf{S_T}\sum_x\rho_o(x)$$

$$\times\left\{\frac{\mu^{\beta_0}_{xJ_1}\,\mu^{\beta_1}_{J_1J_2}\,\mu^{\beta_2}_{J_2J_3}\,\mu^{\beta_3}_{J_3J_4}\cdots\mu^{\beta_{n-1}}_{J_{n-1}J_n}\,\mu^{\beta_n}_{J_nx}}{\left(\omega_{J_1x}-\omega_1-\omega_2-\cdots-\omega_n\right)^{\alpha_{J_1x}}\left(\omega_{J_2x}-\omega_2-\cdots-\omega_n\right)^{\alpha_{J_2x}}\cdots\left(\omega_{J_nx}-\omega_n\right)^{\alpha_{J_nx}}}\right\}\,.$$

$$(2.13)$$

The α_{J_ix} are the power law exponents for the transition between levels J_i and x, corresponding to the transition energy ω_{J_ix}. This formula has been given for the general susceptibility equation without dephasing terms, as the inclusion of the α_{J_ix} exponents is not modified by that procedure.

2.1.3 Time Response Functions

While the frequency domain approach (Equations (2.1), (2.7), (2.8)) is often used, it is sometimes convenient to use the analogous time domain approach when dealing with time-resolved data. Inserting the Fourier transform definition for $E_{\beta_i}(\omega_i)$ into the time dependent polarization expression (Equation (2.1)), the polarization expression transforms into

$$P^{(n)}_{\beta_0}(t;\overrightarrow{\mathbf{r}}) = \epsilon_o\int_{-\infty}^{+\infty}dt_1\cdots\int_{-\infty}^{+\infty}dt_n\,R^{(n)}_{\beta_0\beta_1...\beta_n}(t_1,\ldots,t_n;\overrightarrow{\mathbf{r}})E^{\beta_1}(t-t_1;\overrightarrow{\mathbf{r}})\cdots E^{\beta_n}(t-t_n;\overrightarrow{\mathbf{r}})$$

$$= \epsilon_o\int_{-\infty}^{+\infty}dt_1\cdots\int_{-\infty}^{+\infty}dt_n\,R^{(n)}_{\beta_0\beta_1...\beta_n}(t-t_1,\ldots,t-t_n;\overrightarrow{\mathbf{r}})E^{\beta_1}(t_1;\overrightarrow{\mathbf{r}})\cdots E^{\beta_n}(t_n;\overrightarrow{\mathbf{r}})\,,$$

$$(2.14)$$

where $\overleftrightarrow{\mathbf{R}}^{(n)}$ is a rank $(n+1)$ tensor, called the nth order response function. It has the same symmetry properties as the susceptibility tensor. From causality, it has the property that it is zero for negative arguments. As one might expect, the Fourier transform changes the multiplication of susceptibility and electric fields in frequency space to a convolution of the response function and electric fields in time space. The susceptibility and response

functions are related to each other through

$$\chi^{(n)}_{\beta_0\beta_1\ldots\beta_n}(-\omega_\Sigma;\omega_1,\ldots,\omega_n;\vec{\mathbf{r}}) = \frac{1}{(2\pi)^{n/2}} \int\limits_{-\infty}^{+\infty} dt_1 \cdots \int\limits_{-\infty}^{+\infty} dt_n$$

$$\times\ R^{(n)}_{\beta_0\beta_1\ldots\beta_n}(t_1,\ldots,t_n;\vec{\mathbf{r}})\quad \exp\left\{i\sum_{j=1}^{n}\omega_j t_j\right\} \quad (2.15)$$

and

$$R^{(n)}_{\beta_0\beta_1\ldots\beta_n}(t_1,\ldots,t_n;\vec{\mathbf{r}}) = \frac{1}{(2\pi)^{n/2}} \int\limits_{-\infty}^{+\infty} d\omega_1 \cdots \int\limits_{-\infty}^{+\infty} d\omega_n$$

$$\times\ \chi^{(n)}_{\beta_0\beta_1\ldots\beta_n}(-\omega_\Sigma;\omega_1,\ldots,\omega_n;\vec{\mathbf{r}})\quad \exp\left\{-i\sum_{j=1}^{n}\omega_j t_j\right\}. \quad (2.16)$$

The denominator terms in the susceptibility tensor, including the power law exponent, are of the form

$$\frac{1}{(\pm\omega_j + \Delta \pm i\Gamma_j)^{\alpha_j}}, \quad \text{where} \quad \Gamma_j > 0 \quad \text{and} \quad 0 < \alpha_j \le 1, \quad (2.17)$$

where Δ contains the frequency components not dependent on j, and may include other $\omega_{i(\ne j)}$ terms as well as the ω_{J_jx} term. Assuming that the susceptibility denominator terms can be separated in this manner, which is always the case for the resonant terms in this work, the equivalent terms in the response function can be found by taking the Fourier transform of Equation (2.17). These form a set of interconnected terms, each with the form [47, Page 364, Section 3.382, equation 4]

$$\frac{(\mp i)^{\alpha_j}\sqrt{2\pi}}{\Upsilon(\alpha_j)}\, \mathbf{H}(t_j)\, t_j^{\alpha_j - 1}\, e^{\pm i\,(\Delta \pm i\Gamma_j)\,t_j}, \quad (2.18)$$

where $\Upsilon(\alpha_j)^\dagger$ is the generalized factorial function and the Heaviside step function, $\mathbf{H}(t_j)$, reflects the causality condition. This expression is subject to the restrictions that $[\mathbb{R}e\{\alpha_j\} > 0, \Gamma_j > 0]$. The restriction $\Gamma_j > 0$ is physically reasonable, as there

---

$\dagger$ The generalized factorial function, or Gamma function, is usually represented by the symbol $\Gamma(z)$. The Greek letter Upsilon (Υ) is used in this work to remove potential confusion between the Gamma function and the dephasing or inhomogeneous broadening terms, both of which use the Gamma symbol (Γ).

is always a finite time scale where coherence is lost or the population recombines. The restriction $\mathbb{R}e\{\alpha_j\} > 0$ means that the discrete-level case we started with ($\alpha_j = 1$) is a valid one and provides a limiting case to check results obtained with the power law exponent. The case $\alpha_j \to 0$ corresponds to the continuum limit.

2.2 Inhomogeneous Broadening

In contrast to homogeneous broadening, inhomogeneous broadening is due to fluctuations in the environment that particles in the system see in different physical areas. This could be due, for example, to fluctuations in the quantum well width either within a well or, in the case of a multiple quantum well sample, in different wells being experimentally probed at the same time. This process leads to a distribution of energy levels within a system that broadens the linear response spectra and generally makes features more difficult to distinguish. In certain nonlinear cases (Section 2.6) inhomogeneous broadening is actually advantageous, as it reveals physical features that would otherwise be unobservable.

The general approach to inhomogeneous broadening is to do a convolution of a weight function with the homogeneous polarization expression, integrating over the distinguishable level frequency(ies) involved, as shown in

$$\overrightarrow{\mathbf{P}}_{inh}^{(n)}\left(\omega;\overrightarrow{\omega}_{\mathbf{o}}^{\mathbf{c}};\overrightarrow{\mathbf{r}}\right) = \int\limits_{-\infty}^{+\infty} d\overrightarrow{\omega}^{\mathbf{c}}\ g_{inh}(\overrightarrow{\omega}^{\mathbf{c}} - \overrightarrow{\omega}_{\mathbf{o}}^{\mathbf{c}})\overrightarrow{\mathbf{P}}_{hom}^{(n)}\left(\omega;\overrightarrow{\omega}^{\mathbf{c}};\overrightarrow{\mathbf{r}}\right) . \tag{2.19}$$

The components of the vector $\overrightarrow{\omega}^{\mathbf{c}}$ are the distinguishable level frequency(ies) $\omega_{J_i x}$ in the expression for the nth order polarization, with the corresponding inhomogeneous central frequency(ies) given by $\overrightarrow{\omega}_{\mathbf{o}}^{\mathbf{c}}$.

The normalized weight function, $g_{inh}(\overrightarrow{\omega}^{\mathbf{c}} - \overrightarrow{\omega}_{\mathbf{o}}^{\mathbf{c}})$, is often taken to be a Gaussian function, expressed in terms of its full-width half maximum (FWHM) parameters $\Gamma_{ij,\,\text{inh}}$. If there is more than one level frequency involved then one has a multivariate distribution, and the integral is taken over a multi-dimensional frequency space, where the dimension equals the number of distinguishable levels. For Gaussian inhomogeneous broadening,

the weight function is [48]

$$g_{inh}(\vec{\omega}^{\mathbf{c}} - \vec{\omega}_{\mathbf{o}}^{\mathbf{c}}) = \left(\frac{4\ln 2}{\pi}\right)^{n/2} |\mathbf{\Gamma}\,\mathbf{\Lambda}\,\mathbf{\Gamma}|^{-1/2}\, e^{-4\ln 2\left((\vec{\omega}^{\mathbf{c}} - \vec{\omega}_{\mathbf{o}}^{\mathbf{c}})\mathbf{\Gamma}^{-1}\,\mathbf{\Lambda}^{-1}\,\mathbf{\Gamma}^{-1}\,(\vec{\omega}^{\mathbf{c}} - \vec{\omega}_{\mathbf{o}}^{\mathbf{c}})\right)}\,.$$

$$(2.20)$$

$\mathbf{\Gamma}^{-1}$ is a 2-D matrix with diagonal elements $\Gamma_{ii}^{-1} = 1/\Gamma_{J_i x,\,\text{inh}}$ and off-diagonal elements zero. The correlation matrix $\mathbf{\Lambda}^{\dagger}$ is a symmetric 2-D matrix with diagonal elements $\Lambda_{ii} = 1$ and off-diagonal elements $\Lambda_{ij} = \Lambda_{ji} = \lambda_{J_i J_j}$, where $0 \le |\lambda_{J_i J_j}| \le 1$. $|\mathbf{\Gamma}\,\mathbf{\Lambda}\,\mathbf{\Gamma}|$ is the determinant of the multiplied matrices. Details of the forms of the 2- & 3-dimensional correlation matrices and their corresponding inhomogeneous polarization expressions are given in Appendix A (Subsection A.1.7).

When all the levels in $\vec{\omega}^{\mathbf{c}}$ are correlated, the multi-dimensional integral reduces to a one-dimensional integral with each $\omega_{J_1 x}$ evaluated according to its respective inhomogeneous broadening $\Gamma_{J_1 x,\,\text{inh}}$. The inhomogeneous polarization equations for first- and nth-order correlated systems are

$$\vec{\mathbf{P}}_{\text{inh}}^{(1)}\left(\omega;\,\omega_{o,\,J_1 x}^{c};\,\vec{\mathbf{r}}\right) = \left(\frac{4\ln 2}{\pi\Gamma_{J_1 x,\,\text{inh}}^{2}}\right)^{1/2} \int\limits_{-\infty}^{+\infty} d\omega_{J_1 x}^{c}\, e^{-\dfrac{4\ln 2}{\Gamma_{J_1 x,\,\text{inh}}^{2}}\left(\omega_{J_1 x}^{c} - \omega_{o,\,J_1 x}^{c}\right)^2}$$

$$\times\ \vec{\mathbf{P}}_{\text{hom}}^{(1)}\left(\omega;\,\omega_{J_1 x}^{c};\,\vec{\mathbf{r}}\right) \qquad (2.21)$$

$$= \int\limits_{-\infty}^{+\infty} dx\, e^{-x^2}\vec{\mathbf{P}}_{\text{hom}}^{(1)}\left(\omega;\,\frac{\Gamma_{J_1 x,\,\text{inh}}}{\sqrt{4\ln(2)}}\,x + \omega_{o,\,J_1 x}^{c};\,\vec{\mathbf{r}}\right)$$

and

$$\vec{\mathbf{P}}_{\text{inh}}^{(n)}\left(\omega;\,\omega_{o,\,J_1 x}^{c};\,\omega_{o,\,J_2 x}^{c};\,\cdots;\,\omega_{o,\,J_n x}^{c};\,\vec{\mathbf{r}}\right) = \int\limits_{-\infty}^{+\infty} dx\ e^{-x^2}$$

$$\times\ \vec{\mathbf{P}}_{\text{hom}}^{(n)}\left(\omega;\,\frac{\Gamma_{J_1 x,\,\text{inh}}}{\sqrt{4\ln(2)}}\,x + \omega_{o,\,J_1 x}^{c};\,\frac{\Gamma_{J_2 x,\,\text{inh}}}{\sqrt{4\ln(2)}}\,x + \omega_{o,\,J_2 x}^{c};\,\cdots\,\frac{\Gamma_{J_n x,\,\text{inh}}}{\sqrt{4\ln(2)}}\,x + \omega_{o,\,J_n x}^{c};\,\vec{\mathbf{r}}\right)\,.$$

$$(2.22)$$

---

† The reference work [48] combines $\mathbf{\Gamma}$ and $\mathbf{\Lambda}$ together. It was noted, however, that the general expression can be separated into component matrices, making the contributions from each part (inhomogeneous broadening and correlation parameters) both easier to construct and to differentiate from each other.

2.3 Linear Absorption

In this section the expression for the linear absorption coefficient is derived from the power law modified susceptibility, including inhomogeneous broadening.

2.3.1 Linear Response and Inhomogeneous Broadening

Following the formula for the nth order polarization (Equation (2.7)), the expression for the first order polarization is given by

$$P_{\beta_0}^{(1)}\left(\omega; \vec{r}\right) = \epsilon_o\, \chi_{\beta_0\beta_1}^{(1)}\left(-\omega; \omega; \vec{r}\right) E^{\beta_1}\left(\omega; \vec{r}\right) \; . \tag{2.23}$$

The linear susceptibility in the above polarization equation is given by

$$\chi_{\beta_0\beta_1}^{(1)}\left(-\omega; \omega; \vec{r}\right) = \frac{N}{\epsilon_o\hbar}\sum_{x, J_1}\rho_o(x)\left\{\frac{\mu_{xJ_1}^{\beta_0}\,\mu_{J_1x}^{\beta_1}}{(\omega_{J_1x} - \omega - i\Gamma_{J_1x})^{\alpha_{J_1x}}} + \frac{\mu_{xJ_1}^{\beta_1}\,\mu_{J_1x}^{\beta_0}}{(\omega_{J_1x} + \omega + i\Gamma_{J_1x})^{\alpha_{J_1x}}}\right\} \; .$$
$$\tag{2.24}$$

Since we are interested in interband transitions from the ground state at low temperatures, this can be simplified to

$$\chi_{\beta_0\beta_1}^{(1)}\left(-\omega; \omega; \vec{\omega}_{\mathbf{ag}}; \vec{r}\right) = \frac{N}{\epsilon_o\hbar}\rho_o(g)\sum_a\frac{\mu_{ga}^{\beta_0}\,\mu_{ag}^{\beta_1}}{(\omega_{ag} - \omega - i\Gamma_{ag})^{\alpha_{ag}}} \; , \tag{2.25}$$

where the sum over a is the sum over bound and continuum excitonic states near the bandgap energy.

Inhomogeneous broadening is included using

$$\chi_{\beta_0\beta_1,\,\text{inhom}}^{(1)}\left(-\omega; \omega; \vec{\omega}_{\mathbf{ag}}^{\mathbf{c}}; \vec{r}\right) = \int_{-\infty}^{+\infty} d\vec{\omega}_{\mathbf{ag}}\,\chi_{\beta_0\beta_1}^{(1)}\left(-\omega; \omega; \vec{\omega}_{\mathbf{ag}}; \vec{r}\right) g_{\text{inh}}\left(\vec{\omega}_{\mathbf{ag}} - \vec{\omega}_{\mathbf{ag}}^{\mathbf{c}}\right)$$

$$= \frac{\sqrt{4\ln(2)}}{\sqrt{\pi}\Gamma_{\text{inh}}}\int_{-\infty}^{+\infty} d\vec{\omega}_{\mathbf{ag}}\,\chi_{\beta_0\beta_1}^{(1)}\left(-\omega; \omega; \vec{\omega}_{\mathbf{ag}}; \vec{r}\right) e^{-\dfrac{4\ln(2)}{\Gamma_{\text{inh}}^2}\left(\vec{\omega}_{\mathbf{ag}} - \vec{\omega}_{\mathbf{ag}}^{\mathbf{c}}\right)^2} \; ,$$

$$\tag{2.26}$$

where we have assumed a normalized Gaussian for the distribution of levels. Carrying

out the integral,

$$
\chi^{(1)}_{\beta_0\beta_1,\text{inhom}}\left(-\omega;\omega;\vec{\mathbf{r}}\right) = \frac{N}{\epsilon_o\hbar}\rho_o(g)\sum_a \mu^{\beta_0}_{ga}\mu^{\beta_1}_{ag}\frac{\sqrt{4\ln(2)}}{\sqrt{\pi}\Gamma_{ag,\text{ inh}}}\int\limits_{-\infty}^{+\infty}d\omega_{ag}\frac{e^{-\dfrac{4\ln(2)}{\Gamma^2_{\text{inh}}}\left(\omega_{ag}-\omega^c_{ag}\right)^2}}{\left(\omega_{ag}-\omega-i\Gamma_{ag}\right)^{\alpha_{ag}}}
$$

$$
= \sqrt{2\pi}\,\frac{N}{\epsilon_o\hbar}\rho_o(g)\sum_a \mu^{\beta_0}_{ga}\,\mu^{\beta_1}_{ag}\,(+i)^{\alpha_{ag}}\left(\frac{\sqrt{8\ln(2)}}{\Gamma_{ag,\text{ inh}}}\right)^{\alpha_{ag}}
$$

$$
\times\;e^{+\dfrac{1}{4}\dfrac{8\ln(2)}{\Gamma^2_{ag,\text{ inh}}}\left(i\Delta_{a\omega}+\Gamma_{ag}\right)^2}\;D_{-\alpha_{ag}}\left(\frac{\sqrt{8\ln(2)}}{\Gamma_{ag,\text{ inh}}}\left(i\Delta_{a\omega}+\Gamma_{ag}\right)\right)\;,
$$

$$(2.27)$$

where $\Delta_{a\omega} = \omega_{ag} - \omega$ and the function $D_{-\alpha_{ag}}(z)$ is called the parabolic cylinder function. For more details of the derivation, see Appendix A (Section A.1.5, page 175).

2.3.2 Susceptibility $\overleftrightarrow{\mathbf{\chi}}^{(1)}$, Permittivity $\overleftrightarrow{\epsilon}$, and the Refractive Index n

Inserting the linear polarization, Equation (2.23), into the wave equation, along with the definition $\mu_o = 1/(\epsilon_o c^2)$, the linear wave equation becomes

$$
\vec{\mathbf{\nabla}}\times\vec{\mathbf{\nabla}}\times\vec{\mathbf{E}}\left(\omega;\vec{\mathbf{r}}\right) = \frac{\omega^2}{c^2}\left(1+\overleftrightarrow{\mathbf{\chi}}^{(1)}_{NR}+\overleftrightarrow{\mathbf{\chi}}^{(1)}\left(-\omega,\omega;\vec{\mathbf{r}}\right)\right)\cdot\vec{\mathbf{E}}\left(\omega;\vec{\mathbf{r}}\right) = \frac{\omega^2}{c^2}\overleftrightarrow{\epsilon}^{(1)}\cdot\vec{\mathbf{E}}\left(\omega;\vec{\mathbf{r}}\right)\;,
$$

$$(2.28)$$

which provides the definition of $\overleftrightarrow{\epsilon}^{(1)}$. We only include a finite range of states in our resonant approximation to $\overleftrightarrow{\mathbf{\chi}}^{(1)}$, and the remaining contributions are taken care of by $\overleftrightarrow{\mathbf{\chi}}^{(1)}_{NR}$. In GaAs, $1+\overleftrightarrow{\mathbf{\chi}}^{(1)}_{NR} \simeq 12.4$ [49].

For GaAs, since $\overleftrightarrow{\mathbf{\chi}}^{(1)}$ is a symmetrical tensor, so is $\overleftrightarrow{\epsilon}^{(1)}$ [8, Chapter 5 & Appendix 3]. This means that principal axes can be found where $\overleftrightarrow{\epsilon}^{(1)}$ is diagonal. Furthermore, for cubic (GaAs) or isotropic materials the components ϵ_{ii} are all the same and the determinant reduces to the more familiar equation

$$
n = \sqrt{\epsilon}\;.
$$

$$(2.29)$$

In the next section, we will relate these results to the absorption coefficient, α_{abs}.

2.3.3 Linear Absorption

From the solution to the wave equation, the imaginary part of the refractive index leads to an exponential rise or decay, depending on whether $n_{\mathbb{I}m}$ is negative or positive. Beer's law relates the exponential coefficient, α_{abs}, to the intensity of the wave, through

$$\partial I / \partial d = -\alpha_{\text{abs}} I \rightarrow I = I_o e^{-\alpha_{\text{abs}} d} \, . \tag{2.30}$$

The intensity of the wave is given by the cycle average of the electric field [8, page 23],

$$I(\omega) = \frac{1}{2} \, \epsilon_o \, c \, n_{\mathbb{R}e}(\omega) \, |\vec{\mathbf{E}}(\omega)|^2 = \frac{1}{2} \, \epsilon_o \, c \, n_{\mathbb{R}e}(\omega) \, |E(\omega)|^2 \, e^{-2 \, (\omega/c) \, n_{\mathbb{I}m}} \, . \tag{2.31}$$

Relating these two, the absorption coefficient is defined as

$$\alpha_{\text{abs}} = 2 \, \frac{\omega}{c} \, n_{\mathbb{I}m} = 2 \, \frac{\omega}{c} \, \mathbb{I}m \left\{ \sqrt{\epsilon} \right\} \simeq \frac{\omega}{c} \frac{\mathbb{I}m \left\{ \overleftrightarrow{\mathcal{X}}^{(1)} \right\}}{\sqrt{\mathbb{R}e \left\{ \epsilon \right\}}} \, , \tag{2.32}$$

where the equation on the right is a valid approximation when absorption is small ($n_{\mathbb{I}m} \ll n_{\mathbb{R}e}$). Note that the imaginary part of $\overleftrightarrow{\epsilon}^{(1)}$ is contained entirely in the expression for $\overleftrightarrow{\mathcal{X}}^{(1)}$, so that $\mathbb{I}m\{\overleftrightarrow{\epsilon}^{(1)}\} = \mathbb{I}m\{\overleftrightarrow{\mathcal{X}}^{(1)}\}$.

2.4 Excitonic States

To this point, the connection between the form of the susceptibility terms and the free carrier or excitonic particles present in the semiconductor wells has not been made explicitly. This connection will be outlined here, before moving on to a discussion of the third-order susceptibility.

The excitonic states consist of a series of hydrogenic-like bound states (1S, 2S, ...) along with a continuum of free electron-hole pairs, with electrons in the conduction band and holes in the valence band [8]. The excitonic ground state corresponds to the 1S exciton state while the crystal ground state, with an electron in the valence band and no hole, corresponds to the ground state of the susceptibility terms.

The electric dipole approximation, which assumes the photon has zero momentum, connects these states through the previously outlined dipole moment terms: $\vec{\mathbf{e}} \cdot \vec{\boldsymbol{\mu}}_{J_i J_f} =$

$\langle \psi_f \mid q\, \vec{\mathbf{e}} \cdot \vec{\mathbf{r}} \mid \psi_i \rangle$. In this expression, ψ_i represents the ground state of the semiconductor and ψ_f represents excited states corresponding to one extra hole in a valence band and one extra electron in the conduction band. The states in the valence band have two spins: $\pm 3/2$ (heavy hole states) or $\pm 1/2$ (light hole states), while the electrons in the conduction band have $\pm 1/2$ spin (in units of $\hbar$). To a good approximation the valence band states in GaAs are derived from p-orbital atomic states and the conduction band states are derived from s-orbital atomic states. The dipole selection rules therefore imply that photons can only excite the spatially symmetric 'singlet' states of the excitons in which the electron and hole spins are anti-symmetric [2, page 230]. Since the photons impart a spin of ± 1 to the particles, the singlet exciton states have a total spin of ± 1. Spin flip forbidden 'triplet' states also exist, with parallel electron and hole spins (± 2 total exciton spin). The triplet states can not be directly dipole-excited, but they do offer a dephasing mechanism (spin flip) for the singlet transition.

All of this means that the relevant states that need to be included in the resonant susceptibility terms are the 1S, 2S, ... , and the continuum, or exciton scattering states, with ± 1 spin. Since the electric dipole approximation implies that the photon momentum is zero this also means that stationary excitons are excited, with center-of-mass wavevector $\vec{\mathbf{K}} = 0$. The absorption coefficient evaluated using this exciton basis in a quantum well is [8, Ch. 8 & 9]

$$\alpha_{\text{abs}}(\omega) = \frac{2(q/m_e)^2}{n_o\, \epsilon_o\, c\, V_{QW}\, \omega} \sum_j |p_j|^2\, \pi\, \mathbb{I}m \left\{ \frac{1}{(E_g - E_j - \hbar\omega) - i\hbar\Gamma_j} \right\}, \qquad (2.33)$$

where j is the sum over the exciton states (1S, 2S, ... , continuum), E_g is the bandgap energy, E_j is the energy of the jth exciton state, and $|p_j|^2$ is the square of the magnitude of the dipole moment term for the jth exciton state. V_{QW} is the quantum well volume. This expression looks similar to the susceptibility expression derived earlier (Equation (2.25)), in the limit $\alpha_j = 1$, but the constants out front are different. The electric-dipole ($\vec{\boldsymbol{\mu}}$) and electric-current ($\vec{\mathbf{p}}$) operators in the expressions are related by [8, page 108]

$$|\mu|^2 = \left(\frac{q}{m_e} \right)^2 \frac{|p|^2}{\omega^2}. \qquad (2.34)$$

By directly comparing the two expressions it is possible to, effectively, determine the appropriate density N to use when applying the generic susceptibility expressions to our semiconductor quantum wells. By comparing Equations (2.24) & (2.32) with Equation (2.33), we see that, effectively,

$$N = \frac{2\pi}{V_{QW}} \, . \tag{2.35}$$

2.5 The Third Order Susceptibility, $\overleftrightarrow{\boldsymbol{\chi}}^{(3)}$, and Polarization, $\overrightarrow{\mathbf{P}}^{(3)}$

Using Equation (2.1) the third order polarization is

$$P_{\beta_0}^{(3)}(t;\overrightarrow{\mathbf{r}}) = \epsilon_o \int\limits_{-\infty}^{+\infty} d\omega_1 \int\limits_{-\infty}^{+\infty} d\omega_2 \int\limits_{-\infty}^{+\infty} d\omega_3 \; \chi_{\beta_0\beta_1\beta_2\beta_3}^{(3)}(-\omega_\Sigma;\omega_1,\omega_2,\omega_3;\overrightarrow{\mathbf{r}})$$

$$\times \quad E^{\beta_1}(\omega_1;\overrightarrow{\mathbf{r}})E^{\beta_2}(\omega_2;\overrightarrow{\mathbf{r}})E^{\beta_3}(\omega_3;\overrightarrow{\mathbf{r}})\exp\{-i\omega_\Sigma t\} \tag{2.36}$$

where $\omega_\Sigma = \omega_1 + \omega_2 + \omega_3$.

The third order susceptibility, derived from Equations (2.10) & (2.13), contains $4! = 24$ distinct terms. Different terms are typically associated with named phenomena such as third harmonic generation, the intensity dependent refractive index, Raman scattering, four-wave mixing, etc. The full 24 term expansion for $\overleftrightarrow{\boldsymbol{\chi}}^{(3)}$, including the dephasing components and power law exponents can be easily generated using

$$\chi_{\beta_0\beta_1\beta_2\beta_3}^{(3)}\left(-\omega_\Sigma;\omega_1,\omega_2,\omega_3;\overrightarrow{\mathbf{r}}\right) = \frac{N}{\epsilon_o\,3!\,\hbar^3\,2\pi}\,\mathsf{S}\sum_x \rho_o(x)$$

$$\times \left\{ \frac{\mu_{xJ_1}^{\beta_0}\,\mu_{J_1J_2}^{\beta_1}\,\mu_{J_2J_3}^{\beta_2}\,\mu_{J_3x}^{\beta_3}}{(\omega_{J_1x}-\omega_\Sigma-i\Gamma_{J_1x})^{\alpha_{J_1x}}(\omega_{J_2x}-\omega_2-\omega_3-i\Gamma_{J_2x})^{\alpha_{J_2x}}(\omega_{J_3x}-\omega_3-i\Gamma_{J_3x})^{\alpha_{J_3x}}} \right.$$

$$+ \frac{\mu_{xJ_1}^{\beta_1}\,\mu_{J_1J_2}^{\beta_0}\,\mu_{J_2J_3}^{\beta_2}\,\mu_{J_3x}^{\beta_3}}{(\omega_{J_1x}+\omega_1+i\Gamma_{J_1x})^{\alpha_{J_1x}}(\omega_{J_2x}-\omega_2-\omega_3-i\Gamma_{J_2x})^{\alpha_{J_2x}}(\omega_{J_3x}-\omega_3-i\Gamma_{J_3x})^{\alpha_{J_3x}}}$$

$$+ \frac{\mu_{xJ_1}^{\beta_2}\,\mu_{J_1J_2}^{\beta_1}\,\mu_{J_2J_3}^{\beta_0}\,\mu_{J_3x}^{\beta_3}}{(\omega_{J_1x}+\omega_2+i\Gamma_{J_1x})^{\alpha_{J_1x}}(\omega_{J_2x}+\omega_1+\omega_2+i\Gamma_{J_2x})^{\alpha_{J_2x}}(\omega_{J_3x}-\omega_3-i\Gamma_{J_3x})^{\alpha_{J_3x}}}$$

$$+ \left. \frac{\mu_{xJ_1}^{\beta_3}\,\mu_{J_1J_2}^{\beta_1}\,\mu_{J_2J_3}^{\beta_2}\,\mu_{J_3x}^{\beta_0}}{(\omega_{J_1x}+\omega_3+i\Gamma_{J_1x})^{\alpha_{J_1x}}(\omega_{J_2x}+\omega_1+\omega_3+i\Gamma_{J_2x})^{\alpha_{J_2x}}(\omega_{J_3x}+\omega_\Sigma+i\Gamma_{J_3x})^{\alpha_{J_3x}}} \right\} \, ,$$

$$\tag{2.37}$$
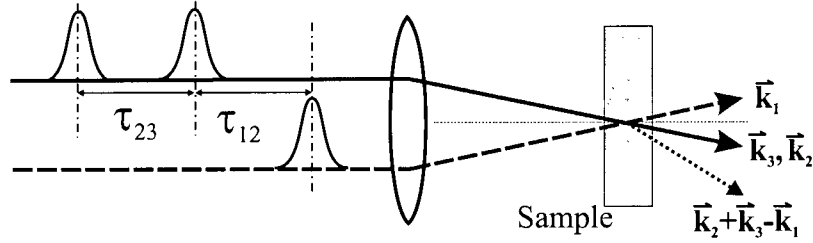
Figure 2.1: Schematic illustration of four-wave mixing. For the two pulse four-wave mixing geometry, $\tau_{23} = 0$.

where the symmetry operator S indicates that the pairs (β_1, ω_1), (β_2, ω_2), and (β_3, ω_3) are to be permuted through each term [generating 6 terms from each of the 4 terms in Equation (2.37)]. All 24 terms are enumerated in Table A.2 (page 171). At this point, to examine which terms are significant requires looking at the specific process under consideration — in this case two-pulse four-wave mixing.

2.5.1 Two-Pulse, Degenerate Four-Wave Mixing – A Special Case of $\overleftrightarrow{\chi}^{(3)}$

Four-wave mixing is a third order sum-difference frequency effect. The usual four-wave mixing case consists of three "strong" input fields that, through the third-order susceptibility $\overleftrightarrow{\chi}^{(3)}$, generate a relatively weak third-order polarization $\overrightarrow{\mathbf{P}}^{(3)}$ that radiates fields that can be detected outside the sample. From the general nth order polarization, Equation (2.1), the general third order polarization is given by

$$P_{\beta_0}^{(3)}\left(t; \overrightarrow{\mathbf{r}}\right) = \epsilon_o \int\!\!\!\int\!\!\!\int_{-\infty}^{+\infty} \chi_{\beta_0\beta_1\beta_2\beta_3}^{(3)\,\text{Resonant}} \left(-\omega_\Sigma; \omega_1; \omega_2; \omega_3; \overrightarrow{\mathbf{r}}\right)$$

$$\times\ E_{\beta_3}\left(\omega_3; \overrightarrow{\mathbf{r}}\right) E_{\beta_2}\left(\omega_2; \overrightarrow{\mathbf{r}}\right) E_{\beta_1}\left(\omega_1; \overrightarrow{\mathbf{r}}\right) \exp\left\{-i\omega_\Sigma t\right\}\ , \quad (2.38)$$

where each of the three electric field terms is given by the sum of field terms in Equation (2.6).

In this work we are concerned with the case where there are two independent pulses that provide the three strong driving fields (see Figure 2.1). The total driving field can

then be written as

$$\mathbf{E}(\omega; \vec{\mathbf{r}}) = \frac{1}{2} \left[\vec{\mathbf{E}}_1(\omega; \vec{\mathbf{r}}) + \vec{\mathbf{E}}_1^*(\omega; \vec{\mathbf{r}}) + \vec{\mathbf{E}}_3(\omega; \vec{\mathbf{r}}) + \vec{\mathbf{E}}_3^*(\omega; \vec{\mathbf{r}}) \right]$$

$$= \frac{1}{2} \left[\quad \hat{e}_1 E_1 \left(\omega - \omega^p; \vec{\mathbf{r}} \right) e^{+i \left(\omega \tau_1 + \vec{\mathbf{k}}_1(\omega) \cdot \vec{\mathbf{r}} \right)} \right. \tag{2.39}$$

$$\left. + \hat{e}_3 E_3 \left(\omega - \omega^p; \vec{\mathbf{r}} \right) e^{+i \left(\omega \tau_3 + \vec{\mathbf{k}}_3(\omega) \cdot \vec{\mathbf{r}} \right)} + \text{c.c.} \right] ,$$

a special case of Equation (2.6). Substituting this field equation into Equation (2.38) results in $4^3 = 64$ terms in the third-order polarization, **for each** susceptibility term. Of these 64 terms there are six that give rise to electric fields that propagate in two forward "background-free" directions, three in the $2\vec{\mathbf{k}}_1 - \vec{\mathbf{k}}_3$ direction and three in the $2\vec{\mathbf{k}}_3 - \vec{\mathbf{k}}_1$ direction. These are called background-free directions because they propagate in physically separate directions from the strong, transmitted input fields ($\vec{\mathbf{k}}_1$ and $\vec{\mathbf{k}}_3$), as shown in Figure 2.1. For the two-pulse four-wave mixing case discussed above, the third-order polarization terms corresponding to fields propagating in these background-free directions are given by

$$\vec{\mathbf{P}}^{(3)}(t; \vec{\mathbf{r}}) = \epsilon_o \int\!\!\!\int\!\!\!\int_{-\infty}^{+\infty} \vec{\chi}_{\text{Resonant}}^{(3)} \left(-\omega_\Sigma; \omega_1; \omega_2; \omega_3; z \right) \exp{-i\omega_\Sigma t}$$

$$\times \left\{ \left[\vec{\mathbf{E}}_3^*(\omega_3)\vec{\mathbf{E}}_1(\omega_2)\vec{\mathbf{E}}_1(\omega_1) + \vec{\mathbf{E}}_1(\omega_3)\vec{\mathbf{E}}_3^*(\omega_2)\vec{\mathbf{E}}_1(\omega_1) + \vec{\mathbf{E}}_1(\omega_3)\vec{\mathbf{E}}_1(\omega_2)\vec{\mathbf{E}}_3^*(\omega_1) \right] e^{+i\left(2\vec{\mathbf{k}}_1 - \vec{\mathbf{k}}_3\right)\cdot\vec{\mathbf{r}}} \right.$$

$$\left. + \left[\vec{\mathbf{E}}_3(\omega_3)\vec{\mathbf{E}}_3(\omega_2)\vec{\mathbf{E}}_1^*(\omega_1) + \vec{\mathbf{E}}_3(\omega_3)\vec{\mathbf{E}}_1^*(\omega_2)\vec{\mathbf{E}}_3(\omega_1) + \vec{\mathbf{E}}_1^*(\omega_3)\vec{\mathbf{E}}_3(\omega_2)\vec{\mathbf{E}}_3(\omega_1) \right] e^{+i\left(2\vec{\mathbf{k}}_3 - \vec{\mathbf{k}}_1\right)\cdot\vec{\mathbf{r}}} \right\} ,$$

$$\tag{2.40}$$

Rigorously, one would insert the linear and nonlinear polarization terms into Maxwell's equations, and solve for the fields radiated by this third-order polarization source in a self-consistent fashion. This is an intractable problem in our case, where the calculation of the third-order polarization alone is very computationally intensive. If we considered the case of a single quantum well, the z-dependence would fall out because the quantum well would essentially act as a thin, delta-function like sheet of polarization with well-defined in-plane momentum. In the realistic case where there are a series of quantum

wells, and where the fields vary slowly in the z-direction, the third order radiated field will be due to a superposition from all of these sheets of dipole radiators. For the purposes of the simulations done in the remainder of this thesis, we are not concerned with the absolute magnitude of the radiated fields, but rather how they depend on frequency and the time delay between pulses. The net effect of summing all of the separate quantum well contributions will not vary significantly with time delay or frequency over the range of parameters considered here, so we continue from here assuming there is a single quantum well in the sample. This removes any spatial dependence from all of the following equations.

All six of the terms n Equation (2.40) contribute to the two-pulse degenerate four-wave mixing polarization $\overleftrightarrow{\mathbf{P}}^{(3)}(\omega^p)$, that oscillates at the common carrier frequency ω^p. Since the pulses propagate in two physically separate directions, it is sufficient to consider one of the directions knowing that, due to the symmetry of the susceptibility under changes of the indices ω_i, the other direction leads to the same solution. Similarly, the three terms propagating in one of the two background-free directions simply correspond to the three resonant susceptibilities $\overleftrightarrow{\chi}^{(3)}(-\omega^p; \omega^p, \omega^p, -\omega^p)$, $\overleftrightarrow{\chi}^{(3)}(-\omega^p; \omega^p, -\omega^p, \omega^p)$, and $\overleftrightarrow{\chi}^{(3)}(-\omega^p; -\omega^p, \omega^p, \omega^p)$ all of which lead to identical results, although the specific terms which are resonant in the susceptibility change. We can thus consider the solution of only one of the driving field terms in the polarization in Equation (2.40), with the other terms contributing a factor of three (3) to the final solution.

To identify the resonant susceptibility terms in Equation (2.37), we start by substituting $\omega_1 = \omega_2 = \omega$, $\omega_3 = -\omega$, and $\omega_\Sigma = \omega$ into the full 24 term expansion of $\overleftrightarrow{\chi}^{(3)}$ in Equation (2.37). If we assume only the ground state is occupied in equilibrium, then $x = g$ only. In this case, due to dipole selection rules, the levels J_1 & J_2 must correspond to single particle (exciton) states, with $\omega_{J_1g} \approx \omega_{J_3g} \approx \omega$. The J_2 level value may take on two values, that of the ground state $\omega_{J_2g} \approx 0$ or that of a double particle (biexciton) state $(\omega_{J_2g} \approx 2\omega)$.

An example of how to identify which of the first 6 of the 24 third order terms are

Table 2.1: Examples of selection of DFWM resonant terms. Shown are the first six terms in the 24 term expansion of $\overleftrightarrow{\chi}^{(3)}$. The numerical values on the right side of the numerator correspond to the β subscripts and are used to identify each term. For DFWM, $\omega_1 = \omega_2 = \omega_\Sigma = \omega$, $\omega_3 = -\omega$, $J_1 \approx J_3 \approx \omega$ and $J_2 \approx 0$ or 2ω. The full expansion is given in Table A.3 (page 173).

Term	J_1	J_2	J_3	Type
$\dfrac{\mu_{gJ_1}^{\beta_0}\,\mu_{J_1J_2}^{\beta_1}\,\mu_{J_2J_3}^{\beta_2}\,\mu_{J_3g}^{\beta_3}\quad(0123)}{(\omega_{J_1g}-\omega)\,(\omega_{J_2g})\,(\omega_{J_3g}+\omega)}$	Single	Ground	—	—
$\dfrac{\mu_{gJ_1}^{\beta_0}\,\mu_{J_1J_2}^{\beta_2}\,\mu_{J_2J_3}^{\beta_1}\,\mu_{J_3g}^{\beta_3}\quad(0213)}{(\omega_{J_1g}-\omega)\,(\omega_{J_2g})\,(\omega_{J_3g}+\omega)}$	Single	Ground	—	—
$\dfrac{\mu_{gJ_1}^{\beta_0}\,\mu_{J_1J_2}^{\beta_1}\,\mu_{J_2J_3}^{\beta_3}\,\mu_{J_3g}^{\beta_2}\quad(0132)}{(\omega_{J_1g}-\omega)\,(\omega_{J_2g})\,(\omega_{J_3g}-\omega)}$	Single	Ground	Single	Single
$\dfrac{\mu_{gJ_1}^{\beta_0}\,\mu_{J_1J_2}^{\beta_2}\,\mu_{J_2J_3}^{\beta_3}\,\mu_{J_3g}^{\beta_1}\quad(0231)}{(\omega_{J_1g}-\omega)\,(\omega_{J_2g})\,(\omega_{J_3g}-\omega)}$	Single	Ground	Single	Single
$\dfrac{\mu_{gJ_1}^{\beta_0}\,\mu_{J_1J_2}^{\beta_3}\,\mu_{J_2J_3}^{\beta_1}\,\mu_{J_3g}^{\beta_2}\quad(0312)}{(\omega_{J_1g}-\omega)\,(\omega_{J_2g}-2\omega)\,(\omega_{J_3g}-\omega)}$	Single	Double	Single	Double
$\dfrac{\mu_{gJ_1}^{\beta_0}\,\mu_{J_1J_2}^{\beta_3}\,\mu_{J_2J_3}^{\beta_2}\,\mu_{J_3g}^{\beta_1}\quad(0321)}{(\omega_{J_1g}-\omega)\,(\omega_{J_2g}-2\omega)\,(\omega_{J_3g}-\omega)}$	Single	Double	Single	Double

resonant is given in Table 2.1. The first two terms only have two of the three denominator terms resonant and so are rejected, while the last four have all three denominator terms resonant. There are eight resonant terms for degenerate four-wave mixing (DFWM) but only four distinguishable terms, since terms due to the permutation of the pairs (β_1, ω_1) and (β_2, ω_2) are indistinguishable in the two-pulse geometry. The solutions for each of the four distinguishable terms will be shown next. The first one will be shown in more detail than the other three to clearly illustrate the methodology.

2.5.2   DFWM – Single (Exciton) & Double (Biexciton) Level Solutions

The four distinguishable resonant terms in the DFWM susceptibility can be split into two sets of two categories. The first set, which will be called '*single level*' terms, correspond

to the third-order excitation of excitonic states in the quantum wells. The second set, called 'double level' terms, correspond to the third-order excitation of biexciton or two-free-exciton states in the quantum wells. The first category, referred to as "A" terms, exist at positive delays (τ) between the two excitation pulses. The second category, called "B" terms, exist only for delays on the order of the excitation pulse duration (for single levels) or at negative delays (for double levels).

2.5.2.1   Single Level, "A", (3201 & 3102) Terms

The derivation given below uses the '3102' term, which is equivalent to the '3201' terms for degenerate four-wave mixing. This derivation is based on the expression for the third order susceptibility (Equation (2.37)) and polarization (Equation (2.36)).

From Equation (2.37), the 3102 term of the third order susceptibility is given by

$$\chi^{(3)}_{\beta_3\beta_1\beta_0\beta_2}\left(-\omega_\Sigma;\omega_1;\omega_2;\omega_3\right) = \frac{1}{\epsilon_o\,3!\,\hbar^3\,V_{QW}}\,\rho_o(g)$$

$$\times\;\frac{\mu^{\beta_3}_{ga}\,\mu^{\beta_1}_{ag}\,\mu^{\beta_0}_{gc}\,\mu^{\beta_2}_{cg}}{(\omega_{ag}+\omega_3+i\Gamma_{ag})^{\alpha_{ag}}(\omega_3+\omega_1+i\Gamma_{gg})(\omega_{cg}-\omega_2-i\Gamma_{cg})^{\alpha_{cg}}}\,. \qquad (2.41)$$

Inserting this susceptibility into the expression for the polarization, Equation (2.38), the integrals are evaluated in the following manner. The integral evaluated at each stage is the one corresponding to the susceptibility denominator term which contains the frequency component ω_j in **only** that term. Using the time response function derived earlier (Equation (2.18)) the product $\chi^{(3)}(\omega_j)G(\omega_j)^\dagger$ is converted to the time domain by taking the Fourier transforms (where the pulse shape is indicated by $g(t_j)$), noting that the result is a convolution between the two functions. The order of integrations is ω_2, ω_1, and ω_3 for this susceptibility term. Calling these three integrals I_2, I_1, and I_3, the

---

† To prevent confusion between the exponential symbol and the electric field time envelope $e(t)$ corresponding to the frequency field profile $E(\omega)$, the symbols $g(t)$ and $G(\omega)$ will be used from this point on.

results of this procedure are

$$I_2 = \frac{\sqrt{2\pi}\,(+i)^{\alpha_{cg}}}{\Gamma(\alpha_{cg})}\,e^{-i\omega_2^p(t-\tau_2)} \int\limits_0^{+\infty} dt_c\; t_c^{\alpha_{cg}-1}\; e^{-i\,[(\omega_{cg}-\omega_2^p)-i\Gamma_{cg}]\,t_c}\; g_{\beta_2}(t-\tau_2-t_c)\,,$$

$$\tag{2.42}$$

$$I_1 = \sqrt{2\pi}\,(-i)\,e^{-i\omega_1^p(t-\tau_1)} \int\limits_0^{+\infty} dt'\; e^{+i\,[(\omega_3+\omega_1^p)+i\Gamma_{gg}]\,t'}\; g_{\beta_1}(t-\tau_1-t')\,, \tag{2.43}$$

and

$$I_3 = \frac{\sqrt{2\pi}\,(-i)^{\alpha_{ag}}}{\Gamma(\alpha_{ag})}\,e^{+i\omega_3^p(t+\tau_3-t')}$$

$$\times \int\limits_0^{+\infty} dt_a\; t_a^{\alpha_{ag}-1}\; e^{+i\,[(\omega_{ag}-\omega_3^p)+i\Gamma_{ag}]\,t_a}\; g_{\beta_3}(t+\tau_3-t'-t_a)\,. \tag{2.44}$$

The $a,\,c$ indices denote the sum over different single level (exciton) states. Note that in the I_1 integral, $\alpha = 1$ and that $\Upsilon(1) = 0! = 1$. In the I_3 integral the $\exp(+i\omega_3 t')$ factor from the I_1 integral is carried over into the I_3 integral. Combining these results gives the general $P^{(3)}_{\beta_0,\,3102}(t,\tau)$ homogeneous polarization,

$$P^{(3)}_{\beta_0,\,3102}(t,\tau) = \frac{1}{3!\,\hbar^3\,V_{QW}}\,\rho_o(g)\,(2\pi)\sqrt{2\pi}\;\;e^{-i\omega_1^p(t-\tau_1)-i\omega_2^p(t-\tau_2)+i\omega_3^p(t+\tau_3)}$$

$$\times \sum_{a,c} \left\{ \frac{(-i)^{\alpha_{ag}}\,(-i)\,(+i)^{\alpha_{cg}}}{\Upsilon(\alpha_{ag})\,\Upsilon(\alpha_{cg})}\, \mu_{ga}^{\beta_3}\,\mu_{ag}^{\beta_1}\,\mu_{gc}^{\beta_0}\,\mu_{cg}^{\beta_2} \right.$$

$$\times \int\limits_0^{+\infty} dt_2\; t_2^{\alpha_{cg}-1}\; e^{-i\,[(\omega_{cg}-\omega_2^p)-i\Gamma_{cg}]\,t_2}\; g_{\beta_2}(t-\tau_2-t_2)$$

$$\times \int\limits_0^{+\infty} dt_3\; t_3^{\alpha_{ag}-1}\; e^{+i\,[(\omega_{ag}-\omega_3^p)+i\Gamma_{ag}]\,t_3}$$

$$\times \left. \int\limits_0^{+\infty} dt_1\; e^{+i\,[(\omega_1^p-\omega_3^p)+i\Gamma_{gg}]\,t_1}\; g_{\beta_1}(t-\tau_1-t_1)\, g_{\beta_3}(t+\tau_3-t_1-t_3) \right\}\Bigg|_{\substack{\tau_1,\,\tau_2=\tau;\\ \tau_3=0;\\ \omega_i^p=\omega^p}}$$

$$\tag{2.45}$$

where $\tau_1 = \tau_2 = \tau$ and $\tau_3 = 0$ due to the fact that we use 2 distinct pulses, not 3, and because only the relative arrival time between the pulses is relevant. Thus, for the

two-pulse degenerate four-wave mixing case,

$$
P^{(3)}_{\beta_0,\,\text{Single, A}}(t,\tau) = \frac{6}{3!\,\hbar^3\,V_{QW}}\,\rho_o(g)\,(2\pi)\sqrt{2\pi}\;\;e^{+i\omega_p(t-2\tau)}
$$

$$
\times \sum_{a,c} \left\{ \frac{(-i)^{\alpha_{ag}}\,(-i)\,(+i)^{\alpha_{cg}}}{\Upsilon\,(\alpha_{ag})\,\Upsilon\,(\alpha_{cg})}\,\mu^{\beta_3}_{ga}\,\mu^{\beta_1}_{ag}\,\mu^{\beta_0}_{gc}\,\mu^{\beta_2}_{cg} \right.
$$

$$
\times \int_0^{+\infty} dt_3\; t_3^{\alpha_{ag}-1}\; e^{+i\,[(\omega_{ag}-\omega^p)+i\Gamma_{ag}]\,t_3}
$$

$$
\times \int_0^{+\infty} dt_2\; t_2^{\alpha_{cg}-1}\; e^{-i\,[(\omega_{cg}-\omega^p)-i\Gamma_{cg}]\,t_2}\; g_{\beta_2}(t-\tau-t_2)
$$

$$
\left. \times \int_0^{+\infty} dt_1\; e^{-\Gamma_{gg}t_1}\; g_{\beta_1}(t-\tau-t_1)\; g_{\beta_3}(t-t_1-t_3) \right\}\;.
$$

(2.46)

The factor of two appears in the numerator because the '3102' and '3201' terms are indistinguishable once the limits are evaluated, while the factor of three in the numerator results from the three field terms that lead to identical solutions, as discussed earlier. The t_1 integral is the convolution of the pulse envelope with itself, damped by the ground-ground state dephasing rate. Since this rate is typically much slower than any other time scale in the problem (the population decay time is $\simeq$ 1-2 ns), this factor is usually taken in the limit as $\Gamma_{gg} \to 0$. The explicit forms of these integrals are given in Table A.1 (page 169).

To retrieve the more often used "delta-function excitation" case, the limiting operations $\alpha_i \to 1$ and $g(t) \to \delta(t)$ are applied to Equation (2.46), resulting in

$$
P^{(3)}_{\beta_0,\,\delta\text{-fcn: Single, A}}(t,\tau) = \frac{6}{3!\,\hbar^3\,V_{QW}}\,\rho_o(g)\,(2\pi)\sqrt{2\pi}\,(-i)\,H^2(t-\tau)\,H(\tau)
$$

$$
\times \sum_{a,c} \mu^{\beta_3}_{ga}\,\mu^{\beta_1}_{ag}\,\mu^{\beta_0}_{gc}\,\mu^{\beta_2}_{cg}\,e^{-i\,[\omega_{cg}-i\Gamma_{cg}]\,(t-\tau)}\,e^{+i\,[\omega_{ag}+i\Gamma_{ag}]\,\tau}\,e^{-\Gamma_{gg}(t-\tau)}\;.\quad (2.47)
$$

The Heaviside step functions $H(t-\tau)$ and $H(\tau)$, being zero for negative arguments and one for positive arguments, mean that polarization signals from these terms exist only for positive delay times and for times, t, *after* the second pulse has interacted with the sample [24–26, 32].

2.5.2.2   Single Level, "B", (0132 & 0231) Terms

The 0132 susceptibility term is given by

$$
\chi^{(3)}_{\beta_0\beta_1\beta_3\beta_2}\left(-\omega_\Sigma;\omega_1;\omega_2;\omega_3\right) = \frac{1}{\epsilon_o\,3!\,\hbar^3\,V_{QW}}\,\rho_o(g)
$$

$$
\times\ \frac{\mu^{\beta_0}_{gc}\,\mu^{\beta_1}_{cg}\,\mu^{\beta_3}_{ga}\,\mu^{\beta_2}_{ag}}{(\omega_{cg}-\omega_1-\omega_2-\omega_3+i\Gamma_{cg})^{\alpha_{cg}}(-\omega_2-\omega_3+i\Gamma_{gg})(\omega_{ag}-\omega_2-i\Gamma_{ag})^{\alpha_{ag}}}\ . \tag{2.48}
$$

By inserting this into the polarization expression (Equation (2.38)) and converting the three integrals into the time domain in the same manner as before, the general expression for the $P^{(3)}_{\beta_0,\,0132}(t,\tau)$ term is found to be

$$
P^{(3)}_{\beta_0,\,0132}(t,\tau) = \frac{1}{3!\,\hbar^3\,V_{QW}}\,\rho_o(g)\,(2\pi)\sqrt{2\pi}\quad e^{-i\omega_1^p(t-\tau_1)\,-\,i\omega_2^p(t-\tau_2)\,+\,i\omega_3^p(t+\tau_3)}
$$

$$
\times \sum_{a,c}\left\{\frac{(+i)^{\alpha_{ag}}\,(+i)\,(+i)^{\alpha_{cg}}}{\Upsilon\left(\alpha_{ag}\right)\,\Upsilon\left(\alpha_{cg}\right)}\mu^{\beta_0}_{gc}\,\mu^{\beta_1}_{cg}\,\mu^{\beta_3}_{ga}\,\mu^{\beta_2}_{ag}\right.
$$

$$
\times \int_0^{+\infty} dt_1\,t_1^{\alpha_{cg}-1}\,e^{-i\left[(\omega_{cg}-\omega_1^p-\omega_2^p+\omega_3^p)-i\Gamma_{cg}\right]t_1}\,g_{\beta_1}(t-\tau_1-t_1)
$$

$$
\times \int_0^{+\infty} dt_2\,t_2^{\alpha_{ag}-1}\,e^{-i\left[(\omega_{ag}-\omega_2^p)-i\Gamma_{ag}\right]t_2}
$$

$$
\times \int_0^{+\infty} dt_3\,e^{-i\left[(\omega_3^p-\omega_2^p)-i\Gamma_{gg}\right]t_3}
$$

$$
\left.\times\ g_{\beta_3}(t+\tau_3-t_1-t_3)\,g_{\beta_2}(t-\tau_2-t_1-t_2-t_3)\right\}\Bigg|_{\substack{\tau_1,\tau_2=\tau;\ \tau_3=0;\\[4pt]\omega_i^p=\omega^p}}
$$

$$
\tag{2.49}
$$

or,

$$
P^{(3)}_{\beta_0,\,\text{Single, B}}(t,\tau) = \frac{6}{3!\,\hbar^3\,V_{QW}}\,\rho_o(g)\,(2\pi)\sqrt{2\pi}\quad e^{+i\omega_p(t-2\tau)}
$$

$$
\times \sum_{a,c}\left\{\frac{(+i)^{\alpha_{ag}}\,(+i)\,(+i)^{\alpha_{cg}}}{\Upsilon\left(\alpha_{ag}\right)\,\Upsilon\left(\alpha_{cg}\right)}\mu^{\beta_0}_{gc}\,\mu^{\beta_1}_{cg}\,\mu^{\beta_3}_{ga}\,\mu^{\beta_2}_{ag}\right.
$$

$$
\times \int_0^{+\infty} dt_2\,t_2^{\alpha_{ag}-1}\,e^{+i\left[(\omega_{ag}-\omega^p)+i\Gamma_{ag}\right]t_2}
$$

$$
\times \int_0^{+\infty} dt_1\,t_1^{\alpha_{cg}-1}\,e^{-i\left[(\omega_{cg}-\omega^p)-i\Gamma_{cg}\right]t_1}\,g_{\beta_1}(t-\tau-t_1)
$$

$$
\left.\times \int_0^{+\infty} dt_3\,e^{-\Gamma_{gg}t_3}\,g_{\beta_2}(t-\tau-t_1-t_2-t_3)\,g_{\beta_3}(t-t_1-t_3)\right\}\ . \tag{2.50}
$$

Note that, similar to the Single A case, this expression also contains an integral (t_3) that results in the same pulse autocorrelation times a pulse envelope function. As for the Single A case, the δ-function case is found by taking the limits $\alpha_i \to 1$, $g(t) \to \delta(t)$, and $\Gamma_{gg} \to 0$. This process gives

$$P^{(3)}_{\beta_0, \text{ }\delta\text{-fcn: Single, B}}(t, \tau) = \frac{6}{3! \, \hbar^3 \, V_{QW}} \, \rho_o(g) \, (2\pi)\sqrt{2\pi} \, (-i) \, H(\tau) \, H(-\tau) \, H(t-\tau)$$

$$\times \sum_{a, c} \mu^{\beta_0}_{gc} \, \mu^{\beta_1}_{cg} \, \mu^{\beta_3}_{ga} \, \mu^{\beta_2}_{ag} \, e^{-i \, [\omega_{cg} \, - \, i\Gamma_{cg}] \, (t - \tau)} \, e^{+i \, [\omega_{ag} \, - \, i\Gamma_{ag}] \, \tau} \, e^{-\Gamma_{gg}\tau} \, . \quad (2.51)$$

Note that the conflicting Heaviside step functions mean that this term exists only at $\tau = 0$ and $(t - \tau) \geq 0$ for the delta function pulse case. For finite length pulses, this term contributes only for $|\tau|$ approximately less than the pulse duration [24–26, 32].

2.5.2.3 Double Level, "A", (3012 & 3021) Terms

The results for the 3012 term are shown here, beginning with the expression for its susceptibility, given by

$$\chi^{(3)}_{\beta_3\beta_0\beta_1\beta_2} \left(-\omega_\Sigma; \omega_1; \omega_2; \omega_3\right) = \frac{1}{\epsilon_o \, 3! \, \hbar^3 \, V_{QW}} \, \rho_o(g)$$

$$\times \frac{\mu^{\beta_3}_{ga} \, \mu^{\beta_0}_{ab} \, \mu^{\beta_1}_{bc} \, \mu^{\beta_2}_{cg}}{(\omega_{ag} + \omega_3 + i\Gamma_{ag})^{\alpha_{ag}} (\omega_{bg} - \omega_1 - \omega_2 - i\Gamma_{bg})^{\alpha_{bg}} (\omega_{cg} - \omega_2 - i\Gamma_{cg})^{\alpha_{cg}}} \, , \quad (2.52)$$

where the arbitrary labels a and c sum over the single levels states as before. The b label sums over the double level (biexciton) states. The expression for the polarization for the

$P_{\beta_0,\,3012}^{(3)}(t,\tau)$ term is thus given by

$$
\begin{aligned}
P_{\beta_0,\,3012}^{(3)}(t,\tau) ={}& \frac{1}{3!\,\hbar^3\,V_{QW}}\,\rho_o(g)\,(2\pi)\sqrt{2\pi}\quad e^{-i\omega_1^p(t-\tau_1)\,-\,i\omega_2^p(t-\tau_2)\,+\,i\omega_3^p(t+\tau_3)} \\
&\times \sum_{a,b,c} \frac{(-i)^{\alpha_{ag}}\,(+i)^{\alpha_{bg}}\,(+i)^{\alpha_{cg}}}{\Upsilon\,(\alpha_{ag})\,\Upsilon\,(\alpha_{bg})\,\Upsilon\,(\alpha_{cg})}\mu_{ga}^{\beta_3}\,\mu_{ab}^{\beta_0}\,\mu_{bc}^{\beta_1}\,\mu_{cg}^{\beta_2} \\
&\times \int_0^{+\infty} dt_3\,t_3^{\alpha_{ag}-1}\,e^{-i\,[(\omega_{ag}-\omega_3^p)\,-\,i\Gamma_{ag}]\,t_3}\,g_{\beta_3}(t+\tau_3-t_3) \\
&\times \int_0^{+\infty} dt_1\,t_1^{\alpha_{bg}-1}\,e^{-i\,[(\omega_{bg}-\omega_1^p-\omega_2^p)\,-\,i\Gamma_{bg}]\,t_1}\,g_{\beta_1}(t-\tau_1-t_1) \\
&\times \left.\int_0^{+\infty} dt_2\,t_2^{\alpha_{cg}-1}\,e^{-i\,[(\omega_{cg}-\omega_2^p)\,-\,i\Gamma_{cg}]\,t_2}\,g_{\beta_2}(t-\tau_2-t_1-t_2)\right|_{\substack{\tau_1,\tau_2=\tau;\ \tau_3=0;\\ \omega_i^p=\omega^p}}
\end{aligned}
$$
(2.53)

or,

$$
\begin{aligned}
P_{\beta_0,\,\text{Double, A}}^{(3)}(t,\tau) ={}& \frac{6}{3!\,\hbar^3\,V_{QW}}\,\rho_o(g)\,(2\pi)\sqrt{2\pi}\quad e^{+i\omega_p(t-2\tau)} \\
&\times \sum_{a,b,c}\left\{ \frac{(-i)^{\alpha_{ag}}\,(+i)^{\alpha_{bg}}\,(+i)^{\alpha_{cg}}}{\Upsilon\,(\alpha_{ag})\,\Upsilon\,(\alpha_{bg})\,\Upsilon\,(\alpha_{cg})}\mu_{ga}^{\beta_3}\,\mu_{ab}^{\beta_0}\,\mu_{bc}^{\beta_1}\,\mu_{cg}^{\beta_2} \right. \\
&\times \int_0^{+\infty} dt_3\,t_3^{\alpha_{ag}-1}\,e^{-i\,[(\omega_{ag}-\omega^p)\,-\,i\Gamma_{ag}]\,t_3}\,g_{\beta_3}(t-t_3) \\
&\times \int_0^{+\infty} dt_1\,t_1^{\alpha_{bg}-1}\,e^{-i\,[(\omega_{bg}-2\omega^p)\,-\,i\Gamma_{bg}]\,t_1}\,g_{\beta_1}(t-\tau-t_1) \\
&\times \left. \int_0^{+\infty} dt_2\,t_2^{\alpha_{cg}-1}\,e^{-i\,[(\omega_{cg}-\omega^p)\,-\,i\Gamma_{cg}]\,t_2}\,g_{\beta_2}(t-\tau-t_1-t_2)\right\} \ .
\end{aligned}
$$
(2.54)

The δ-function pulse limit is again taken by using $\alpha_i \to 1$ and $g(t) \to \delta(t)$, resulting in the expression

$$
\begin{aligned}
P_{\beta_0,\,\delta\text{-fcn: Double, A}}^{(3)}(t,\tau) ={}& \frac{6}{3!\,\hbar^3\,V_{QW}}\,\rho_o(g)\,(2\pi)\sqrt{2\pi}\,(+i)\,H(t)\,H(t-\tau)\,H(0) \\
&\times \sum_{a,b,c} \mu_{ga}^{\beta_3}\,\mu_{ab}^{\beta_0}\,\mu_{bc}^{\beta_1}\,\mu_{cg}^{\beta_2}\,e^{+i\,[\omega_{ag}+i\Gamma_{ag}]\,t}\,e^{-i\,[\omega_{bg}-i\Gamma_{bg}]\,(t-\tau)}\ .
\end{aligned}
$$
(2.55)

Note that the sum over c reduces to a sum over the dipole moment strengths. Alternatively this can be looked at as the c sum being evaluated at zero, using $H(0) = 1/2$. The Heaviside step functions $H(t)$ and $H(t-\tau)$ mean that these signals are not directly dependent on the pulse delay, τ. These terms generate signals at negative pulse delays as

well as positive delays, but for only real times, t, greater than the pulse delay. Since they are also restricted to exist for real times greater than zero only, the signals at positive delay times all start at the real time zero and decay from this point [24–26, 32].

2.5.2.4 Double Level, "B", (0312 & 0321) Terms

The final term to examine is the 0312 term, where the susceptibility term is given by

$$
\chi^{(3)}_{\beta_0\beta_3\beta_1\beta_2}\left(-\omega_\Sigma;\omega_1;\omega_2;\omega_3\right) = \frac{1}{\epsilon_o \, 3! \, \hbar^3 \, V_{QW}} \, \rho_o(g)
$$

$$
\times \frac{\mu^{\beta_0}_{ga} \, \mu^{\beta_3}_{ab} \, \mu^{\beta_1}_{bc} \, \mu^{\beta_2}_{cg}}{(\omega_{ag} - \omega_1 - \omega_2 - \omega_3 - i\Gamma_{ag})^{\alpha_{ag}} (\omega_{bg} - \omega_2 - \omega_1 - i\Gamma_{bg})^{\alpha_{bg}} (\omega_{cg} - \omega_2 - i\Gamma_{cg})^{\alpha_{cg}}} \, .
$$

$$(2.56)$$

Again, a and c are sums over single level states, while b is a sum over the double level states.

Integrating over the three ω_i terms as before, the general third order polarization term $P^{(3)}_{\beta_0, \, 0312}(t, \tau)$ is

$$
P^{(3)}_{\beta_0, \, 0312}(t, \tau) = \frac{1}{3! \, \hbar^3 \, V_{QW}} \, \rho_o(g) \, (2\pi)\sqrt{2\pi} \quad e^{-i\omega^p_1(t-\tau_1) - i\omega^p_2(t-\tau_2) + i\omega^p_3(t+\tau_3)}
$$

$$
\times \sum_{a,b,c} \left\{ \frac{(+i)^{\alpha_{ag}} \, (+i)^{\alpha_{bg}} \, (+i)^{\alpha_{cg}}}{\Upsilon\left(\alpha_{ag}\right) \, \Upsilon\left(\alpha_{bg}\right) \, \Upsilon\left(\alpha_{cg}\right)} \mu^{\beta_0}_{ga} \, \mu^{\beta_3}_{ab} \, \mu^{\beta_1}_{bc} \, \mu^{\beta_2}_{cg} \right.
$$

$$
\times \int\limits_0^{+\infty} dt_3 \, t_3^{\alpha_{ag}-1} \, e^{-i\left[(\omega_{ag} + \omega^p_3 - \omega^p_1 - \omega^p_2) - i\Gamma_{ag}\right]t_3} \, g_{\beta_3}(t + \tau_3 - t_3)
$$

$$
\times \int\limits_0^{+\infty} dt_1 \, t_1^{\alpha_{bg}-1} \, e^{-i\left[(\omega_{bg} - \omega^p_1 - \omega^p_2) - i\Gamma_{bg}\right]t_1} \, g_{\beta_1}(t - \tau_1 - t_3 - t_1)
$$

$$
\times \left. \int\limits_0^{+\infty} dt_2 \, t_2^{\alpha_{cg}-1} \, e^{-i\left[(\omega_{cg} - \omega^p_2) - i\Gamma_{cg}\right]t_2} \, g_{\beta_2}(t - \tau_2 - t_3 - t_1 - t_2) \right\} \Bigg|_{\substack{\tau_1, \tau_2 = \tau;}}
$$

$$\tau_3 = 0;$$

$$\omega^p_i = \omega^p$$

$$(2.57)$$

or,

$$
\begin{aligned}
P^{(3)}_{\beta_0,\text{ Double, B}}(t,\tau) = {} & \frac{6}{3!\,\hbar^3\,V_{QW}}\,\rho_o(g)\,(2\pi)\sqrt{2\pi}\quad e^{+i\omega_p)(t-2\tau)} \\
& \times \sum_{a,b,c}\left\{\frac{(+i)^{\alpha_{ag}}\,(+i)^{\alpha_{bg}}\,(+i)^{\alpha_{cg}}}{\Upsilon\,(\alpha_{ag})\,\Upsilon\,(\alpha_{bg})\,\Upsilon\,(\alpha_{cg})}\mu^{\beta_0}_{ga}\,\mu^{\beta_3}_{ab}\,\mu^{\beta_1}_{bc}\,\mu^{\beta_2}_{cg}\right. \\
& \times \int_0^{+\infty} dt_3\; t_3^{\alpha_{ag}-1}\; e^{-i\,[(\omega_{ag}-\omega^p)-i\Gamma_{ag}]\,t_3}\; g_{\beta_3}(t-t_3) \\
& \times \int_0^{+\infty} dt_1\; t_1^{\alpha_{bg}-1}\; e^{-i\,[(\omega_{bg}-2\omega^p)-i\Gamma_{bg}]\,t_1}\; g_{\beta_1}(t-\tau-t_3-t_1) \\
& \left.\times \int_0^{+\infty} dt_2\; t_2^{\alpha_{cg}-1}\; e^{-i\,[(\omega_{cg}-\omega^p)-i\Gamma_{cg}]\,t_2}\; g_{\beta_2}(t-\tau-t_3-t_1-t_2)\right\}.
\end{aligned}
\tag{2.58}
$$

Finally, the δ-function limit is taken once again ($\alpha_i \to 1$ and $g(t) \to \delta(t)$), giving

$$
\begin{aligned}
P^{(3)}_{\beta_0,\text{ δ-fcn: Double, B}}(t,\tau) = {} & \frac{6}{3!\,\hbar^3\,V_{QW}}\,\rho_o(g)\,(2\pi)\sqrt{2\pi}\,(-i)\,H(t)\,H(-\tau)\,H(0) \\
& \times \sum_{a,b,c}\mu^{\beta_0}_{ga}\,\mu^{\beta_3}_{ab}\,\mu^{\beta_1}_{bc}\,\mu^{\beta_2}_{cg}e^{-i\,[\omega_{ag}-i\Gamma_{ag}]\,t}\,e^{+i\,[\omega_{bg}-i\Gamma_{bg}]\,\tau}.
\end{aligned}
\tag{2.59}
$$

Similar to the "A" terms, the sum over the c states reduces to a sum over the dipole moment strengths or, alternatively, is only evaluated at $H(0) = 1/2$. The Heaviside step functions for the double level "B" terms are $H(t)$ and $H(-\tau)$. These restrictions mean that these terms interact only with the double level "A" terms. This results in a signal that shows biexciton beats in homogeneous time-integrated DFWM signals at negative pulse delay values [24–26, 32].

2.5.3 DFWM – Inhomogeneous Broadening

Inhomogeneous broadening has several effects on the measured DFWM signals. It is included here using the method outlined in Section 2.2. Examining the effect of this on the DFWM terms obtained in the delta-function pulse excitation limit, from Equation (2.22),

$$
\vec{\mathbf{P}}^{(3)}_{\text{inhom, δ-fcn}}(t,\tau) \approx \vec{\mathbf{P}}^{(3)}_{\text{hom, δ-fcn}}(t,\tau)\,e^{-\dfrac{\Gamma^2_{\text{inh}}}{16\ln 2}\,(t-2\tau)^2},
\tag{2.60}
$$

assuming that the inhomogeneous broadening is the same for all the levels. This modifies the DFWM signal from one that exponentially decays in time after the second pulse leaves
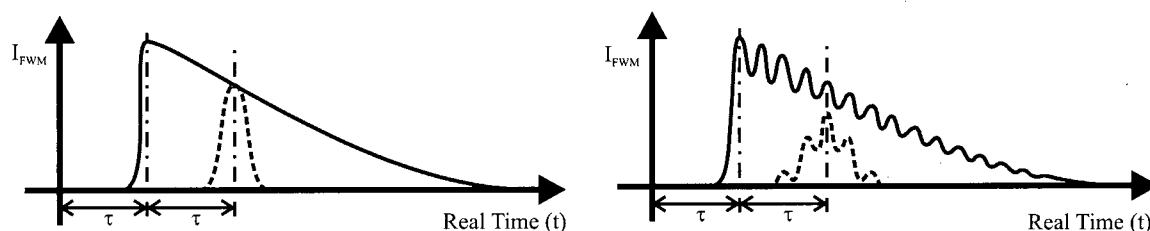
Figure 2.2: Homogeneous vs Inhomogeneous FWM Signals. Schematic illustration of the DFWM signal in time, where τ is the delay between the two pulses, for a single level (left) and two levels (right). The solid line indicates homogeneous broadening, which decays exponentially after the second pulse passes. The dashed line indicates inhomogeneous broadening, which leads to a *photon echo*, or Gaussian peak, which 'samples' the homogeneous signal at $t = 2\tau$.

the sample to one that has a Gaussian shaped peak, called a '*photon echo*', centered at $t = 2\tau$. The width of the photon echo is proportional to the inverse of the inhomogeneous broadening width. This is schematically illustrated in Figure 2.2.

The photon echo due to inhomogeneous broadening has an effect on both the measured dephasing rates and the beat terms in the time-integrated signals. For single level excitation it is well known that the time-integrated intensity of the signal decays exponentially at twice the rate, with respect to τ, in the inhomogeneous case $(4\Gamma_i)$ than it does in the homogeneous case $(2\Gamma_i)$. When two levels are excited, the coherent excitation pulses lead to an oscillating, exponentially decaying 'beat' signal in addition to the single level exponential decays. These beat signals decay at the sum of the decay rates for the individual levels, or twice this sum for inhomogeneous signals [24–26, 32].

The disorder leading to inhomogeneous broadening which obscures fine details in linear absorption is thus not a barrier to obtaining information with the DFWM signals, where accurate measures of the dephasing rates and energy level separations (beats) can be obtained.

2.6 Linear Absorption

This section presents simulations that exhibit the features of the theoretical model important for comparison to the experimental results. The linear absorption coefficient is simulated using the relations derived for the susceptibility (Equations (2.25) & (2.27)), permittivity (Equation (2.28)), and absorption coefficient (Equation (2.32)). The linear absorption function is evaluated analytically – details can be found in Section A.2.1 (page 182). The effects of dephasing and the power law exponent are presented first, and are followed with a comparison of homogeneous and inhomogeneous broadening.

2.6.1 Power Law Exponent

The resonant linear susceptibility is obtained by summing over the exciton levels and near edge continuum states in the system. The power law exponent broadens the absorption peaks on the high energy side, going from the case of a sharp exciton peak with $\alpha_j \approx 1$ towards a 2-D continuum step function with $\alpha_j \approx 0$. We use $\alpha_j \neq 0$ to fit the main absorption threshold in the doped quantum wells, and to represent the continuum in all of the samples.

Figure 2.3 shows the effect of varying the power law exponent for a single level. It shows the expected asymmetric broadening on the high energy side of the peak (positive energy values in the figure). The dephasing broadens, but does not shift the peak for α_j values near 1. However, the peak shifts to higher energies for lower α_j, and the threshold energy is in the middle of the low energy absorption edge for alpha values near zero. This is similar to that observed in quantum wells with excess electron doping [5,6].

Figure 2.4 illustrates how, in the case of an undoped quantum well, both a 1S exciton (low energy level with $\alpha \approx 1$) and continuum (higher lying level with $\alpha = 0.20$) absorption lineshape can be simulated within the same theoretical formalism used to illustrate the case of doped quantum wells which was shown previously. The figure also shows how, by allowing the power law exponent to increase from zero, the Sommerfeld enhancement factor can also be simulated within this model.
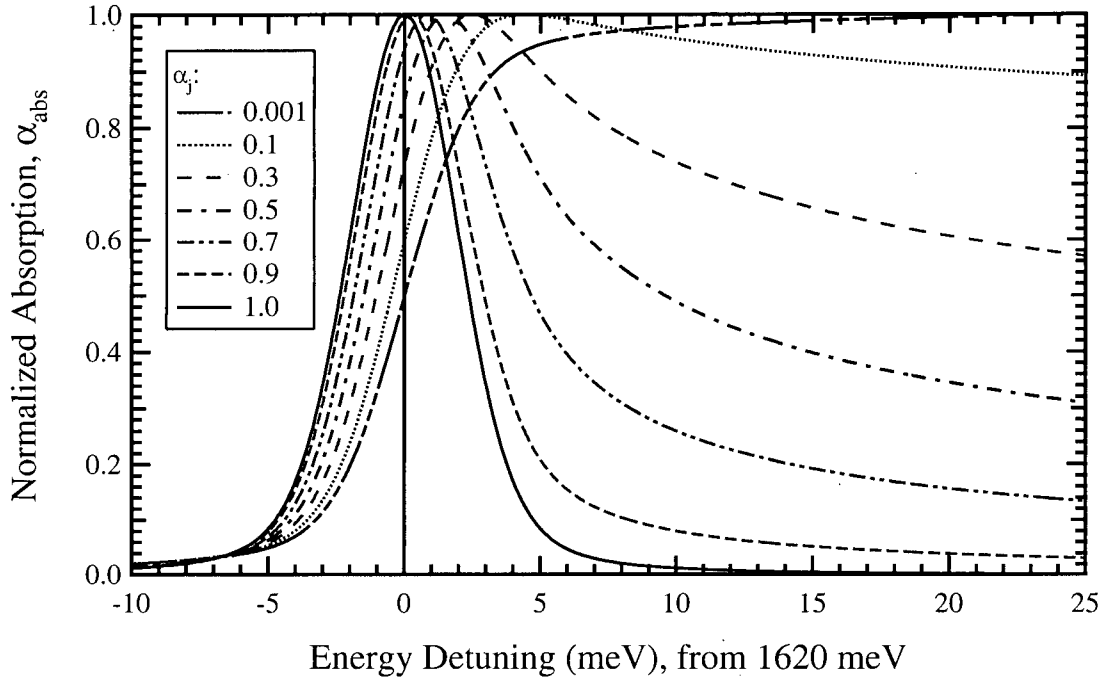
Figure 2.3: Linear absorption and the effects of the power law exponent, α_j, from Equations (2.27) & (2.32). The traces are normalized with respect to their peak value. $\Gamma_j = 1.0\,\text{ps}^{-1}$ and $\Gamma_{j,\,\text{inh}} = 4.0\,\text{meV}$.

2.7 Two-Pulse DFWM Theoretical Results

After summarizing the formulae used to simulate the DFWM data, the main features of the simulations relevant to the DFWM experiments are discussed in the following order:

- Homogeneous and inhomogeneous broadening

- Comparison of the full solution and the delta-function pulse solution

- Input laser pulse detuning effects

- Nature of beat signals (Quantum beats vs Polarization beats)

- Double (biexciton) levels - homogeneous & inhomogeneous broadening

- Input beam polarization effects on the DFWM signals

- Effects of varying the power law exponent
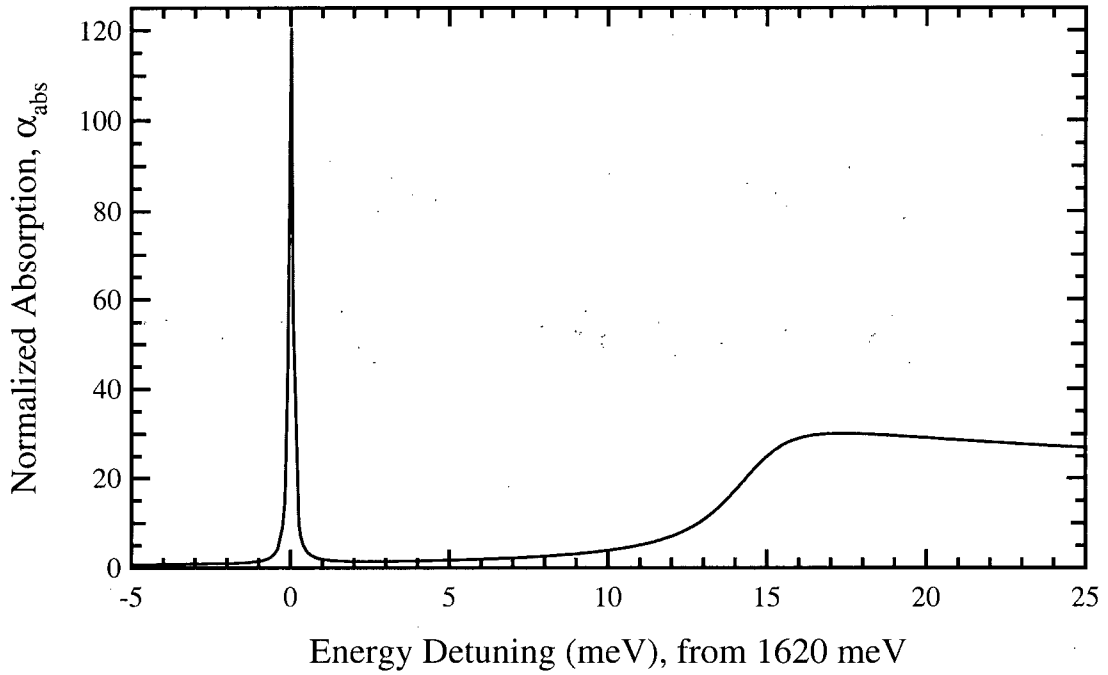
Figure 2.4: Homogeneous linear absorption for one discrete transition and a continuum state, from Equations (2.27) & (2.32). The power law exponents for the two energy levels, spaced 14.5 meV apart, are $\alpha_j = 0.99$ and 0.20, while the dephasing rates are $\Gamma_j = 0.1$ and 2.5 ps^{-1} for the lower and upper levels. $\Gamma_{j,\,\text{inh}} = 0.01$ meV for both levels.

2.7.1 Two Pulse DFWM — Full Combined Solution

Combining the two pulse DFWM solutions from Equations (2.46), (2.50), (2.54), and (2.58) gives the following expression for the total third order polarization due to degenerate four-wave mixing

$$P_{\beta_0}^{(3)}(t,\tau) = \frac{1}{\hbar^3 V_{QW}} \, \rho_o(g) \, (2\pi)\sqrt{2\pi} \quad e^{+i\omega_p(t-2\tau)}$$

$$\times \left\{ \sum_{a,c} \left(\frac{\mu_{gc}^{\beta_0} \, \mu_{ga}^{\beta_3} \, (+i)^{\alpha_{cg}}}{\Upsilon(\alpha_{ag}) \, \Upsilon(\alpha_{cg})} \quad \int_0^{+\infty} dt_a \, t_a^{\alpha_{ag}-1} \, e^{+i\,[(\omega_{ag}-\omega^P)+i\Gamma_{ag}]\,t_a} \right. \right.$$

$$\times \int_0^{+\infty} dt_c \, t_c^{\alpha_{cg}-1} \, e^{-i\,[(\omega_{cg}-\omega^P)-i\Gamma_{cg}]\,t_c} \, g_{\beta_2}(t-\tau-t_c)$$

$$\times \int_0^{+\infty} dt' \, e^{-\Gamma_{gg}t'} \left[(-i)^{\alpha_{ag}} \, (-i) \, \mu_{ag}^{\beta_1} \, \mu_{cg}^{\beta_2} \, g_{\beta_1}(t-\tau-t') \, g_{\beta_3}(t-t'-t_a) \right.$$

$$\left. + (+i)^{\alpha_{ag}} \, (+i) \, \mu_{cg}^{\beta_1} \, \mu_{ag}^{\beta_2} \, g_{\beta_2}(t-\tau-t_c-t_a-t') \, g_{\beta_3}(t-t_c-t') \right] \Bigg)$$

$$+ \sum_{a,b,c} \left(\frac{\mu_{bc}^{\beta_1} \, \mu_{cg}^{\beta_2} \, (+i)^{\alpha_{bg}} \, (+i)^{\alpha_{cg}}}{\Upsilon(\alpha_{ag}) \, \Upsilon(\alpha_{bg}) \, \Upsilon(\alpha_{cg})} \right. \qquad (2.61)$$

$$\times \int_0^{+\infty} dt_a \, t_a^{\alpha_{ag}-1} \, e^{-i\,[(\omega_{ag}-\omega^P)-i\Gamma_{ag}]\,t_a} \, g_{\beta_3}(t-t_a)$$

$$\times \int_0^{+\infty} dt_b \, t_b^{\alpha_{bg}-1} \, e^{-i\,[(\omega_{bg}-2\omega^P)-i\Gamma_{bg}]\,t_b}$$

$$\times \int_0^{+\infty} dt_c \, t_c^{\alpha_{cg}-1} \, e^{-i\,[(\omega_{cg}-\omega^P)-i\Gamma_{cg}]\,t_c}$$

$$\times \left[(-i)^{\alpha_{ag}} \, \mu_{ga}^{\beta_3} \, \mu_{ab}^{\beta_0} \, g_{\beta_1}(t-\tau-t_b) \, g_{\beta_2}(t-\tau-t_b-t_c) \right.$$

$$\left. \left. + (+i)^{\alpha_{ag}} \, \mu_{ga}^{\beta_0} \, \mu_{ab}^{\beta_3} \, g_{\beta_1}(t-\tau-t_a-t_b) \, g_{\beta_2}(t-\tau-t_a-t_b-t_c) \right] \right) \right\} \, .$$

An important point to note about this equation is the phase difference that occurs at positive times between the Single 'A' term, $(-i)$, and Double 'A' term, $(+i)^{\alpha_{bg}}$. This is directly responsible for the 180° phase shift that occurs between the double (biexciton) beats and the single (exciton) beats. This will be explored further during the discussion of the dependence of the DFWM signal on the input beam polarizations.

Γ_{gg} is the ground-ground dephasing rate. The limit $\Gamma_{gg} \to 0$ is implicitly present in all the existing, published theoretical derivations that were found. The upper limit on this dephasing rate is the particle recombination time in the material, since these recombination processes will occur randomly. This leads to random phase changes and should affect Γ_{gg} on the same time scale as the recombination time. The recombination time in GaAs is on the order of 1-2 ns [2]. The laser pulses are on the order of 100 fs in

this work and 1 ps in earlier published DFWM experiments, and the DFWM dephasing processes are less than or on the order of a few tens of ps. Considering these time scales, it is a valid approximation to neglect Γ_{gg}. It should be noted, however, that a non-zero Γ_{gg} dephasing rate guarantees **and** improves the numerical convergence of the single level integrals that it affects.

The regions over which the four different terms (Single - 'A', Single - 'B', Double - 'A', & Double - 'B') affect the solutions are shown in Figure 2.5, where the various solution regions that produce a homogeneous DFWM signal are shaded. A discussion of the differences between the homogeneous and inhomogeneous signals is made later in the chapter. Note the small excursions across the axes due to the finite pulse width, compared with the delta-function excitation limit discussed in Section 2.7.5, where these are absent. Since the terms are approximately equal in the regions where they overlap, their relative phases can drastically alter the final solution. This is shown in the bottom two contour plots, where the phase of the double level beats changes by 180° when both single and double 'A' terms are combined. Double level beats also become visible at negative delay values, when both of the double level terms are included.

2.7.2 Two Pulse DFWM — Delta-Function Excitation Solution

The delta-function excitation formulae are summarized below and consist of simple oscillatory terms with exponential decays. In the limits that $\alpha_j = 1$ and $\Gamma_{gg} \to 0$, these match those found in the literature (Single or exciton levels: [24, 25], and Double or biexciton systems: [26]).
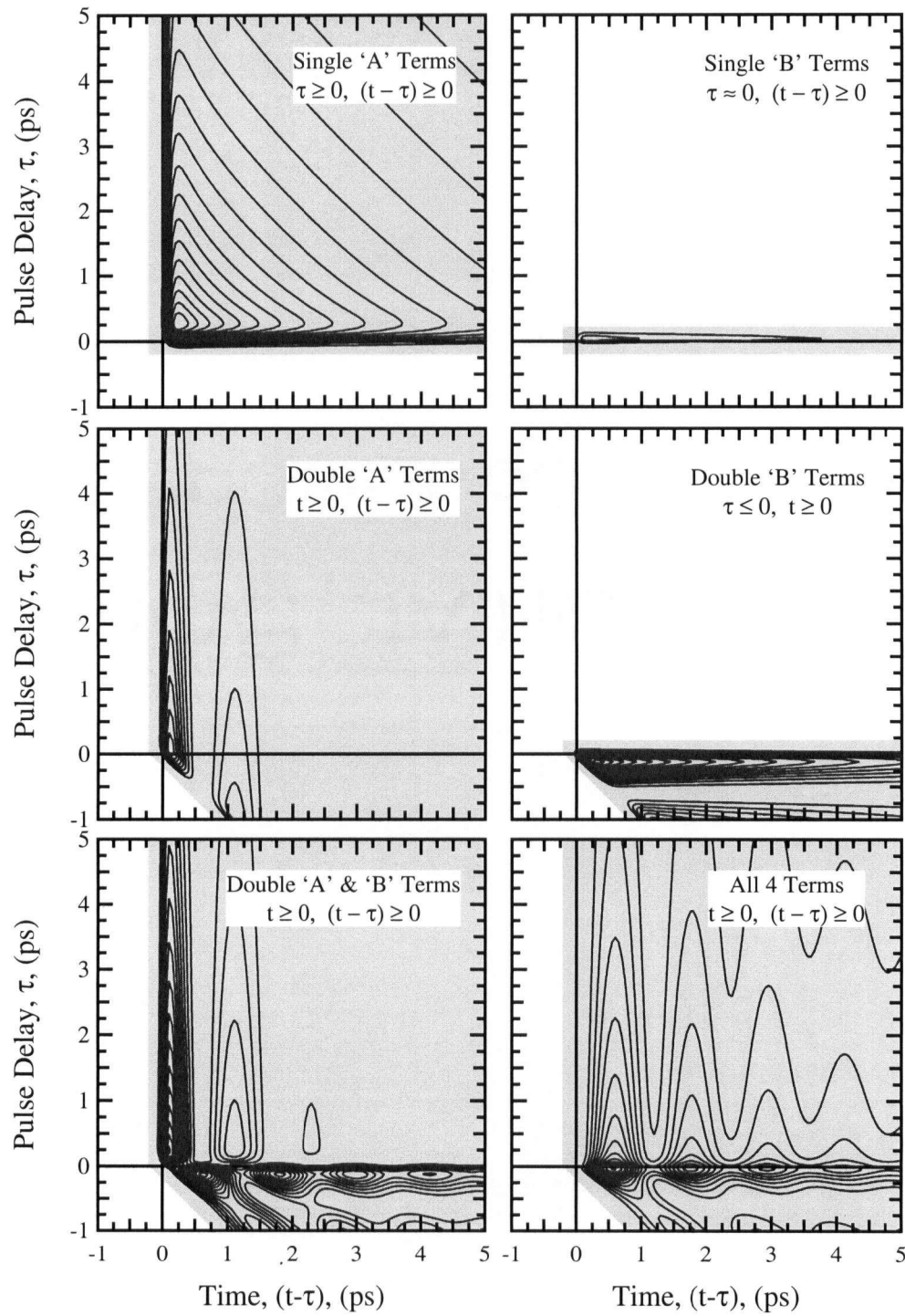
Figure 2.5: Illustration of the solution regions of the four (homogeneous) DFWM terms, with contour plots of the simulated signals overlaying the shaded solution regions.

$$P_{\beta_0}^{(3)}(t,\tau) = \frac{1}{\hbar^3 \, V_{QW}} \, \rho_o(g) \, (2\pi)\sqrt{2\pi} \, (-i)$$

Single: $\times \left\{ \left[H(\tau) \, H(t-\tau) \sum_{a,c} \mu_{gc}^{\beta_0} \, \mu_{ga}^{\beta_3} \, e^{-i \, [\omega_{cg} - i\Gamma_{cg}](t-\tau)} \right. \right.$

'A': $\left(\quad H(t-\tau) \, \mu_{ag}^{\beta_1} \, \mu_{cg}^{\beta_2} \quad e^{+i \, [\omega_{ag} + i\Gamma_{ag}]\tau} \, e^{-\Gamma_{gg}(t-\tau)} \right.$

'B': $\left. + \, H(-\tau) \quad \mu_{cg}^{\beta_1} \, \mu_{ag}^{\beta_2} \quad e^{+i \, [\omega_{ag} - i\Gamma_{ag}]\tau} \, e^{-\Gamma_{gg}\tau} \right) \Big]$ $\qquad$ (2.62)

Double: $+ \left[H(t) \, H(0) \sum_{a,b,c} \mu_{bc}^{\beta_1} \, \mu_{cg}^{\beta_2} \right.$

'A': $\left(-H(t-\tau) \, \mu_{ga}^{\beta_3} \, \mu_{ab}^{\beta_0} \quad e^{+i \, [\omega_{ag} + i\Gamma_{ag}]t} \, e^{-i \, [\omega_{bg} - i\Gamma_{bg}](t-\tau)} \right.$

'B': $\left. \left. + \, H(-\tau) \quad \mu_{ga}^{\beta_0} \, \mu_{ab}^{\beta_3} \quad e^{-i \, [\omega_{ag} - i\Gamma_{ag}]t} \, e^{+i \, [\omega_{bg} - i\Gamma_{bg}]\tau} \right) \Big] \right] \right\}$

2.7.3 Simulations and Simulation Approximations

Approximations made in the numerical evaluation of Equation (2.61) were guided by the requirement that the resulting simulations must be able to account for:

- General pulse shapes with varying pulse widths, pulse detuning, and input polarization.

- Inclusion of the power law exponent with a continuous range of $0 < \alpha \leq 1$, a wide range of dephasing rates, and variable energy level spacings, which can vary for each individual level.

- Simulation of both single level and double level terms, with the ability to vary the number and type of system levels, along with the polarization and dipole moment dependence of each level.

- Inclusion of inhomogeneous broadening, and the ability to simulate time- and spectrally-integrated (TI-SI-), spectrally- resolved (SR-), and time-resolved (TR-) degenerate four-wave mixing (DFWM) signals.

The ability to treat finite pulse shapes puts the largest demands on the numerical implementation. The much simpler equations obtained in the delta-function excitation limit (Equation (2.62)) have often been used for semi-quantitative analysis of data, and for the phenomenological treatment of processes that are not easily included in the general expressions for $\vec{\mathbf{P}}^{(3)}$. Examples include excitation induced dephasing, due to excitation of large numbers of particles, local field corrections, and fifth-order effects [44, 45].

By maintaining the finite pulse duration in our simulations, it is possible to fit spectra at a variety of pulse detunings in order to substantially constrain the material parameters (relative oscillator strengths, dephasing rates, power law exponents) extracted from the experimental data. This is possible because the spectral width of the pulses is comparable to the energy level spacings and inhomogeneous broadening width in these samples: small changes in detuning yield large changes DFWM spectra.

The numerical method chosen to implement Equation (2.61) is described in Appendix A. It is based on a Gaussian-quadrature, orthogonal-polynomial expansion of the exponential decay and pulse envelope functions. The terms are then integrated along with the orthogonal-polynomials that the functions have been expanded into, using known, closed form solutions for the integral of these polynomials with singularities and oscillatory factors. These methods were modified slightly, to account for the convolutions present in the integrals being evaluated in this work.

The simulation program was written in Fortran 95. As well as the above mentioned features, it simulates both the homogeneous and inhomogeneous delta-function expressions given in Equation (2.62). In addition to the generation of time & spectrally-integrated (TI-SI-), time-resolved (TR-), and spectrally-resolved (SR-) DFWM signals, it also has the capability to generate 'partially-spectrally integrated' signals, designed to simulate the finite resolution of the experimentally measured SR-DFWM signals.

Several assumptions are applied to the theory to speed execution. The previously mentioned assumption that $\Gamma_{gg} \rightarrow 0$ is made, allowing the convolution integrals over the pulse shapes to be done analytically for the single level terms. The explicit expressions

for these are in Table A.1 (page 169). Expressions for the pulse correlation integrals are in Table B.1 (page 209) and the pulse shapes can be found in Table 3.3 (page 81). As will be mentioned in Chapter 3, the pulse shapes that most closely match our experimental pulses have hyperbolic secant profiles.

Although this method works well for the 1-D integrals in the single level 'A' terms, the other terms contain higher dimensional integrals (2- & 3-D) and evaluate too slowly to be useful computationally. For the single level 'B' terms a delta-function like simplification was made in the dt' integral ($t_c \approx t - \tau$), which uncouples this integral from the dt_c integral, making this again a product of two 1-D integrals times a pulse correlation integral depending only on t_a. Investigations of the behaviour of the single level 'B' solutions and comparison with the analytic delta-function pulse solutions indicates that the solution retains its expected behaviour: it exists only around $\tau \approx 0$, $(t - \tau) \gtrsim 0$, and has a magnitude approximately equal to the single level 'A' term at the same time and delay values where its magnitude peaks.

For the double level (biexciton) 'A' terms, the assumption $t_b \approx t - \tau$ is made in the pulse envelope involving t_c, decoupling the three integrals. For the 'B' terms $t_a \approx t$ is first made in the coupled pulse envelope expressions and then $t_b \approx -\tau$ is made in the pulse envelope involving t_c. The numerical simulation then proceeds in a similar manner to the single level cases, except that the envelope function approach cannot be taken because of the presence of the double level (biexciton) singularity at $t_b = 0$, from the $t_b^{\alpha_{bg}-1}$ term in Equation (2.61).

Similar to the single level 'B' terms the main effect is that, due to the decoupling of the integrals, a convolution is missed that would be expected to 'smear-out' features (beat terms) slightly in the solutions, decreasing their magnitude with respect to the uncoupled solutions implemented here. For the short pulses used in this work ($\sim 0.1\,\mathrm{ps}$) and the long beat times ($\sim 1.3\,\mathrm{ps}$) this will affect the strength of the oscillations only slightly. Again, the results of this have been tested and were compared to the delta-function results to confirm that the simulations exhibited the expected behaviour: they
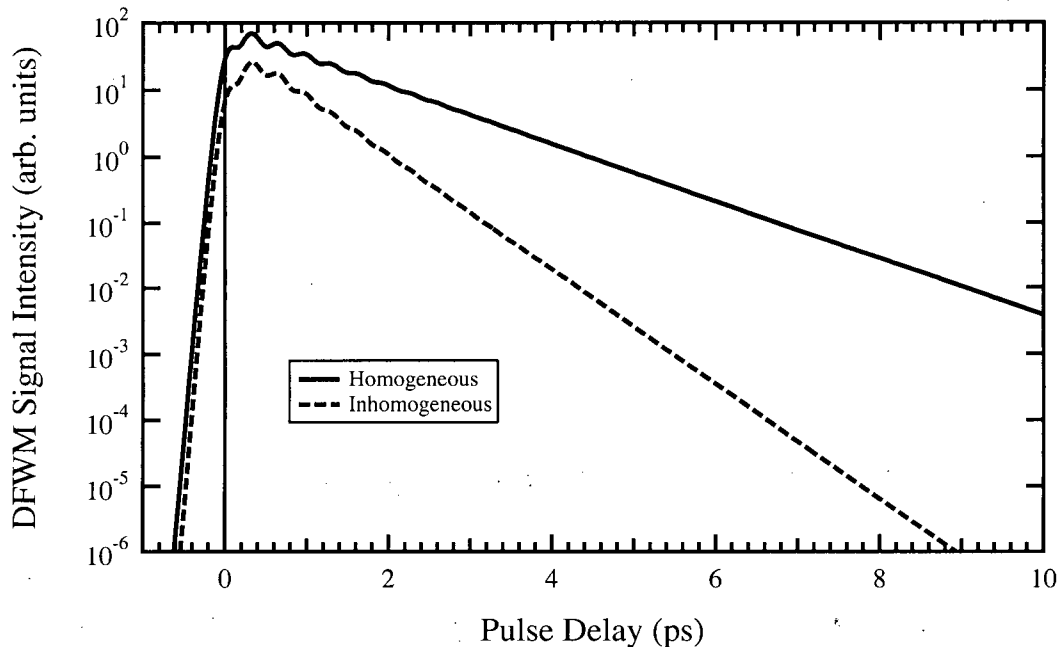
Figure 2.6: Homogeneous vs inhomogeneous DFWM signal simulation. The system consists of 2 single-level states 12.75 meV apart. The colinearly polarized 100 fs sech pulses are resonant with the lower state. $\alpha_j = 1$, $\Gamma_{inh} = 4.19$ meV, the dipole moment strengths are equal, and the dephasing rates are 0.5 ps^{-1} (lower state) and 1.5 ps^{-1} (upper state).

decrease the strength of the beat terms when compared to the delta-function results. Figure 2.5 on page 49 showed the general time-resolved (TR-) DFWM behaviour of each of these terms, along with the combined results for co-linear input polarization and both the single and double level terms.

2.7.4 Homogeneous vs Inhomogeneous Broadening

The differences between homogeneous and inhomogeneous single level systems are shown in Figure 2.6 for a system consisting of two single-level states. The main feature in this time and spectrally integrated signal simulation is that the inhomogeneously broadened signal decays at twice the rate that the homogeneous one does.

To show more clearly the nature of the difference between the homogeneous and inhomogeneous broadening signals, time resolved (TR-) DFWM signals are shown in
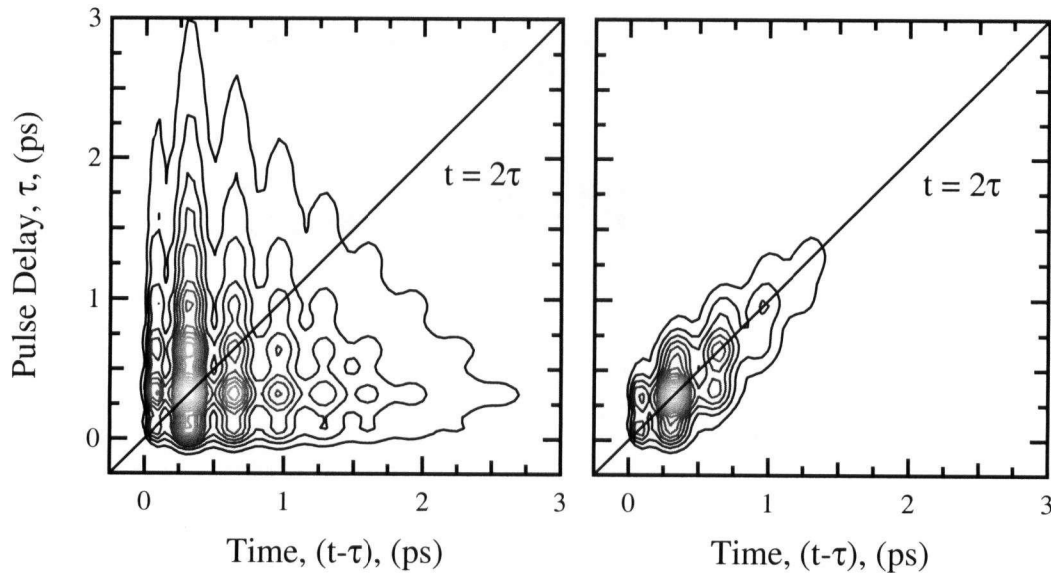
Figure 2.7: Homogeneous (left) vs inhomogeneous (right) TR-DFWM signal simulations. The system consists of 2 single level states, described in Figure 2.6.

Figure 2.7. The contour plot on the left is the TR-DFWM homogeneous case and shows that the signal decays when the time is greater than the delay (τ). In contrast, the TR-DFWM inhomogeneous signals exists as a 'photon echo' pulse centered at $t = 2\tau$ (the diagonal line in the picture). The beats between the two single-level states are visible in both the homogeneous and inhomogeneous cases, since the oscillations occur both in the delay (τ) and time ($t - \tau$) directions.

2.7.5   General DFWM Results versus Delta-Function Pulse Results

The importance of including the pulse shape in DFWM signal simulations is highlighted in Figure 2.8, which presents a comparison between delta-function excitation pulse results and full TI-DFWM simulations with varying pulse width. The system simulated consists of an inhomogeneously broadened system of two excited levels (corresponding to a 1S-2S exciton system).

The delta-function excitation approach implicitly assumes that the exciting field strength is independent of frequency. As Figure 2.8 shows, the main effect of increasing
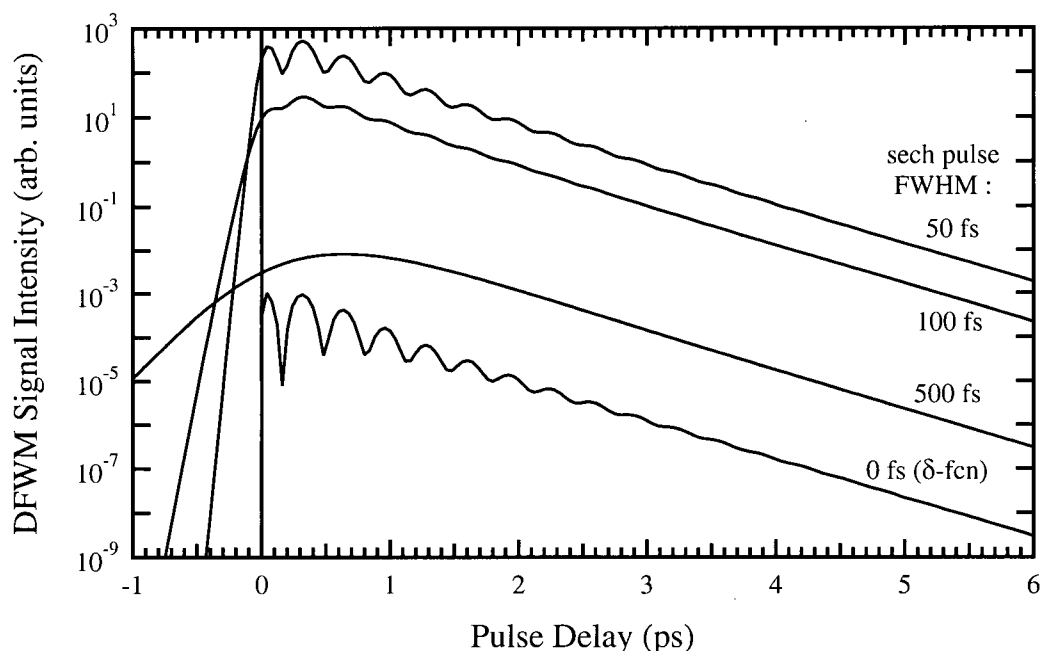
Figure 2.8: Inhomogeneous DFWM signal simulations – δ-function vs varying pulse width. The system has two excited levels, both with $\alpha_j = 0.95$ and $\Gamma_{\mathrm{inh}} = 4.2\,\mathrm{meV}$. $\Gamma_j = 0.5\,\mathrm{ps}^{-1}$ for the lower level, while the upper level, $12.75\,\mathrm{meV}$ above the lower, has $\Gamma_j = 1.5\,\mathrm{ps}^{-1}$. The pulses are resonant with the lower level.

the pulse width is to decrease the modulation depth of the beats. When the pulses are larger than the beat period, they disappear entirely. In the frequency domain this corresponds to an increasingly narrow frequency excitation spectrum as the pulses get longer in time, so that eventually only one level is excited.

The modulation depth of the beats is controlled by the relative amplitudes of the 1S and 2S states excited by the pulses. This, in turn, is determined by the spectral width of the excitation pulses and the dipole moments of the two transitions. As shown below, knowing the pulse spectrum it is possible to measure the beat modulation depth as a function of laser detuning in order to accurately estimate the relative dipole moments of the two levels. This would be impossible in the delta-function limit of the simulations. The dephasing rates of faster decaying levels are also decreased by the delta-function approach, due to it's inherent inaccuracy at shorter delay times and partially by the over-estimation of the dipole-moment strength.
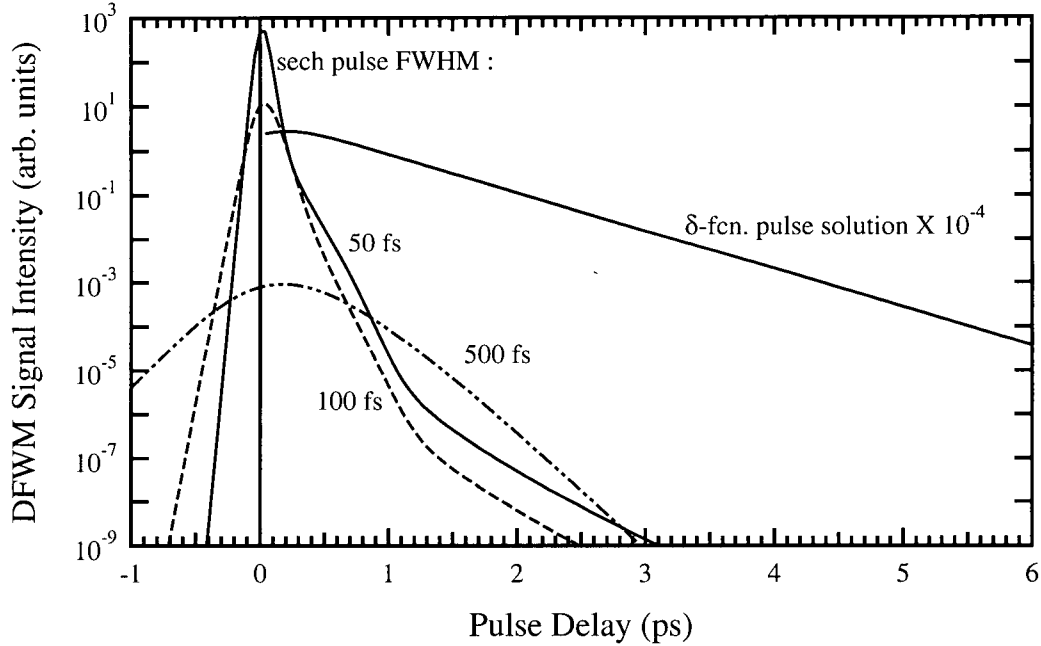
Figure 2.9: Inhomogeneous DFWM signal simulations – δ-function vs varying pulse width. The system has one continuum level, with $\alpha_j = 0.05$, $\Gamma_{inh} = 4.2\,\text{meV}$, $\Gamma_j = 0.5\,\text{ps}^{-1}$, and the pulses are resonant with the level.

The delta-function approach's lack of ability to properly estimate the short time limit is shown in Figure 2.9, where three pulse widths are shown for a single, continuum state with $\alpha = 0.05$. The main feature is a large peak (several orders of magnitude in size) that is independent of the dephasing rate. The peak gives a significant contribution to the signal for pulse delays within 3-4 pulse widths of zero delay. The delta function approach, by contrast, does not simulate this continuum effect or its interaction with the other states around zero delay.

2.7.6 Pulse Detuning Effects

In this section we qualitatively investigate the model predictions for the effect of pulse detuning (varying the central frequency of the laser pulse) on the FWM response. Figure 2.10 shows a series of FWM versus τ plots, where the pulse detuning is taken with respect to the energy of the lowest energy state in the system.
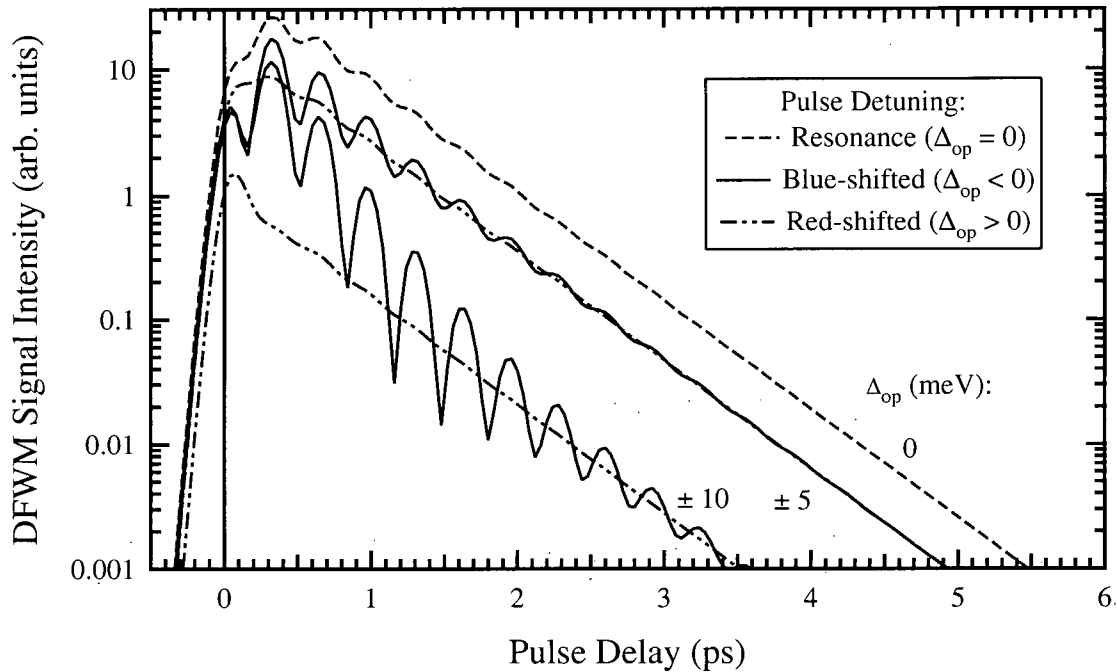
Figure 2.10: Pulse detuning effects on 1S-2S DFWM signal simulations. The system simulated consists two excited (1S,2S exciton) states, 12.4 meV apart. Except for the pulse detuning away from the system reference (1S state) energy of 1619.82 meV, the parameters are the same as for Figures 2.6 and 2.7.

As the pulse is detuned off of the 1S resonance the signal decreases. The phase of the beats remains unchanged, but the modulation depth of the beats varies substantially. The modulation depth is largest when exciting closer to the 2S resonance because the oscillator strength of the 2S resonance is less than that of the 1S resonance: The net polarization is therefore nearly equally distributed between the 1S and 2S levels when the pulse preferentially excites the 2S level.

2.7.7 Double Level Terms

Thus far in Section 2.7 we have implicitly used only one-photon resonant terms in $\overset{\leftrightarrow}{\chi}^{(3)}$, because we have not included any higher lying state with energy close to 2ω. In our model, states with energy near 2ω can consist of either bound (biexciton) or unbound (two-free-exciton) states, with unbound states at exactly twice the energy of the single
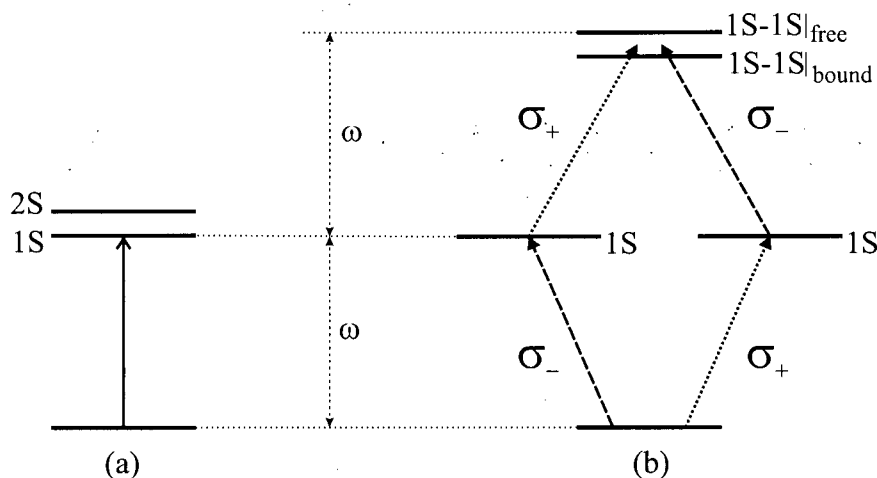
Figure 2.11: Schematic comparison of single and double level systems. The single level system (a) is shown with 1S and 2S exciton levels. The double level system is shown with two 1S states and two-exciton states: a bound, or biexciton state and an unbound, or two-free-exciton state. The $\sigma_{\pm}$ symbols indicate the two circularly polarized components of the exciting light.

(exciton) states. The biexciton level is reduced in energy from the two-free-exciton level by the biexciton binding energy. When dealing with two particle states it is convenient to use intrinsic angular momentum (or, spin) labels for all of the many states involved in the excitation. Figure 2.11 illustrates the relevant levels in a manner where the spin label of the states is implied by position along the horizontal axis. To assist with interpretation, the exciting light is resolved into its circularly polarized basis components, with spins of $\pm\hbar$ [50, page 515].

Figure 2.12 shows the simulated DFWM decay curves obtained when all of the levels shown in Figure 2.11 (b) are included. The homogeneous signal shows no visible sign of beating terms at positive delay, while the inhomogeneous signal shows a strong beat term. The phase of these beats are shifted by 180° as compared to the 1S-2S single-exciton beats shown previously in this section (Figure 2.10, for example). The homogeneous signal exhibits beats at negative pulse delay times. The beat period corresponds to the biexciton binding energy in both cases.

To further illustrate the nature of these very different beats, the corresponding TR-
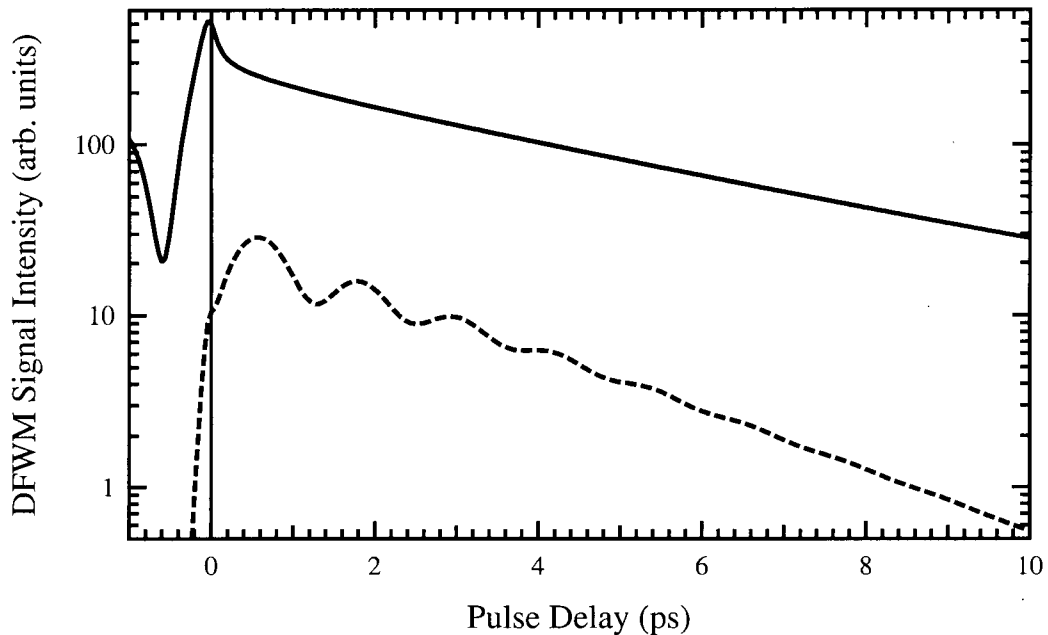
Figure 2.12: Double level DFWM signal simulations. The system considered is shown in Figure 2.11 (b). Both homogeneous (solid) and inhomogeneous (dashed) signal simulations are shown. The parameters used are given in Figure 2.16 (on page 63).

DFWM signal simulations are shown in Figure 2.13. The left contour plot shows the homogeneous case. The double level (biexciton) beats are clearly visible along the $(t - \tau)$ axis, but they are averaged out of the time integrated signal.

The case of inhomogeneous broadening (right contour plot) is dramatically different. The signal is only present during the 'photon echo', which peaks at $t = 2\tau$ as it did for the single levels. This allows the oscillations to become visible in the time-resolved signal, as the 'photon echo' effectively samples the oscillating polarization seen in Figure 2.13 (a) at positive delay times. Thus, somewhat counter-intuitively, inhomogeneous broadening renders beat terms easily visible in the TI-DFWM signals associated with two-photon resonant processes [25, 26, 32]. This provides a means of probing the nature of the biexciton state. To more completely understand the processes that contribute to these biexciton beats, it is useful to consider the effects of varying the exciting pulse polarization.
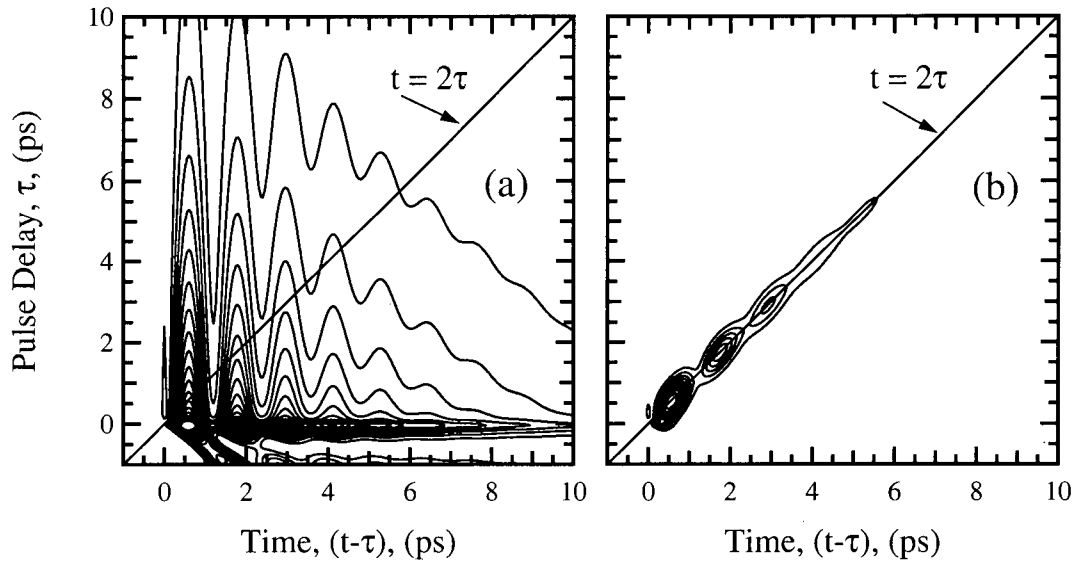
Figure 2.13: Contour plot, double-level DFWM signal simulations, with homogeneous (a) and inhomogeneous (b) broadening. The system simulated corresponds to Figure 2.11 (b) and the DFWM simulations in Figure 2.12.

2.7.8 Input Beam Polarization Effects

The behaviour of the DFWM signal has a strong dependence on the input beam polarizations. As illustrated in Figure 2.14, co-circularly polarized (CCP) input beams lead only to single level (excitonic) systems, as the excitation of two-exciton states **requires** the presence of both left- and right-circularly polarized light. The black line in Figure 2.14 (a) indicates the excited level under σ_+ excitation, while the grey lines indicate the levels that are not excited. Figure 2.14 (b) illustrates co-linearly polarized (CLP) input beams results in both the one-exciton and two-exciton states generating DFWM signals. For the cross-linearly polarized (XLP) input beam case, Figure 2.14 (c), the two-exciton states generate the detected DFWM signals [26,51,52].

For CLP input beams, both one-exciton and two-exciton states are excited, leading to a beating between the ground–to–one-exciton and one-exciton–to–two-exciton polarizations, indicated by the solid lines and the dashed/dotted lines in Figure 2.14 (b), respectively. The phase of the ground–to–exciton and exciton–to–biexciton polarizations
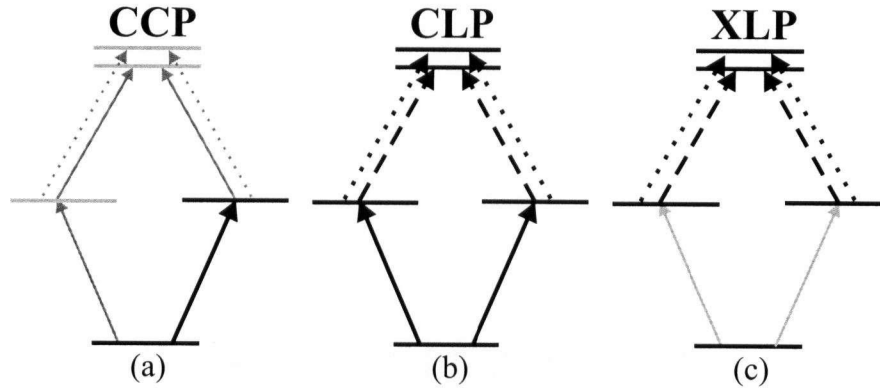
Figure 2.14: Schematic illustration of the effects of input beam polarization on DFWM systems. The transitions contributing to the detected DFWM signal are connected with black arrows, with others being shown in grey. Three input pulse polarizations are illustrated in the Figure: (a) co-circular polarization (CCP), (b) co-linear polarization (CLP), and (c) cross- or orthogonal-linear polarization (XLP).

differ by 180°, which explains why the first maximum in the DFWM signal is delayed along the $(t - \tau)$ axis in Figure 2.13 (a). Recall that this delay is responsible for the 180° phase shift of the beats in the inhomogeneously broadened systems.

For XLP input pulses, it turns out that there is no net polarization due to the ground–to–one-exciton transitions. Beats are, however, still observed. They correspond to interference between the one-exciton–to–two-free-exciton and the one-exciton–to–biexciton polarizations (dotted and dashed lines in Figures 2.14 (b-c), respectively). Since these are in-phase, the corresponding DFWM beats return to being in-phase with the excitation pulse [26, 51, 52].

Figures 2.15 and 2.16 summarize the effect of input polarization on the DFWM signals associated with two-exciton resonances. In Figure 2.15 the phase shift of the double level beats between CLP and XLP input polarizations is clearly seen, as is the lack of beats in the CCP case. Figure 2.16 shows homogeneous, time-resolved intensity contour plots for the three input polarization combinations. The CCP and CLP cases show similar results to those pictured previously, while the XLP case shows how the exclusively two-exciton beats shift back in phase with the input pulses in the absence of the ground–to–one-exciton polarization.
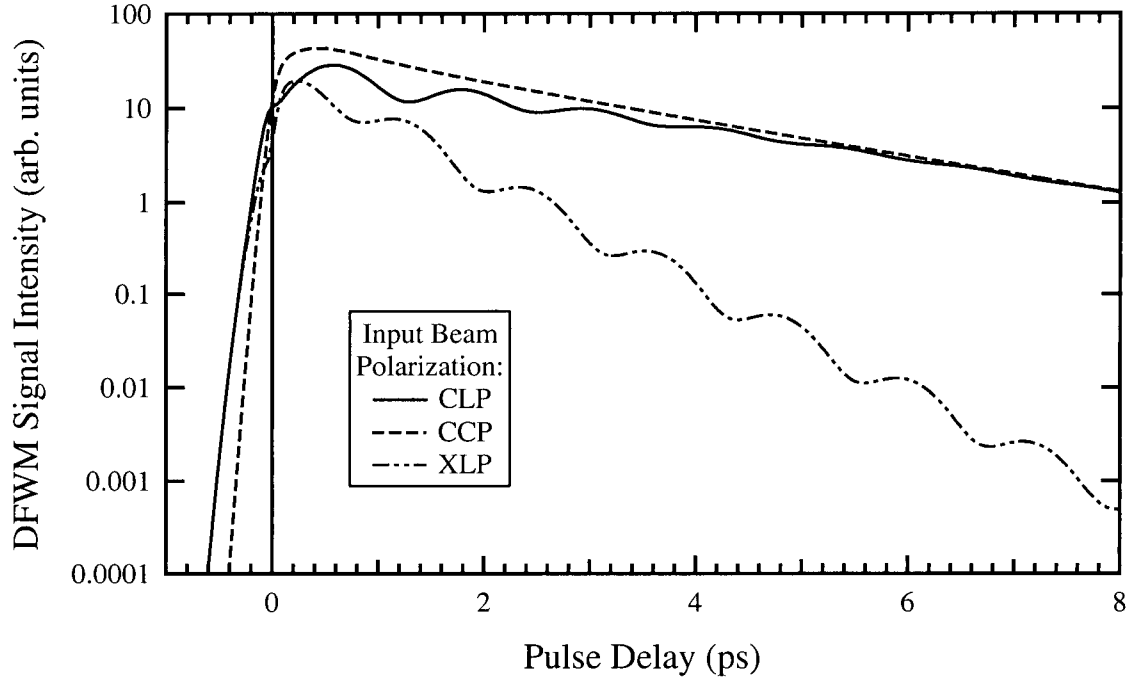
Figure 2.15: Inhomogeneous DFWM signal simulations for CLP, CCP, & XLP input beam polarizations. The system considered is that illustrated in Figure 2.14 (a one-exciton level, a biexciton level, and a two-free-exciton level). For all 3 levels $\alpha_j = 0.95$ and $\mu_j/\mu_{\rm ref} = 1$. The biexciton binding energy is set to 3.5 meV, while $\Gamma_j = 0.1/0.44\,{\rm ps}^{-1}$ for the one/two-exciton levels, respectively. The 100 fs sech pulses are resonant with the one-exciton level, and $\Gamma_{\rm inh} = 4.2\,{\rm meV}$.

2.7.9   The Power Law Exponent

The effect of varying the power law exponent describing the non-Lorentzian nature of a single inhomogeneously broadened level is shown in Figure 2.17 (a). In some respects the curves in Figure 2.17 (a) are the FWM equivalents of the linear absorption spectra shown in Figure 2.3 (page 45). As the power law decreases towards zero, corresponding to a step-edge-continuum, the peak shifts towards zero delay, and the signal decays at a monotonically increasing rate. This "continuum peak" increases in magnitude relative to the longer decaying component as the power law exponent approaches zero, leaving a contribution only around zero pulse delay in the pure step-edge-continuum limit.

The shift to zero delay, and the evolution to a fast and non-exponential decay as the
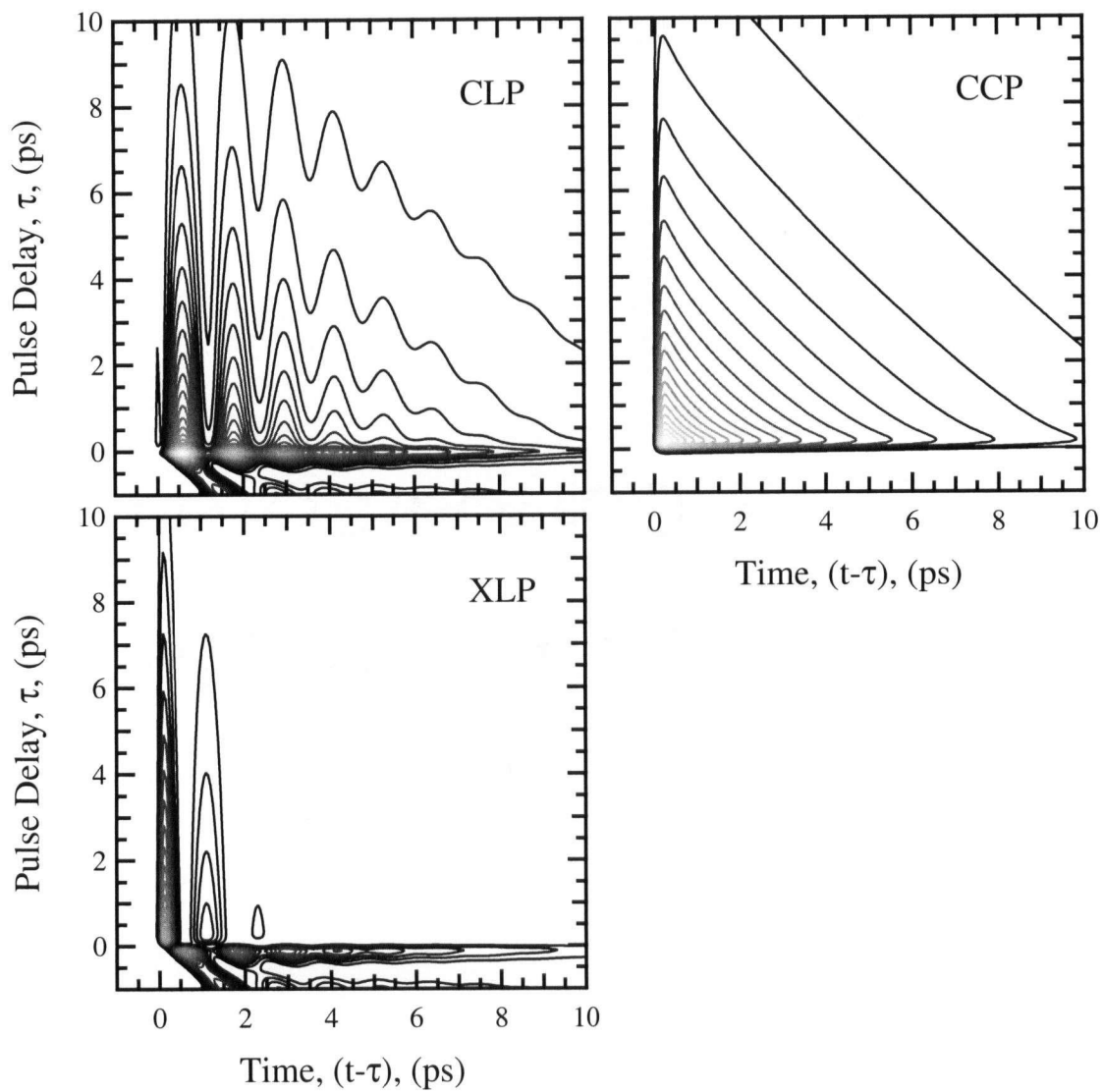
Figure 2.16: Contour plots of homogeneous DFWM signal simulations for CLP, CCP, & XLP input beam polarizations, including both one-exciton (1-X) and two-exciton (two-free-exciton, XX_f, and biexciton, biX) states. The system is the same as was used for Figure 2.15, illustrated schematically in Figure 2.14.
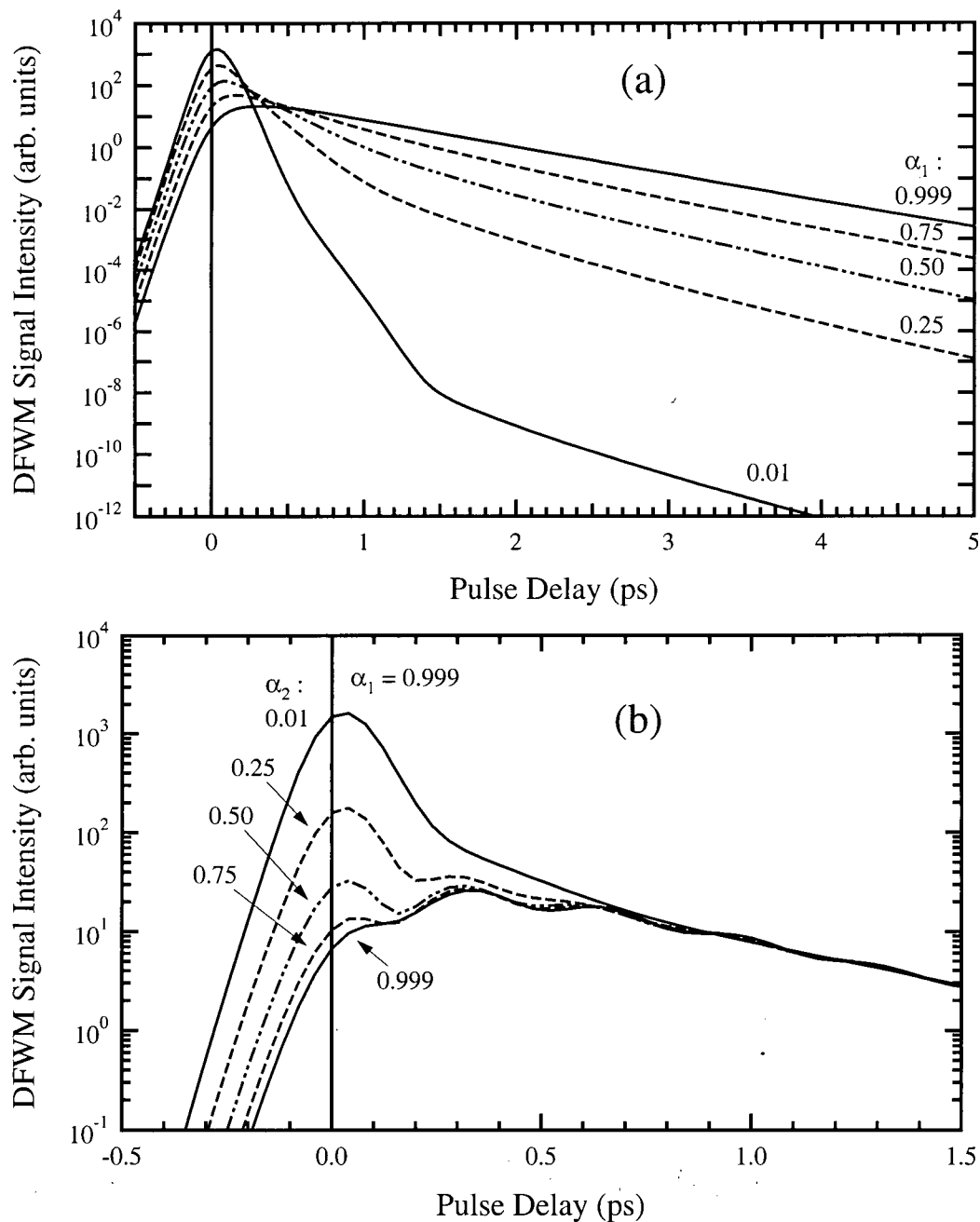
Figure 2.17: Inhomogeneous DFWM signal simulations with varying power law exponent. (a) consists of 1 single-particle state, while (b) shows the interaction of a discrete exciton state (α_1) with a second state that varies from discrete ($\alpha_2 = 0.999$, corresponding to regular 1S-2S exciton beating) to an idealized, "pure" continuum state ($\alpha = 0.01$). For both plots, $\Gamma_1 = 0.5\,\mathrm{ps}^{-1}$ and $\Gamma_{\mathrm{inh}} = 4.2\,\mathrm{meV}$. For the lower plot, (b), $\Gamma_2 = 1.5\,\mathrm{ps}^{-1}$ and $\Delta E_{1,2} = 12.75\,\mathrm{meV}$. The 100 fs sech input pulses have zero pulse detuning with respect to the lower level.

power law decreases from unity can be qualitatively understood as follows. As the power law decreases, the pulse is effectively exciting more and more "off-resonant" transitions that are all blue-shifted with respect to the excitation. As previously illustrated in Figure 2.10 (page 57), the FWM response of a single inhomogeneously broadened level peaks near zero delay when far off-resonance, but peaks later when excited on-resonance. As the power law decreases, the large number of effectively blue-shifted resonances start to dominate the near-resonant transitions, shifting the peak to zero delay. The non-exponential and rapid decay of the signal reflects the destructive interference of a continuum of transitions as manifested in the time-domain. If the continuum was described by a Gaussian, the dephasing in the time-domain would also be Gaussian-like (as in the case of inhomogeneously broadened free-induction decay). The power law form of our frequency response function corresponds, rather, to a power law decay in the time-domain (ultimately associated with the power law time domain character of the time-time correlation function derived for the Fermi-edge singularity [3,53]). The short-time decay behaviour in Figure 2.17 (a) associated with smaller power law exponents is thus power law-like. We expect that the FWM signals from our doped samples might therefore be fit by curves such as those in Figure 2.17 (a).

Even in the undoped sample, where the 1S and 2S exciton states can be well described by simple Lorentzians, the power law response function is useful for phenomenologically simulating the contribution of exciton scattering states (or, equivalently, the Sommerfeld-enhanced continuum). To illustrate how the enhanced continuum interacts with discrete levels, we next consider the case of a single Lorenzian and a second level, blue-shifted by $12.4\,\mathrm{meV}$, that is described by the power law response function. As the power law exponent of the upper state is decreased from 1 to 0, Figure 2.17 (b) shows that the modulation depth of the beats decreases and the position of the first minimum shifts dramatically to longer delays. This is consistent with the DFWM expressions, where the decrease of the power law exponent towards zero causes up to a 90° phase shift in the term with the varying power law (Equation (2.61)). A peak appears at short time

delays, increasing in relative magnitude and shifting to within one pulse width of zero delay as the power law exponent decreases toward zero. This is the "continuum peak" identified earlier in this section. Below it will be shown that an $\alpha \approx 0.06$ best describes the experimentally observed DFWM signals. The main contribution of the continuum is therefore to add a peak near zero delay. The relative importance of this peak depends on the detuning of the excitation pulse.

This chapter has presented the linear and non-linear polarization model developed to simulate the experimental results described in the following chapters. The model incorporates finite, realistic excitation pulse-shapes together with inhomogeneous broadening, exciton, and continuum contributions to both the linear and nonlinear susceptibilities. The usual Lorentzian resonances are generalized to power-law form in order to more easily simulate the continuum in undoped samples, and the many-body influence of carriers in the case of doped samples, where the absorption threshold is theoretically expected to have a power law form.

Chapter 3

Samples & Experimental Techniques

This chapter starts, in Section 3.1, with a discussion of the samples and sample preparation. This is followed by a description of the technique used to study linear absorption in these samples (Section 3.2). Finally, a detailed description of the two-pulse degenerate four-wave mixing (DFWM) experimental technique that was used to examine some of the samples is described, in Section 3.3.

3.1   Samples & Sample Preparation

The sample parameters are summarized in Tables 3.1 & 3.2. They each contain a series of $50 - 5\,\mathrm{nm}$ GaAs quantum wells with $\mathrm{Al_{0.3}Ga_{0.7}As}$ barrier layers. This multiple quantum well stack is surrounded on both sides by thicker $\mathrm{Al_{0.3}Ga_{0.7}As}$ barriers and GaAs cap layers. The samples were grown by Z. Wasilewski at the Institute for Microstructural Sciences, National Research Council of Canada (NRC), using the Molecular Beam Expitaxy (MBE) technique. They were prepared by S. A. Brown, who also studied the linear absorption through these samples.

The doping in the barriers (as well as their thickness) was designed to provide as pure an electron gas in the wells as possible, formed due to the small ionization potential of the Si δ-doped atoms in the barrier layer and the lower potential of the quantum wells attracting the freed electrons. The Si *delta*-doping in the barrier layers also minimizes the opportunity for donor atoms in the barrier to diffuse into the wells. As well, the Si δ-doping near the surfaces was designed to prevent electrons in the wells from being

Table 3.1: Sample growth information for the Multiple Quantum Well (MQW) samples (50 – 5 nm quantum wells). Barrier dopings are listed in Table 3.2. Layers are listed in the reverse order to which they were grown. Note that the barrier doping layers are twice as thick for the highest doped sample (1694) only.

Material	Dopant	Concentration (cm^{-3})	Stop ?	Width (nm)	Repeat
GaAs				5	1
$Al_{0.3}Ga_{0.7}As$				30	1
$Si - \delta$	Si	1×10^{12}	Y	0	1
$Al_{0.3}Ga_{0.7}As$				160	1
$Al_{0.3}Ga_{0.7}As$				20	50
$Al_{0.3}Ga_{0.7}As$	Si	See Table 3.2		5/10	50
$Al_{0.3}Ga_{0.7}As$				15	50
GaAs				5	50
$Al_{0.3}Ga_{0.7}As$				20	1
$Al_{0.3}Ga_{0.7}As$	Si	See Table 3.2		5/10	1
$Al_{0.3}Ga_{0.7}As$				175	1
$Si - \delta$	Si	1×10^{12}	Y	0	1
$Al_{0.3}Ga_{0.7}As$				30	1
GaAs				5	1
AlAs				50	1

removed by surface states, reducing the density variations from well-to-well [4]. These MQW layers were lifted off their substrate and bonded to a glass slide, as described next.

As shown in Table 3.1, there is a 50 nm AlAs layer underneath the structure. As described in [5, 54, 55], the as-grown samples were coated with wax on the epitaxially grown side and then chemically etched using a hydrofluoric (HF) acid solution. The HF acts as an extremely selective etch in this system so that the AlAs layer is preferentially etched away, causing the MQW layers to float free from their substrate. The thin layers are then attached to the substrates by Van der Waals bonding.

3.2 Linear Absorption Experiments

Quantitative linear absorption experiments were conducted on all samples by S. Brown [4, 5], using a white light source and a Fourier Transform spectrometer (Bomem, model

Table 3.2: 2-dimensional electron gas concentration and corresponding barrier dopant layer concentrations for MQW samples described in Table 3.1. Note that the barrier dopant layer for sample 1694 is twice the thickness of the others. 2-D Fermi Energies are calculated using the constant 2-D density of states for free carriers [1, page 141], $E_F = \pi \hbar^2 n_{2D}/m_e^* e = 0.368\,289\,78\,meV \cdot n_{2D}$, with n_{2D} in units of $10^{10}\,cm^{-2}$ and $m_e^* = 0.065\,m_e$. 2-D well doping densities, n_{2D}, were verified by low temperature transport measurements at NRC [6].

Sample	2-D Well Doping, n_{2D} (cm^{-2})	Barrier Growth Doping (cm^{-3})	2-D Fermi Energy (meV)
1657	0	0	0.000
1658	2.5×10^{10}	0.5×10^{17}	0.921
1656	5×10^{10}	1×10^{17}	1.841
1659	10×10^{10}	2×10^{17}	3.683
1694	20×10^{10}	2×10^{17}	7.366

DA-8). The samples were mounted in a constant flow cryostat (Janis Research Co., Model ST-4) to allow measurements at temperatures from 4.2 K (liquid helium) to 300 K (room temperature). The light source was p-polarized relative to the sample surface and incident on the sample near Brewster's angle[†], where the reflectivity of the p-polarized light goes to zero. This was done in order to reduce Fabry-Perot interference effects by reducing the finesse of the multi-layer stack — as the reflectivity goes to zero, the difference between the maximum and minimum in the Fabry-Perot fringes also goes to zero [56, Chapters 14 & 23]. This technique also simplifies the extraction of absorption information from the transmission measurements. Transmission data was also collected on some of the samples using the four-wave mixing apparatus described in Section 3.3.5.

The absorption spectrum between 625 nm and 885 nm (1984-1401 meV) is calculated from the transmission by considering the equation relating the normalized intensities of reflection (R) and transmission (T), and the fractional absorption (A):

$$R + T + A = 1 \,. \tag{3.1}$$

[†] Brewster's angle for air-GaAs varies from $\theta_B = 74.5°$ to $\theta_B = 75.3°$ over the measured energy range (1.4-1.9 eV). From data in [49, pages 108-9].
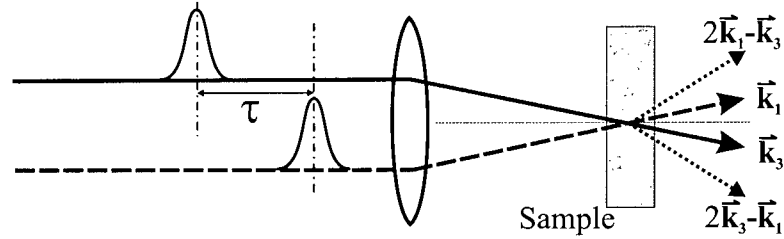
Figure 3.1: Schematic illustration of 2 pulse, degenerate four-wave mixing (DFWM). The two pulses impact on the sample in the directions $\vec{k}_1$ and $\vec{k}_3$ (solid & dashed lines). They have a relative time delay, τ. Two four-wave mixing signals are generated (dotted lines), in the directions $2\vec{k}_1 - \vec{k}_3$ and $2\vec{k}_3 - \vec{k}_1$.

At Brewster's angle this reduces to

$$A = 1 - T \ . \tag{3.2}$$

The absorption is often expressed in terms of

$$A = \left(1 - \exp\{-\alpha_{abs}d\}\right) \ , \tag{3.3}$$

where d is the thickness of the absorbing component of the material and α_{abs} is the absorption coefficient (usually expressed in units of cm^{-1}). Substituting Equation (3.3) into Equation (3.2) and solving for α_{abs} gives

$$\alpha_{abs}d = -\ln\left(T\right) \ . \tag{3.4}$$

The results of the experimental studies of white light transmission through the samples are presented in Section 4.1.

3.3   Nonlinear Four-Wave Mixing Experiments

The four-wave mixing experiments were conducted in a degenerate, two pulse transmission geometry, illustrated schematically in Figure 3.1. The term degenerate refers to the fact that the two laser pulses are derived from a common source, using a beam splitter.

Two degenerate four-wave mixing signals (DFWM) are generated, in the directions $2\vec{k}_1 - \vec{k}_3$ and $2\vec{k}_3 - \vec{k}_1$. The signals in these two directions are basically the same, except
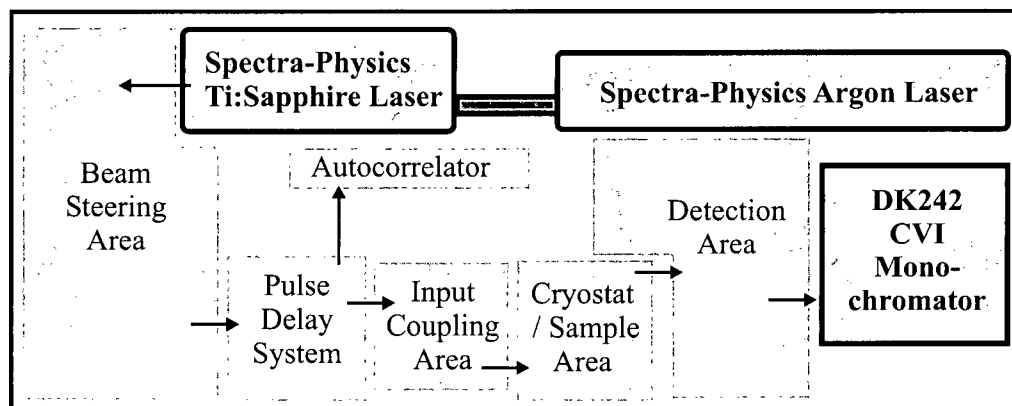
Figure 3.2: Major optical system sub-units (shaded areas) and general photon flow (arrows).

that the time reference is inverted ($\tau \rightarrow -\tau$) and the DFWM polarization signals are proportional to $E_1^2 E_3$ and $E_3^2 E_1$, respectively. Due to this square-linear dependence of the generated DFWM polarization on the electric fields, the magnitude of the measured DFWM signals can be significantly different in the two directions. For example, if $E_1 > E_3$, then acquiring the signal in the $2\vec{k}_1 - \vec{k}_3$ direction will give a larger measured DFWM signal.

An overall view of the optical setup is shown in Figure 3.2. It consists of six main areas: the lasers and beam steering area, the pulse delay system, the autocorrelator, the input coupling area, the cryostat/sample area, and the detection area. Each of these will be discussed separately in the following sections.

The entire DFWM system is monitored with software developed using LabView 4.0 from National Instruments. The command and control software consists of three main components that are described below in conjunction with the relevant apparatus.

3.3.1 Lasers and Beam Steering System

The laser used in this work is a Spectra-Physics Tsunami model 3960-S1S Ti:Sapphire laser, pumped by a 7W Spectra-Physics BeamLok Argon ion (blue-green) laser. With this pump power from the Argon ion laser and the installed femtosecond (fs) optics, the

Tsunami laser has a wavelength range of 735-820 nm. The laser produces pulses with a full-width at half-maximum (FWHM) of ~100 fs, has an average beam power of about 750 mW, vertical polarization (> 500:1), and a repetition rate of 82 MHz.

The experimental setup for the laser and the beam steering system is shown in Figure 3.3. As well as the Ti:Sapphire laser, it contains a grating and two beam deflecting components, along with several mirrors and apertures. The grating is used to assist in tuning the laser wavelength as well as monitoring whether the laser is mode-locking (producing laser pulses) or is in a continuous-wave (CW) mode. It is mounted on a kinematic mount so that it can be inserted and removed from the system without needing to realign other components. Beam deflecting elements, on a kinematic mount near the grating, allow various components (mirrors, beam-splitters) to be inserted into the beam path if it is required to deflect the beam to other regions.

Mirrors M3 & M4 are used to align the laser beam through apertures A1 & A2, respectively. They also serve to raise the beam from the Ti:Sapphire laser height to the height (165 mm, or 6.5 in) used by the rest of the DFWM system. Once the beam is aligned on apertures A1 & A2 it enters the pulse-delay system, discussed next.

3.3.2 Pulse Delay System

The purpose of the pulse delay system is to split the beam path into two, delaying one of the pulses by a measurable time with respect to the other. This time delay was indicated by τ in Figure 3.1. A schematic illustration of the pulse delay system is illustrated in Figure 3.4.

The initial splitting of the incoming laser beam into two arms is done by the beam-splitter, BS2, which has a 52:48 splitting ratio for s-polarized light at 45° (52 ± 2) % transmission from 720-920 nm, with an 800 nm center wavelength). The first component in the fixed arm (dashed line in Figure 3.4) is the gold coated, three mirror retro-reflector (RR2). The reflected beam from this retro-reflector comes out parallel to the input beam, displaced by about 1 cm. It is mounted on three translation stages, two of which are used
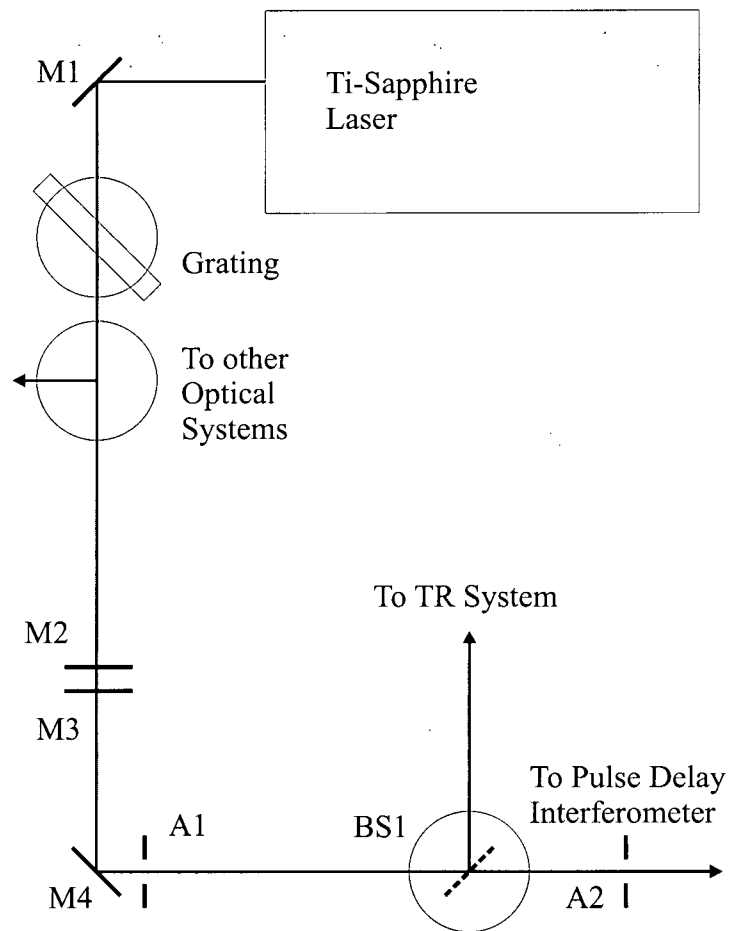
Figure 3.3: Schematic illustration of driving laser and beam steering area. M1-M4 are 25.4 mm broadband mirrors (0.6-18 μm), used to align the laser beam through the apertures A1 & A2. The grating (flat, 1200 grooves/mm, blaze angle of 36° 52′) assists in tuning the laser and monitoring whether it is mode-locked (producing pulses). BS1 is a 52:48 beam splitter used to deflect part of the beam to other optical systems on the table. Large circles are kinematic mounts.
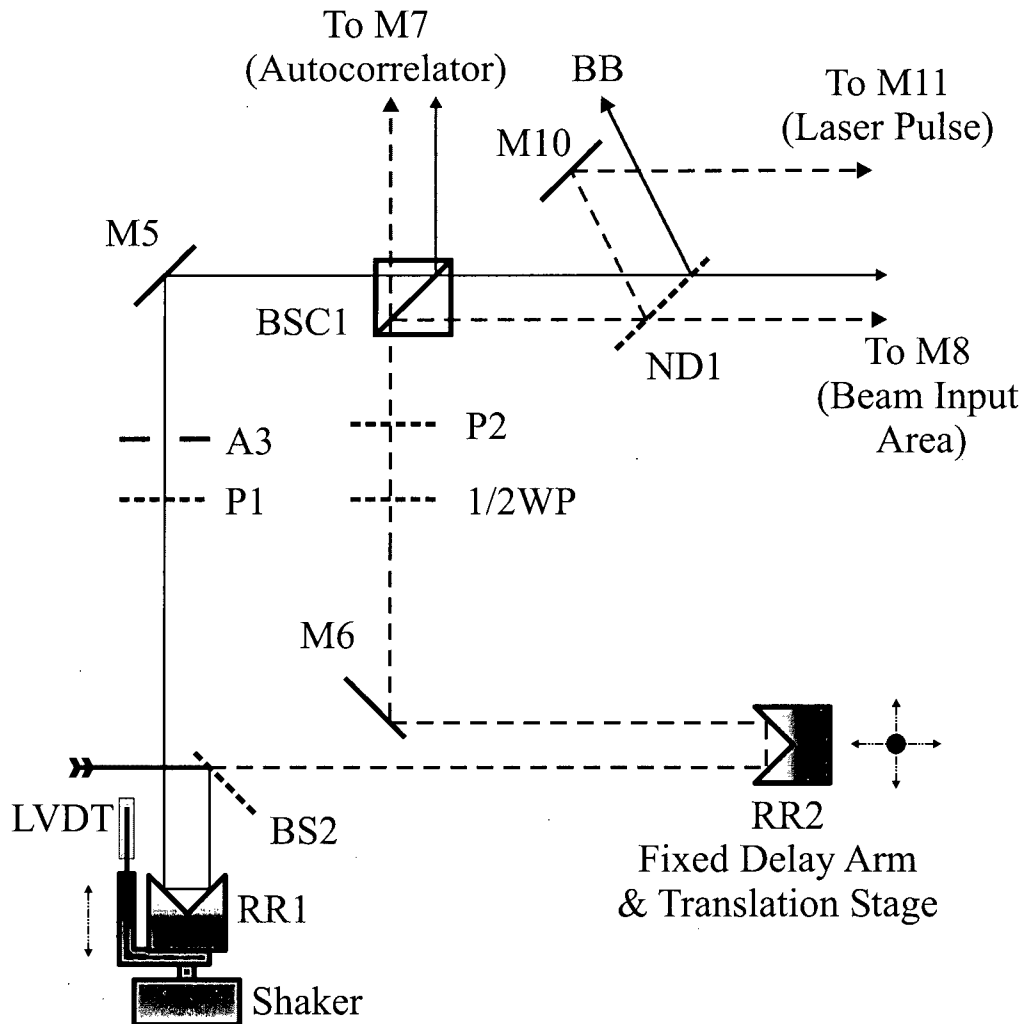
Figure 3.4: Schematic illustration of pulse delay system. Components, discussed in text, are: 52:48 beam-splitter (BS2), gold coated retro-reflectors (RR1 & RR2), rotatable linear polarizers (P1 & P2), rotatable 1/2 wave plate, mirrors (M5, M6, & M10), beam-splitter cube (BSC1), beam blocker (BB), aperture (A3),and neutral density filters (ND1). The variable delay arm is indicated by a solid line, while the fixed delay arm is indicated by a dashed line.

for aligning the beam with the variable delay arm. The third translation stage offers manual control of the time delay, τ. Moving the time delay stage by a distance d shifts τ by $2d/c$: for $d = 1\,\text{mm}$, $\Delta\tau = 6.67\,\text{ps}$.

Mirror M6 is used to reflect the beam into the beam-splitter cube and is also used for long range alignment of the beams, as discussed in Section 3.3.4. The fixed delay arm beam then passes through the 1/2 wave plate (800 nm center wavelength, 100 nm bandwidth) and linear polarizer. This allows the linear beam polarization of the fixed delay arm to be rotated with respect to the vertical polarization of the variable delay arm. The rotating polarizer acts both to assist with the polarization adjustment and to help remove any unwanted, orthogonal polarization component. When intensity dependent measurements are conducted there are additional neutral density filters or glass slides in this arm, to compensate for the delay introduced by neutral density filters inserted into the variable delay arm.

The first component in the variable delay arm is the retro-reflector (RR1), attached to the Mini-Shaker. The Mini-Shaker (Brüel & Kjaer, model 4810) is an extremely stable, single axis vibrator with a maximum displacement of 6 mm. It is mounted horizontally so that its central axis is 165.1 mm off the optical table. It is driven by a current source that is, in turn, driven with a sine wave from a function generator (usually at $\sim$19 Hz).

The position sensor is a linear variable differential transducer (LVDT), with a nominal linear sensing range of ±2.50mm from its central position (Shaevitz Engineering, model 100 MHR). This translates into a maximum nominal linear delay range of 33.1 ps. The LVDT is controlled by a LVM-110 series signal conditioner and the signal is measured using a 12-bit A/D board. The LVDT and signal conditioner provide a signal of 2.3611 V/mm, or 0.70784 V/ps for this system. The measured noise is approximately 1 mV, corresponding to a change in delay of 1.41 fs. Currently the LVDT and signal conditioner are operated over a range of ± 4.75 V, giving a delay range of 13.42 ps. Since the range of the 12-bit A/D board used for these LVDT measurements is ±5 V the A/D board resolution of 2.44 mV is the limiting factor over this range. This corresponds to

changes in the pulse delay of 3.45 fs. The LVDT signal is acquired in conjunction with either the autocorrelation signal or the DFWM signal, to "mark" the appropriate delay, τ, for each sample of the signal.

After the retro-reflector, the variable delay arm beam passes through the rotatable linear polarizer P1. This polarizer, kept in the vertical position, helps to reduce remaining horizontal polarization components. The aperture A3 is used to help align the beam, along with apertures A1 & A2. In addition, intensity dependent studies require the insertion of neutral density filters or glass slides into the beam path, as was discussed for the fixed delay arm.

For both co-linear (CLP) and cross-linear (XLP) beam polarization configurations, the two arms of the interferometer are combined at the 10 mm beam-splitting cube, BSC1. It has a transmission of $(45 \pm 6)\%$ for 700-1100 nm, with $\pm 5\%$ variation with wavelength, and is polarization insensitive to within 10%. The two beams are positioned at the same height and at opposite sides of the cube. Short range alignment is done at the exit of the beam-splitting cube and then at mirror M8 in the beam input area (Figure 3.10), by adjusting the fixed delay arm translation stage. The neutral density filters are placed after the beam splitting cube to adjust the intensities of both arms together. One of the two beams reflected from these filters is deflected towards mirror M11 (Figure 3.12) so it can be coupled directly into the spectrometer, while the other is blocked by a beam dump. The second set of beams from the interferometer is sent towards the autocorrelator, discussed next.

3.3.3 Autocorrelator

The purpose of the autocorrelator is threefold: it provides the 'zero' delay position for DFWM measurements, it allows the laser pulse full-width half-maximum (FWHM) to be measured, and it provides a continuous indication of when the laser is mode-locked (producing pulses). These objectives are accomplished by taking the signals from the pulse delay system and focusing them on a nonlinear crystal. The resultant frequency
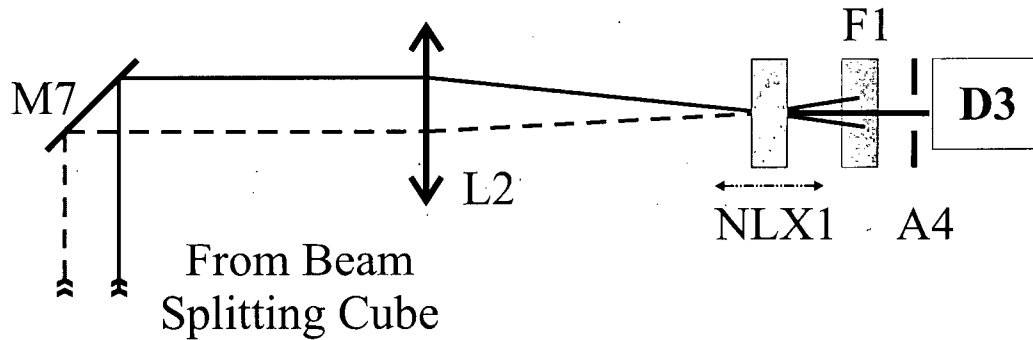
Figure 3.5: Diagram of the experimental setup of the second harmonic generation (SHG) autocorrelator which, along with the pulse delay system (Figure 3.4), is used to measure the zero delay position and pulse width of the laser pulses.

doubled, or second harmonic generation (SHG), signal is then measured. The delay at which the SHG signal is a maximum corresponds to the pulses overlapping with each other; the corresponding LVDT level then corresponds to $\tau = 0$. The pulse FWHM can be obtained from a fit to the autocorrelator pulse shape, as discussed theoretically in Appendix B. If the laser loses its mode-locking and reverts to continuous-wave (CW) operation, the SHG signal is extinguished, making it a useful mode-lock monitor.

The pulse autocorrelator components are illustrated in Figure 3.5. The 200 mm focal length lens focuses the light onto a $LiIO_3$ nonlinear crystal (0.5 mm thick, cut at 44.51°) in a Type I configuration (input beams are co-linearly polarized), and is optimized such that the second harmonic autocorrelation signal intensity is maximized. The intensity of the autocorrelated signal, as viewed on fluorescent paper, varies at twice the frequency of the shaker. This is due to the pulses overlapping in both the forward and reverse directions of the mirror as the shaker vibrates. The upconverted light, at twice the frequency of the laser light, propagates with the transmitted laser beams behind the nonlinear crystal. The unwanted infrared beams are blocked by a blue-UV bandpass filter (Newport BG40, > 50% transmission from 350-575 nm) inserted between the nonlinear crystal and the Si-PIN detector (455-UV, UDT Sensors, Inc.). The aperture (A4) is placed to allow only the autocorrelated signal through while blocking stray upconverted light in the system.

This stray light is mostly generated from the second harmonic of the individual input beams, even though these are far from being optimally phase matched.

The autocorrelation signal is gathered by the data collection system together with the LVDT signal. The data collection system is written in National Instruments Lab-View 4.0 software, with a 12-bit analog-to-digital (A/D) board (National Instruments model PCI-MIO-16E-1). Initial software development was done by Rong Zhu and then Dr. Paul Paddon. Extensive software modifications and calibration of the system was conducted by Dr. Jennifer Watson and the author. The autocorrelation and DFWM data acquisition software development was done in conjunction with the monochromator control and data acquisition software system, whose details are described with the detector systems (Section 3.3.5).

The data acquisition and signal averaging is done in real-time, allowing the raw and averaged signals to be monitored as the data is being acquired. This allows for the flexibility of halting the program if the signal averaging is better than expected, or if the acquisition process needs to be aborted.

The data signals are acquired at $200\,\text{kHz}$ ($\Delta t = 5\,\mu s = 1\,\text{bin}$), with the LVDT and detector (autocorrelation or DFWM) signal pairs acquired in series, $2.5\,\mu s$ apart. Although the board is capable of larger scan rates, this was found to be the maximum practical range before cross-talk between the data channels became too large. The LVDT and signal conditioner are inductive, so there is a phase delay between the LVDT and detector signals, measured to be $1.175\,\text{ms}$ ($235\,\text{bins}$). There is also a delay of $1.875\,\text{ms}$ ($375\,\text{bins}$) between the trigger pulse and the two acquired signals. The number of scan points measured ($6250\,\text{bins}$, $31.25\,\text{ms}$) is greater than that needed for a single direction sweep of the shaker ($5263\,\text{bins}$, or $26.32\,\text{ms}$ at a $19\,\text{Hz}$ scan rate), in order to allow for the phase and zero corrections, as well as an extra safety factor for frequency variations in the $\sim 19\,\text{Hz}$ driving frequency of the shaker.

After acquisition, the software shifts both data sets to account for the zero position. Due to the signal pairs being acquired in series, each LVDT signal point is averaged with

the previous data point in its array. Finally, the detector (autocorrelator or DFWM) signal data set is shifted, to account for the phase shift between it and the LVDT signal. Once acquired, the data is binned according to the LVDT signal voltage values. Signal averaging is accomplished by specifying the number of scans, each of which has the data binned and averaged according to the LVDT (pulse delay) signal voltage values. Results of the current LVDT signal, current single-shot detector signal, and averaged detector signal can all be displayed as the program is running. The software acquires either autocorrelation (SHG) or DFWM signals using the same method, and the choice is software selectable.

Due to the 12-bit resolution limitation in the A/D board, the $\pm\,5\,$V LVDT signal can only be acquired in increments of $2.44\,$mV, corresponding to delay increments of $3.45\,$fs. This resolution can be increased by decreasing the travel range on the shaker and moving to a corresponding higher gain on the A/D board. Although useful for short delay studies such as interferometric studies, this is impractical for our experimental signals which require a larger range of delays to measure the DFWM signals adequately. The limiting factor in delay resolution at this point is thus the 12-bit A/D board, although this is not a difficulty for the signals currently being measured.

The software also allows the flexibility to subtract a background signal from the data signal, as well as the option to select whether the data is acquired from forward or backward directions of the shaker motion. The limiting factor in this part of the data acquisition software appears to be a combination of the computer processing speed and software efficiency, which only allows 1/3 to 1/5 of all possible scans ($\sim$19 per second) to be acquired by the software, especially when the graphing options are selected.

Once collected, the delay axis values (in ps) are stored in a data file along with the averaged detector signal (autocorrelation or DFWM) values. A separate file contains the program parameters, along with the temperature and monochromator settings, if these options are selected. Software for these is described below, in Sections 3.3.4 and 3.3.5.

Since the autocorrelation signal provides a measure of not only the pulse width, but

also the pulse delay zero point, it must be taken **before** any DFWM data is acquired in order that the delay axis for the DFWM data can be correctly adjusted. This is accomplished by a separate LabView program, written for this purpose, which fits the data assuming a hyperbolic secant pulse profile. As described in more detail in Appendix B, the autocorrelation SHG signal measured in this system is a **pulse intensity autocorrelation**, meaning

$$I_{\text{measured}}(\tau) = \int\limits_{-\infty}^{+\infty} dt \; I(t)I(t+\tau) \,. \tag{3.5}$$

Since this autocorrelation signal is symmetric regardless of the pulse shape, the peak represents the point at which the two pulses overlap with zero delay. To further analyze the pulse intensity autocorrelation and extract the pulse parameters, a pulse shape must be assumed [57, page B-4]. Typical choices are Gaussian, Lorentzian, and hyperbolic secant (sech) pulse profiles. The time and frequency profiles for these three pulses are shown in Table 3.3, while the pulse autocorrelation and pulse intensity autocorrelation solutions are shown in Table 3.4.

Analysis of the SHG laser pulse data indicates that the sech pulse shape gave the best overall fit to the data over the measured range of central wavelengths ($\sim$750-780 nm) and pulse widths ($\sim$90-130 fs). This is also borne out by examination of semi-log plots, which indicates an exponential decay in the pulse wings.

A typical fit from a SHG autocorrelation signal is shown in Figure 3.6. Pulse shape analysis, conducted with IgorPro (Wavemetrics, Inc.) routines, indicates that the peak position fits equally well (to within 0.01 fs) regardless of which pulse shape is chosen, even including fitting to sech or Lorentzian profiles. Unlike the peak position, the pulse FWHM is model dependent, varying by as much as 25-30% for various pulse shape choices. The autocorrelation signal shown in Figure 3.6 was acquired with a typical 100 scans for signal averaging, with more averaging scans only being required for low pulse powers or cross-polarized input beams.

Table 3.3: Electric field (time & frequency) profiles for various pulse shapes. Shown are the Gaussian, hyperbolic secant, and Lorentzian pulse profiles [47, 58, 59, Maple 6]. The pulse shapes are normalized such that the integral over the pulse shape equals one, to allow for the proper behaviour in the delta-function pulse shape limit. Note that σ_t and σ_ω are the **intensity** Full-Width Half-Maximum (FWHM) values, found by solving for $g^2 = 1/2$ or $G^2 = 1/2$ (from their peak value).

	Gaussian	Sech	Lorentzian
$g(t)$	$\exp\left\{-a_t^2 t^2\right\}$	$\mathrm{sech}\left\{a_t t\right\}$	$\dfrac{1}{1 + a_t^2 t^2}$
a_t	$\dfrac{\sqrt{2\ln(2)}}{\sigma_t}$	$\dfrac{2\ln\left(\sqrt{2}+1\right)}{\sigma_t}$	$\dfrac{2\sqrt{\sqrt{2}-1}}{\sigma_t}$
$A_{\mathrm{norm},t}$	$\dfrac{a_t}{\sqrt{\pi}}$	$\dfrac{a_t}{\pi}$	$\dfrac{a_t}{\pi}$
$G(\omega)$	$\exp\left\{-a_\omega^2 \omega^2\right\}$	$\mathrm{sech}\left\{a_\omega \omega\right\}$	$\exp\left\{-a_\omega |\omega|\right\}$
a_ω	$\dfrac{\sqrt{2\ln 2}}{\sigma_\omega} = \dfrac{1}{2a_t}$ $= \dfrac{\sigma_t}{2\sqrt{2\ln 2}}$	$\dfrac{2\ln\left(\sqrt{2}+1\right)}{\sigma_\omega} = \dfrac{\pi}{2a_t}$ $= \dfrac{\pi\sigma_t}{4\ln\left(\sqrt{2}+1\right)}$	$\dfrac{\ln 2}{\sigma_\omega} = \dfrac{1}{a_t}$ $= \dfrac{\sigma_t}{2\sqrt{\sqrt{2}-1}}$
$A_{\mathrm{norm},\omega}$	$\dfrac{1}{\sqrt{2\pi}}$	$\dfrac{1}{\sqrt{2\pi}}$	$\dfrac{1}{\sqrt{2\pi}}$

Table 3.4: 1st (pulse autocorrelation – G_0^1), & 2nd (intensity autocorrelation – G_0^2) correlation profiles for various pulse shapes. These are the "background free" correlations [59] corresponding to this co-linear, Type I autocorrelation configuration, as shown in Figure 3.5. The term a_t is specified in Table 3.3 for each pulse shape. τ is the time delay between the pulses. Pulse autocorrelation profiles are derived due to their usefulness in the theoretical simulation expressions.

	G_0^1	G_0^2
General	$\int\limits_{-\infty}^{+\infty} dt\, g(t)g(t-\tau)$	$\int\limits_{-\infty}^{+\infty} dt\, g^2(t)g^2(t-\tau)$
Gaussian	$\dfrac{a_t}{\sqrt{2\pi}}\exp\left\{-\dfrac{a_t^2\tau^2}{2}\right\}$	$\dfrac{\sqrt{2}a_t^3}{(2\pi)^{3/2}}\exp\left\{-a_t^2\tau^2\right\}$
Sech	$\dfrac{2a_t}{\pi^2}\dfrac{(a_t\tau)}{\sinh(a_t\tau)}$	$\dfrac{4a_t^3}{\pi^4}\dfrac{(a_t\tau)\cosh(a_t\tau)-\sinh(a_t\tau)}{\sinh^3(a_t\tau)}$
Lorentzian	$\dfrac{a_t}{2\pi}\dfrac{1}{1+\left(\dfrac{a_t\tau}{2}\right)^2}$	$\dfrac{a_t^3}{(4\pi)^3}\dfrac{(20+a_t^2\tau^2)}{\left(1+\left(\dfrac{a_t\tau}{2}\right)^2\right)^3}$

3.3.4 Cryostat & Coupling Optics

This section describes the cryostat, used to control the sample temperature in the range 2 K to 300 K, as well as the optics used to couple the beams from the pulse delay system onto the sample and from the sample to the DFWM detection system. An overall schematic of the cryostat, coupling optics, and associated support systems is shown in Figure 3.7.

The input coupling optics are used for final beam alignment and then to focus the beam onto the sample. The output coupling optics allow for the measurement of time- and spectrally- integrated DFWM signals (TI-SI-DFWM) and spectrally resolved DFWM signals (SR-DFWM). They also allow for transmission measurements through the sample and laser spectral profile measurements. The cryostat temperature is monitored and controlled by a temperature controller and heater system, which the data collection system is capable of monitoring. Also constructed as part of this work is the cryostat
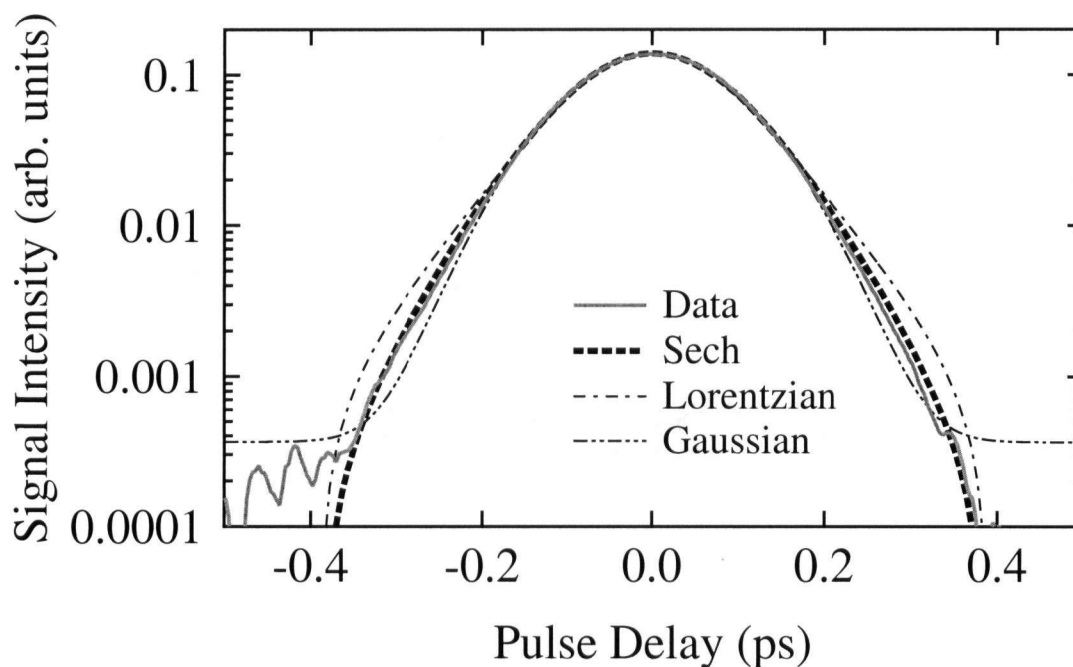
Figure 3.6: Typical second-harmonic generation signal from the pulse autocorrelator, fit with hyperbolic secant (sech), Gaussian, and Lorentzian pulse profiles. The peak position is arbitrary, and the corresponding pulse FWHM fit values are (122.4 ± 0.1) fs, (150.7 ± 0.1) fs, and (123.9 ± 0.4) fs. The laser central frequency was 1624.9 meV (763.1 nm). This signal was averaged using 100 scans, with beam powers of 1.55 & 1.05 mW in the variable and fixed arms, respectively.

manifold. Along with two roughing pumps, this is used both in cooling down the system and replenishing cryogenic liquids. The manifold assists in reducing the presence of water vapour in the system, which interferes with optical experiments.

The Janis Research Co. model SVT-300 (BNCDT, option 2) cryostat is shown in cross-section in Figure 3.8. It is capable of using either liquid nitrogen (LN) or liquid helium (LHe) to obtain sample temperatures from ~ 2 K (with pumping) to 300 K. The samples are mounted on a copper plate which has a hole through it to allow for optical transmission experiments. The sample holder can be easily rotated or raised and lowered inside the cryostat. The entire cryostat is mounted in a frame attached to a translation stage to provide side-to-side motion. Combined with the raising and lowering shaft, this allows for experiments to be conducted over the entire sample without removing it from

```
┌─────────────┐   ┌──────────────┐  ┌──────────────┐
│ Temperature │   │ Computer     │  │ He & N₂      │
│ Controller  │   │ Control System│ │ Gas Supplies │
└─────────────┘   └──────────────┘  └──────────────┘

┌──────────┐ ┌──────────┐ ┌────────────────┐ ┌──────────┐
│ Input    │ │ Cryostat │ │ Cryostat Manifold│ │ Roughing │
│ Coupling │ │          │ │                │ │ Pumps    │
│ Optics   │ │ Sample   │ │ Output Coupling│ │ Detector │
│          │ │          │ │ Optics         │ │ Area     │
└──────────┘ └──────────┘ └────────────────┘ └──────────┘
```
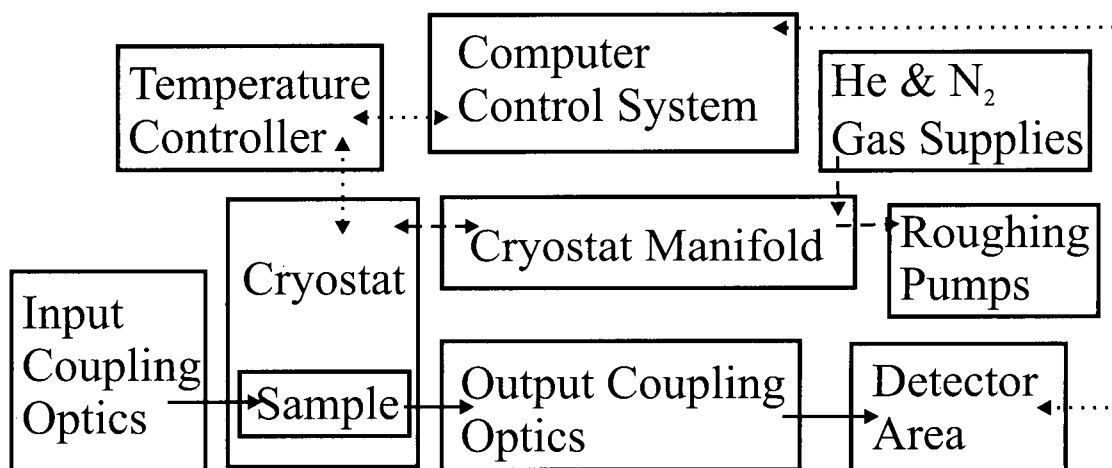
Figure 3.7: Overall schematic of cryostat & coupling optics. Solid lines indicate light flow, dashed lines gas flow, and dotted lines are data paths.

the laser beam focal plane or needing to change the optical axis. The cryostat mount base has a grid of tapped holes, used for mounting components.

The cryostat contains two sets of heating coils and temperature sensors. One set is attached to the sample mount, just above the sample holder. The other is situated where the helium enters the sample chamber and is used to control the temperature of the gas in the chamber. The temperature is monitored and controlled by a Lakeshore model 330 autotuning temperature controller and a LabView program designed to both measure and set the temperature. The temperature controller is capable of measuring both temperature sensors, but of controlling only one heater at a time. The temperature is controlled by varying the gas flow rate with the helium valve, and by passing current through the heater(s). This results in the helium or nitrogen gas being heated to the required temperature before entering the sample chamber and flowing past the sample.

In addition, by using the cryostat manifold system shown in Figure 3.9, the rate at which gases exit the sample chamber can be varied, which also assists in stabilizing the temperature. For pressures greater than atmospheric pressure, this can be accomplished using the one-way valve (N_2) or by venting to atmosphere (He or N_2). To stabilize the gas flow and to remove the possibility of condensates backstreaming into the sample

SAMPLE POSITIONER
ASSEMBLY WITH 2
ELECTRICAL FEEDTHROUGHS

HELIUM RESERVOIR
PUMPING PORT

HELIUM FILL/VENT
PORTS (2)

NITROGEN FILL/VENT
PORTS (2)

SAMPLE TUBE
PUMPING PORT

HELIUM VALVE
OPERATOR

HELIUM RESERVOIR
(5 LITERS)

NITROGEN RESERVOIR
(4 LITERS)

ISOLATION TUBE

EVACUATION VALVE WITH
ELECTRICAL FEEDTHROUGH

DEWAR MOUNTING
FLANGE

HELIUM VALVE

8 EPOXY SEALED SUPRASIL II
(QUARTZ) WINDOWS
Window Diameters (mm):

(2) 16.00

(2) 6.35

(1) 31.75

(1) 12.70

(1) 38.10

(1) 18.05

SAMPLE WINDOW
BLOCK CROSS SECION

RADIATION SHIELD

CONCENTRICITY
SPACER

SAMPLE CHAMBER

SAMPLE MOUNT,
HEATER & SENSOR

OPTICAL SAMPLE HOLDER

HELIUM VAPORIZER,
HEATER & SENSOR

Figure 3.8: Cut-away view of Janis model SVT-300 (BCNDT, option 2) 5 liter cryostat.
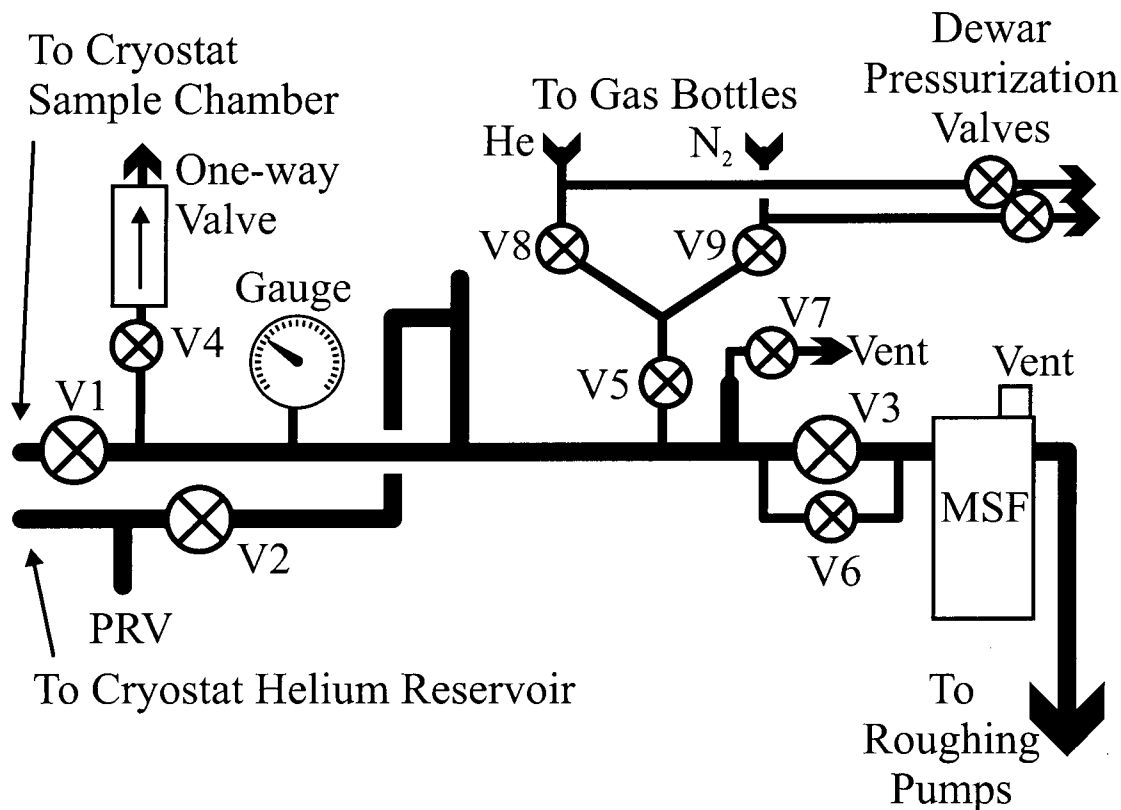
Figure 3.9: Schematic of vacuum system manifold. Valves V1-V7 are VAT diaphragm valves. MSF is a molecular sieve filter. Thick lines indicate 25.4 mm I.D. pipe, while thin lines indicate 12.7 mm I.D. pipe. PRV is a pressure relief valve for the cryostat helium reservoir.

chamber, the manifold and a roughing pump can be used. When using the roughing pump, the gas flow is regulated using valves V3 and V6.

For higher temperatures, the temperature is stabilized by raising the temperature of both the helium gas and sample mount in sequence until both stabilize, with the gas being heated to the required temperature before it enters the sample chamber. In either case, the temperature of the gas flowing past the sample can be further controlled and stabilized by varying the rate at which gases exit the sample chamber using the cryostat manifold system, shown in Figure 3.9. This can be done by either using the one-way valve, for pressures greater than atmospheric pressure, or by pumping on the manifold using the roughing pump and valves (V3, V6) to control the flow rate.

The manifold system illustrated in Figure 3.9 was built to simplify the operation of the cryostat. It is imperative to control the vapour composition in both the helium reservoir and the sample chamber at all times while the cryostat is cooled. Failure to do so results in freezing of the He valve and/or the accumulation of opaque condensates on the cryostat windows. Both problems require the cryostat to be warmed and re-flushed before experiments can be resumed. The manifold was designed such that it never has to be removed for any of the standard operations, and it can be used with both liquid helium and liquid nitrogen. The manifold is attached to both the sample chamber and helium reservoir, and is capable of flushing these chambers with either dry He or N_2 gas, as well as pumping them out with the roughing pumps. The molecular sieve filter is used to prevent back-streaming of oil from the roughing pumps into the reservoir or sample chamber and is equipped with a separate vent so that this part of the system can be brought to atmospheric pressure independently from the rest of the manifold.

The one-way valve can be used to control gas flow out of the sample chamber while preventing the atmosphere from entering the chamber, but only for pressures higher than atmosphere. A roughing pump can also be used for this purpose, instead of the one-way valve, connected to the manifold in place of the main roughing pump used for pumping out the system. Attached with plastic tubing to reduce vibration at the cryostat, its flow is controlled using valves V3 & V6. Compared to the one-way valve, the roughing pump allows finer control over the gas flow, can be used with cryostat gas pressures above and below atmospheric pressure, and allows frost-free operation over longer periods at cold temperatures, especially when liquid helium is used as the cryogenic fluid.

A schematic of the beam input and sample areas is illustrated in Figure 3.10. The first two components, mirrors M8 & M9, are both mounted on kinematic mounts. With mirror M9 removed, mirror M8 is used to align the variable delay arm beam to the correct height off the optical table. Mirror M6 from the pulse delay system (Figure 3.4) is then used for long range alignment of the fixed delay arm. This consists of first doing a near alignment of the fixed delay beam to make it at the same height and distance from the
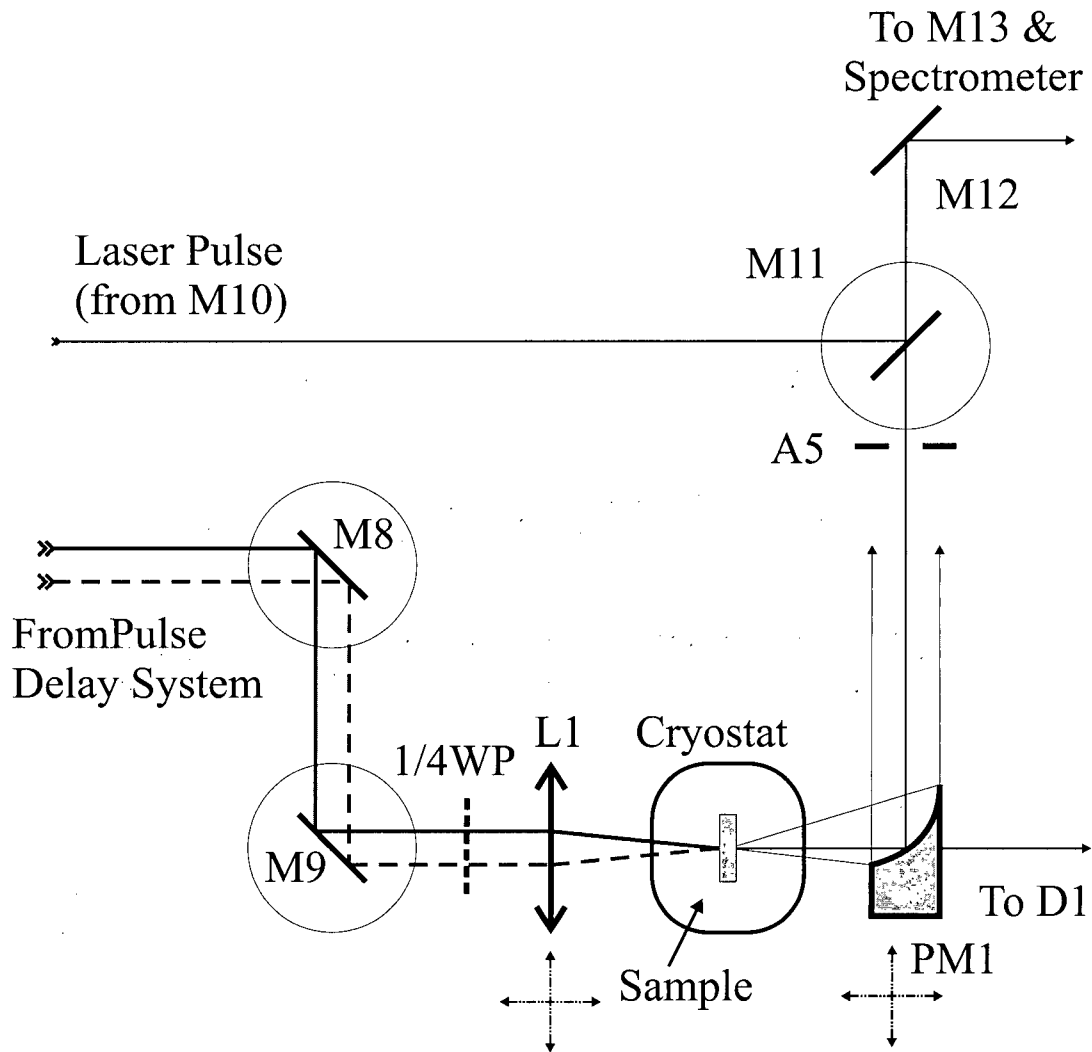
Figure 3.10: Schematic illustration of coupling optics. The solid line indicates the variable delay arm, while the dashed line indicates the fixed delay arm from the pulse delay system. For time- and spectrally- integrated signals (TI-SI-DFWM), PM1 is removed from the beam path. Dash-dot-dot lines indicate translation stage mount directions, while the large thin circles indicate kinematic mounts.

variable beam at mirror M8, and then at the optical table edge. This procedure is then repeated for the long range alignment at a distance of ~4-5 m. This ensures that the two beams are parallel and will focus to the same spot on the sample.

Once mirror M9 is replaced, the beams are reflected through a removable, rotatable 1/4 wave plate. The 1/4 wave plate (from CVI Laser Corp.) has a 15 mm diameter, with an 800 nm center wavelength and bandwidth of 100 nm. The 1/4 wave plate can change the polarization of both beams, from linear to circular, depending on its rotation.

The beams then pass through a 185 mm focal length lens, L1, that focuses them to the same spot on the sample. The lens is mounted on a two axis translation stage so that fine adjustments can be made to center the beams with respect to the optical axis and shift the focal plane within the sample. The beam powers are measured by inserting a power meter before or after the lens. A mount for a CCD camera was also designed for the system to view the sample from the output side and assist in a final alignment of the beams to confirm that the beams are optimally overlapped in the sample. If not, adjustments can be made with mirror M6 and the long range alignment re-checked after the adjustments, as described earlier.

Once the beams pass through the sample there are four beams: two DFWM signal beams and the two original, now partially absorbed, laser beams. These are all collimated by the parabolic mirror (PM1) and sent to the spectrometer. The mirror is a 25.4 mm gold coated parabolic mirror with a focal length of 28.75 mm, 90° off-axis (57.5 mm from the center of the mirror to the focal point). The parabolic mirror is mounted on a two axis translation stage, used to collimate the diverging beams from the sample. It can be backed out of the optical path for the measurement of time- and spectrally- integrated DFWM signals or left in when spectrally-resolved DFWM signals are measured.

The aperture A5 is used to block out unwanted beams from the optical path. It can be moved laterally to isolate one of the four beams. Once past the aperture, signals are reflected towards the spectrometer with a 50.8 mm diameter mirror, M12. Mirrors M12 and M13 (also 50.8 mm dia.) are used to align the signal into the spectrometer. Mirror

M11, on a kinematic mount, is inserted when spectra of the laser pulses are taken. Mirrors M11 & M10 (pulse delay system, Figure 3.4) are used to independently align the laser signal into the spectrometer so that M12 & M13 do not need to be moved once they are aligned.

3.3.5 Detection System Area

The detection system had to be capable of measuring four signal types: time- and spectrally-integrated (TI-SI-DFWM) signals, spectrally resolved (SR-DFWM) signals, laser pulse spectra, and transmission spectra.

The time- and spectrally-integrated DFWM (TI-SI-DFWM) experimental configuration is illustrated in Figure 3.11. Parabolic mirror PM1 is moved completely out of the beam path, allowing both transmitted laser beams and both DFWM signals to expand out into the space behind the cryostat. The unwanted beams are blocked about 0.46 m (18 in) from the cryostat. The DFWM signal of interest is passed through aperture A6 to reduce the background caused by the scattering of the transmitted laser beams, and is then centered on the detector (D1). The detector is mounted on a single axis translation stage to assist in optimizing the DFWM signal. It is a silicon-PIN detector (455-UV, UDT Sensors, Inc.), which was found to have adequate detection capability for these signals.

The spectrally-resolved portion of the detection area is illustrated in Figure 3.12. Mirrors M12 & M13 are used to align the beams through apertures A7 & A8. For laser spectra, mirrors M10 & M11 from the pulse delay system and output coupling optics area are used to align the beam through A7 & A8, so that re-alignment of M12 & M13 is not necessary after these spectra are taken. Once aligned through the apertures, parabolic mirror PM2 (identical to PM1) is used to couple the light into the monochromator. To assist with this, PM2 is mounted on a two axis translation stage. The dual-grating monochromator (CVI Laser Corp., model DK-242) is controlled by LabView programs using a serial port connection. After the monochromator is a silicon-PIN detector (D2),
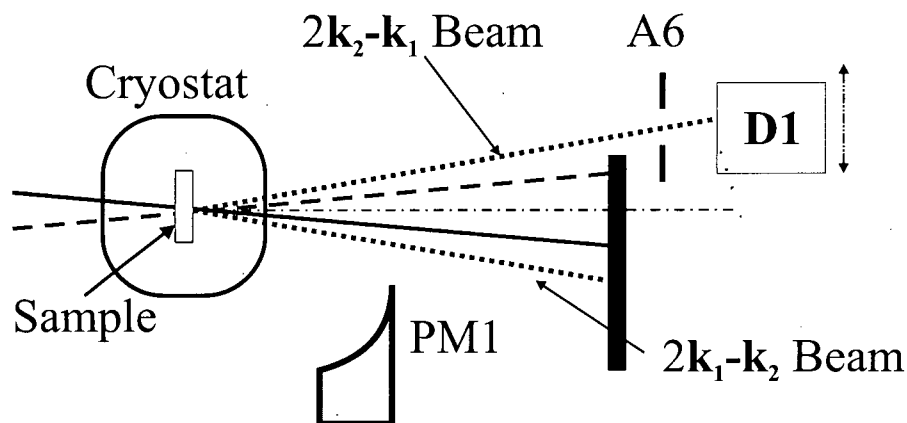
Figure 3.11: Schematic illustration of TI-SI-DFWM signal detection. The transmitted, partially absorbed laser beams are indicated by the solid and dashed lines, while the two DFWM signals are indicated by the dotted lines. The thick solid line indicates the beam block and the dash-dot line indicates the optical axis. Detector D1 is placed 0.46 m (18 in) from the cryostat.

on a single axis translation stage to assist in optimizing the signal.

The data acquisition of TI-SI-DFWM and SR-DFWM signals uses the same LabView program as was discussed in the autocorrelator section. The DFWM signals are averaged according to the LVDT position sensor signals, and the zero delay position from the autocorrelation SHG signal is used to calculate an absolute pulse delay for these signals. Background signals are taken with the same number of signal averages as the DFWM signal, and the DFWM data files have the background level subtracted from the acquired signal averages. Background signals are acquired by using the fixed arm translation stage to separate the pulses by introducing a large time delay ($\gtrsim 5$ mm, or $\gtrsim 33$ ps). For spectrally-resolved signals, the monochromator settings are also written to the DFWM data acquisition parameter file, using one of the LabView programs developed for the monochromator. The spectral position of the monochromator for SR-DFWM signals is set separately from the data acquisition program.

A different program from the one described above is required to spectrally resolve DFWM signals at a fixed delay (τ), measure the spectra of the laser pulses, or measure the transmission spectra. A set of LabView routines were developed to control the
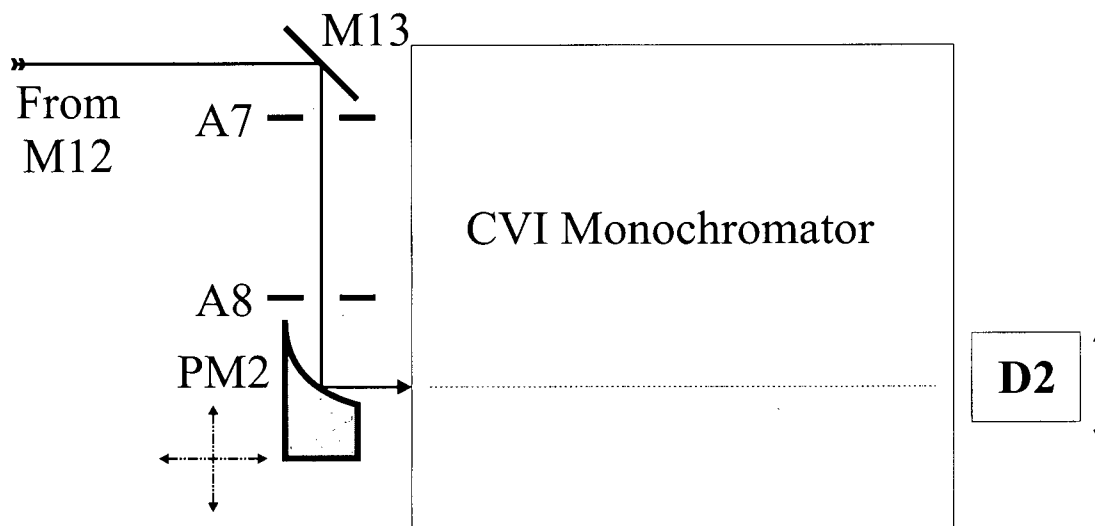
Figure 3.12: Schematic illustration of SR-DFWM signal detection.

monochromator and allow spectra to be acquired with it. The main LabView program allows for the selection of various detectors, and scans over a specified range of wavelengths. It is capable of signal averaging a selectable number of data points at each wavelength, at a frequency that can be selected in the software. A separate graph window from the final display shows the data as it is acquired, to allow the scan to be aborted if necessary. An option exists to fit the acquired data to a hyperbolic secant pulse profile, extracting the peak position and FWHM of the laser pulse. As with the DFWM programs, a separate document file accompanies each data file. This file contains the experimental settings as well as optionally reading the temperature, through the temperature controller connected to the cryostat.

The detector selection routines, controllable from the main program, allow one to select and measure signals from different detectors. The Si-PIN detectors used in this experimental setup are included, as well as options to use a photomultiplier tube. The photomultiplier tube program allows for use of both higher signal levels as well as a photon counting mode, all selectable from the main program. As well, separate routines are available for setting and reading all the monochromator parameters, including delays for operations that require wait times before other monochromator operations can pro-

ceed. Another routine, used in the DFWM data acquisition main program as well as the monochromator main program, reads in all the monochromator settings and writes them to a specified document file.

The experimental system that has been discussed is used to extract information about both the laser pulses and DFWM signals, both spectrally-resolved and spectrally-integrated. In the next chapter the results of experiments with these systems, linear and nonlinear (DFWM), will be discussed for both undoped and doped multiple quantum well samples.

Chapter 4

Experimental Results

This Chapter presents and qualitatively discusses the experimental results of the linear and nonlinear degenerate four-wave mixing (DFWM) studies that were conducted on the multiple quantum well samples. Here emphasis is placed on identifying the processes contributing to the observed signals. A quantitative comparison of the experimental and model results follows in Chapter 5.

4.1 Linear Absorption Data

The linear absorption data most relevant to the bulk of the DFWM experiments was obtained at 4 K by S. Brown, as part of an earlier study of the effects of excess electron doping in a series of 50–5 nm multiple quantum well samples [4–6]. The linear absorption data is shown for the undoped and four doped samples in Figure 4.1. These spectra clearly show the evolution of the Fermi-edge singularity as an asymmetric broadening on the high energy edge of the heavy-hole (hh) exciton peak at ~1620 meV, as was reported earlier [4–6]. The Fermi-edge singularity's asymmetric broadening can also be seen in the light-hole (lh) exciton peak (~1648 meV).

Earlier work [4–6] studying the linear absorption in these samples was concentrated in two areas. First, fitted values for the power law exponent were compared to theoretical models of the linear absorption lineshape in doped 2–D systems. Second, subtle features in the hh lineshape that were not well described by a power law function were scrutinized as evidence for negatively charged excitons (or, trions). The theoretical model actually

94
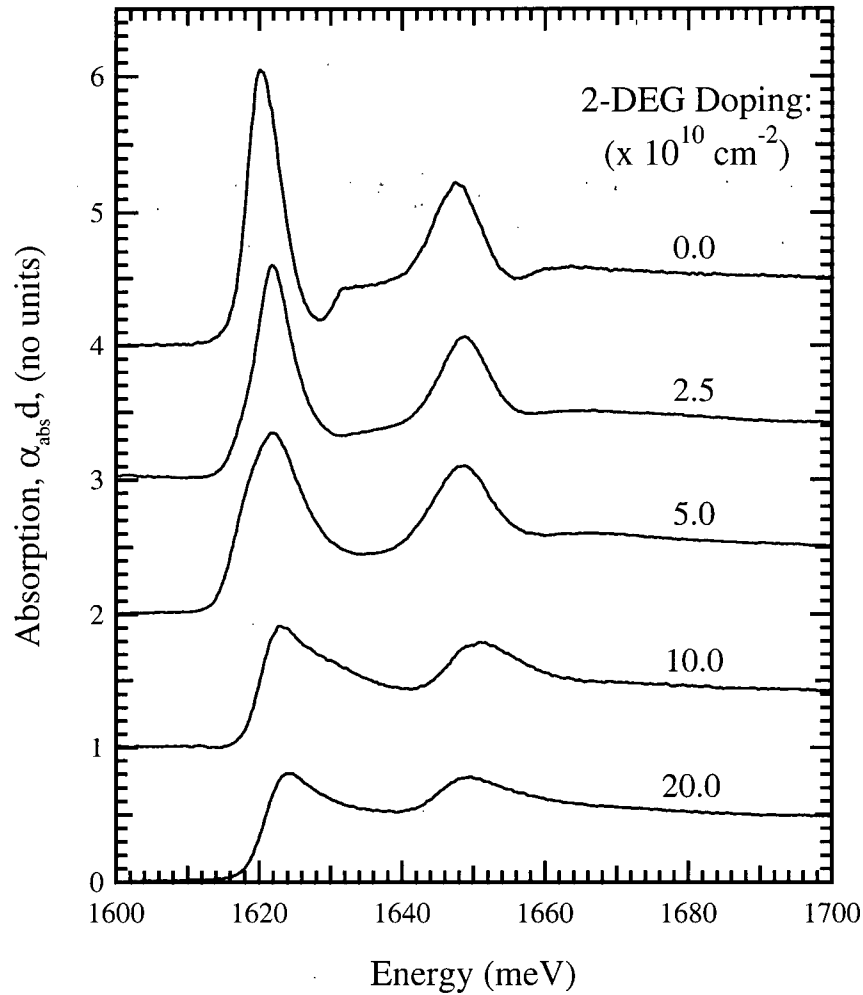
Figure 4.1: Low temperature (4 K) linear absorption of n-doped and undoped samples. All traces are on the same scale, with the baseline of each trace shifted vertically above the next lower trace. Data taken by S. Brown [4–6]. Samples are described in more detail in Tables 3.1 & 3.2 (page 68).

predicts that the main threshold is due to the creation of dressed trions, and that there should be a weaker peak due to the dressed excitons, shifted up in energy by the chemical potential plus the trion binding energy [22, 53].

The power laws were obtained in the previous works by fitting the heavy hole lineshape with a function of the form given in Equation (2.25) (with $\Gamma_{ag} = 0$), convolved with a single 6.4 meV wide Gaussian. The excess electron density dependence of the α values so

extracted were in quite good agreement with corresponding values obtained by forcing a power law fit to the (more general) theoretical spectra. A more detailed discussion of the power laws deduced in the present work follows in Section 5.4 (page 145).

The ~6.4 meV wide inhomogeneous broadening in the samples is roughly equivalent to energy shifts due to fluctuations in the well width of one monolayer in the 5 nm wells (1/2 of the lattice spacing – 0.283 nm in GaAs). The inhomogeneous broadening and the possible contribution of well width fluctuations prohibits any conclusive assignment of features to excitons or trions. This amount of inhomogeneous broadening also makes identification of the 2S excited exciton states uncertain. For the same reason, precise determination of the continuum edge is even more difficult to assign from the linear absorption data alone. As mentioned earlier, these difficulties provided some of the motivation for the nonlinear DFWM studies, the results of which will be discussed in the next section.

4.2 DFWM Experimental Results - Undoped Sample

Extensive experiments were conducted on the undoped multiple quantum well (MQW) sample both because of the interesting properties that the experiments revealed, and as a baseline before studying the doped samples. This DFWM data is presented below, starting with a general discussion of the results.

4.2.1 General Features

At liquid helium (LHe) temperatures (~4 K), the time- and spectrally-integrated (TI-SI) DFWM signals show two sets of beats with strikingly different behaviour. Figure 4.2 shows the TI-SI-DFWM signals for co-linearly polarized (CLP) input pulses, at six laser pulse detunings: (a) red-shifted, (b) close to resonance, and (c)-(f) blue-shifted. Note that laser pulse detunings are taken with respect to the reference (1S exciton) energy of 1619.8 meV.

Starting with the blue-shifted data ((f)→(c) in Figure 4.2), there is a peak close to a
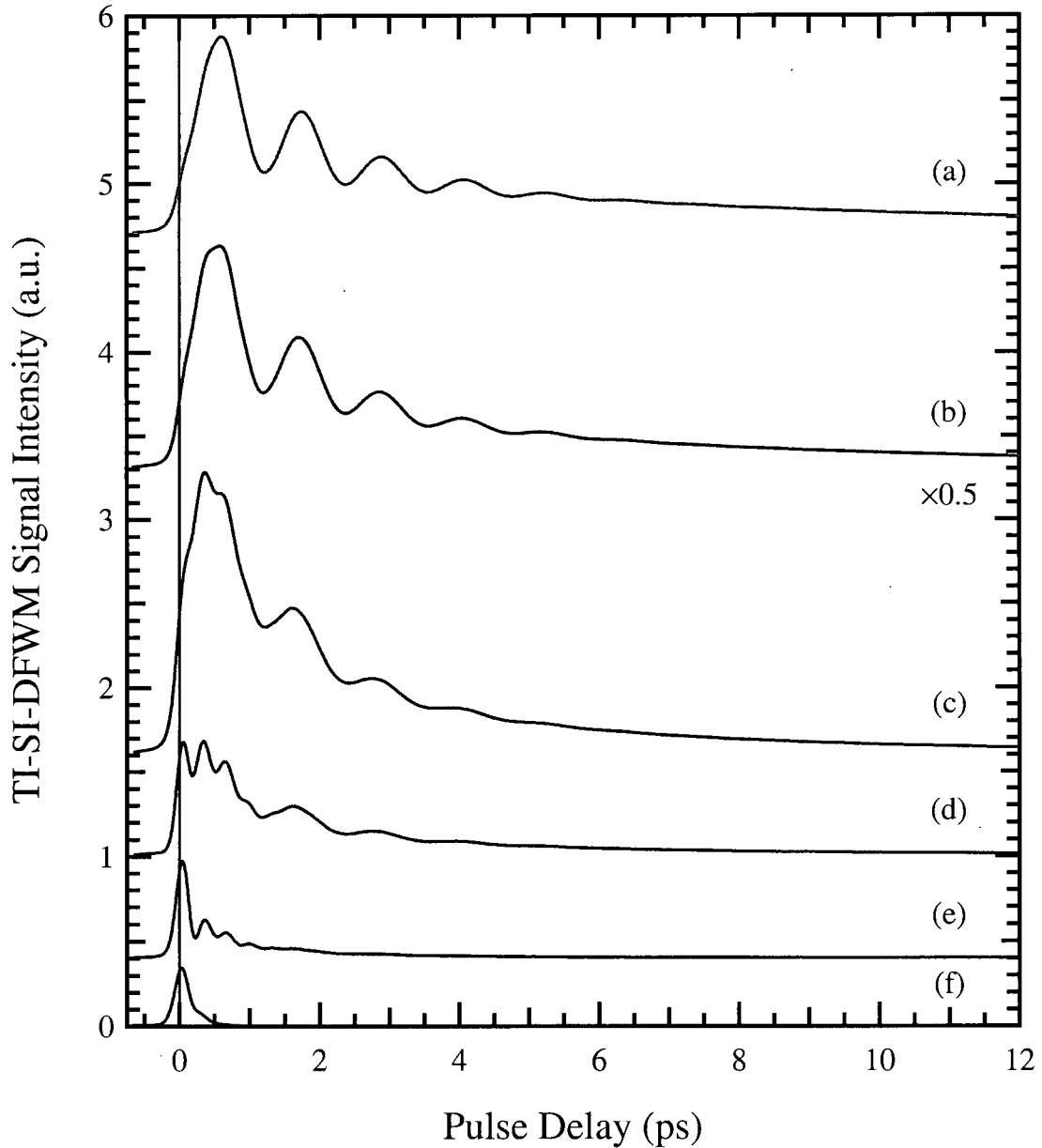
Figure 4.2: General behaviour of DFWM signals for the undoped sample. The reference energy for defining the detuning of the excitation pulse is taken to be 1619.8 meV. The pulse detunings ($\Delta_{op} = \omega_{\text{resonance}} - \omega_{\text{pulse}}$) are (a) +3.3, (b) −0.1, (c) −3.4, (d) −4.3, (e) −5.1, (f) −9.8 meV. Traces are shifted vertically for clarity, and signal (b) has been multiplied by 0.5. Input laser pulses are co-linearly polarized (CLP), and the temperature was 7.5 K.

delay of 0 ps in the most blue-shifted signal (f). The continuum is situated ∼4 meV above the pulse central frequency for (f), providing a fast dephasing component to the signal (Section 2.7 & [28]). Also noticeable is a slight beat in the signal, the modulation depth of which increases as the pulse detuning is decreased toward resonance. In trace (e), this is the dominant component in the TI-SI-DFWM signal. Its beat period corresponds to an energy level separation of approximately 12.5 meV. The beat signal is "in phase" with a pulse delay of 0 ps, with "in phase" meaning that a maximum in the beats occurs if they are extrapolated back to zero delay. In the next two sections, it will be shown that this beat can be assigned to the 1S-2S exciton energy splitting. As the laser pulse is tuned further towards and through the main 1S exciton resonance, (d)→(a), the contribution of the 1S-2S exciton beats decreases, becoming hardly noticeable as the pulse is red shifted (trace (a)).

A new signal, with a longer beat period corresponding to an energy spacing in the range of ∼3.3 meV is noticeable as the laser pulses are tuned below the continuum and 2S exciton levels. Unlike the 1S-2S beats, this signal has a minimum when extrapolated back to zero delay, or is "180° out-of-phase" with a zero pulse delay. To provide a direct comparison of the two beat components, Figure 4.3 shows two spectrally-resolved (SR-) DFWM signals with (a) blue-shifted and (b) red-shifted laser pulse detuning. In (a), the signal shows the 1S-2S beats, while in (b) the SR-DFWM signal shows the longer beat component.

The 1S-2S beats can be explained within the theoretical framework of the one-exciton resonance response in Chapter 2. However, this framework does not allow the pulses to be 180° out-of-phase. The longer period, out-of-phase beats are explained within the theoretical framework of the two-exciton resonant response, also developed in Chapter 2. In undoped quantum wells, two-exciton states correspond to biexcitons, or two-exciton molecules.
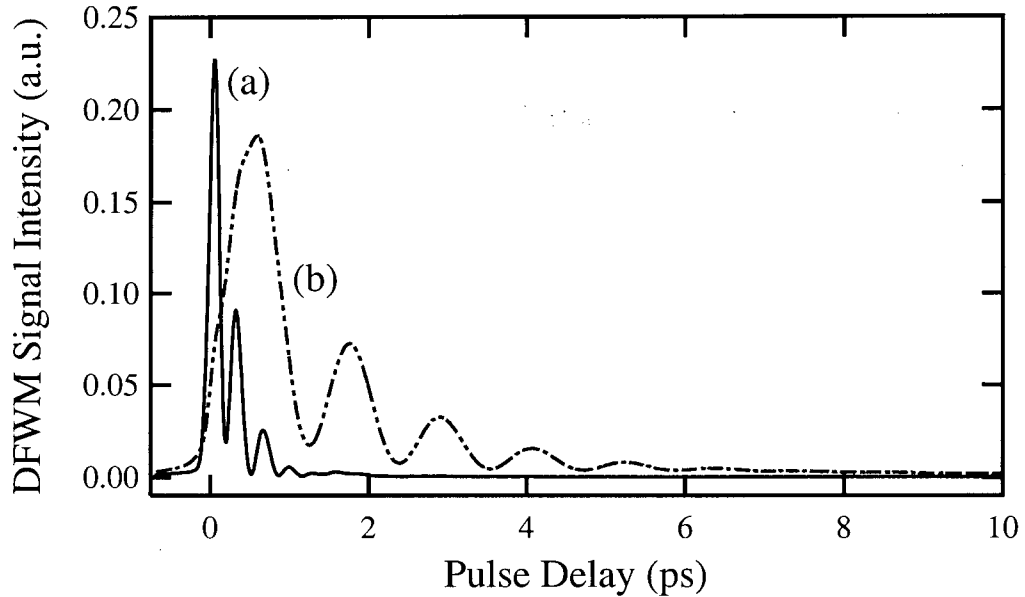
Figure 4.3: Red vs blue laser pulse detuning for SR-DFWM signals. The CLP input laser pulses have pulse detunings (Δ_{op}) from a reference energy of 1619.8 meV of: (a) −10.1 meV (blue-shifted) and (b) +9.9 meV (red-shifted). The laser pulse FWHMs are, respectively, (117.1 ± 0.2) fs and (97.7 ± 0.3) fs. The signals are spectrally resolved (a) 0.7 meV and (b) 4.3 meV below the reference energy. The temperatures were 6 & 9 K, respectively.

4.2.2   Input Pulse Polarization Dependence

The dependence on input beam polarization is shown in Figure 4.4, for spectrally-resolved DFWM signals. The main features are that:

(i)   for co-circularly polarized (CCP) input beams, the two-exciton levels do not contribute to the DFWM signal, while the one-exciton level signals do contribute.

(ii)   for co-linearly polarized (CLP) input beams, both one-exciton and two-exciton levels contribute to the DFWM signal.

(iii)   for the case of orthogonal (or cross) linearly polarized (XLP) input beams, only the two-exciton levels contribute to the DFWM signal.
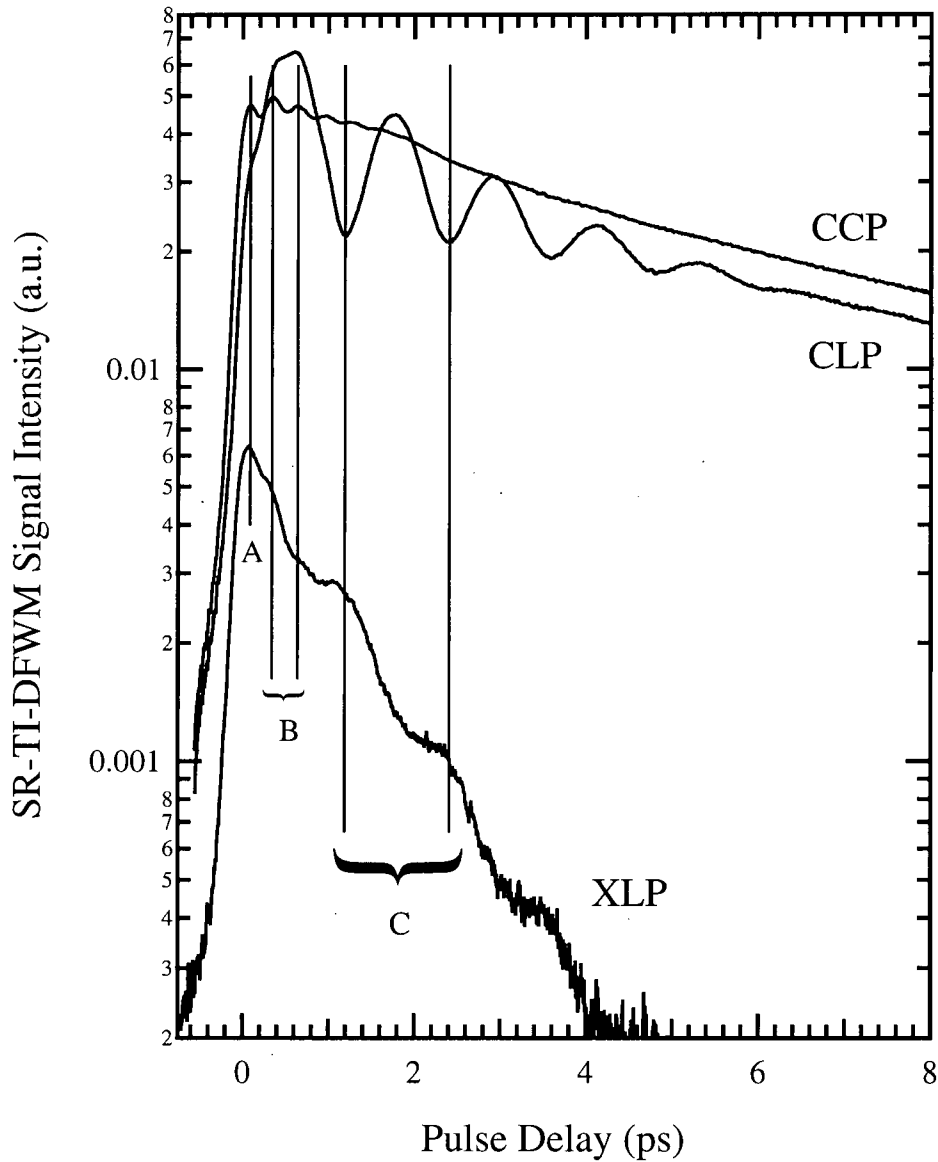
Figure 4.4: Polarization dependence of SR-TI-DFWM signals for the undoped sample. Laser input pulses (Variable/Fixed Arm Powers, in mW) are co-circularly polarized – CCP (2.40/1.72), co-linearly polarized – CLP (2.40/1.72), and cross-linearly polarized – XLP (2.40/1.40). The input laser pulses are centered at 1612.9 meV (red shifted 6.9 meV). Temperatures were 5.6/5.5/9.4 K and the data was spectrally resolved at 1619.8/1619.8/1617.9 meV ($\pm$2.5 meV), respectively.

As was explained in Chapter 2, two of the signatures of beats from two-exciton levels are that the beats: (1) change phase by 180° when the input beam polarization is changed from CLP to XLP; and (2) disappear under CCP input polarizations [51,52]. The latter, discussed above, is obvious from Figure 4.4. To assist in assessing the former, vertical lines have been placed on the figure. Lines C identify the positions of the minima (CLP) and maxima (XLP), showing that the beats change phase when the input polarization is changed from CLP to XLP.

From these observations it can be concluded that the long-period beats are due to the biexciton process described in Chapter 2. Line A corresponds to the contribution from the continuum, which only contributes at short times for all the input polarizations. Lines B correspond to the 1S-2S beating signal and do not change phase as the input polarization is changed.

4.2.3 Spectrally Resolved Data

Although the above discussion strongly supports a biexciton beat interpretation, there was a possibility that the long-period beats were actually associated with polarization beating from inequivalent quantum wells. Quantum beats are due to signals radiated from coherently excited quantum states (1S-2S-continuum excitons, or biexcitons) *with a common ground state*. On the other hand, polarization beating is due to signals from energy levels *with separate ground states* [24]. The distinction between the two can be made by spectrally-resolving the DFWM signal. Polarization beats change phase as the spectral position at which they are detected is varied through a resonance, while the phase of quantum beats is independent of the detection energy [24].

A set of spectrally resolved (SR-) DFWM signals is shown in Figure 4.5, as a function of the shift of the detection energy, $\Delta_{\omega o} = \omega_{\text{measured}} - \omega_o$, from the reference level, ω_o (1619.8 meV). The vertical lines are a guide to the eye to show the phase of the beat signals. If the signals were from polarization beating, they would be expected to change phase by 180° as the monochromator is tuned through a level. Neither the short nor the
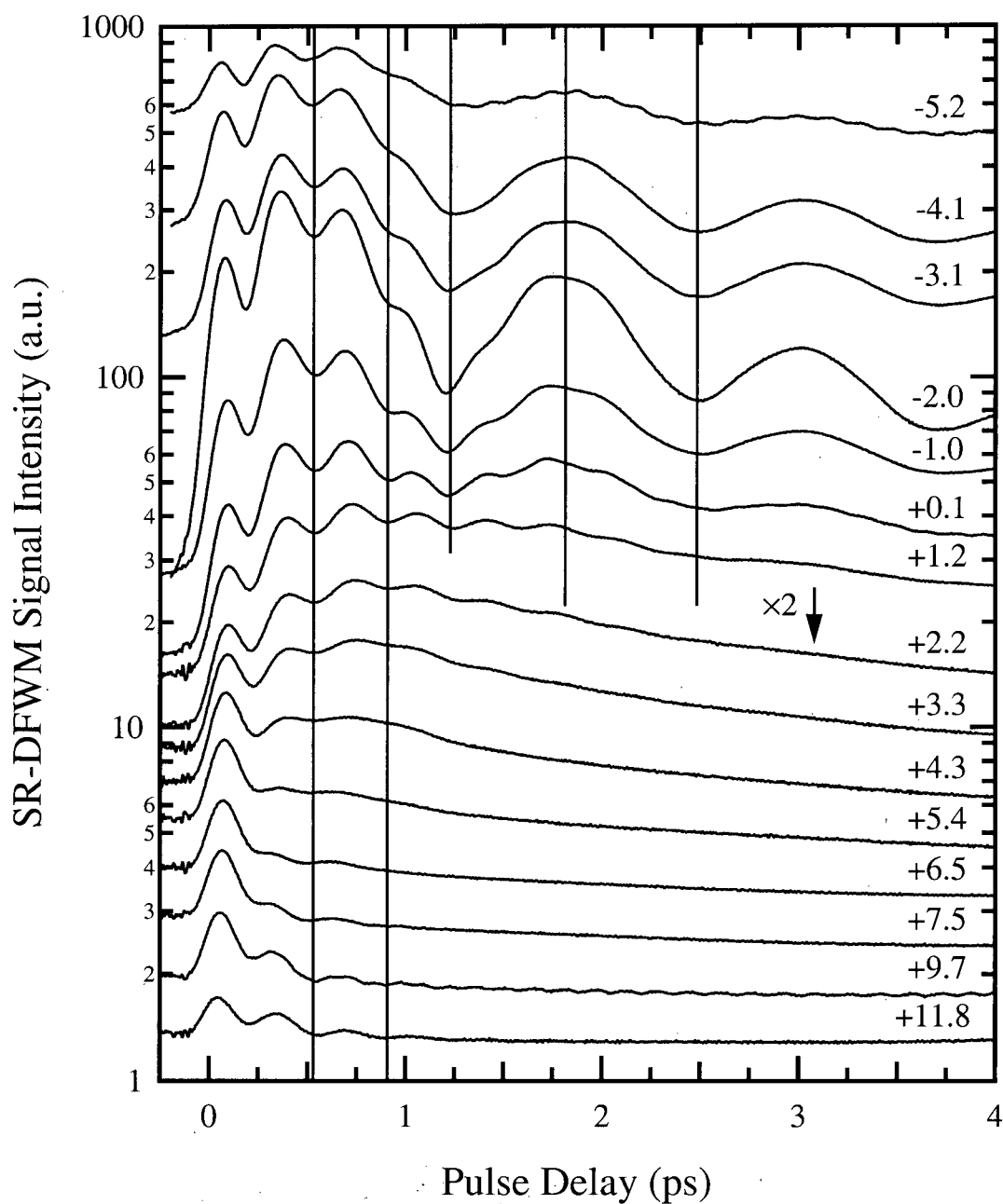
Figure 4.5: SR-TI-DFWM signal for the undoped sample. All traces are taken at different detection energies, with the shift from a detection energy of 1619.8 meV noted on the right side of the graph. Input laser pulses are co-linearly polarized (CLP). The laser excitation pulse had a FWHM of (98.2 ± 0.1) fs and central frequency of (1621.5 ± 0.1) meV. All traces blue-shifted from +2.2 meV up have been multiplied by a factor of 2. The traces have been shifted vertically for clarity.

long period beats change phase as the monochromator is tuned through the resonances, confirming that these signals are true quantum beats.

One other feature evident in the SR-DFWM signals confirms that the longer period beats are associated with the biexciton process discussed in Chapter 2. Notice that the modulation depth of the beats is strongest for detection energies ranging from just above the ground–to–1S resonance to just below the 1S–to–biexciton resonance. This is precisely what one would expect [24], and the model predicts, for the biexciton beating process. With all of this data then, we assign the long period beats to the biexciton process and deduce that the biexciton binding energy in this sample is ∼3.3 meV.

4.2.3.1   Spectrally Resolved Data at Fixed Pulse Delay

By fixing the pulse delay (τ) and spectrally resolving the resulting DFWM signal, information about the absolute energy and inhomogeneous broadening of the levels can be obtained. Figure 4.6 shows one set of these signals as a function of the input pulse polarization. Also shown is the transmission spectrum (dashed line) for comparison. Due to the large amount of inhomogeneous broadening in these samples, sharp transitions are not visible.

The spectra show three main features: (a) the width of the peaks are ∼3× narrower than the inhomogeneously broadened linear absorption peak, (b) all the peaks are centered at the 1S exciton resonance from the white light, and (c) there are slight shifts and asymmetries in the peaks.

The observation that the width of the peaks are ∼3× narrower than the inhomogeneously broadened linear absorption peak may be expected, since $\vec{P}^{(1)} \propto \vec{E}$ and $\vec{P}^{(3)} \propto \vec{E}^3$. The signal being centered around the 1S exciton energy for all three input polarizations shows that the dipole strength of this level, along with the two-free-exciton level in the CLP and XLP cases, is dominating the signal. For the CCP and CLP input polarizations the signals are taken with a delay of 1.75 ps, at the position of the second biexciton beat maximum (see Figure 4.4). The much weaker XLP signal was taken at a
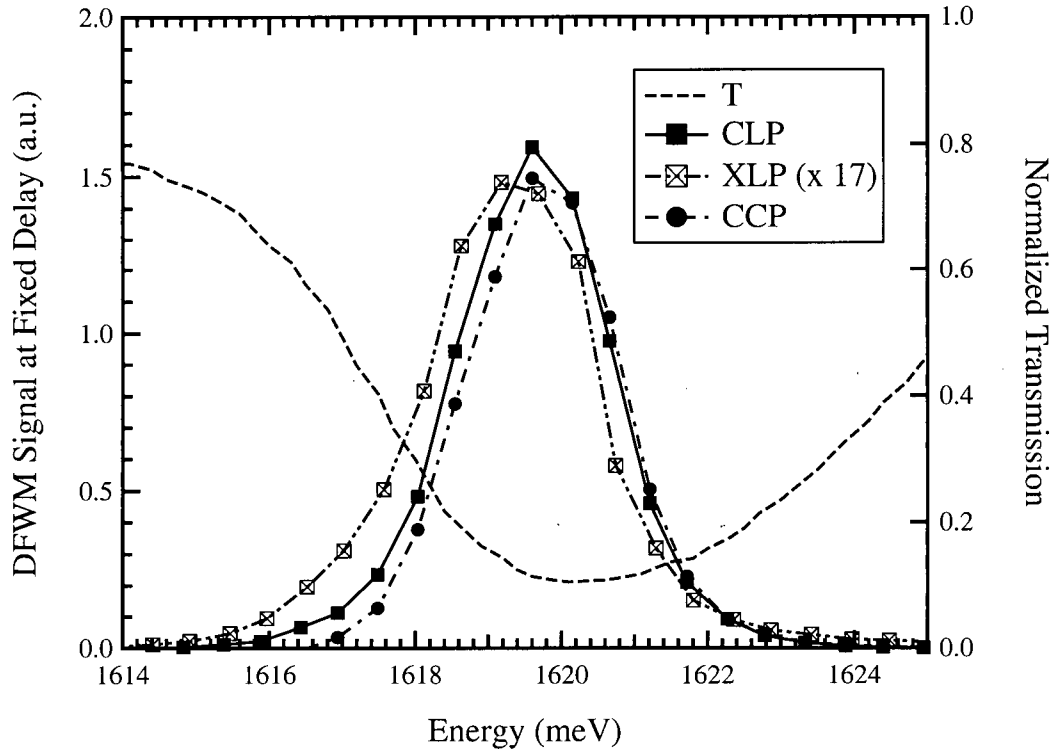
Figure 4.6: DFWM spectra with fixed delay, τ, for the undoped sample (left vertical axis). The delays shown in the figure for the CLP/CCP/XLP data are 1.75/1.75/0.03 ps, respectively. The laser had a FWHM of (98.7 ± 0.3) fs and a center frequency of (1611.8 ± 0.1) meV. The dashed line shows the corresponding white light transmission through the sample (right vertical axis). The DFWM spectra have been normalized by dividing by the absorption (multiplying by the transmission spectra).

delay of 0.75 ps, approximately at the first biexciton beat minimum (see Figure 4.4).

The slight shift of the peak in the XLP case is consistent with the previous discussion and the development in Chapter 2, where only two-exciton states contribute to the signal. The slight asymmetries also are consistent with the previous discussion, as the lower energy biexciton states would contribute to the signal more in the XLP case and less in the CCP case (where the biexciton contributions are absent), when compared with the CLP data.
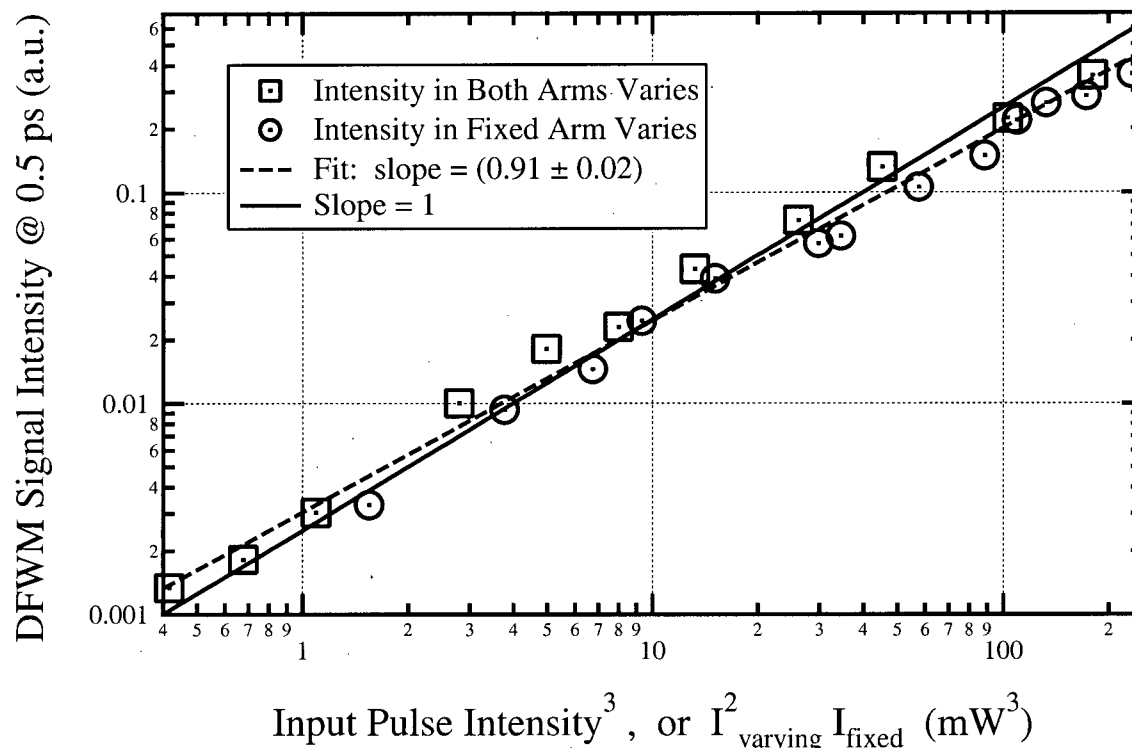
Figure 4.7: DFWM signal intensity (at 0.5 ps) versus input pulse power. For both pulse powers varying, the input powers vary from 6.20/4.70 mW to 0.800/0.650 mW. For only the fixed arm pulse power varying, the powers vary from 6.70/5.20 mW to 6.30/0.039 mW.

4.2.4 Input Pulse Intensity Dependence

If the intensity is high enough, the excited electron-hole pairs can start to influence the dephasing rates and energy levels [45]. As well, fifth-order polarization effects can also become a factor at higher intensities [44], and have terms that propagate in the same direction as the third-order terms. Their existence shows in the signal as an additional 'beat-like' component at twice the frequency of the third-order beats [44, 45]. To investigate whether these effects are important at the pulse intensities used in this work, a study of the effect of input pulse intensity on the DFWM signals was conducted.

A summary of the intensity data is shown in Figure 4.7. This shows the strength of the DFWM signal at 0.5 ps as a function of input pulse intensity. The log-log plot shows a slope close to one (solid line) over about two orders of magnitude in both signal intensity and input pulse intensity cubed, indicating that the response is close to third
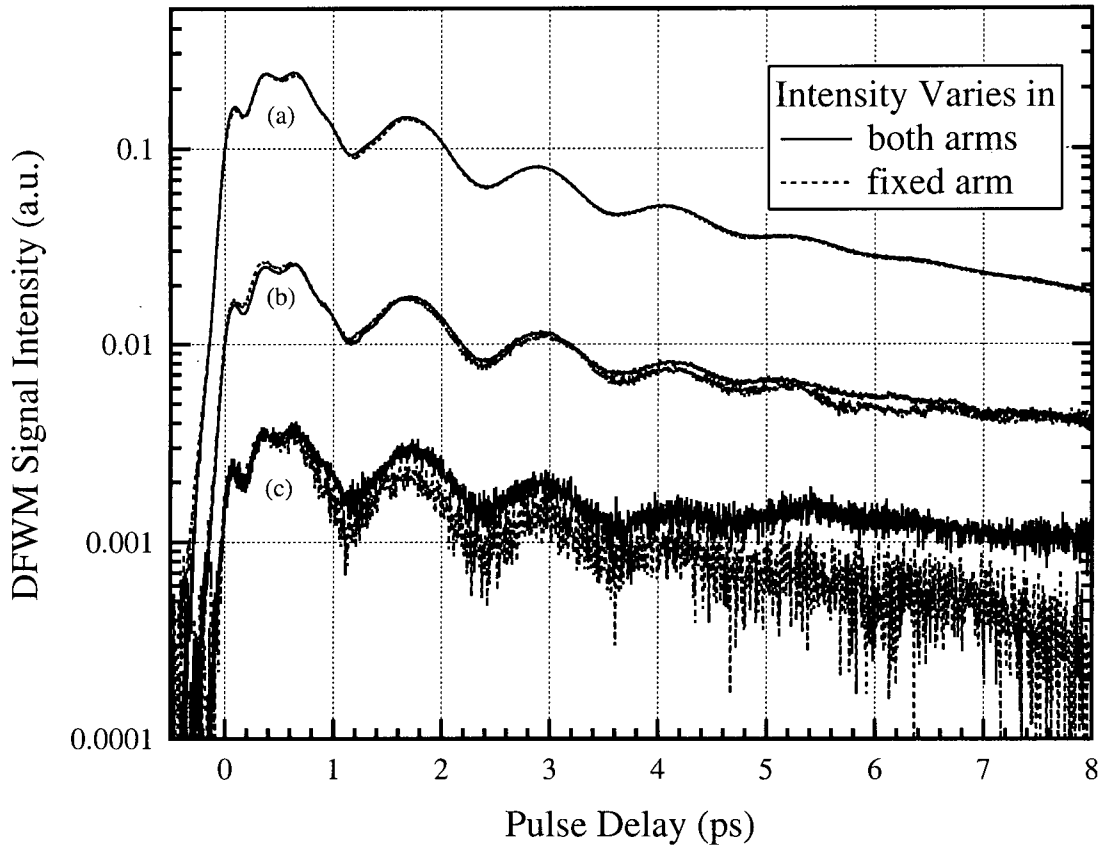
Figure 4.8: SI-TI-DFWM signals versus input pulse intensity. Six traces with three different values of $I_{varying}^2 \, I_{fixed}$ are shown. Power levels are listed as (variable arm / fixed arm / $I_{varying}^2 \, I_{fixed}$), in units of $mW/mW/mW^3$. For both input arm powers varying, they are: (a) (5.20/3.82/103.3), (b) (2.20/1.65/7.986), and (c) (1.12/0.870/1.091). For **only** the fixed arm varying they are: (a) (6.50/2.60/109.9), (b) (6.30/0.235/9.327), and (c) (6.30/0.039/1.548). The input laser pulses had a FWHM of (83.0 ± 0.1) fs and a central frequency of (1623.1 ± 0.2) meV.

order. A fit to the data (dashed line) yielded a slope of (0.91 ± 0.02). In the DFWM signals, shown in Figure 4.8, fifth-order effects do not appear to be significantly affecting the signal, even at the highest input pulse intensities.

The intensities used for the results reported in Chapter 5 (1 to 2.5 mW) correspond to horizontal axis values $\lesssim 12$ in Figure 4.7. Since the maximum intensities used in this test (5-6.7 mW) correspond to input pulse intensities at least 3-4 times greater than those used in the rest of the work, the data reported here should be substantially free of

fifth-order effects.

Even if fifth-order effects are not significant, enough real carriers may be excited to have a significant effect on, in particular, the dephasing rates. To illustrate that this effect is not significant, several DFWM signals as a function of signal input intensity are shown in Figure 4.8. These correspond to signals from higher power excitation (a) to low power excitation (c).

The effect of input pulse intensity on the modulation depth and decay rates of both the long and short period beats is negligible. The long-time dephasing rate (associated with the 1S exciton) is the most sensitive to the incident power level, but it changes by at most a factor of two over the entire range. The actual change is likely less than a factor of two, but the signal to noise at low powers limits the accuracy of this estimate. A more detailed study of the changes in the dephasing rate as a function of input pulse intensity is left for the next chapter.

4.2.5 DFWM Signals and Laser Pulse Detuning

One of the major goals of the theoretical development was to simulate the third-order DFWM process *including* the laser pulse shape. A major advantage of this approach is that it allows for a quantitative analysis of the large effects due to tuning the laser pulse center frequency through the resonances. Although similar studies have been reported in the past, these were conducted either with ps laser pulses [27], or no attempts were made to *quantitatively* study the data (especially the 1S-2S beats) [26, 28]. Although the ps pulse studies allow for a much narrower spectral excitation, and therefore give an accurate estimate of the variation of the 1S exciton dephasing rates, the 1S-2S beats are not observed because the excitation spectrum is narrower than the 1S-2S separation.

Accordingly, a study of the DFWM signals as a function of laser pulse detuning was conducted. A subset of the results from this study is shown in Figure 4.9. The data in this plot is similar to that shown earlier, in Figures 4.2 and 4.3, but on a log scale. Plotting the data in this manner allows for a direct measure of the exponential decay of
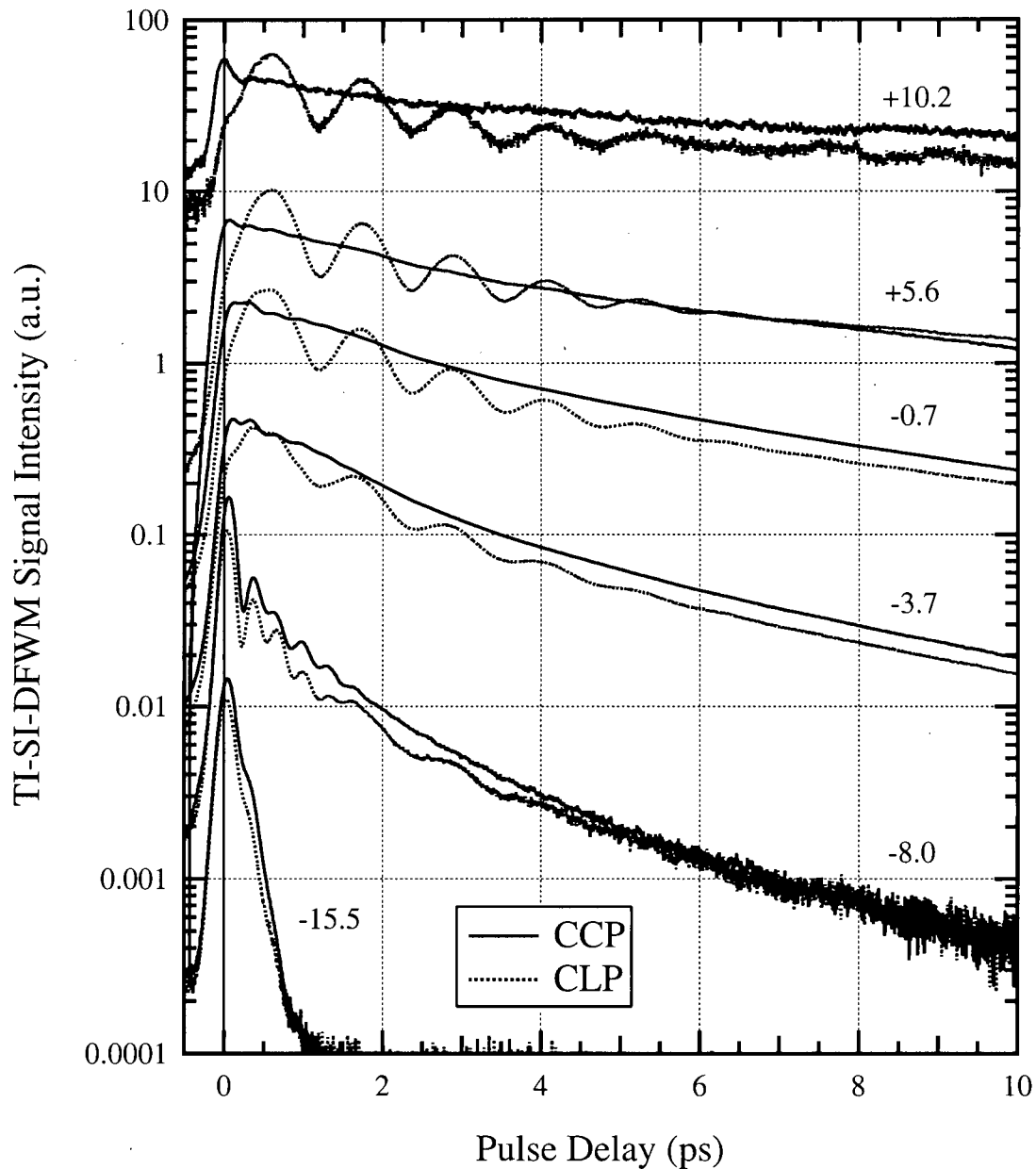
Figure 4.9: TI-SI-DFWM signals versus input laser pulse detuning, for both CLP & CCP input polarizations. Pulse detuning, $\Delta_{op} = \omega_o - \omega_{\text{pulse}}$, in meV, is shown adjacent to each set of plots. Pulse widths are 104-120 fs for the red-shifted and range from 125-175 fs for the blue-shifted data. The data has been shifted for each set (CLP,CCP) of plots for clarity.

the signals, and also allows one to determine when the assumption of exponential decays, an inherent feature of the simpler dephasing models, breaks down. Figure 4.9 shows the DFWM signals as a function of both the input polarization (CCP & CLP) and pulse detuning. Notable features in the figure are:

(i) the shortening of the long dephasing time constant, measured as a function of the delay between the two excitation pulses, and the lack of a single exponential decay.

(ii) well defined long period beats, almost insensitive to pulse detuning from −4 to +10 meV.

(iii) the fast beats are present but difficult to see for pulse detunings from −8 to +6 meV, and are strongest at −8 meV.

(iv) the large drop of the time constant with pulse detunings between −8 and −15 meV.

(v) the distinctive short time peak at zero delay in the CCP data with large positive pulse detuning.

From the previous ps pulse studies [27], it is expected that the long time dephasing rate in an inhomogeneously broadened system will decrease as the pulse is tuned below the main resonance. This is evident in this study as well, in both the CLP and CCP input pulse cases. The previous work indicated that this was due to the excitation of states localized at potential fluctuations in the wells at lower energies, versus more delocalized excitons at higher energies. Comparisons with the model calculations, presented in the following chapter, show that the lack of a single exponential decay is noticeable at shorter time delays (< 4 ps) in all the CCP data, and is especially pronounced in the blue-shifted data (−0.7 and −3.7 meV). This is consistent with the spectrally broad excitation of both localized and delocalized (free) exciton states that occurs with ~ 100 fs pulses, when compared to the ps pulses used in previous studies.

However, short pulse excitation offers the significant advantage of accessing the dephasing due to 2S and biexciton states. From Figure 4.9, the decay rate of the biexciton

beats is observed to be approximately constant over a wide range of pulse detunings, from +10 to ~ −4 meV. The 1S-2S beats, although not as visible as the biexciton beats in the CLP data, are visible for pulse detunings from −8 to +6 meV in the CCP data. Like the biexciton beats, the decay of the 1S-2S beats remains relatively constant over this wide range of energies.

The contribution of the continuum increases as the pulse is blue-shifted relative to the 1S exciton peak. The major effect of this is a large increase in the effective dephasing rate, consistent with the discussions in Chapter 2. Even so, a small residual contribution from the 1S-2S beats can be seen even with the excitation pulse detuned to −15.5 meV, its peak being ~1.5 meV into the continuum.

A distinctive short time peak is visible in CCP data with large, positive pulse detunings (+10.2 meV in Figure 4.9). This fast decay is predicted theoretically for large, red-shifted pulse detunings (Figure 2.10, on page 57), even in the absence of a contribution from the continuum. However, a residual contribution from the continuum may still contribute to at least a portion of this zero delay peak in the weak DFWM signals at large, red-shifted pulse detunings.

4.2.6 Temperature Dependence

As the temperature is increased the dephasing rates increase. The main mechanisms for this increase in dephasing rates are expected to be from acoustic and optical phonon scattering. Since the zone center LO (longitudinal optical) phonon energy in GaAs is 35.3 meV [49, page 105] and the laser pulses are tuned within 15-18 meV of the band edge, the acoustic phonon coupling mechanism is expected to dominate at low temperatures [33]. The temperature dependence of the 1S dephasing rate has been reported by several authors [2, page 53], [27, 33]. In [2, 27], fits of dephasing rates to various semi-empirical acoustic and optical phonon models were made, but since ~1 ps pulses were used only temperature dependencies for the 1S excitons were obtained. Using shorter pulses, the temperature dependence of 1S exciton and two-exciton state (biexciton and two-free

exciton state) dephasing rates have also been made [33], although in 25 nm wide quantum wells.

In this work the dephasing rates of not only the 1S exciton states, but those of the 2S excitons and biexcitons are examined as a function of temperature through the decays of the corresponding beat terms. A detailed analysis is given in Chapter 5, but here we provide a qualitative summary of the most significant findings. Figure 4.10 shows DFWM signals at three temperatures, for CLP, CCP, and XLP input pulse polarizations. The dominant feature is the monotonic increase in the dephasing rate of the long-time portion of the signal, associated with 1S excitons.

The dephasing rates of the biexciton and 1S-2S beat signals appear to decay more slowly than those of the 1S levels, as shown by the 5 K and 25 K traces. In these, the 1S-2S and biexciton beat signals last almost as long at 25 K as they did at 5 K, but the 1S dephasing rate has increased by a significant factor. Evidence of the biexciton portion of the DFWM signals can be seen in the data up to 50 K. DFWM signals due to 1S-2S beating are observed in the data up to 120 K.

As a cautionary note, an examination of the linear absorption threshold energy dependence on temperature in these samples indicates that it follows the temperature dependence of the bulk GaAs continuum edge energy level, given empirically by [49]

$$\Delta E(T)_{GaAs} = -0.5408T^2/(T + 204) \ \ \text{meV (T in K)}. \tag{4.1}$$

This implies that the pulse detuning will decrease as a function of increasing temperature under fixed laser excitation conditions. For the data shown in Figure 4.10 the laser pulse central frequency was initially 8.4 meV below the 1S level ($\Delta_{op} > 0$). The pulse detuning for this data becomes zero at 65 K.

The 1S-2S beats are visible in the DFWM data up to temperatures of $\sim$120 K, where the temperature shift of the exciton energy levels would cause the laser pulse to be detuned through the 2S energy level. Since the laser pulse would then be blue-shifted with respect to the 1S exciton level, it would decay more quickly in a similar manner to that observed when the pulse detuning was varied at constant temperature. The
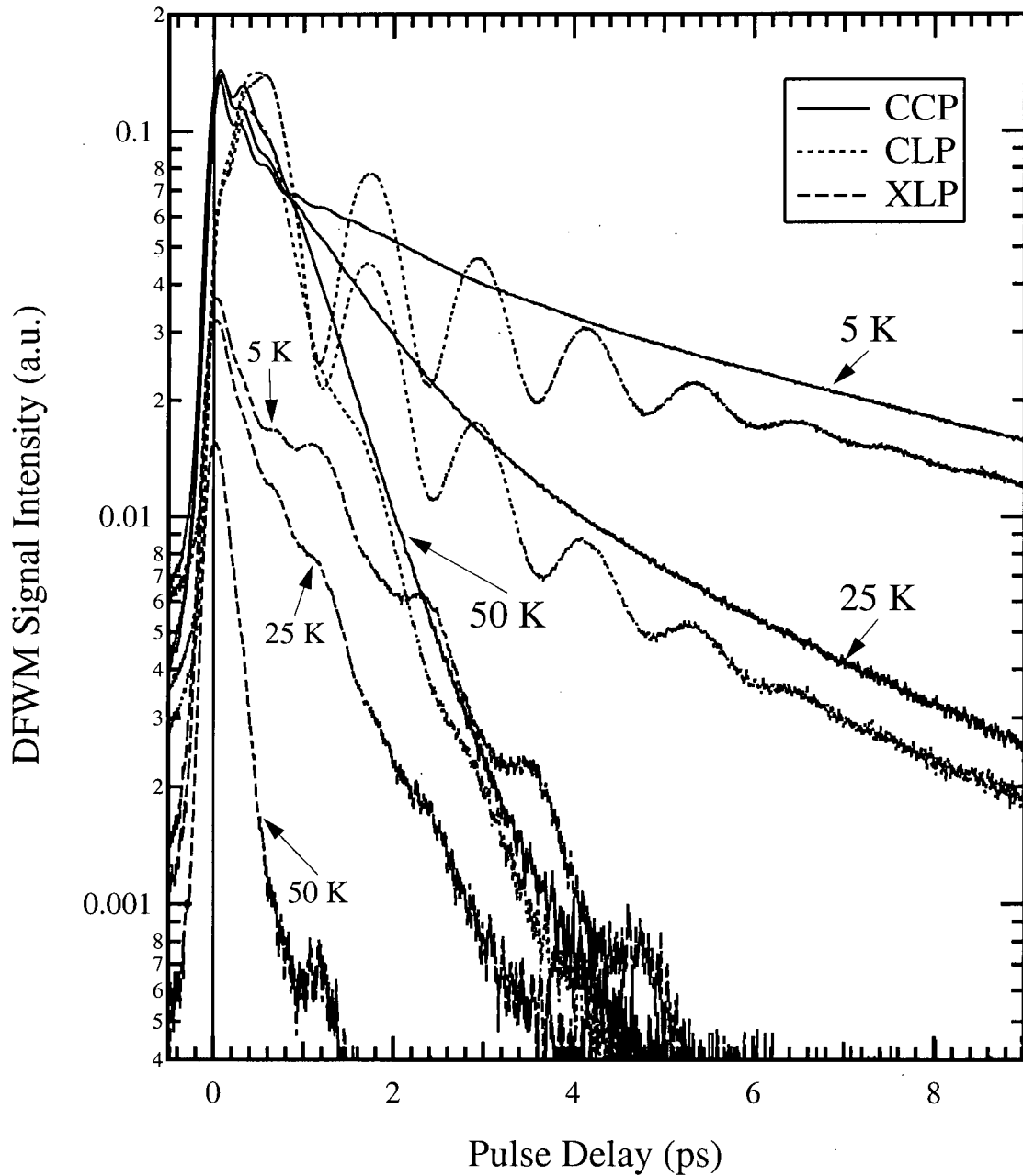
Figure 4.10: SR-DFWM signals as a function of temperature. The signals were spectrally resolved at 1617.8 meV. Laser input pulses had a FWHM of (96.5 ± 0.3) fs and a center frequency of (1611.4 ± 0.1) meV.

biexciton beats disappear well before this, when the pulses are still red-shifted below both the 1S and biexciton energy levels.

4.3   DFWM Experimental Results - Doped Samples

The original motivation for studying the doped samples was to obtain evidence for the existence and dominance of the negatively charged exciton (or, trion) in the doped samples. The earlier linear absorption experiments [4–6] did not conclusively answer this question in these samples. Two of the doped samples were therefore studied using the DFWM technique.

4.3.1 2.5×10^{10} cm^{-2} Sample

The sample with the lowest doping has a 2-D electron density of 2.5×10^{10} cm^{-2}, corresponding to a Fermi energy in the wells of 0.9 meV. Earlier work [4–6] led to the expectation that, at least theoretically, the dominant mechanism for absorption would be negatively charged excitons (trions), even at these low doping densities. Work using photoluminescence detection with far-infrared excitation of excited states in a sample with similar doping to this one has shown evidence of negatively charged excitons (trions), and their corresponding excited states, but no evidence of the excited states (2S, ...) of neutral excitons [16], confirming the presence and dominance of trion particles in these doped quantum wells.

Photoluminescence measurements of trions in n-doped quantum wells [60, 61] indicate a binding energy of ∼2.1 meV in 8 nm wells and an unresolved feature in the 6 nm wells with a 2.6 meV separation. These studies both confirmed the existence of trion particles in doped quantum wells, as well as showing that they contribute significantly to the measured signal. From these studies, we would expect to see trion effects in this sample as well, although the large inhomogeneous broadening (∼4 meV) would make photoluminescence detection of the trions in our narrower (5 nm) wells difficult. This is one reason for the inconclusiveness of the previous studies of these samples [4–6], even
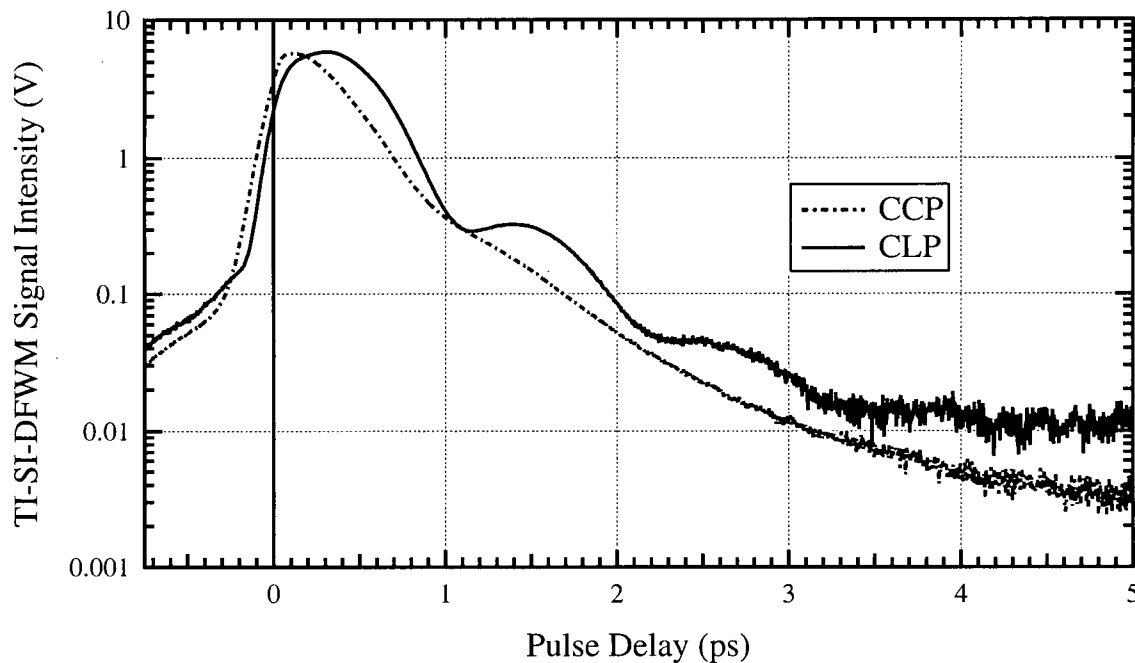
Figure 4.11: DFWM signal for lowest doped sample. The laser input pulse has a FWHM of (106.5 ± 0.2) fs and a central frequency of (1619.8 ± 0.1) meV. The linear absorption peak is at 1622 meV.

with an expected larger binding energy in these narrow wells. However, there have been no reported DFWM studies (to our knowledge) of these low doped samples.

4.3.1.1 Input Pulse Polarization Dependence

The TI-SI DFWM signals as a function of input pulse polarization for this doped sample are shown in Figure 4.11. They exhibited similar behaviour to the undoped sample, with the CLP data showing a long beat with a corresponding energy of about 4 meV. The decay is much faster ($\sim 10 \times$) than the slow decays in the undoped case, and it is never exponential, out to delays corresponding to the noise floor. In contrast to the undoped sample, however, this sample shows no evidence of an excited 2S exciton level in either the CLP data or the CCP data. In particular, no 1S-2S like beats were observed for any pulse detunings or detection energies where signals were detectable.

The presence of the beat signal in the CLP data, but not in the CCP data, suggests

that there is still a distinct two-exciton-like state being excited. The possible presence of similar, but much smaller beats in the CCP data is most likely an artifact of slightly elliptical polarization (non-perfect circular polarization). It could however, be a property of excited two-exciton states in the presence of a background electron gas. The most obvious candidate for this distinct, dressed two-exciton state is a bound, negatively-charged biexciton. Theoretically, there is still some debate over the existence of five-particle charged-exciton complexes [62, 63], and we are unaware of any relevant experimental data in semiconductors. However, none of these theoretical studies has included in-plane localization in the derivations. It is known that in-plane localization has a large effect on the binding energy of the biexciton in undoped wells, which can increase over 50% from that expected for a uniform quantum well [17].

4.3.1.2 Spectrally Resolved Data at Fixed Pulse Delay

A set of spectrally resolved DFWM signals at fixed delay, τ is shown in Figure 4.12.[†] The CCP and CLP polarized signals both appear to peak at the same energy in these SR-DFWM signals, although the signal-to-noise ratio is much lower in these weak signals. The DFWM spectra in this sample are $\sim$3.5$\times$ narrower than the linear absorption peak, compared to a ratio of $\sim$3$\times$ for the undoped case. Since an $\sim$3$\times$ difference in width between the linear and nonlinear spectra are only expected in the undoped sample, where $\alpha \approx 1$, there is no real reason to expect it to stay the same when α varies significantly from one.

4.3.2 20×10^{10} cm^{-2} Sample

Study of the highest doped sample was motivated by a DFWM study of a sample with similar 2-D doping density [37, 38], which argued that the dephasing rate, due to electron-electron scattering, decreased in doped samples when the excitation pulses are tuned near

---

[†] The small negative excursions in Figure 4.12 are artifacts of the background subtraction procedure when applied to the doped samples. Since the nonlinear signals are relatively weak, and the luminescence is relatively strong in these doped samples, any nonlinearity in the photoluminescence response appears as "DFWM signal" in the processed data.
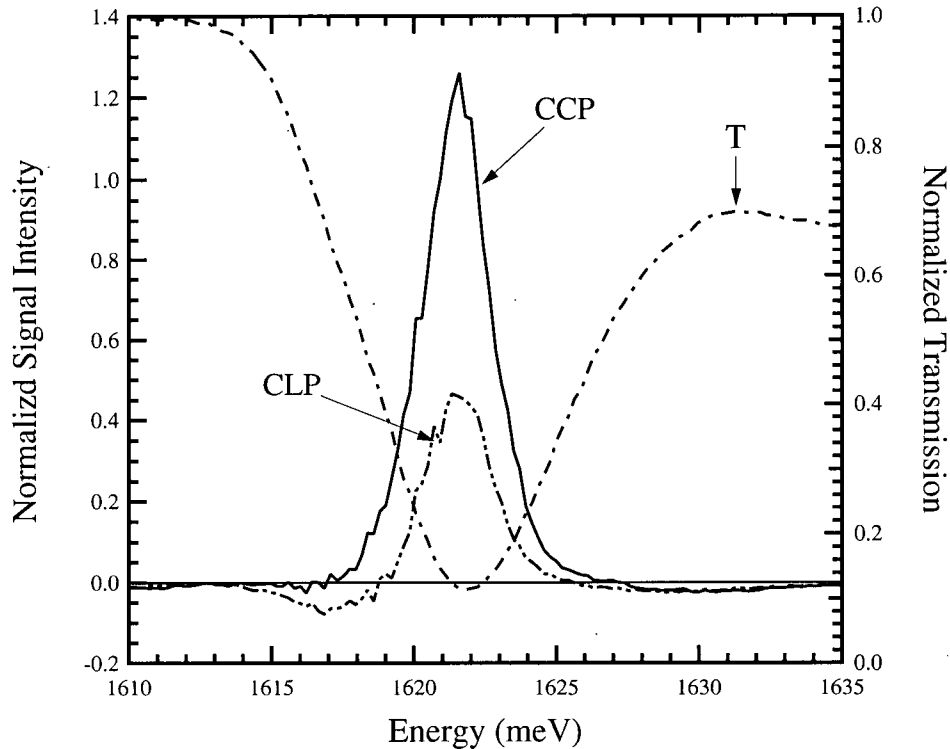
Figure 4.12: DFWM spectra with fixed delay, $\tau = (0.37 \pm 0.03)$ ps, for the lowest doped sample (left vertical axis). Laser excitation pulse has a FWHM of (106.5 ± 0.2) fs and a center frequency of (1619.8 ± 0.1) meV. The dashed line is the white light transmission spectra (right vertical axis).

the Fermi energy. These studies were conducted in similar samples (8 nm wide quantum wells with excess electron doping of $2 \times 10^{11} \, cm^{-2}$), with similar excitation conditions (~ 100 fs pulses) to ours.

The highest doped sample in our series has a 2-D density of $20 \times 10^{10} \, cm^{-2}$, corresponding to a Fermi energy of 7.4 meV. Examination of the DFWM signals from this sample, obtained using a wide variety of pulse central frequencies and pulse widths, showed no evidence of the decrease in dephasing rate when the pulse is tuned through the Fermi energy, reported by Kim, et. al. [37,38]. The TI-DFWM signals showed only a single, fast decay when the excitation pulses were tuned over the range of energies where they were visible, with no change noted in the DFWM signal.

A TI-SI DFWM signal for this sample is shown in Figure 4.13. It exhibits a single
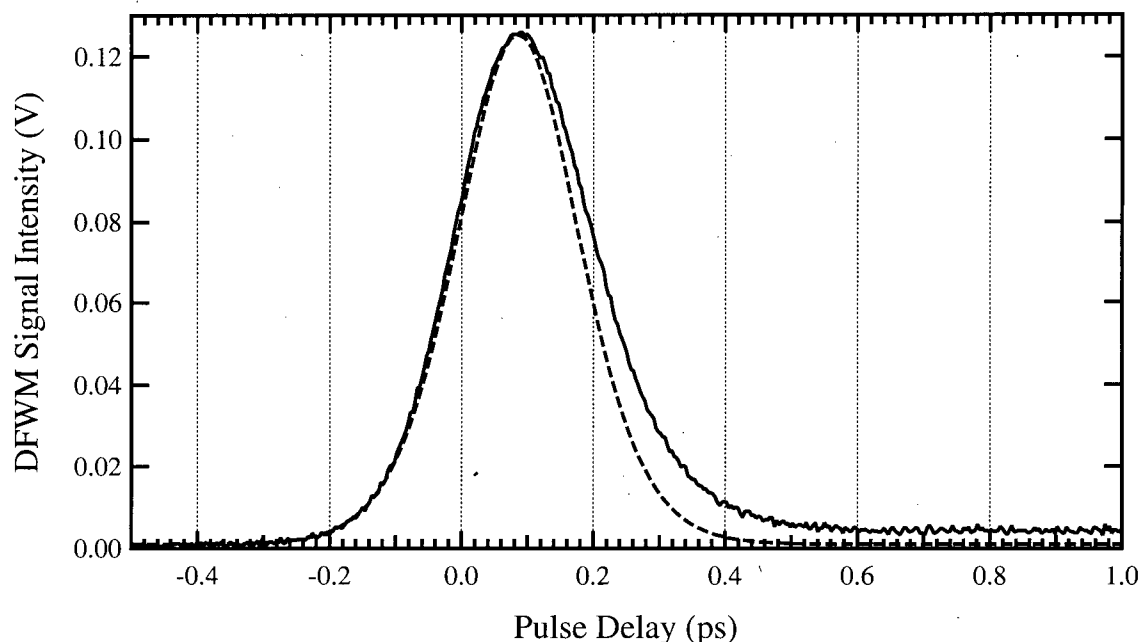
Figure 4.13: DFWM signal for highest doped sample. Laser excitation pulse was tuned to maximize the signal and has a FWHM of (129.5 ± 0.1) fs, with a center frequency of (1629.4 ± 0.1) meV. The linear absorption peak is at 1624.7 meV. The dashed line is the calculated intensity profile of the input pulse autocorrelation for comparison.

fast decay, with the decay being only slightly slower than the pulse auto-correlation (also shown in the figure as a dashed line). SR-DFWM signals showed the same behaviour, with no evidence either of beat signals or a change in the decay characteristics with laser detuning.

The DFWM spectra as a function of fixed delay, τ, is shown in Figure 4.14, for both CLP and CCP input pulse polarizations.[†] The spectra from this heavily doped sample are quite broad and flat topped, in contrast to the narrow, Gaussian-like peaks observed in the undoped and lightly doped samples. The nonlinear signal from this doped sample rises slowly at the absorption edge, is relatively flat over a range approximately equal to the Fermi energy in this sample, $\sim$7 meV, and then decreases slowly to higher energies.

The nonlinear response of this highly doped sample is thus drastically different from

---

[†] Small negative excursions similar to those in Figure 4.12 are also visible here and, as discussed in the footnote on page 115, are attributed to artifacts of the background subtraction procedure when it is applied to the doped samples.
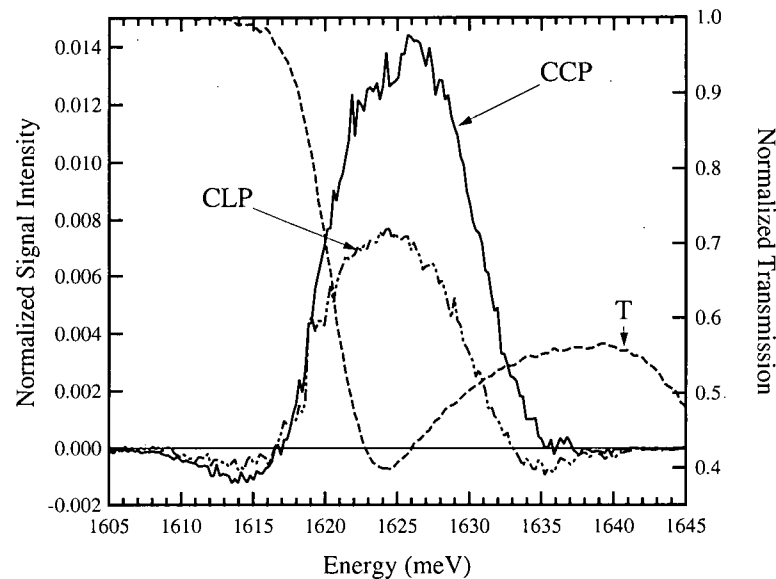
Figure 4.14: DFWM spectra with fixed delay, $\tau = (0.10 \pm 0.03)\,\text{ps}$, for the highest doped sample (left vertical axis). Laser excitation pulses have a FWHM of $(129.5 \pm 0.1)\,\text{fs}$, and a center frequency of $(1629.4 \pm 0.1)\,\text{meV}$. The dashed line (T) is the white light transmission spectra (right vertical axis).

the undoped and low doped samples. Both of the nonlinear spectra from those samples were considerably narrower than the prominent peaks in their corresponding absorption spectra, as expected for a resonant system. In the highly doped sample, characterized by a clear power law linear response ($\alpha \sim 0.33$), the DFWM spectral width (FWHM of $\sim 12\,\text{meV}$) is considerably larger than even the inhomogeneous linewidth characteristic of this set of quantum well samples ($\sim 4\,\text{meV}$).

In this chapter the linear and nonlinear data obtained from the doped and undoped samples has been presented. Various trends in the data were discussed on a qualitative level, and compared both with the qualitative predictions of the numerical modelling results presented in Chapter 2, and, where appropriate, with the literature. In the next chapter, the results of a quantitative analysis of the data will be presented.

Chapter 5

Quantitative Analysis

In this Chapter, the results of a quantitative analysis of the linear and nonlinear (DFWM) data will be presented. Using the detailed model developed in Chapter 2, parameters (dipole moments, decay rates, and energy level spacings) were extracted from the various one- and two-particle transitions. The chapter starts with a discussion of the fitting procedure, pointing out which parameters can be more reliably estimated from the linear versus the nonlinear data. By ultimately demanding that the same set of system parameters be used to explain both the linear and nonlinear data from the same sample, more constraints are placed on the range of values that are consistent with all of the available data.

5.1   Simulations and Model Parameter Sensitivity

The combined linear and nonlinear extraction of parameters from the model was accomplished in two parts. First, due to the length of time that the full simulations take ($\sim$15-30 minutes for single level system simulations and $\sim$2-8 hours for two-exciton level systems), detailed least-squares fits of the linear data are done in conjunction with initially crude fits of the nonlinear data. Moving back and forth between these two models allows one to get a rough estimate of the parameters. The crude estimation of the DFWM data is based on a shortened version of the time-integrated delta-function limit (Equation (2.62), also given in [24, 25]). In this limit, the time- and spectrally-integrated DFWM signals decay as $\exp\{-4\Gamma\tau\}$ for inhomogeneously broadened systems [2]. The beat signals decay

Parameter		Linear	DFWM
Absolute Energy Level	E_j	✓✓✓✓✓	✓✓✓
Energy Level Separations	Δ_{jo}	✓✓✓	✓✓✓✓✓
Dipole Strength	$\vec{\mu}_j$	✓✓✓	✓✓✓✓✓
Dephasing Rate	Γ_j	✓	✓✓✓✓✓
Power Law Exponent	α_j	✓✓✓✓	✓✓✓✓
Inhomogeneous Broadening	$\Gamma_{j,\,inh}$	✓✓✓✓	✓✓✓✓

Table 5.1: Sensitivity of linear and nonlinear (DWM) model parameters. The scale goes from zero (0) checkmarks (parameter insensitive to fitting of data with the model) to five (5) checkmarks (highly sensitive).

with a behaviour similar to $\exp\{-2(\Gamma_1 + \Gamma_2)\tau\}cos(\Delta_{12}\tau + \phi)$, where the subscripts 1 and 2 refer to the two beating levels, Δ_{12} is the energy separation between the levels and the angle ϕ is: zero for single-exciton and two-exciton (XLP case) level beats, and 180° for two-exciton level beats in the CLP input pulse case [26].

The second main part to the fitting procedure involves switching from the fast, crude estimates to the full simulations, to fine tune the parameter estimation. This is especially important for quickly decaying levels such as the 2S exciton and continuum levels, where the crude estimates do not provide accurate estimates of the parameters. Since changing these parameters also affects the dipole moment magnitudes, these are also an important part of the more rigorous fits. In the same procedure as for the cruder fits, this involved switching back and forth between the linear fitting routine and the nonlinear DFWM simulations.

The sensitivities of the various parameters to the fitting of the data with the model varies depending on which process (linear or nonlinear) is being considered. This sensitivity is summarized in Table 5.1.

For the linear absorption data, the absolute energy level, power law exponent, and inhomogeneous broadening parameters are the most sensitive when fitting the data with the model (Equations (2.27) & (2.32), on pages 27 & 28). In contrast, the dephasing rates can vary over a large range in the linear absorption fits before they start to contribute to the simulated absorption spectra. In our samples this is due to the inhomo-

geneous broadening ($\sim$4.5 meV) being large compared to the magnitude of the dephasing rates which, in the absence of inhomogeneous broadening, would determine the spectral width of the features. For a dephasing rate comparable to the inhomogeneous broadening ($\hbar\Gamma \approx 4.5$ meV), this would require the dephasing rate to be $\Gamma \approx 6.8$ ps^{-1}) (or, a dephasing time of less than 150 fs). The large inhomogeneous broadening also makes identification of closely spaced peaks difficult, decreasing the accuracy with which the energy levels of excited states (2S exciton, continuum) can be assigned. The shape of the absorption features (especially the high energy tail) makes the power law exponent a very sensitive parameter in the fits of linear absorption spectra to the model. The model is also dependent on the dipole strengths, as the theoretical equations result in the linear absorption coefficient being proportional to the dipole moment squared of each level in the system.

In contrast to the linear absorption data, the DFWM theoretical data and the fitting of it with the model outlined in Equation (2.61) on page 47, is sensitive to all the parameters. The beats in the DFWM signals give accurate measures of the differences in energy between levels in a system, and are thus very sensitive to these energy level separations. This allows accurate estimates of, for example, the 1S-2S exciton energy level separation, where the 2S exciton level was not clearly defined in the linear absorption data. The decays of the DFWM signals give accurate measures of the dephasing rates, even in the presence of large amounts of inhomogeneous broadening. For biexcitons in particular, inhomogeneous broadening is necessary for the signals to be visible in the time-integrated DFWM signals [26]. The power law exponents are also sensitive parameters, as changes in α away from one cause beat magnitudes to decrease. For small power law exponent values (close to zero) the DFWM signal also turns into a single, fast decaying peak that is centered close to zero pulse delay, and is insensitive to the dephasing rate until it decays by a few orders of magnitude. The DFWM signal intensity depends on the dipole strengths to the eighth power (or to the fourth power for each of the levels involved in a beat signal), making the fitting of the DFWM data with the model much more sensitive

to the dipole strengths than it was in the linear absorption case.

Since the spectral overlap of the pulses determines which levels are excited and, with the pulse detuning, how much they are excited, the DFWM signals are very sensitive to both the pulse central frequency and pulse width. Since the simulations depend on these excitation pulse shapes, they are measured independently, and can be fit to give accurate measures of the pulse central frequency and pulsewidth (see the discussions in Section 3.3.3 and Appendix B). The DFWM portions of the model are dependent on the detuning, or differences between the pulse central frequency and the level frequencies.

The delta-function pulse limit of the model (Equation (2.62) on page 50) is used to provide quick, cruder estimates of the model parameters, sensitive to energy level separations, dephasing rates, dipole moment magnitudes, and inhomogeneous broadening. Since the full, or non-delta-function, simulations are also sensitive to these parameters, the delta-function simulations provide a quick way of roughly estimating the parameter values. Differences in the parameters between the two simulation methods are caused mainly by the power law exponent and excitation pulse parameters. These two parameters are present only in the full simulations, resulting in differences between the two simulation methods, which grow larger at short pulse delays.

5.2 Experimental Results and Simulations - Undoped Sample

This section compares the linear and DFWM experimental data to the models presented in Chapter 2. Self-consistent fits, using both the linear and nonlinear data, including input laser pulse detuning and polarization dependence are used to simulate the data. From these comparisons, 1S, 2S, and continuum energies, dephasing rates and inhomogeneous broadening are extracted, along with the biexciton binding energies and dephasing rates. These are all examined as a function of input pulse detuning, pulse intensity, and temperature.

5.2.1 Comparison of Experimental Data with Models – Undoped Sample

Selection of a model system to emulate the physical system involves examining the linear absorption data, as well as the time-integrated and spectrally-resolved DFWM signal data as a function of input pulse polarization. From a qualitative examination of the input polarization dependence of the TI-SI-DFWM and SR-DFWM signals in the previous Chapter, the shorter (12.75 meV) beats can be assigned to a 1S-2S exciton system. As well, the polarization dependence indicates that the longer 3.5 meV beats are due to a double, or biexciton type system.

Early attempts to fit the 1S exciton peak in the linear absorption data indicated that a single peak did not fit the data well and the presence of two levels approximately 2.8 meV apart, corresponding to approximately a half-monolayer change in $GaAs/Al_{0.3}Ga_{0.7}As$ well widths of this size (5 nm), needed to be assumed for the simulations to accurately model the data. The 2S level fits also benefitted from the inclusion of this second level. As will be shown in the nonlinear analysis section, the inclusion of two *incoherently coupled* [64] 1S-2S-biexciton systems actually helped in getting better fits there too (shown by the two exponentially decaying 1S levels present in both the CLP and CCP data).

The results of fitting two polarization beating 1S-2S-continuum systems to the linear absorption data is shown in Figure 5.1, with the parameters for the fit given in Table 5.2. The linear absorption simulation fits the data well. The dipole moment magnitude of the lower energy (A) states was found to be larger than that of the corresponding levels in the higher energy (B) states. The presence of a large amount of inhomogeneous broadening makes the linear absorption spectra insensitive to the dephasing rates and, as such, these parameters are taken from the fits to the DFWM data discussed later. The inclusion of the light-hole exciton and light-hole continuum levels were also found to be a necessary component of the linear absorption fits, with the light-hole exciton dephasing rate determined by the fitting routine. The parameter errors are from the fits to the linear data except where parameters have been fixed using values from the fits to the DFWM data (dephasing rates and dipole moment ratios).
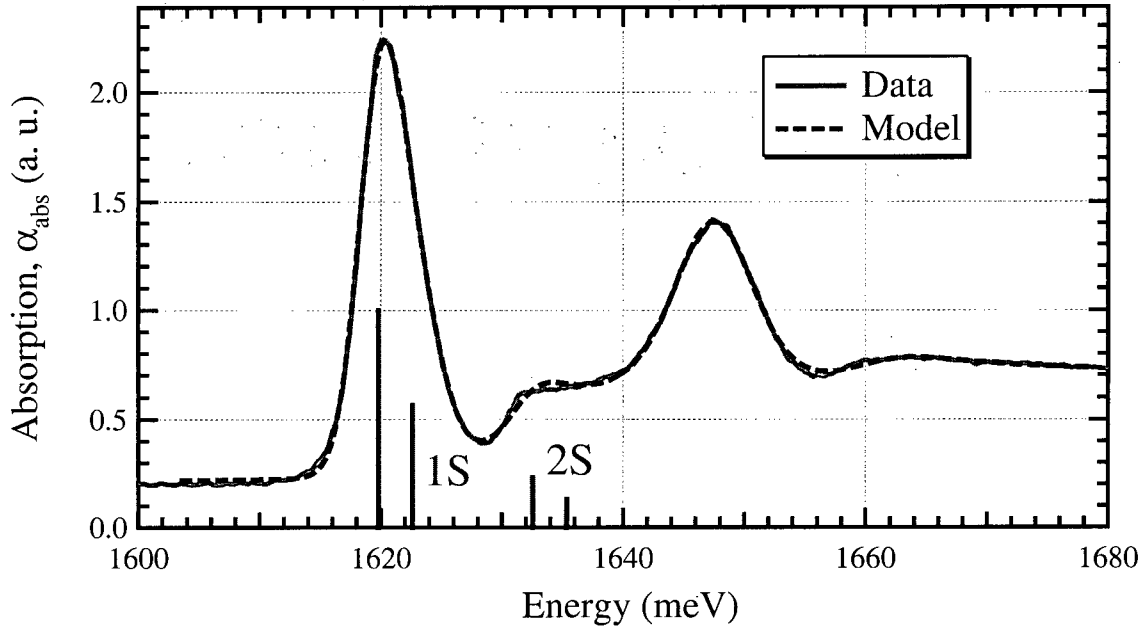
Figure 5.1: Linear Absorption for undoped sample at 4 K - simulations and data. The system parameters used are listed in Table 5.2.

i	ΔE_{io} (meV)	$\mu_i/\mu_{1S(A)}$	Γ_i (ps^{-1})	α_i	$\Gamma_{i,\text{inh}}$ (meV)
X-1S (A)	$1619.8 \pm 0.1^\dagger$	$0.00773^\dagger$	0.6579	0.965	$4.191 \pm 0.009^\S$
X-1S (B)	2.82	0.75	0.38	0.965	$4.65 \pm 0.03^\S$
X-2S (A,B)	12.75	0.483 ± 0.002	1.77	0.999	
Continuum	16.39 ± 0.07	0.73	2.5	0.062	
BiX¶	3.486	1.41	0.30	0.965	
X-1S (lh)	27.68 ± 0.02	0.878 ± 0.003	0.426	0.99	$7.01 \pm 0.02^\S$
Cont. (lh)	$13.2 \pm 0.3^\ddagger$	$0.293 \pm 0.004^\ddagger$	2.5	0.31 ± 0.03	

Table 5.2: Linear absorption fit parameters for undoped sample, corresponding to the fit and data shown in Figure 5.1. Errors are 1 in the last digit unless otherwise noted. The system consists of two polarization-beating 1S-2S-continuum exciton systems, 2.82 meV apart. An 1S-continuum light hole (lh) system has been added to assist with fitting the data around the heavy-hole 2S exciton and continuum levels.

---

† These are absolute fit values. Energy levels (ΔE_{io}) are expressed as a shift from the X-1S (A) energy level. The dipole moments are expressed as ratios, relative to the X-1S (A) fit value. The dipole moment ratios of levels in the (B) system are all multiplied by $\mu_{X\,1S\,(B)}/\mu_{X\,1S\,(A)}$

‡ These values are relative to the X-1S (lh) energy and dipole strength.

§ The inhomogeneous broadening is set constant for all (1S, 2S, continuum) levels within each system.

¶ Biexciton levels are not included in the linear simulations.

In Figure 5.1, the vertical lines show the positions and relative strengths of the square of the dipole moment magnitude for the 1S and 2S exciton levels in the simulation. To compare the dipole moment ratios for the 2S and continuum states to existing theoretical treatments, the simple theoretical predictions of the dipole moment strengths of ($\mu^2 \propto (n - 1/2)^{-3}$) for 2–D excitons and ($\mu^2 \propto n^{-3}$) for 3–D excitons [1, page 167], where n refers to the nth exciton state, are often used. A more rigorous approach [65] gives a more complex dependence for the optical absorption strength which becomes, for two dimensions,

$$O(\hbar\omega) = O_0 \left\{ \sum_{n=1}^{+\infty} \frac{Ry^*}{(n - 1/2)^3} \delta(\hbar\omega - E_n) + \frac{|\Upsilon(i\gamma + 1/2)|^2 e^{\pi\gamma}}{4\pi} \mathbf{H}(\hbar\omega - E_g) \right\} , \quad (5.1)$$

with

$$O_0 = \frac{8\pi\omega|\mu|^2}{n_B c Ry^* a_B^2} , \quad (5.2)$$

where Ry^* is the effective Rydberg, or 3-D binding energy of the exciton, $\sim 4.4\,\text{meV}$ in GaAs. The integer n labels the excitonic states, $E_n = E_g - Ry^*/(n - 1/2)^2$ is their binding energy in 2-D, E_g is the bandgap energy, a_B is the effective 3-D Bohr radius of the exciton, and $\gamma = (Ry^*/(\hbar\omega - E_g))^{1/2}$. n_B is the background refractive index. In 2-D the behaviour of the factor in front of the 'continuum' Heaviside step function term equals 1/2 for the band-edge ($\gamma \to \infty$) and approaches 1/4 for energies high above the band-edge ($\gamma \to 0$).

Using this more rigorous equation and taking the ratio μ_{2S}/μ_{1S} of the 1S and 2S exciton terms gives a predicted ratio of 0.43, in good agreement with the fit value of 0.48. By contrast, the simpler expression in [1, page 167] gives a value of $1/\sqrt{27} = 0.193$. The $\mu_{\text{continuum}}/\mu_{1S}$ ratio from the fits gives 0.73, while the predicted value is 0.34. This varies quite strongly with small power law exponent values, and so the error for these two parameters combined may be much larger than the values indicated in the tables. Owing to the complicated nature of the continuum, and the fact that we chose to phenomenologically represent its lineshape using the power law function, we can't really expect to be able to quantitatively interpret the continuum dipole moments coming out

of these fits.

TI-SI-DFWM signals for the undoped sample are shown in Figure 5.2, for both CCP and CLP input pulse polarizations. Examination of the DFWM simulations (shifted from the data in the Figure for ease in comparing the data and simulations) show that the simulations reproduce the general shape of the DFWM data quite well over a wide variety of pulse detunings, for both CLP and CCP input polarizations. The only parameters changed in these pulse detuning simulations were the dephasing rates (discussed next), and the continuum dipole strength (following the dephasing rate discussion).

5.2.2 Input Pulse Intensity Dependence

As mentioned in the previous chapter (Figure 4.7, page 105), the intensity dependence of the DFWM signals in this work indicate that higher order $\overleftrightarrow{\chi}^{(n)}$ contributions can be neglected. However, the dephasing rates could still be affected at higher laser excitation powers by the density of excited carriers, a process referred to as excitation induced dephasing (EID) [44,45]. Figure 5.3 shows the variation of dephasing rates as a function of input pulse excitation intensity, for the long time 1S exciton, 2S exciton, and biexciton levels.

The biexciton and 2S exciton dephasing rates show no significant dependence on input pulse intensity. The 1S exciton dephasing rate does increase with intensity, by approximately 45% over the range tested (from 0.045 to $0.065\,\mathrm{ps}^{-1}$). Since the beam powers used in this work correspond to x-axis values on the graph < 12, however, the excitation induced change in the dephasing rate will not be a significant factor when compared to the much larger changes observed with variation of pulse detuning.

5.2.3 Effects of Input Laser Pulse Detuning

A comparison of the dephasing rates extracted from the DFWM data as a function of input laser pulse detuning is given in Figure 5.4. The lines on the graph are fits to the
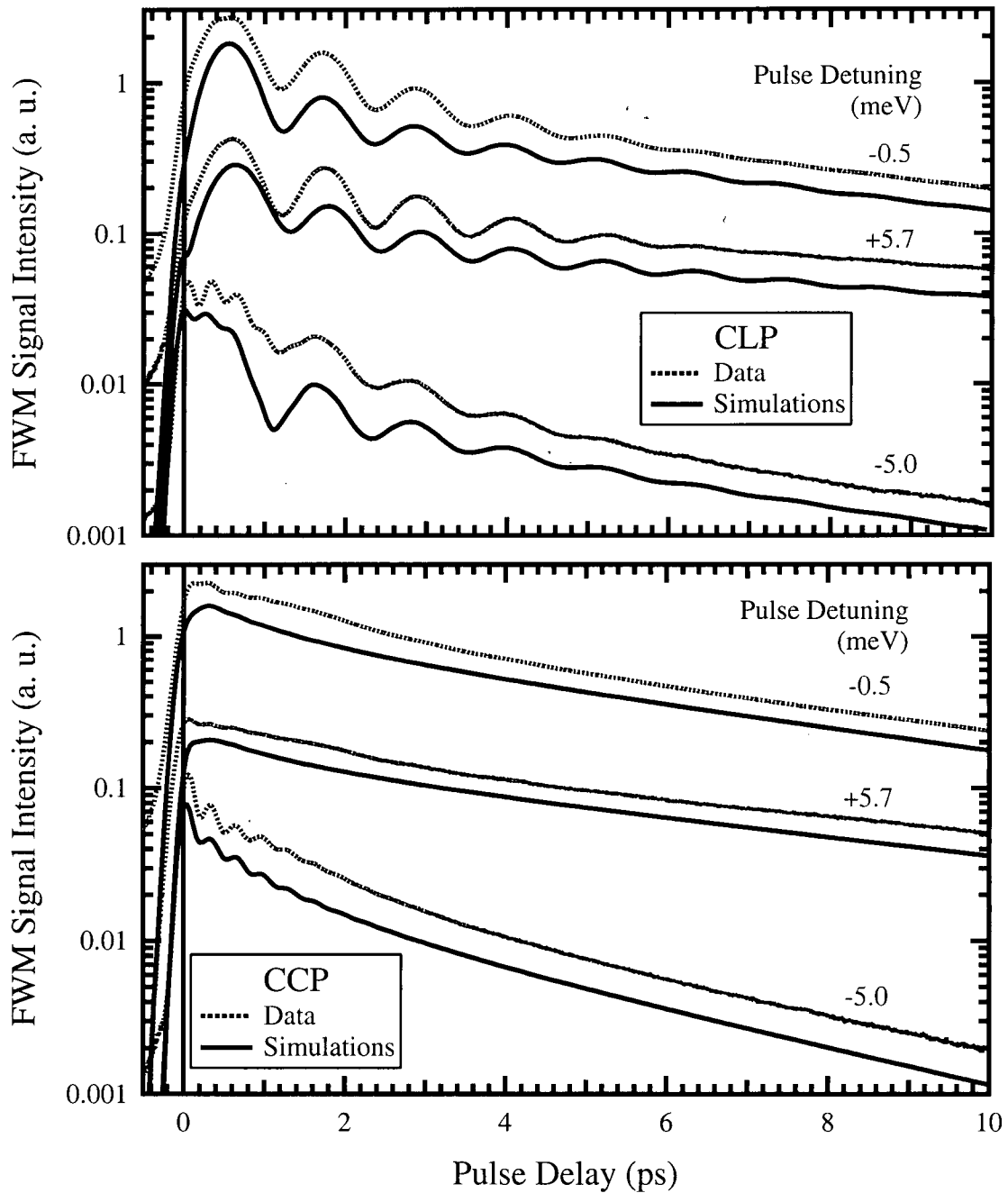
Figure 5.2: CLP & CCP simulations and data. Parameters are from Table 5.2 along with dephasing rates, that vary with pulse detuning, from Figure 5.4.
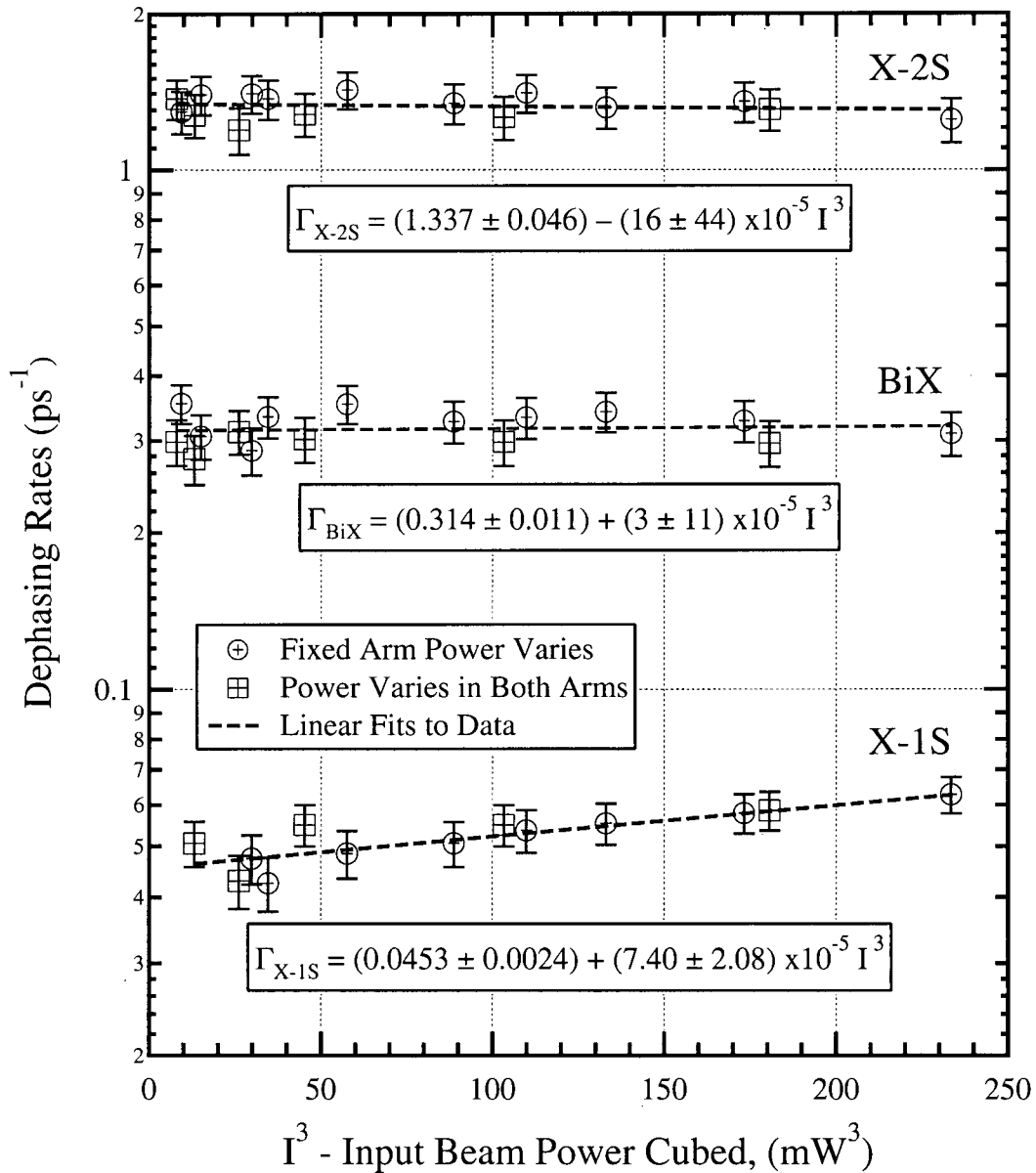
Figure 5.3: Dependence of dephasing rates on input pulse intensity. Input pulses are centered 4 meV above the 1S resonance.

data using the empirical equation

$$\Gamma(E) = \Gamma_0 + \Gamma_1 \exp\left\{ (E - E_o)/E_a \right\} , \qquad (5.3)$$

with the E_o values set to equal the corresponding level energies from Table 5.2. The fit parameters obtained in this way are summarized in Table 5.3.

The 1S (A) exciton dephasing rates match extremely well to the exponential equation. The small value of Γ_o (decay time $\sim 1\,\text{ns}$) indicates that these excitons are limited by recombination in the extreme red-shifted limit. The dephasing rate increase with increasing excitation pulse central frequency is qualitatively similar to what others have observed [26–28], usually with longer pulses. Using $\sim 1\,\text{ps}$ laser pulses and $9.6\,\text{nm}$ quantum wells, [27] shows a dephasing rate of $\sim 0.5\,\text{ps}^{-1}$ at the absorption peak, close to the value of $0.3\,\text{ps}^{-1}$ at the 1S exciton energy that we report. No attempt to extract a fit to the data was made, however. In other studies, no attempts were made to *quantitatively* study the data [26, 28].

Except for the long 1S (A) exciton decay, the other level decays are dominated by the large offset decay rate Γ_o, that is independent of pulse tuning. To our knowledge, there are no existing reports to compare against the 2S and biexciton data shown here. The values for the biexciton rates ($\sim 0.3\,\text{ps}^{-1}$) are similar to those reported in a temperature dependence study of dephasing rates of excitons and biexcitons in a single $25\,\text{nm}$ GaAs quantum well [33] ($0.15\text{-}0.2\,\text{ps}^{-1}$ at $10\,\text{K}$).

This behaviour can be qualitatively explained by the fact that only the 1S (A) exciton state shows a long time decay and all the higher level states must, in principle, be allowed to scatter into close by, lower energy states. This scattering mechanism would not be available, at low temperatures, to the lowest lying energy state. These additional scattering channels, available to all but the lowest lying 1S (A) states, seem to have a large, dominant effect on their dephasing rates.
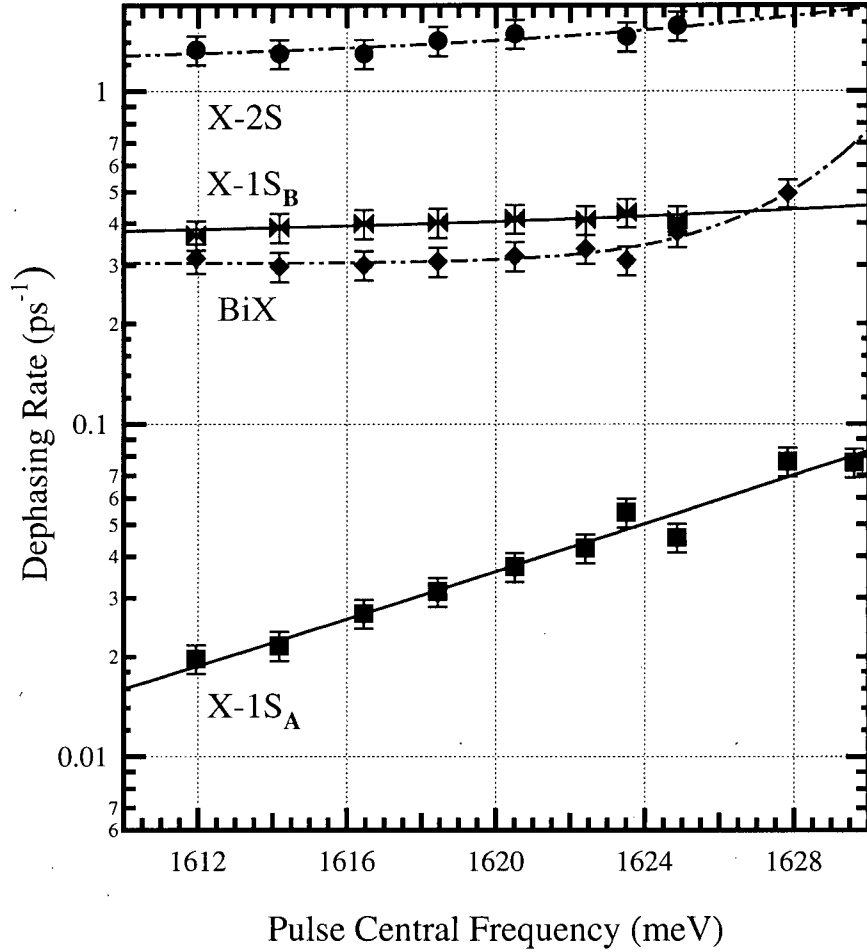
Figure 5.4: Pulse detuning dependence of dephasing rates. The dephasing rates of the 1S levels vary independently for the two 1S-2S-biX-continuum systems, while the 2S, biexciton, and continuum dephasing rates are set the same for both systems.

	Γ_0 (ps^{-1})	Γ_1 (x10^{-2}ps^{-1})	E_a (meV)	E_o (meV)
X - 1S (A)	$0.001 +0.02 -0.001$	(4 ± 2)	(12 ± 5)	1619.8
X - 1S (B)	(0.30 ± 0.02)	(11.5 ± 0.5)	(29 ± 8)	1622.6
X - 2S	(1.2 ± 0.3)	(40 ± 10)	(11 ± 3)	1632.6 & 1635.4
biX	(0.303 ± 0.008)	(0.1 ± 0.1)	(2.5 ± 0.3)	1616.5 & 1619.3

Table 5.3: Pulse detuning dephasing fit coefficients corresponding to Equation (5.3) and Figure 5.4. The values of E_o are the level energies, from Table 5.2.
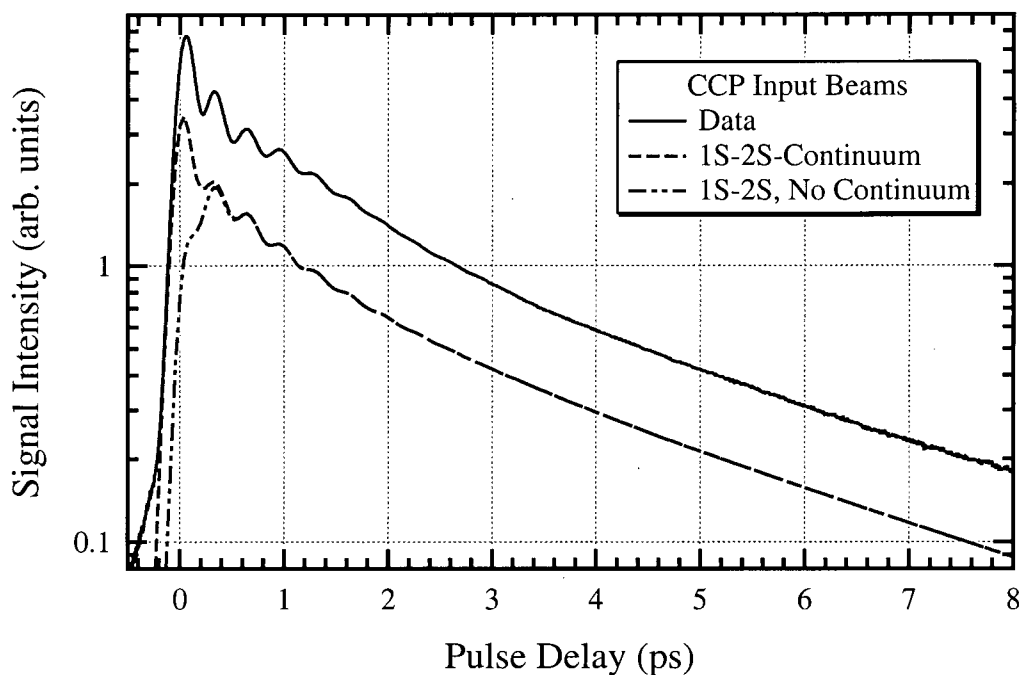
Figure 5.5: Continuum effects on DFWM signals — simulations and experimental data. 122 fs (FWHM) excitation pulses were centered at 1625.8 meV (blue shifted 6 meV above the 1S exciton level for this TI-SI-DFWM signal. The simulations have been divided by a factor of ~2 to distinguish them from the data.

5.2.4 Continuum

The inclusion of the continuum in FWM simulations has been attempted using two approaches: by introducing a finite, closely spaced set of two level systems [29], or by including continuum states in a more theoretically self-consistent manner [41–43, 46]. Similar to this work, both of these methods qualitatively conclude that the continuum states result in a quickly decaying component of the DFWM signal, that exists only for small excitation pulse delays. The first [29], reproduces the general shape of the data, but is not used to attempt to extract information from the FWM spectra. The others [41–43, 46] are theoretical, and do not compare the results to experimental data. Our approach to the inclusion of the continuum, outlined in Chapter 2, allows us to compare the effect of the continuum to those of discrete states in a quantitative and consistent fashion, for both linear and nonlinear data.

The effect of the simulated continuum on the DFWM signal is shown with the corresponding experimental data in Figure 5.5. The dashed line in the figure shows the results of a simulation with two polarization beating 1S-2S-continuum systems, while the dash-dot-dot line shows the results of a simulation with the same values as the first simulation, but no continuum levels. The simulations show that the continuum visibly affects the signal only at short pulse delay times, for about four pulse-widths (0.4 ps), in qualitative agreement with other works [29, 41, 46]. The agreement between the theoretical simulations and experimental data is only possible if we include both the finite pulse duration and all the different terms in $\vec{\chi}^{(3)}$. This allows a direct comparison to be made with the experimental data, unlike the previously mentioned works where only qualitative (or theoretical only) comparisons with experimental data are made.

Excellent accounting for the continuum works well only for blue excitation pulse detunings, where the pulse directly excites some of the continuum. Similar quality fits as shown in Figure 5.5 are obtained for all DFWM spectra obtained at negative (blue) detunings using a unique set of dipole moments for the 1S, 2S, biX and continuum levels. However, for positive (red) detuning, while the dipole moments of the discrete levels could be maintained, the strength of the continuum level had to be reduced for each increment of detuning, in order to avoid "overestimating" the continuum's contribution to the DFWM signal at short times. This effect is summarized in Figure 5.6 where the adjusted dipole moment strength of the continuum is shown as a function of detuning in the case where the power law exponent for the continuum was held constant at 0.065.

This problem is likely related to the particular form that was assumed for the continuum response, as well as its numerical implementation, as was discussed in Section 2.1.2. While convenient, this form probably isn't accurate enough when far off resonance. Several authors report theoretical justification for the inclusion of a cut-off function for large difference frequencies away from the level frequency [66–68]. This would modify the power law response most significantly for low power law exponent values. The approximations used to speed up the numerical simulations could also be responsible, as mentioned in
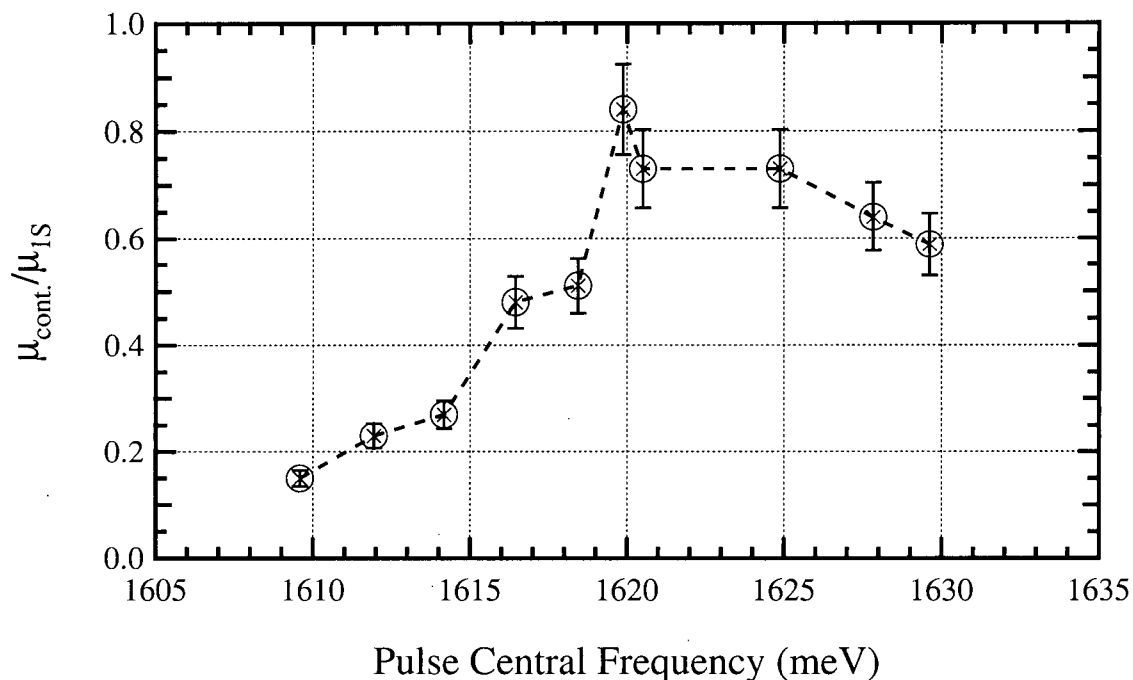
Figure 5.6: Model continuum dipole strength required to fit to data versus input excitation pulse central frequency.

Chapter 2. These would sharpen features, increasing the peak values when off resonance, although numerical testing indicated that this would not account for the entire difference noted while fitting the data. Both of these likely account for some part of the difference in continuum dipole moment strengths as a function of input pulse tuning.

5.2.5 Input Pulse Polarization Dependence

A comparison of data versus simulations with varying input pulse polarization is given in Figure 5.7. This data was spectrally resolved, in an attempt to increase the signal-to-noise ratio, especially for the cross-linearly polarized (XLP) input pulse case. The simulations are also spectrally resolved, at energies 2 meV below those of the data. This is still within the resolution of the instrument ($\sim$2.5 meV) at the settings used to extract this data. The systems simulated included two 1S-2S-biX-continuum systems as has previously been shown for the time- and spectrally-integrated data (with the parameters
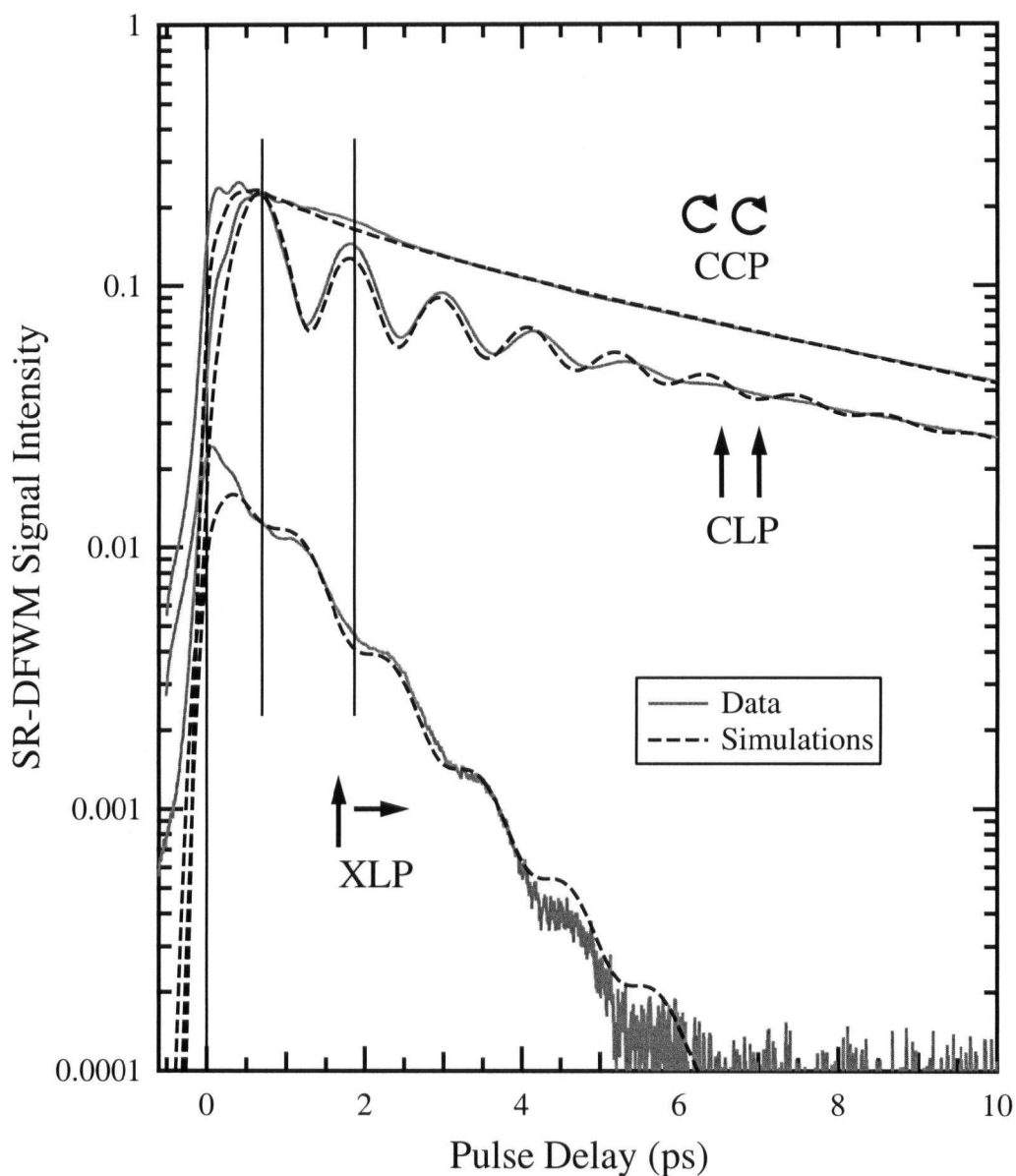
Figure 5.7: Polarization dependence of SR-DFWM signals. The input laser pulses are centered at 1612.9 meV (red shifted 6.9 meV) and the CCP, CLP, & XLP data were spectrally resolved at 1619.8, 1619.8, & 1617.9 meV ($\pm$2.5 meV), respectively. Simulations are spectrally resolved 2 meV below the data values and use the parameters from the input laser pulse detuning data and simulations, as discussed in the text.

listed in Tables 5.2 & 5.3).

The simulations and data have excellent agreement for the three input polarizations. The simulations and data agree with the conclusions drawn in previous works [26, 51, 52] and the theoretical discussions in Chapter 2. In particular, there is a lack of two-exciton (biexciton) beats when the signals are excited with co-circularly polarized (CCP) input pulses and there is a 180° phase change in the beats when going from co-linearly polarized (CLP) input pulses (out-of-phase at zero pulse delay) to cross-linearly polarized (XLP) input pulses (in-phase at zero pulse delay) for the two-exciton states. As in [26], the theoretical model here also indicates that the origin of the beats is from single-exciton/two-exciton states in the CLP input pulse case, and is between two-exciton states (the biexciton and two-free-exciton states here) for the XLP input pulse case.

To fit the data, a transition probability, ν_x, was assumed for the transitions between the 1S exciton and the two-exciton states. The sum of the probabilities for transitions to the free and bound biexciton states is forced to be unity, as in [26]. The dipole moment used in the simulations is then multiplied by this probability. The probability values that were found to work well were the same as was reported in that work: $\nu_{biX} = 0.65$ for the biexciton state and $\nu_{XX} = 0.35$ for the two-free-exciton state. Varying this ratio directly affects only the XLP data beat magnitudes, confirming the origin of the beats in the theoretical treatment, as described above. Unlike [26], however, where the dipole moment of the two-exciton states was assumed to be equal to the one-exciton states, our ratio of $\mu_{2 \text{ exciton}}/\mu_{1S \text{ exciton}}$ was found to be 2.175, likely due to the delta-function pulse simplifications made in theoretical developments in [26], which are not made in our more rigorous approach.

5.2.6 Temperature Dependence

Temperature dependent fits to the dephasing rates usually use semi-empirical formulae designed to reflect the processes that are relevant in the system [2, page 53] [27, 33]. The main mechanism affecting the dephasing rates as a function of temperature is expected

to be coupling to phonon modes, both acoustic and optical. At low temperatures and with excitation energies near the bottom of the conduction band, coupling to acoustic phonon modes is expected to dominate the temperature dependence of the dephasing rates. Accordingly, previous studies have fit the temperature dependence of the dephasing rates with semi-empirical formulae including an exponential optical phonon component that contributes at high temperatures, and either a linear temperature dependence [2, page 53], [33] or an exponential power-law of the form $\exp\{BT^\alpha\}$ [27], to account for the acoustic modes.

Results of fits to co-linearly polarized (CLP) input beam data as a function of temperature are shown in Figure 5.8. Attempts to fit the data using the models from the reference works [2, 27, 33] matched the data poorly, and an equation of the form

$$\Gamma(T) = \Gamma_0 + \Gamma_1\, T^2 + \frac{\Gamma_2}{(\exp\{\hbar\omega_{LO}/k_B T\} - 1)} \tag{5.4}$$

was found to fit the data far better. This was discovered by examining several sets of data under both CCP and CLP input polarizations, all of which exhibited a T^2 dependence in the range 5 K to 40 K. Coefficients of fits to the data in Figure 5.8, indicated by the lines in the figure, are shown in Table 5.4. The large errors associated with the optical LO phonon (Γ_2) fit component are likely due simply to the lack of data at higher temperatures. The LO phonon value, $\hbar\omega_{LO}$, of 35.3 meV was taken from existing literature [49] as with other studies [2, 33].

Two previous studies [2, page 53], [27], used picosecond excitation pulses to examine the temperature dependence and were thus only able to examine the long time decay behaviour of the DFWM signals. The results presented here used $\sim$100 fs excitation pulses, allowing an examination of both the long time 1S exciton decay rates and the more quickly decaying 2S, biexciton, and faster 1S decay rates. Another work [33], using excitation pulses similar to those in this work, assumed a linear (acoustic phonon) T dependence for low temperatures. Above 60 K, an optical phonon component dominated, the term being the same as that used in Equation (5.4) above. Only exciton and biexciton dephasing rates are shown in [33], derived from a simplified model. As well, the thicker
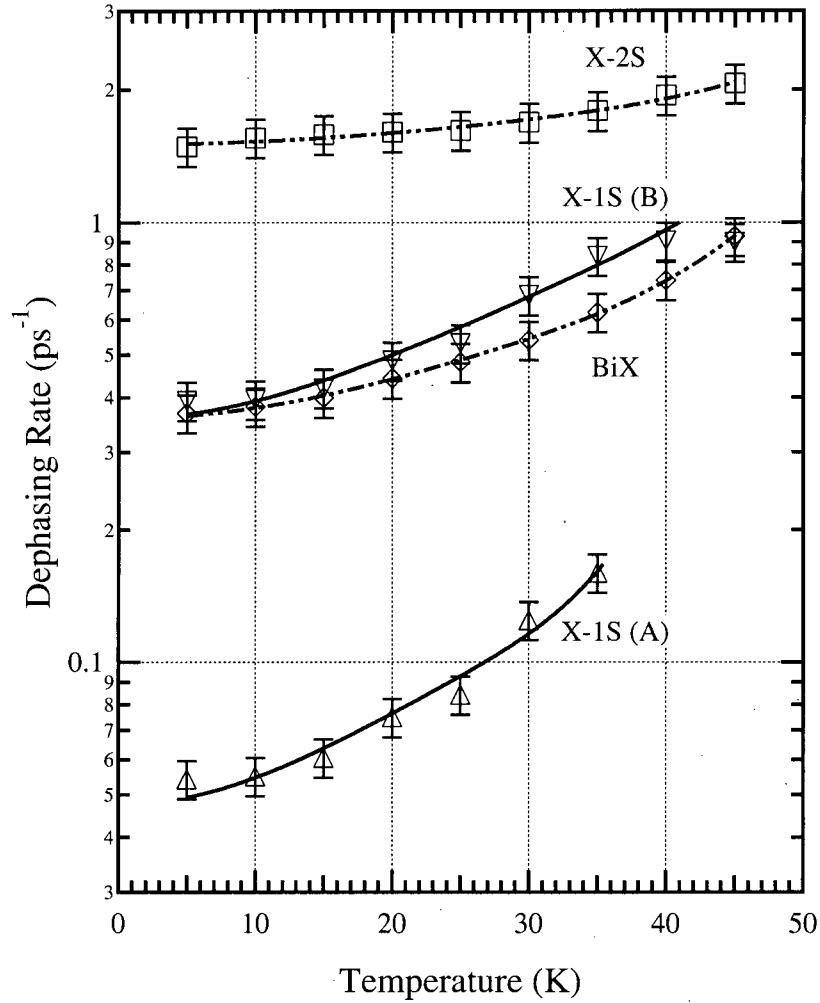
Figure 5.8: Temperature dependence of dephasing rates. The CLP input laser pulses $(\omega_p = (1616.9 \pm 0.1)\,\text{meV}$ and $\sigma_{FWHM} = (89.5 \pm 0.2)\,\text{fs})$ are centered $3\,\text{meV}$ below the low temperature $(4\,\text{K})$ heavy hole absorption peak.

	Γ_0 (ps^{-1})	Γ_1 ($\times 10^{-4}\,\text{ps}^{-1}\,\text{K}^{-2}$)	Γ_2 (ps^{-1})
X - 1S (A)	(0.0474 ± 0.005)	(0.7 ± 0.1)	(3000 ± 2000)
X - 1S (B)	(0.36 ± 0.07)	(4 ± 1)	(1000 ± 2000)
X - 2S	(1.51 ± 0.02)	(2.3 ± 0.3)	(1100 ± 500)
biX	(0.359 ± 0.003)	(2.03 ± 0.04)	(1600 ± 80)

Table 5.4: Dephasing rate temperature fit coefficients corresponding to Equation (5.4) and the data in Figure 5.8.

quantum wells (25 nm) in [33] would not have the stronger localization effects expected to be seen in the narrow (5 nm) wells used in this work. In contrast with these previous works, the results here indicate that **all** of the visible beat components decay with a T^2 dependence over the 5-40 K temperature range. This could indicate that the theoretical mechanism behind the temperature dependence may need re-examination and that the results may be more sample dependent than was previously thought, especially for thinner quantum well samples where localization effects are important.

Since all the temperature studies were conducted with the laser pulse red-shifted at low temperature (5 K), the levels will shift through the laser center frequency as the temperature rises, due to the band gap shifting to lower energies as a function of increasing temperature. For the data shown in Figure 4.10 and the extracted dephasing rates shown in Figure 5.8, the pulse detuning becomes zero at 60 K. The dephasing rate of all except the 1S (A) exciton state are insensitive to pulse detuning through the exciton resonance energy (Figure 5.4) and so the shift in resonance frequency with temperature should not affect the results for these levels. The dominance of the T^2 term for all the levels, including the 1S (A) exciton level, over the temperature range in Figure 5.4 indicates that a similar mechanism is affecting the temperature dependence of all the levels, although correcting for the pulse detuning could affect the absolute value of the 1S (A) state.

The biexciton beat magnitudes become too weak to measure around 50 K, while the signals from the 1S-2S beating are observed up to 120 K. At higher temperatures, the blue-shifted laser pulses and the resultant decrease of signal strength into the noise level distort the results and prevent extraction of accurate values for the dephasing rates. This prevents a more rigorous analysis of the temperature dependence of the decay rates of the DFWM signals with the existing data. To concretely show that the temperature dependence of the dephasing rate is not affected by pulse detuning would require additional study of the dephasing rate as a function of both temperature and pulse detuning, a problem with data reported in the existing literature [2, 27, 33] as well.

5.3 Experimental Results and Simulations - Doped Samples

As discussed in Chapter 4, the dominant absorption mechanism in the doped multiple quantum well samples is expected to be from charged excitons, or trions. With the excess electrons in the wells, the charged excitons in the samples studied would consist of two electrons and one hole. However, previous studies of linear absorption in these samples did not find clear experimental evidence of the presence of trions in the doped samples to confirm the theoretical predictions [4–6]. DFWM experiments were thus used to probe a sample with a low concentration of excess electrons, looking for further evidence of the existence of trions.

5.3.1 2.5×10^{10} cm^{-2} Sample

The multiple quantum well sample with the lowest doping has an electron concentration of 2.5×10^{10} cm^{-2} in the wells, with a corresponding 2-D (T $= 0$ K) Fermi energy of 0.92 meV. The low temperature linear absorption for this sample is shown in Figure 5.9, with the corresponding fit parameters in Table 5.5.

The most striking difference between the linear absorption in this sample and the undoped sample is the lack of a sharp excited (2S) exciton-continuum transition above the heavy hole peak. The heavy hole peak itself is asymmetrically broadened at higher energies, blending smoothly into the continuum.

The fit to the linear absorption data indicated that the heavy hole peak consists of two peaks ~ 2.7 meV apart with the lower peak at 1619.8 meV. For the linear absorption data two polarization beating single-particle–continuum systems were modelled, along with light-hole single-particle and continuum levels. No excited single-particle state was included as there were no beats similar to the 1S-2S exciton beats, that were present in the undoped sample, visible in either the CLP or CCP data of this doped sample. The energy levels in these fits are similar to those determined for the undoped sample, as is the separation of the two polarization beating systems. The power law exponent for the two single-particle, heavy-hole levels was found to be (0.775 ± 0.003), showing a
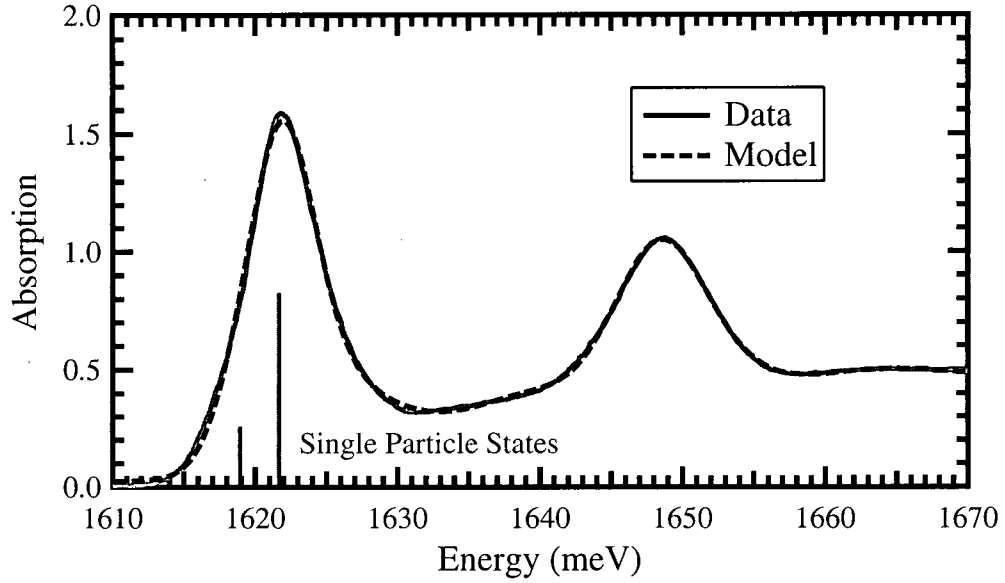
Figure 5.9: Linear Absorption for $2.5 \times 10^{10}\,\text{cm}^{-2}$ sample at $4\,\text{K}$ - simulations and data. The system parameters used are listed in Table 5.5.

	ΔE_{io} (meV)	μ_i/μ_j	Γ_i (ps^{-1})	α_i	$\Gamma_{i,\text{inh}}$ (meV)
X_{single} (A)	$1618.9 \pm 0.1^{\dagger}$	$0.0037^{\dagger}$	0.258	0.775 ± 0.003	
X_{single} (B)	2.76 ± 0.02	1.81 ± 0.06	0.34	0.775 ± 0.003	$4.62 \pm 0.02^{\S}$
Continuum	15.2 ± 0.2	0.55 ± 0.04	2.5	0.09 ± 0.02	
$XX_{\text{double}}^{\P}$	4.0	1.41	0.55	0.775 ± 0.003	
X_{single} (lh)	29.21 ± 0.06	1.62 ± 0.04	0.426	0.867 ± 0.005	$7.06 \pm 0.06^{\S}$
Cont. (lh)	$12.9 \pm 0.3^{\ddagger}$	$0.45 \pm 0.02^{\ddagger}$	2.5	0.17 ± 0.02	

Table 5.5: Linear absorption fit parameters for the lowest doped sample, corresponding to the fit and data shown in Figure 5.9. Errors are 1 in the last digit unless otherwise noted. The system consists of two polarization-beating single-particle–continuum systems, 2.76 meV apart. A single-particle–continuum light hole (lh) system assists with fitting the data around the heavy hole continuum levels.

$\dagger$ As other values are relative to the X_{single} (A) values, these are absolute values.

$\ddagger$ These values are relative to the X_{single} light hole energy and dipole strength.

$\S$ The inhomogeneous broadening is set constant for all (X_{single}, X_{double}, continuum) levels within each system.

$\P$ Two-particle states are not included in the linear simulations.

significant decrease from the undoped sample value (0.965). The relative dipole moment strength of the two systems has changed as well, with the lower polarization beating system now having a smaller strength than the upper system (opposite to the undoped case).

DFWM simulations and data for this sample are shown in Figure 5.10. There is clear evidence of the existence of a two-exciton state in the DFWM signals, with the CLP input polarization case having strong, 180° out-of-phase beats visible, which disappear with CCP input pulse excitation. There is no evidence of excited state beats in either the CLP or CCP input polarization signals, in agreement with other studies in doped samples [16]. The continuum state still affects the signal at short times (visible as a bump at short times in the CCP data and a slight kink in the CLP data), even with the lower power law exponent. Using the same set of parameters for the CLP and CCP TI-DFWM simulations resulted in a reasonable fit at longer times, but a poorer fit close to zero pulse delay.

Since it isn't available from fits to the linear absorption data, the power law of the two-particle state that causes the CLP beat signal must be determined from the DFWM data. The fits turn out not to be particularly sensitive to this parameter. While the best fit is obtained for a two-particle state power law of ~ 0.7, values up to unity do not drastically degrade the fit, although power law values outside the 0.7-0.8 range peak closer to zero pulse delay than the data.

The longest dephasing rates in this sample are 3-5 times faster than in the undoped sample. This might be expected given that the excess free carriers will contribute to the overall dephasing of the induced polarization. In contrast, the dephasing rate for the two-exciton state is only about 1.5× greater than that for the biexcitons in the undoped sample. The beat energy found for the two-particle state was 4.0 meV, ~ 0.5 meV larger than that determined from the undoped sample, biexciton beats.

The evidence for the existence of trion particles [16,17,60,61] in these n-doped samples indicates that the beats visible in the CLP data are from a five-particle, charged biexciton
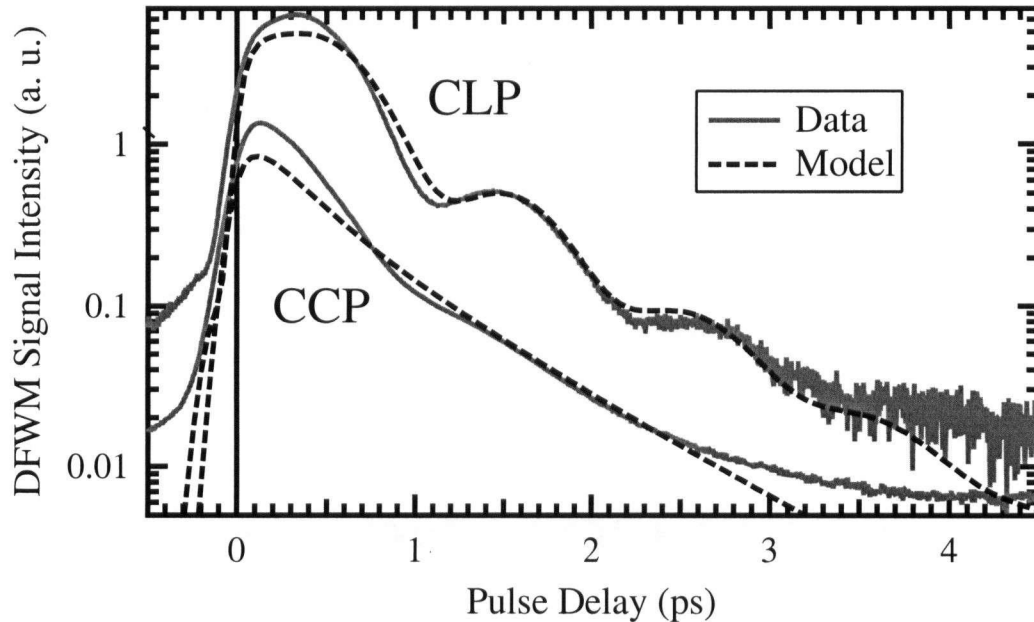
Figure 5.10: DFWM signal and simulation for $2.5 \times 10^{10} \, \text{cm}^{-2}$ sample at 6.4 K. The laser input pulse frequency is centered at 1619.8 meV and has a FWHM of 106.5 fs. The system parameters used for the simulation are listed in Table 5.5.

state. Similar to the biexciton case, where it is energetically more favourable for the two excitons to bind into a four-particle state, the system here corresponds to the interaction of a negatively charged trion with an neutral 1S exciton. Although theoretical evidence for this state is unclear at this point [62, 63], none of these studies have included the in-plane localization known to lead to a dramatic increase in biexciton binding energies in narrow quantum wells [17], which would be expected to have a similar effect on a charged biexciton state.

In principle, it might be the case that an unbound, "resonant", negatively charged biexciton state might have sufficient oscillator strength to cause beats in the FWM experiment. A simulation of this scenario would involve making the negatively charged biexciton binding energy -3.3 meV, instead of $+3.3$ meV as was used in the simulation of Figure 5.10. In order to retain the strong beats, the oscillator strength would have to increase and the power law exponent would have to be closer to unity. Both of these

changes seem to be in the wrong direction if one assumes a resonant unbound state instead of a bound state. We therefore believe that the FWM data and analysis favours a bound state interpretation.

5.3.2 20×10^{10} cm^{-2} Sample

The multiple quantum well sample with the largest doping was also studied with the DFWM technique. Its well doping, 20×10^{10} cm^{-2}, corresponds to a Fermi energy (at 0 K) of 7.4 meV. A fit to the linear absorption data is shown in Figure 5.11, with the corresponding fit parameters in Table 5.6. The small power law exponent and large inhomogeneous broadening means that the dephasing time does not significantly affect either the linear absorption or DFWM signals, and cannot be as accurately extracted from the data as it could from the undoped and low-doped samples.

The simulation of the TI-DFWM data, shown in Figure 5.12, indicated that the model system, when the laser pulses are tuned around the linear absorption peak, are described well by a single level with a power law exponent value of 0.33. Both the linear absorption and DFWM data fit very well to the data with this model system. The light-hole peak added to the linear absorption is lacking from the DFWM fits as the laser pulse does not significantly excite these higher energy states. An additional continuum was found not to be necessary in these higher doped samples, due to the small power law exponent. As well, the TI-DFWM model fit more poorly to the data with an added continuum, with the simulation resembling the input excitation pulse autocorrelation (shown in the figure as a dash-dot line).

As was mentioned in Section 4.3.2 (page 115), study of the highest doped sample was partly motivated by a DFWM study of a sample with similar 2-D doping density, excitation pulse conditions, but in 8 nm wide quantum wells [37, 38]. That study argued that the dephasing rate, due to electron-electron scattering, decreased in doped samples when the excitation pulses were tuned near the Fermi energy. Study of the samples in this work show no evidence of the decrease in dephasing rate when the pulse is tuned
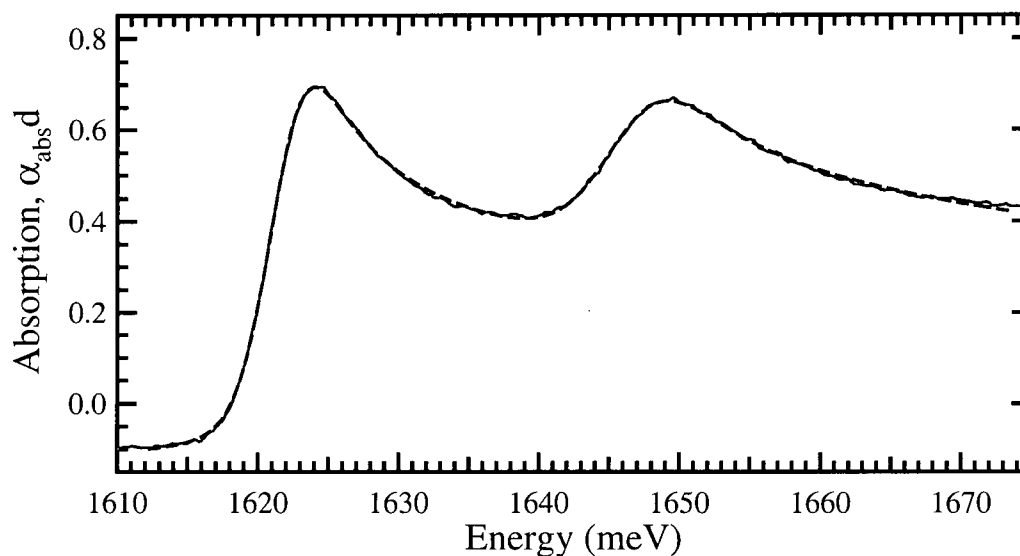
Figure 5.11: Linear Absorption for $20 \times 10^{10}\,\mathrm{cm}^{-2}$ sample at $4\,\mathrm{K}$ - simulations and data. The system parameters used for the simulation are listed in Table 5.6.

	ΔE_{io} (meV)	μ_i/μ_j	Γ_i (ps^{-1})	α_i	$\Gamma_{i,\,\mathrm{inh}}$ (meV)
X_{single}	$1621.6 \pm 0.1^\dagger$	$0.00537^\dagger$	1.24	0.325	4.04 ± 0.03
X_{single} (lh)	24.80 ± 0.03	0.704 ± 0.002	2.14 ± 0.03	0.394 ± 0.002	1.52 ± 0.01

Table 5.6: Linear absorption fit parameters for $20 \times 10^{10}\,\mathrm{cm}^{-2}$ sample, corresponding to the fit and data shown in Figure 5.11. Errors are 1 in the last digit unless otherwise noted. The system consists of two single-particle states, a heavy hole (hh) level and light hole (lh) level.

---

† As other energies and dipole strengths are relative to the X_{single} value, these are absolute values.
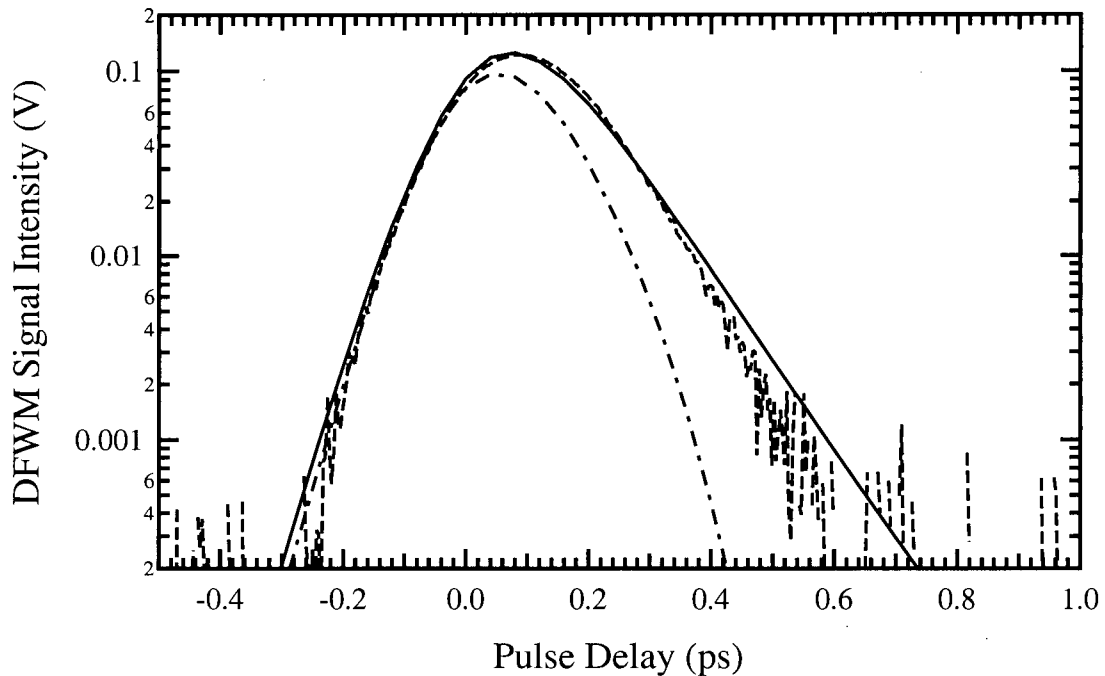
Figure 5.12: TI-DFWM signal and simulation for $20 \times 10^{10} \, \text{cm}^{-2}$ sample at 5.8 K. The laser input pulse frequency is centered at 1629.4 meV and has a FWHM of 129.5 fs. The system consists of one single-particle heavy hole state, with the parameters taken from Table 5.6, and the simulated laser pulse detuned 5 meV above the state's energy level.

through the Fermi energy. The small power law exponent means that one is effectively exciting a continuum of states in this highly doped sample, which leads to only a single, fast decay in the DFWM signal. Further, extracting a dephasing rate from this type of data is difficult, if not impossible, and will at best lead to inaccurate results if a simple exponential decay model is assumed. For this reason, it is concluded that the results reported in the previous work [37, 38] should be considered erroneous, unless experimental evidence can be found to substantiate their results.

5.4 Comparison with Previous Power Law Exponent Results

The results of the earlier work on extracting the power law exponent from linear absorption data are shown in Figure 5.13. The data was extracted from Figure 4 of Brown, et. al. [5], which is based on fits to the linear absorption from a series of doped and un-
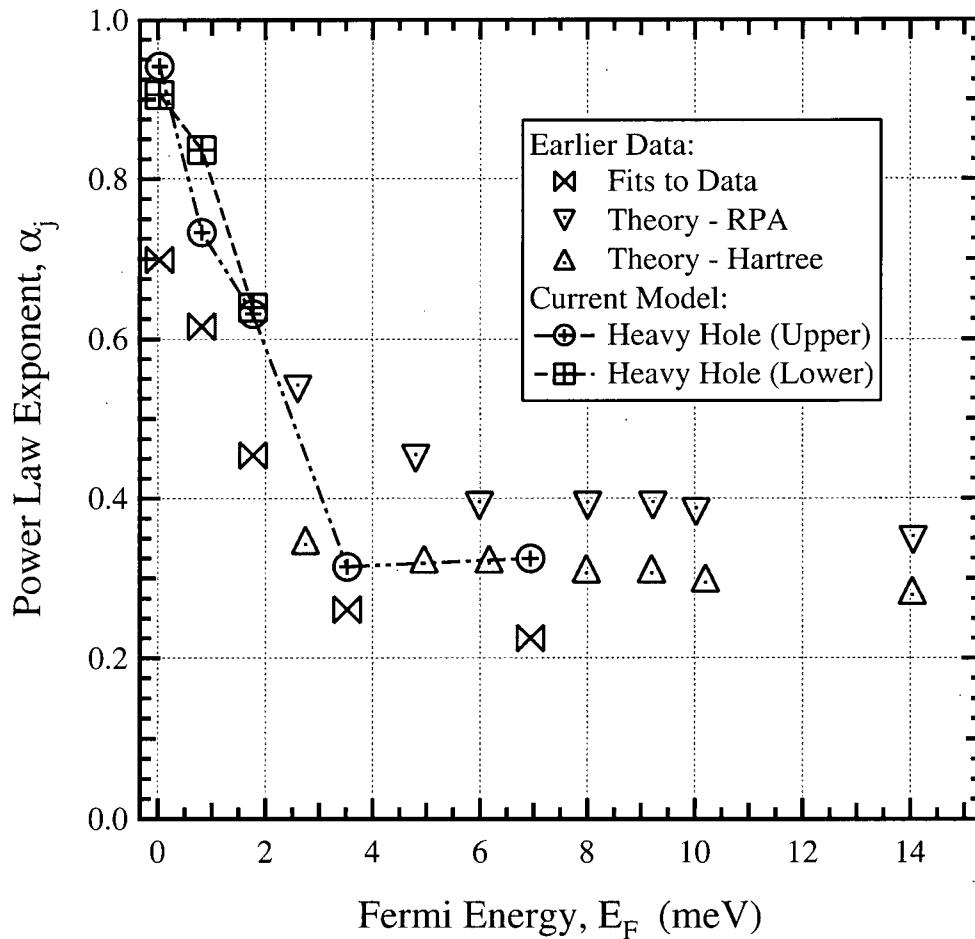
Figure 5.13: Comparison of current power law exponents to previous data. The data has been extracted from Brown, et. al. (PRB **54**, p.11082) [5]. The sideways hourglass is from fits to the heavy-hole exciton peak while the diamonds are theoretical predictions. The downward pointing triangles are from a RPA model, while the upward pointing triangles correspond to a more rigorous Hartree model. Fits to the heavy hole peak from this work are shown by the squares and circles.

doped samples. The results shown here are based on more thorough fits to the same linear absorption data as was used in that work. These fits use the more rigorous linear absorption portion of the theoretical model outlined in Chapter 2, which also benefited from cross-referencing the linear absorption data with the DFWM data.

Qualitatively the power law exponents show the same behaviour, with a large initial drop in the power law exponent at low doping density and a levelling out at a power law exponent around 0.3 at higher densities. The theoretical models [5, 53] are unfortunately not able to model the lower excess electron doping densities with corresponding Fermi energies below 2 meV, to provide a comparison to the values extracted from the experimental data.

At higher densities, the fits to the linear absorption data agree well with the theoretical predictions provided by the Hartree model, which is the more accurate of the two models reported in [4, 5]. This model predicts that the linear absorption peak is dominated by absorption around the negatively charged exciton with the contribution of the neutral exciton being very small by comparison, predicting that the results we observe from the doped samples should be predominantly from trions and not the 1S exciton state.

Chapter 6

Conclusions & Recommendations for Future Work

This thesis has reported a systematic study of the linear and nonlinear, near-band edge optical properties of undoped and doped multiple quantum well samples. These studies aimed to separate the numerous contributions to the material response from photon excitation, quantifying these responses. After summarizing the findings of these studies, some recommendations for future experiments, theoretical developments, and numerical analysis will be given.

6.1 Conclusions

In order to quantify these material responses to the optical excitation in the undoped and doped samples, and to include the continuum in a consistent manner, theoretical extensions to the standard Lorentzian susceptibility expressions were made. These involved incorporating the power law exponent from Fermi-edge singularity theory in a manner that allowed the same theoretical development to be used for both the linear and nonlinear susceptibilities and polarizations. Elaborate numerical routines were developed to numerically simulate these theoretical models, including the pulse shape and central frequency which are measured experimentally. These allowed quantitative information to be extracted from both linear absorption experiments and nonlinear, third-order, degenerate four-wave-mixing experiments, by simultaneously fitting the linear and nonlinear simulations to the data.

Experimentally, equipment and a data acquisition system were developed to allow the

acquisition of spectrally-integrated and spectrally-resolved degenerate four-wave-mixing signals over a wide range of temperatures and input pulse excitation conditions.

6.1.1 Undoped Sample

Study of the undoped sample and comparison to the theoretical model predictions allowed several quantitative measures to be extracted from the nonlinear experimental data. For the first time (to our knowledge) accurate measurements of the 1S-2S exciton binding energy (12.75 meV), 2S exciton dephasing rate ($\sim 1.8\,\mathrm{ps}^{-1}$ at low temperature), and oscillator strength ($\mu_{2S}/\mu_{1S(A)} = 0.48$) were extracted from the data. 1S-2S beat signals were measured over a wide range of temperatures and input pulse excitation energies, and were visible in data up to 120 K. Measures of the dephasing rates of the 1S exciton levels were also extracted over the same range of temperatures and pulse excitation energies. Evidence for a second, faster decaying 1S level was found during fits to the experimental data, ~ 2.5 meV in energy above the lower 1S level, likely originating from areas of the sample where excitons are less localized. Its dephasing properties were found to be similar to that of the biexciton levels: $\sim 0.3\,\mathrm{ps}^{-1}$ in contrast to the lower 1S level's dephasing rate of $\sim 0.05\,\mathrm{ps}^{-1}$ at low temperature. The oscillator strength ratio was found to be 0.75 times that of the upper 1S exciton state. The results of temperature studies indicate that the dephasing rates of all the levels follow a T^2 dependence in the temperature range 5 K to 40 K, in contrast to data reported elsewhere [2,27], where linear or exponential dependencies on temperature were reported.

Signals from biexcitons (two-bound excitons) were also observed in the data. The biexciton binding energy (3.5 meV), dephasing rates ($\sim 0.3\,\mathrm{ps}^{-1}$), and oscillator strength ($\mu_{biX}/\mu_{1S(A)} = 1.4$) were extracted from the data. These parameters were measured over the same range of pulse detunings and temperatures, to our knowledge for the first time. The biexcitons beat signals also showed a T^2 temperature dependence over the range of 5 to 40 K, the same as that of the 1S and 2S excitons. By comparison with theories reported in the literature [17,26] in-plane localization effects in 5 nm GaAs quantum wells

have a significant influence on the biexciton binding energy, doubling the values expected from quantum wells with an assumption of no in-plane localization.

The first systematic attempt to quantitatively account for the continuum contribution to the nonlinear response was conducted. A series of spectra obtained at various input laser pulse detunings was fit and the continuum was found to have a small power law exponent ($\sim$0.06). It contributes to the DFWM signals at short time delays only, within 3-4 pulsewidths of zero pulse delay, and was found to be insensitive to the magnitude of the dephasing rate of the continuum level. Further theoretical developments were found to be needed to more accurately simulate nonlinear response of the continuum in the DFWM signals, most importantly the magnitude of the oscillator strength as excitation pulse is red-shifted. Some suggestions for further work are given below. The current studies show that the inclusion of the continuum is an important part of accurate, realistic simulations of degenerate four-wave mixing signals, especially at short input pulse delay times.

6.1.2 Doped Samples

In the lightly doped sample, with a 2-D electron doping density of $2.5 \times 10^{10}\,\mathrm{cm}^{-2}$, evidence of coherent beating between one-exciton and two-exciton complexes was found in the signals. A continuum level was still found to be a necessary component in the theoretical model even though, with a power law exponent of 0.775, the linear absorption data showed no clear absorption edge as was evident in the undoped case. Due to the presence of excess electrons in these wells, the dominant response is from bound, charged exciton states, or trions [4–6, 16, 17, 60, 61]. No evidence of 1S-2S beating was found in this sample, again in agreement with another study of excited excitonic states done in a similar sample [16], where only excited trion states were found. With the response attributed to trions, the observed two-exciton complexes present the first experimental evidence for negatively-charged biexciton states in lightly doped quantum wells.

For the highest doped sample, with a 2-D electron doping density of $20 \times 10^{10}\,\mathrm{cm}^{-2}$,

only a single, fast transition was observed in the DFWM signals, over a wide variety of input pulse excitation conditions. A power law exponent of 0.33 was found for this sample, indicating that highly doped samples are exciting a continuum of states, with no separate, distinct continuum level present in addition to that of the peak that has evolved from the undoped sample's exciton peak. The excitation of a continuum of states in this sample, leads to a single, fast decay in the DFWM signal that does not change with input pulse detuning. Reevaluating the results from a previous study [37], which reported that the dephasing rate decreased in these highly doped samples when the excitation pulses are tuned through the Fermi energy, we conclude that these results must be considered erroneous without the presence of more experimental evidence.

A comparison of the power law exponents to previous work [4-6], indicated that the higher doped samples fit well to the exponents predicted by the more accurate Hartree models used in that work, where negatively charged excitonic complexes were predicted to be the dominant mechanism behind the linear absorption spectra.

6.2 Recommendations for Future Work

This section contains several suggestions for directions in which this work could be extended, from theoretical and experimental techniques to areas where improvements in equipment and analysis techniques could be achieved.

6.2.1 Experimental

6.2.1.1 Experiments/Experimental Techniques

Suggestions for further experiments and the implementation of other experimental techniques are:

- The time-resolved DFWM technique could potentially give information that would compliment the time-integrated and spectrally-resolved data used in this work, such as additional confirmation that the beats are originating from photon echoes [64]. Time-resolved photoluminescence could also be used on these samples to obtain information about the population decay times of particles in the quantum wells.

- For the undoped wells, more experiments looking at the DFWM signals as a function of temperature, while simultaneously tuning the pulse central frequency to match the shift in bandgap with temperature, would give a more concrete understanding of the temperature dependence of the DFWM signals and help confirm the current experimental data's results.

- For the doped samples, attempting to examine the remaining doped samples could potentially assist with the question of the origin of the beat signals in the doped samples, which were expected to be predominantly from charged excitons. Studying the temperature dependence of these samples might also be able to assist with this process, although better signal-to-noise ratios would be needed for more details to be extracted from these signals.

- Better coupling of signals through the monochromator would allow better resolution to be achieved with SR-FWM signals, with both fixed and variable pulse delays, allowing more detailed analysis to be conducted with the SR-FWM signals.

6.2.1.2 Equipment - Hardware and Associated Control Software

Several improvements to the equipment and associated control software would make the acquisition of the nonlinear signals easier and faster. These are:

- Reflective optics for input beam focussing could eliminate chromatic aberrations inherent in the input focussing lenses. This would require re-designing the beam input area, to retain the combinations of beam rotation and conversion from circular to linear polarization that is a part of the current system.

- Automate the background measurement (fixed delay arm) by the addition of a linear translation stage to replace the micrometer. This could allow the background subtraction/signal acquisition to take place automatically, adding repeatability to the process. It could also allow the fixed pulse delay data to be acquired in an automatic fashion. Both of these would also require small modification of the LabView control software.

- Incorporate the time-resolved (TR) equipment, currently used for time-resolved photoluminescence experiments into experimental DFWM setup.

- Re-design output stages of the experimental setup to allow for easy switching between TR-DFWM, TI-DFWM, TR-PL, and TI-PL, without dismantling portions of the experimental setup.

- Having a computer controllable heating element switch would allow for automated temperature control of experiments, so that automated acquisition of temperature dependent DFWM signals could be accomplished.

- The current analog-to-digital board limits both the signal resolution and time resolution and a board with higher resolution and faster acquisition speed would improve both of these.

- A 2-4X increase in computer speed (adding more RAM would likely also speed data acquisition, but probably less than a factor of 2) would allow data acquisition close to the oscillation rate of the shaker ($\sim$19 Hz) instead of the 3-4 Hz that now occurs. Acquisition of signals with poor signal-to-noise, especially important for doped samples, typically requires 1-10 thousand signal averages. This currently takes 5-50 minutes; at 19 Hz this time would be reduced to 0.9-4.4 minutes. If fast enough, the computer may also allow double-sided signals to be decoded (both forward and backward motion of the shaker), potentially allowing for another factor of two improvement in acquisition time. The LabView program could also be revisited to see if improvements could be made to the acquisition program.

6.2.2 Theoretical

As outlined in the discussions in Chapter 5, the continuum limit still presents a challenge to the current theoretical development. A more complete theoretical development would be preferable to more accurately simulate the data, but in the absence of this it has been noted by several authors [66–68] that non-Markovian (i.e., non-exponential decay) extensions to the Lorentzian ($\alpha = 1$) limit are justified. Although [66–68] take frequency and time domain approaches, they essentially both extend the theory to multiply the frequency response with a Gaussian lineshape. This would improve the behaviour in our case by eliminating the semi-infinite extent of the susceptibility as the power law exponent for the continuum approaches zero. The inclusion of propagation effects in the third order polarization terms (to include reflections and linear absorption as these signals propagate through the quantum wells) would also be useful to evaluate the strength of the effects, especially in the case of doped quantum wells.

Other theoretical extensions that would be useful would be if theoretical calculations of binding energies of charged excitons (three- and five-particle states) [62, 63] could be extended to include localization effects as a function of well width, to compare to experimental data. This has been attempted theoretically for biexcitons and charged excitons, and led to the conclusion that increases in the binding energy of about 50%

occurred [16, 17], but has not, to our knowledge, been attempted so far for five-particle charged exciton states.

6.2.2.1 Analysis/Numerical

With a theoretical model that uses a consistent approach to study linear and nonlinear experimental data, the ultimate goal of the numerical analysis would be to simultaneously fit all the data. To accomplish this, the theoretical models need to be numerically evaluated quickly enough to allow automatic parameter estimation routines to be computer evaluated. For the current DFWM simulations, which take up to 6 hours to run on a 400 MHz Pentium II computer, this means that speed improvements of about 5 orders of magnitude are necessary.

To attain such speed improvements, two approaches may be taken. Several authors have outlined an approach to convolution integrals that separates out the integral into a matrix calculation [69–72] of predetermined coefficients. If these methods could be extended to the case of evaluating singular, oscillatory integrals, this should allow for dramatic speed improvements. This is because it would remove the necessity of evaluating the large number of coefficients (called $b_k(\theta)$ in Appendix A) that currently need to be continuously recalculated in the convolution integrals. Further refinements to the evaluation of these coefficients could also result in noticeable improvements in execution time. The second approach would involve finding and evaluating partial or fully analytic solutions to the third order polarization, similar to that accomplished for the first order linear absorption (involving parabolic cylinder functions). The non-Markovian theoretical extensions mentioned in the beginning of this section should greatly assist with this task.

In either case, routines would also need to be developed to handle the "global", nonlinear parameter estimation needed to simultaneously fit the linear and nonlinear data. This, however, is a relatively straightforward extension of current nonlinear parameter estimation techniques [73, 74].

List of Abbreviations

1-D	1-Dimensional
2-D	2-Dimensional
3-D	3-Dimensional
A/D	Analog to Digital
AlAs	Aluminum Arsenide
AlGaAs	Aluminum Gallium Arsenide
CCP	Co-Circularly Polarized
CLP	Co-Linearly Polarized
CW	Continuous Wave
DFWM	Degenerate Four Wave Mixing
FWHM	Full Width at Half Maximum
FWM	Four Wave Mixing
GaAs	Gallium Arsenide
He	Helium (Gas)
HF	Hydrofluoric Acid
hh	Heavy-Hole
lh	Light-Hole
LHe	Liquid Helium
LiO_3	Lithium Iodate
LN	Liquid Nitrogen
LVDT	Linear Variable Differential Transducer
MBE	Molecular Beam Epitaxy
MQW	Multiple Quantum Well(s)
N_2	Nitrogen (Gas)
NRC	National Research Council of Canada
QW	Quantum Well(s)
SHG	Second-Harmonic Generation
Si	Silicon
SR-(DFWM)	Spectrally Resolved-(DFWM)
TI-SI-(DFWM)	Time & Spectrally Integrated-(DFWM)
TR-(DFWM)	Time Resolved-(DFWM)
UV	Ultra-Violet
XLP	Cross-Linearly Polarized (i.e., orthogonally polarized)

List of Symbols

$\overleftrightarrow{\chi}^{(n)}$	nth order Susceptibility.
Γ_{ij}	Dephasing Rate between the ith & jth levels.
Γ^{inh},i	Inhomogeneous Broadening parameter
λ,λ_{ij}	Inhomogeneous Broadening Correlation Parameters
$\mathcal{FT}\left[f(t)\,;t\,;\omega\right]$, or $\mathcal{FT}$	Fourier Transform: $\dfrac{1}{\sqrt{2\pi}}\int\limits_{-\infty}^{+\infty}dt\,f(t)\,e^{i\omega t}$
$\mathcal{FT}\left[\overline{f(t)}\,;t\,;\omega\right]$	$\overline{F(-\omega)}$ (Overbar indicates complex conjugate)
$\mathcal{FT}^{-1}\left[F(\omega)\,;\omega\,;t\right]$, or $\mathcal{FT}^{-1}$	Inverse Fourier Transform: $\dfrac{1}{\sqrt{2\pi}}\int\limits_{-\infty}^{+\infty}d\omega\,F(\omega)\,e^{-i\omega t}$
$f\circledast g\,(\tau)=g\circledast f\,(\tau)$	Convolution (Fourier): $\dfrac{1}{\sqrt{2\pi}}\int\limits_{-\infty}^{+\infty}dt\,f(t)g(\tau-t)$ $\mathcal{FT}\left[f\circledast g\,(\tau)\,;\tau\,;\omega\right]=F(\omega)\,G(\omega)$
$f\circledast g\,(\tau)$	Correlation (Fourier): $\dfrac{1}{\sqrt{2\pi}}\int\limits_{-\infty}^{+\infty}dt\,f(t)g(\tau+t)$ $=\dfrac{1}{\sqrt{2\pi}}\int\limits_{-\infty}^{+\infty}dt\,f(t)g(t-\tau)$
$\sigma_+=\dfrac{\hat{x}+i\hat{y}}{2}$ $\sigma_-=\dfrac{\hat{x}-i\hat{y}}{2}$ $\sigma_i^*\cdot\sigma_j=\begin{cases}1 & i=j\\ 0 & i\neq j\end{cases}$	**Circular Polarization:** Right ($\circlearrowright$) Left ($\circlearrowleft$) Normalization condition Related Symbols & Acronyms: CLP $\quad\uparrow\uparrow\quad$ Co-Linear Polarization XLP $\quad\uparrow\rightarrow\quad$ Cross-Circular Polarization CCP $\quad\circlearrowright\circlearrowright\quad$ Co-Circular Polarization XCP $\quad\circlearrowright\circlearrowleft\quad$ Cross-Circular Polarization

$\mathbf{H}\left(t\right)$	The Heaviside Step Function, $\mathbf{H}\left(t\right) = \begin{cases} 1, & t > 0 \\ \frac{1}{2}, & t = 0 \\ 0, & t < 0 \end{cases}$
$D_\nu\left(z\right)$	Parabolic Cylinder Function
$\left\|z\right\|$	Absolute value $\left(\sqrt{z\overline{z}}\right)$
$\left\|t\right\|$	Vector norm $\left(\sqrt{\overrightarrow{\overline{\mathbf{z}}}\cdot\overrightarrow{\mathbf{z}}}\right)$
$\Upsilon\left(z\right)$	General factorial function. For integers, $\Upsilon\left(n+1\right) = n!$ (See also footnote on page 23.)
$\mathbb{R}e,\ \mathbb{R}e\left\{z\right\}$	Real Part of a Complex Number
$\mathbb{I}m,\ \mathbb{I}m\left\{z\right\}$	Imaginary Part of a Complex Number
$\delta\left(t-\tau\right)$	Delta-function
$\delta\left(\omega-\omega_\Sigma\right)$	One definition: $\dfrac{1}{2\pi}\displaystyle\int\limits_{-\infty}^{+\infty} dt\ e^{i\left(\omega-\omega_\Sigma\right)t}$
$\mathcal{L},\ \mathcal{L}\left[f(t)\,;t\,;s\right]$	Laplace Transform
$\mathcal{L}^{-1},\ \mathcal{L}^{-1}\left[F(s)\,;s\,;t\right]$	Inverse Laplace Transform

List of Fundamental Constants

The following is a list of fundamental constants in units appropriate to this work. For an exhaustive list and description of the current recommended values of fundamental constants see reference [75].

c	299 792 458 m·s^{-1} (exact)
	299.792 458 μm·ps^{-1}
e	1.602 176 46 $\times 10^{-19}$ C
h	6.626 0755 $\times 10^{-34}$ J·s
	4.1361 meV·ps
$\hbar = h/2\pi$	1.054 572 66 $\times 10^{-34}$ J·s
	0.658 28 meV·ps
$1/\hbar$	1.5191 ps·meV
1 wavenumber (cm^{-1})	0.123 996 6 meV
(c$\tilde{k}= c/\lambda$)	29.979 245 8 GHz
hc	1 239 966 meV·nm
	0.123 996 6 meV·cm
$1/(\hbar \cdot$ c) (for $\omega/$c)	50.672 07 meV^{-1}· cm^{-1}

Bibliography

[1] Claus F. Klingshirn. Semiconductor Optics. Springer-Verlag, New York, NY, USA, 1995. ISBN 3-540-58312-2.

[2] Jagdeep Shah. Ultrafast Spectroscopy of Semiconductors and Semiconductor Nanostructures. Springer Series in Solid State Sciences 115. Springer-Verlag, New York, NY, USA, 1996. ISBN 3-540-60912-1, ISSN 0171-1873.

[3] M. Combescot and P. Nozières. *Infrared Catastrophy and Excitons in the X-Ray Spectra of Metals.* Le Journal de Physique **32** pages 913-929, (1971).

[4] J. A. Brum, S. Brown, P. Hawrylak, J. F. Young, and Z. Wasilewski. *Mobile excitons and Fermi edge singularities in an interacting 2D electron gas.* Surface Science **361/362** pages 424-427, (1996).

[5] S. A. Brown, Jeff F. Young, J. A. Brum, P. Hawrylak, and Z. Wasilewski. *Evolution of the interband absorption threshold with the density of a two-dimensional electron gas.* Physical Review B **54**(16) pages 11082-11085, (1996).

[6] S. A. Brown, Jeff F. Young, Z. Wasilewski, and P. T. Coleridge. *Fermi-edge singularities in photoluminescence from modulation-doped GaAs quantum wells.* Physical Review B **56**(7) pages 3937-3940, (1997).

[7] R. C. Miller, D. A. Kleinman, W. T. Tsang, and A. C. Gossard. *Observation of the excited level of excitons in GaAs quantum wells.* Physical Review B **24**(2) pages 1134-1136, (1981).

[8] P. N. Butcher & D. Cotter. The Elements of Nonlinear Optics. Cambridge University Press, New York, NY, USA, 1990. ISBN 0-521-34183-3.

[9] K. J. Moore, P. Dawson, and C. T. Foxon. *Observation of luminescence from the 2s heavy-hole exciton in GaAs-(AlGa)As quantum-well structures at low temperature.* Physical Review B **34**(8) pages 6022-6025, (1986).

[10] P. Dawson, K. J. Moore, G. Duggan, H. I. Ralph, and C. T. B. Foxon. *Unambiguous observation of the 2s state of the light- and heavy-hole excitons in GaAs-(AlGa)As multiple-quantum-well structures.* Physical Review B **34**(8) pages 6007-6010, (1986).

[11] D. C. Reynolds, K. K. Bajaj, C. Leak, G. Peters, W. Theis, P. W. Yu, K. Alavi, C. Colvard, and I. Shidlovsky. *Well-resolved higher excited states of the light- and heavy-hole free excitons in a 225-Å $Al_x Ga_{1-x} As$ -GaAs multi-quantum-well structure.* Physical Review B **37** (6) pages 3117-3119, (1988).

[12] Emil S. Koteles and J. Y. Chi. *Experimental exciton binding energies in GaAs / $Al_x Ga_{1-x} As$ quantum wells as a function of well width.* Physical Review B **37**(11) pages 6332-6335, (1988).

[13] Lucio Claudio Andreani and Alfredo Pasquarello. *Accurate theory of excitons in $GaAs-Al_x Ga_{1-x} As$ quantum wells.* Physical Review B **42**(14) pages 8928-8938, (1990).

[14] D. W. Kim, Y. A. Leem, S. D. Yoo, D. H. Woo, D. H. Lee, and J. C. Woo. *Measurement of the exciton binding energy in a narrow $GaAs-Al_x Ga_{1-x} As$ quantum well by photoluminescence excitation spectroscopy.* Physical Review B **47**(4) pages 2042-2047, (1993).

[15] G. Oelgart, M. Proctor, D. Martin, F. Morier-Genaud, F.-K. Reinhart, B. Orschel, L. C. Andreani, H. Rhan. *Experimental and theoretical study of excitonic transition energies in $GaAs/Al_x Ga_{1-x} As$ quantum wells.* Physical Review B **49**(15) pages 10456-10465, (1994).

[16] H. A. Nickel, T. Yeo, G. Kioseoglou, Z. X. Jiang, B. D. McCombe, and A. Petrou. *Observation of internal transitions of negatively charged excitons in GaAs/AlGaAs quantum wells,* Proceedings of the 24th International Conference on the Physics of Semiconductors (ICPS 24), August 2-7, 1998, Jerusalem, Israel. World Scientific Publishing Co., Ltd., Singapore, 1999. ISBN 981-02-3613-1.

[17] Takuma Tsuchiya and Shin'ichi Katayama. *Binding energy of biexcitons and charged excitons in quantum wells: a diffusion monte carlo study,* Proceedings of the 24th International Conference on the Physics of Semiconductors (ICPS 24), August 2-7, 1998, Jerusalem, Israel. World Scientific Publishing Co., Ltd., Singapore, 1999. ISBN 981-02-3613-1.

[18] M. S. Skolnick, J. M. Rorison, K. J. Nash, D. J. Mowbray, P. R. Tapster, S. J. Bass, and A. D. Pitt. *Observation of a Many-Body Edge Singularity in Quantum Well Luminescence Spectra.* Physical Review Letters, **58**(20) pages 2130-2133, (1987).

[19] Gleb Finkelstein, Hadas Shtrikman, and Israel Bar-Joseph. *Optical Spectroscopy of a Two-Dimensional Electron Gas near the Metal-Insulator Transition.* Physical Review Letters, **74**(6) pages 976-979, (1995).

[20] A. J. Shields, M. Pepper, D. A. Ritchie, M. Y. Simmons, and G. A. C. Jones. *Quenching of excitonic transitions by excess electrons in GaAs quantum wells.* Physical Review B, **51**(24) pages 18049-18052, (1995).

[21] H. Buhmann, L. Mansouri, J. Wang, P. H. Beton, N. Mori, L. Eaves, M. Henini, and M. Potemski. *Electron-concentration-dependent quantum-well luminescence: Evidence for a negatively charged exciton.* Physical Review B, **51**(12) pages 7969-7972, (1995).

[22] Pawel Hawrylak. *Optical properties of a two-dimensional electron gas: Evolution of spectra from excitons to Fermi-edge singularities.* Physical Review B **44**(8) pages 3821-3828, (1991).

[23] E. L. Hahn. *Spin Echoes.* Physical Review **80**(4) pages 580-594, (1950).

[24] J. Erland and I. Balslev. *Theory of quantum beat and polarization interference in four-wave mixing.* Physical Review A **48**(3) pages 1765-1768, (1993).

[25] J. Erland, K.-H. Pantke, V. Mizeikis, V. G. Lyssenko, and J. M. Hvam. *Spectrally resolved four-wave mixing in semiconductors: Influence of inhomogeneous broadening.* Physical Review B **50**(20) pages 15047-15055, (1994).

[26] G. Bongiovanni, S. Gürtler, A. Mura, F. Quochi, and J. L. Staehli. *The contribution of biexcitons to the four-wave mixing response of quantum wells with inhomogeneously broadened transitions.* Semiconductor Science and Technology **12** pages 300-308, (1997).

[27] M. D. Webb, S. T. Cundiff, and D. G. Steel. *Stimulated-picosecond-photon-echo studies of localized exciton relaxation and dephasing in $GaAs/Al_xGa_{1-x}As$ multiple quantum wells.* Physical Review B **43**(15) pages 2658-12661, (1991).

[28] Martin Koch, Gero von Plessen, Jochen Feldmann, and Ernst O. Göbel. *Excitonic quantum beats in semiconductor quantum well structures.* Chemical Physics **120** pages 367-388, (1996).

[29] J. Feldman, T. Meier, G. von Plessen, M. Koch, E. O. Göbel, P. Thomas, G. Bacher, C. Hartmann, H. Schweizer, W. Schäfer, and H. Nickel. *Coherent Dynamics of Excitonic Wave Packets.* Physical Review Letters **70**(20) pages 3027-3030, (1993).

[30] F. Jahnke, M. Koch, T. Meier, J. Feldmann, W. Schäfer, P. Thomas, S. W. Koch, E. O. Göbel, and H. Nickel. *Simultaneous influence of disorder and Coulomb interaction on photon echoes in semiconductors.* Physical Review B **50**(11) pages 8114-8117, (1994).

[31] M. Koch, M. Volk, T. Meier, J. Feldmann, W. Stolz, P. Thomas, and E. O. Göbel. *Determination of excitonic binding energies in symmetrically strained (GaIn)As / Ga(AsP) multiple quantum wells using quantum beat spectroscopy.* Superlattices and Microstructures **15**(3) pages 329-332, (1994).

[32] H. Nickolaus and F. Henneberger. *Biexcitonic four-wave-mixing signal in quantum wells: Photon-echo versus free-induction decay*. Physical Review B **57**(15) pages 8774-8777, (1998).

[33] W. Langbein and J. M. Hvam. *Dephasing in the quasi-two-dimensional exciton-biexciton system*. Physical Review B, **61**(3) pages 1692-1695, (2000).

[34] W. Langbein and J. M. Hvam. *Localized Biexcitons in Quasi-2D and Quasi-3D Systyems*. Physica Status Solidi B, **206** pages 111-118, (1998).

[35] W. Langbein and J. M. Hvam. *Localization-enhanced biexciton binding in semiconductors*. Physical Review B, **59**(23) pages 15405-15408, (1998).

[36] I. Bar-Joseph, G. Finkelstein, S. Bar-Ad, H. Shtrikman, and Y. Levinson. *Four-Wave Mixing in Modulation-Doped GaAs Quantum Wells under Strong Magnetic Fields*. Physica Status Solidi B **188** pages 457-463, (1995).

[37] Dai-Sik Kim, Jagdeep Shah, W. Schäfer, and S. Schmitt-Rink. *Femtosecond Coherent Spectroscopy of GaAs Quantum Wells*. Physica Status Solidi B **173** pages 11-20, (1992).

[38] D.-S. Kim, J. Shah, J. E. Cunningham, and T. C. Damen. *Carrier-Carrier Scattering in a Degenerate Electron System: Strong Inhibition of Scattering near the Fermi Edge*. Physical Review Letters **68**(18) pages 2838-2841, (1992).

[39] M. Jaros. Physics and Applications of Semiconductor Microstructures. Oxform University Press, New York, New York, USA, 1990. ISBN 0-19-853927-4.

[40] Robert W. Boyd. Nonlinear Optics. Academic Press, Inc., San Diego, CA, USA, 1992. ISBN 0-12-121680-2.

[41] S. Glutsch, U. Siegner, and D. S. Chemla. *Spatiotemporal dynamics of photon echos from continuum states in semiconductors*. Physical Review B, **52** (7) pages 4941-4950, (1995).

[42] S. Hughes. *Polarization decay in ultrafast collinear nondegenerate four-wave mixing in a semiconductor amplifier*. Optics Letters, **23** (12) pages 948-950, (1998).

[43] S. Hughes. *Carrier-carrier interaction and ultrashort pulse propagation in a highly excited semiconductor laser amplifier beyond the rate equation limit*. Physical Review A, **58** (3) pages 2567-2576, (1998).

[44] T. F. Albrecht, K. Bott, T. Meier, A. Schulze, M. Koch, S. T. Cundiff, J. Feldmann, W. Stolz, P. Thomas, S. W. Koch, and E. O. Göbel. *Disorder mediated biexcitonic beats in semiconductor quantum wells*. Physical Review B **54**(7) pages 4436-4439, (1996).

[45] A. E. Paul, W. Sha, S. Patkar, and A. L. Smirl. *Excitation-induced phase shifts of heavy- and light-hole quantum beats in* $GaAs/Al_x Ga_{1-x} As$ *multiple quantum wells.* Physical Review B **51**(7) pages 4242-4246, (1995).

[46] K. El Sayed, D. Birkedal, V. G. Lyssenko, and J. M. Hvam. *Continuum contribution to excitonic four-wave mixing due to interaction-induced nonlinearities: A numerical study.* Physical Review B, **55**(4) pages 2456-2465, (1997).

[47] I. S. Gradshteyn & I. M. Ryzhik. Alan Jeffrey, Editor. Table of Integrals, Series, and Products, Fifth Edition. Academic Press, Inc., San Diego, CA, USA, 1994. ISBN 0-12-294755-X.

[48] Norman Lloyd Johnson and Samuel Kotz. Distributions in Statistics: Continuous Multivariate Distributions, Volume 4. John Wiley & Sons, Inc., New York, NY, USA, 1972.

[49] Otfried Madelung, editor. Semiconductors: Group IV Elements and III-V Compounds. Springer-Verlag, Berlin, Germany, 1991. ISBN 3-540-53150-5.

[50] B. H. Bransden and C. J. Joachain. Introduction to Quantum Mechanics. Longman Group UK Ltd., Essex, England (and John Wiley & Sons, Inc., New York, NY, USA), 1990. ISBN 0-470-21161-X (USA only).

[51] S. Schmitt-Rink, D. Bennhardt, V. Heuckeroth, P. Thomas, P. Haring, G. Maidorn, H. Bakker, K. Leo, D.-S. Kim, J. Shah, and K. Köhler. *Polarization dependence of heavy- and light-hole quantum beats.* Physical Review B **46**(16) pages 10460-10463, (1992).

[52] Y. Z. Hu, R. Binder, S. W. Koch, S. T. Cundiff, H. Wang, and D. G. Steel. *Excitation and polarization effects in semiconductor four-wave-mixing spectroscopy.* Physical Review B **49**(20) pages 14382-14386, (1994).

[53] José A. Brum and Pawel Hawrylak. *Fermi Edge Singularity in the Optical Properties of Two-Dimensional Electron Gas.* Comments on Condensed Matter Physics **18**(3) pages 135-161, (1997).

[54] E. Yablonovitch, D. M. Hwang, T. J. Gmitter, L. T. Florez, and J. P. Harbison. *Van der Waals bonding of GaAs epitaxial liftoff films onto arbitrary substrates.* Applied Physics Letters **56**(24) pages 2419-2421, (1990).

[55] Eli Yablonovitch, T. Gmitter, J. P. Harbison, and R. Bhat. *Extreme selectivity in the lift-off of epitaxial GaAs films.* Applied Physics Letters **51**(26) pages 2222-2224, (1987).

[56] Frank L. Pedrotti & Leno S. Pedrotti. Introduction to Optics. Prentice-Hall, Inc., Englewood Cliffs, NJ, USA, 1987. ISBN 0-13-491465

[57] Tsunami Mode-Locked Ti:Sapphire Laser User's Manual. Spectra-Physics Lasers, Mountain View, CA, USA, May 1995.

[58] Murray R. Spiegel. Mathematical Handbook of Formulas and Tables. Schaum's Outline Series in Mathematics. McGraw-Hill Book Company, New York, USA, 1968.

[59] Kenneth L. Sala, Geraldine A. Kenney-Wallace, and Gregory E. Hall. *CW Autocorrelation Measurements of Picosecond Laser Pulses.* IEEE Journal of Quantum Electronics, **QE-16**(9) pages 990-996, (1980).

[60] Z. C. Yan, E. Goovaerts, C. Van Hoof, A. Bouwen, and G. Borghs. *Photoluminescence of the electron-dressed confined X^- exciton in an n-type AlAs/GaAs resonant tunneling device.* Physical Review B **52**(8) pages 5907-5912, (1995).

[61] C. Riva, F. M. Peeters, and K. Varga. *Excitons and charged excitons in semiconductor quantum wells.* Physical Review B **61**(20) pages 13873-13881, (2000).

[62] A. Thilagam. *Two-dimensional charged-exciton complexes.* Physical Review B, **55** (12), 1997, pages 7804-7808. Also, comments: Physical Review B **57**(20) pages 13305-13306 and pages 13307-13308, (1998).

[63] J. Usukura, Y. Suzuki, and K. Varga. *Stability of two- and three-dimensional excitonic complexes.* Physical Review B **59**(8) pages 5652-5661, (1999).

[64] A. Euteneuer, E. Finger, M. Hofmann, W. Stolz, T. Meier, P. Thomas, S. W. Koch, W. W. Rühle, R. Hey, and K. Ploog. *Coherent Excitation Spectroscopy on Inhomogeneous Exciton Ensembles.* Physical Review Letters **83**(10) pages 2073-2076, (1999).

[65] Pierre Lefebvre, Philippe Christol, and Henry Mathieu. *Unified formalism of excitonic absorption spectra of semiconductor quantum wells, superlattices, and quantum wires.* Physical Review B **48**(23) pages 17308-17315, (1993).

[66] F. de Rougemont and R. Frey. *Two-level approach to saturation properties in semiconductor materials.* Physical Review B, **37**, (3) pages 1237-1244, (1988).

[67] Masamichi Yamanishi and Yong Lee. *Phase Dampings of Optical Dipole Moments and Gain Spectra in Semiconductor Lasers.* IEEE Journal of Quantum Electronics, **QE-23**(4) pages 367-370, (1987).

[68] Tsukuru Ohtoshi and Masamichi Yamanishi. *Optical Line Shape Functions in Quantum-Well and Quantum-Wire Structures.* IEEE Journal of Quantum Electronics, **27**(1) pages 46-53, (1991).

[69] Chyi Hwang and Yen-Ping Shih. *Solution of Integral Equations via Laguerre Polynomials.* Computers & Electrical Engineering **9**(3-4) pages 123-129, (1982).

[70] Rong-Yeu Chang and Maw-Ling Wang. *Solutions of integral equations via shifted Legendre polynomials.* International Journal of Systems Science **16**(2) pages 197-208, (1985).

[71] Tsu-Tian Lee and Yih-Fong Chang. *Solutions of convolution integral and integral equations via double general orthogonal polynomials.* International Journal of Systems Science **19**(3) pages 415-430, (1988).

[72] N. Mastronardi and D. Occorsio. *The numerical computation of some integrals on the real line.* Journal of Computational and Applied Mathematics **115** pages 433-450, (2000).

[73] W. H. Press, S. A. Teukolsky, W. T. Vetterling, and B. P. Flannery. Numerical Recipes in FORTRAN, the Art of Scientific Computing, 2nd edition. Cambridge University Press, New York, NY, USA, 1992.

[74] W. H. Press, S. A. Teukolsky, W. T. Vetterling, and B. P. Flannery. Numerical Recipes in Fortran 90, the Art of Parallel Scientific Computing. Cambridge University Press, New York, NY, USA, 1996.

[75] Peter J. Mohr and Barry N. Taylor. *CODATA recommended values of the fundamental physical constants: 1998.* Reviews of Modern Physics **72**(2) pages 351-495, (April 2000). Published simultaneously in the Journal of Physical and Chemical Reference Data. Also available on the World Wide Web at physics.nist.gov/constants.

[76] Shanjie Zhang and Jianming Jin. Computation of Special Functions. John Wiley & Sons, Inc., New York, NY, USA, 1996. ISBN 0-471-11963-6.

[77] Philip J. Davis and Philip Rabinowitz. Methods of Numerical Integration, 2nd Edition. Academic Press, Inc., Orlando, FL, USA, 1983. ISBN 0-12-206360-0.

[78] Bing-Yuan Ting. Evaluation of Integrals Whose Integrands are Oscillatory and Singular. Ph.D. Thesis, Mathematics, University of Miccouri-Kansas City, Kansas City, MI, USA, 1979.

[79] A. H. Stroud and Don Secrest. Gaussian Quadrature Formulas. Prentice-Hall, Inc., Englewood Cliffs, NJ, USA, 1966.

[80] N. S. Bakhvalov and L. G. Vasil'eva. *Evaluation of the Integrals of Oscillating Functions by Interpolation at Nodes of Gaussian Quadratures.* USSR Computational Mathematics & Mathematical Physics **8** pages 241-249, (1968).

[81] T. N. L. Patterson. *On High Precision Methods for the Evaluation of Fourier Integrals with Finite and Infinite Limits.* Numerische Mathematik **27** pages 41-52, (1976).

[82] Bing-Yuan Ting and Yudell L. Luke. *Computation of Integrals With Oscillatory and Singular Integrands.* Mathematics of Computation **37**(155) pages 69-183, (1981).

[83] Robert Piessens and Maria Branders. *On the computation of Fourier transforms of singular functions.* Journal of Computational and Applied Mathematics **43** pages 159-169, (1992).

[84] G. V. Milovanović *Numerical Calculation of Integrals Involving Oscillatory and Singular Kernels and Some Applications of Quadratures.* Computers & Mathematics with Applications, **36**(8) pages 19-39, (1998).

[85] T. S. Shao, T. C. Chen, and R. M. Frank. *Tables of Zeros and Gaussian Weights of Certain Associated Laguerre Polynomials and the Related Generalized Hermite Polynomials.* Mathematics of Computation **18**(88) pages 598-616, (1964).

Appendix A

Additional Theoretical & Numerical Details

This appendix contains additional details about the theoretical derivations and the numerical approaches used to simulate them. The information contained here does not, in general, repeat derivations presented elsewhere, only supplementing the material to provide more detailed results of various points. The following table is a quick guide to the Appendix.

A.1 Additional Theoretical Details

A.1.1 Pulse Envelope Functions

As mentioned during the evaluation of the third order DFWM polarization terms, the integral

$$
\int\limits_{0}^{+\infty} dt \, g(b_1 - t)g(b_2 - t) = \int\limits_{-\infty}^{+\infty} dt \, g(b_1 - t)g(b_2 - t) - \int\limits_{-\infty}^{0} dt \, g(b_1 - t)g(b_2 - t)
$$

$$
= g \circledast g \, (b_1 - b_2) - \int\limits_{0}^{+\infty} dt \, g(b_1 + t)g(b_2 + t) \tag{A.1}
$$

appears in more than one polarization term when the limit $\Gamma_{gg} \to 0$ is taken. When evaluated for the Gaussian, Lorentzian, and Hyperbolic secant pulse profiles, this integral takes the form

$$
\int\limits_{0}^{+\infty} dt \, g(b_1 - t)g(b_2 - t) = g \circledast g \, (b_1 - b_2) \left[1 - \text{envelope}(b_1, b_2) \right] , \tag{A.2}
$$

where the 'envelope' functions are listed in Table A.1 for the Gaussian, Lorentzian, and hyperbolic secant pulse profiles. Surface plots of these profiles as a function of b_1 and b_2 are shown in Figure A.1. The pulse shape functions these are based on are listed in Table 3.3, page 81. The pulse autocorrelation functions are listed in Table 3.4, on page 82.

A.1.2 Algorithm for Generating $\overleftrightarrow{\chi}^{(n)}$ – Damping and Resonant Terms

The following is a list of steps for generating the nth order susceptibility, $\overleftrightarrow{\chi}^{(n)}$, including the damping terms, and identifying the resonant terms.

1. Expand $\chi^{(n)}$ into $(n+1)$ terms, with the S permutation symmetry. Note that, with damping, the overall permutation symmetry, S_T, is **not** preserved.

2. Insert damping terms, $i\Gamma_{J_i x}$. The sign in front of the damping terms is determined by making it the same as the sign in front of the ω_i's for that term, all of which will have the same sign (NOTE: this comes from the definition of the complex Fourier transform and ensures that the integrals will converge).

3. Determine the resonant terms from the $n!$ terms in each of the generated susceptibility terms. These can be found by setting the $\Gamma_{J_i x}$ terms to zero and looking for terms where **all** the denominators are zero. This is done by looking at the permuted terms with the specific values for $\omega_1, \omega_2, \cdots \omega_n$ substituted in.

Table A.1: Envelope functions for the Gaussian, hyperbolic secant, and Lorentzian pulse shapes. a_t for each pulse shape is defined in Table 3.3, page 81.

	Gaussian	Hyperbolic Secant
Envelope	$\frac{1}{2}\text{erfc}\left\{\frac{a}{\sqrt{2}}\left(b_1+b_2\right)\right\}$	$\frac{1}{2}\dfrac{\ln\left(\dfrac{1+e^{-2a_tb_2}}{1+e^{-2a_tb_1}}\right)}{a_t\left(b_1-b_2\right)}$
$b_1=b_2$	$\frac{1}{2}\text{erfc}\left(\sqrt{2}a_tb_2\right)$	$\dfrac{1}{1+e^{2a_tb_2}}$
$b_1=0$	$\frac{1}{2}\text{erfc}\left(\dfrac{a}{\sqrt{2}}b_2\right)$	$\frac{1}{2}\dfrac{\ln(2)-\ln\left(1+e^{-2a_tb_2}\right)}{a_tb_2}$
$b_2=0$	$\frac{1}{2}\text{erfc}\left(\dfrac{a}{\sqrt{2}}b_1\right)$	$\frac{1}{2}\dfrac{\ln(2)+\ln\left(1+e^{-2a_tb_1}\right)}{a_tb_1}$
$b_1=b_2=0$	$\dfrac{1}{2}$	$\dfrac{1}{2}$

|	Lorentzian
Envelope	$\frac{1}{2}\dfrac{a_t\left(b_1-b_2\right)\left[\pi-\arctan\left(ab_1\right)-\arctan\left(a_tb_2\right)\right]+\ln\left(\dfrac{1+a_t^2b_1^2}{1+a_t^2b_2^2}\right)}{\pi a_t\left(b_1-b_2\right)}$
$b_1=b_2$	$\dfrac{1}{2\pi}\left\{\dfrac{2a_tb_2}{1+a_t^2b_2^2}+\pi-2\arctan\left(a_tb_2\right)\right\}$
$b_1=0$	$\frac{1}{2}\dfrac{a_tb_2\left[\pi-\arctan\left(a_tb_2\right)\right]+\ln\left(1+a_t^2b_2^2\right)}{\pi a_tb_2}$
$b_2=0$	$\frac{1}{2}\dfrac{a_tb_1\left[\pi-\arctan\left(a_tb_1\right)\right]+\ln\left(1+a_t^2b_1^2\right)}{\pi a_tb_1}$
$b_1=b_2=0$	$\dfrac{1}{2}$
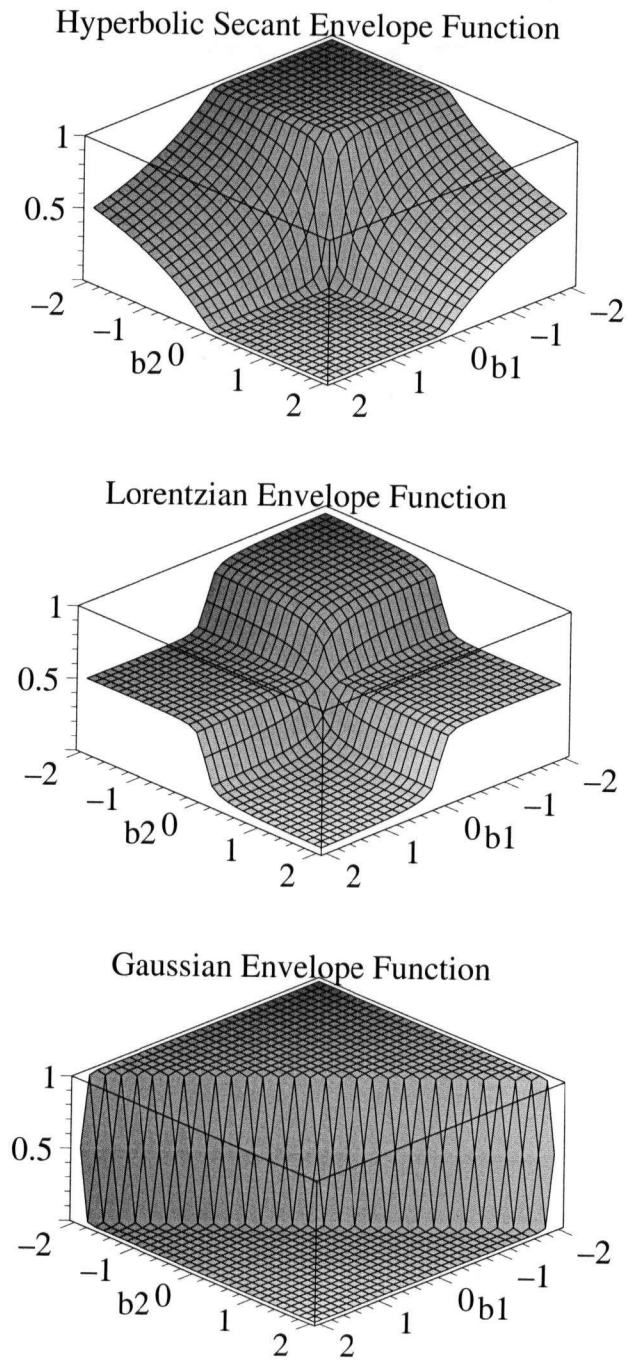
Figure A.1: Envelope function plots for the Gaussian, Lorentzian, and hyperbolic secant pulse profiles. These are plots of the functions listed in Table A.1.

The algorithm for doing the second step is presented below

1. Note that there are $n + 1$ dipole moment terms, μ^{β_k}.

2. Label them $\mu^{\beta_0} \mu^{\beta_1} \cdots \mu^{\beta_n}$.

3. Let i equal the **position** of μ^{β_0} in $\mu^{\beta_0}\mu^{\beta_1}\mu^{\beta_2} \cdots \mu^{\beta_n}$ (eg. $i = 0$ for the first term in the second step.

4. For the jth denominator term (there are n of them) we have, $(\omega_{J_j x} \pm \square \pm \Gamma_{J_j x})$, where the sign and terms ($\square$) are determined according to

$i\ ?\ j$	Sign	Terms ($\square$)
$i < j$	$-$	$\displaystyle\sum_{k=j}^{n} \omega_k$
$i = j$	$+$	$\displaystyle\sum_{k=1}^{j} \omega_k$
$i > j$	$+$	$\displaystyle\sum_{k<j} \omega_k + \omega_i$
the last two can be combined into		
$i \geq j$	$+$	$\displaystyle\sum_{k<j} \omega_k + \omega_i$

The possible values of the variables are $0 \leq i \leq n$ and $1 \leq j, k \leq n$.

A.1.3 Full Expansion of the $\overleftrightarrow{\chi}^{(3)}$ Expression

Table A.2 lists all 24 terms in the full expansion of $\overleftrightarrow{\chi}^{(3)}$, including the dephasing components. This table is an expansion of Equation (2.10) (page 19) in Chapter 2.

Table A.2: Full 24 term expansion of $\chi^{(3)}$, including the dephasing terms $\Gamma_{J_i x}$.

$$\chi^{(3)}_{\alpha\beta_1\beta_2\beta_3}\left(-\omega_\Sigma; \omega_1, \omega_2, \omega_3\right) = \frac{N}{\epsilon_o\, n!\, \hbar^3\, 2\pi} \sum_{x=g,J_1,J_2,J_3} \rho_o(x)$$

$$\times \left\{ \frac{\mu^{\beta_0}_{xJ_1}\mu^{\beta_1}_{J_1 J_2}\mu^{\beta_2}_{J_2 J_3}\mu^{\beta_3}_{J_3 x}}{\left(\omega_{J_1 x} - \omega_1 - \omega_2 - \omega_3 - i\Gamma_{J_1 x}\right)\left(\omega_{J_2 x} - \omega_2 - \omega_3 - i\Gamma_{J_2 x}\right)\left(\omega_{J_3 x} - \omega_3 - i\Gamma_{J_3 x}\right)} \quad (0123) \right.$$

$$\left. + \frac{\mu^{\beta_0}_{xJ_1}\mu^{\beta_1}_{J_1 J_2}\mu^{\beta_3}_{J_2 J_3}\mu^{\beta_2}_{J_3 x}}{\left(\omega_{J_1 x} - \omega_1 - \omega_3 - \omega_2 - i\Gamma_{J_1 x}\right)\left(\omega_{J_2 x} - \omega_3 - \omega_2 - i\Gamma_{J_2 x}\right)\left(\omega_{J_3 x} - \omega_2 - i\Gamma_{J_3 x}\right)} \quad (0132) \right.$$

Table A.2: (continued)

$$+\frac{\mu_{xJ_1}^{\beta_0}\mu_{J_1J_2}^{\beta_2}\mu_{J_2J_3}^{\beta_1}\mu_{J_3x}^{\beta_3}}{\left(\omega_{J_1x}-\omega_2-\omega_1-\omega_3-i\Gamma_{J_1x}\right)\left(\omega_{J_2x}-\omega_1-\omega_3-i\Gamma_{J_2x}\right)\left(\omega_{J_3x}-\omega_3-i\Gamma_{J_3x}\right)} \quad (0213)$$

$$+\frac{\mu_{xJ_1}^{\beta_0}\mu_{J_1J_2}^{\beta_2}\mu_{J_2J_3}^{\beta_3}\mu_{J_3x}^{\beta_1}}{\left(\omega_{J_1x}-\omega_2-\omega_3-\omega_1-i\Gamma_{J_1x}\right)\left(\omega_{J_2x}-\omega_3-\omega_1-i\Gamma_{J_2x}\right)\left(\omega_{J_3x}-\omega_1-i\Gamma_{J_3x}\right)} \quad (0231)$$

$$+\frac{\mu_{xJ_1}^{\beta_0}\mu_{J_1J_2}^{\beta_3}\mu_{J_2J_3}^{\beta_1}\mu_{J_3x}^{\beta_2}}{\left(\omega_{J_1x}-\omega_3-\omega_1-\omega_2-i\Gamma_{J_1x}\right)\left(\omega_{J_2x}-\omega_1-\omega_2-i\Gamma_{J_2x}\right)\left(\omega_{J_3x}-\omega_2-i\Gamma_{J_3x}\right)} \quad (0312)$$

$$+\frac{\mu_{xJ_1}^{\beta_0}\mu_{J_1J_2}^{\beta_3}\mu_{J_2J_3}^{\beta_2}\mu_{J_3x}^{\beta_1}}{\left(\omega_{J_1x}-\omega_3-\omega_2-\omega_1-i\Gamma_{J_1x}\right)\left(\omega_{J_2x}-\omega_2-\omega_1-i\Gamma_{J_2x}\right)\left(\omega_{J_3x}-\omega_1-i\Gamma_{J_3x}\right)} \quad (0321)$$

$$+\frac{\mu_{xJ_1}^{\beta_1}\mu_{J_1J_2}^{\beta_0}\mu_{J_2J_3}^{\beta_2}\mu_{J_3x}^{\beta_3}}{\left(\omega_{J_1x}+\omega_1+i\Gamma_{J_1x}\right)\left(\omega_{J_2x}-\omega_2-\omega_3-i\Gamma_{J_2x}\right)\left(\omega_{J_3x}-\omega_3-i\Gamma_{J_3x}\right)} \quad (1023)$$

$$+\frac{\mu_{xJ_1}^{\beta_1}\mu_{J_1J_2}^{\beta_0}\mu_{J_2J_3}^{\beta_3}\mu_{J_3x}^{\beta_2}}{\left(\omega_{J_1x}+\omega_1+i\Gamma_{J_1x}\right)\left(\omega_{J_2x}-\omega_3-\omega_2-i\Gamma_{J_2x}\right)\left(\omega_{J_3x}-\omega_2-i\Gamma_{J_3x}\right)} \quad (1032)$$

$$+\frac{\mu_{xJ_1}^{\beta_2}\mu_{J_1J_2}^{\beta_0}\mu_{J_2J_3}^{\beta_1}\mu_{J_3x}^{\beta_3}}{\left(\omega_{J_1x}+\omega_2+i\Gamma_{J_1x}\right)\left(\omega_{J_2x}-\omega_1-\omega_3-i\Gamma_{J_2x}\right)\left(\omega_{J_3x}-\omega_3-i\Gamma_{J_3x}\right)} \quad (2013)$$

$$+\frac{\mu_{xJ_1}^{\beta_2}\mu_{J_1J_2}^{\beta_0}\mu_{J_2J_3}^{\beta_3}\mu_{J_3x}^{\beta_1}}{\left(\omega_{J_1x}+\omega_2+i\Gamma_{J_1x}\right)\left(\omega_{J_2x}-\omega_3-\omega_1-i\Gamma_{J_2x}\right)\left(\omega_{J_3x}-\omega_1-i\Gamma_{J_3x}\right)} \quad (1023)$$

$$+\frac{\mu_{xJ_1}^{\beta_3}\mu_{J_1J_2}^{\beta_0}\mu_{J_2J_3}^{\beta_1}\mu_{J_3x}^{\beta_2}}{\left(\omega_{J_1x}+\omega_3+i\Gamma_{J_1x}\right)\left(\omega_{J_2x}-\omega_1-\omega_2-i\Gamma_{J_2x}\right)\left(\omega_{J_3x}-\omega_2-i\Gamma_{J_3x}\right)} \quad (3012)$$

$$+\frac{\mu_{xJ_1}^{\beta_3}\mu_{J_1J_2}^{\beta_0}\mu_{J_2J_3}^{\beta_2}\mu_{J_3x}^{\beta_1}}{\left(\omega_{J_1x}+\omega_3+i\Gamma_{J_1x}\right)\left(\omega_{J_2x}-\omega_2-\omega_1-i\Gamma_{J_2x}\right)\left(\omega_{J_3x}-\omega_1-i\Gamma_{J_3x}\right)} \quad (1023)$$

$$+\frac{\mu_{xJ_1}^{\beta_1}\mu_{J_1J_2}^{\beta_2}\mu_{J_2J_3}^{\beta_0}\mu_{J_3x}^{\beta_3}}{\left(\omega_{J_1x}+\omega_1+i\Gamma_{J_1x}\right)\left(\omega_{J_2x}+\omega_1+\omega_2+i\Gamma_{J_2x}\right)\left(\omega_{J_3x}-\omega_3-i\Gamma_{J_3x}\right)} \quad (1203)$$

$$+\frac{\mu_{xJ_1}^{\beta_1}\mu_{J_1J_2}^{\beta_3}\mu_{J_2J_3}^{\beta_0}\mu_{J_3x}^{\beta_2}}{\left(\omega_{J_1x}+\omega_1+i\Gamma_{J_1x}\right)\left(\omega_{J_2x}+\omega_1+\omega_3+i\Gamma_{J_2x}\right)\left(\omega_{J_3x}-\omega_2-i\Gamma_{J_3x}\right)} \quad (1302)$$

$$+\frac{\mu_{xJ_1}^{\beta_2}\mu_{J_1J_2}^{\beta_1}\mu_{J_2J_3}^{\beta_0}\mu_{J_3x}^{\beta_3}}{\left(\omega_{J_1x}+\omega_2+i\Gamma_{J_1x}\right)\left(\omega_{J_2x}+\omega_2+\omega_1+i\Gamma_{J_2x}\right)\left(\omega_{J_3x}-\omega_3-i\Gamma_{J_3x}\right)} \quad (2103)$$

$$+\frac{\mu_{xJ_1}^{\beta_2}\mu_{J_1J_2}^{\beta_3}\mu_{J_2J_3}^{\beta_0}\mu_{J_3x}^{\beta_1}}{\left(\omega_{J_1x}+\omega_2+i\Gamma_{J_1x}\right)\left(\omega_{J_2x}+\omega_2+\omega_3+i\Gamma_{J_2x}\right)\left(\omega_{J_3x}-\omega_1-i\Gamma_{J_3x}\right)} \quad (2301)$$

$$+\frac{\mu_{xJ_1}^{\beta_3}\mu_{J_1J_2}^{\beta_1}\mu_{J_2J_3}^{\beta_0}\mu_{J_3x}^{\beta_2}}{\left(\omega_{J_1x}+\omega_3+i\Gamma_{J_1x}\right)\left(\omega_{J_2x}+\omega_3+\omega_1+i\Gamma_{J_2x}\right)\left(\omega_{J_3x}-\omega_2-i\Gamma_{J_3x}\right)} \quad (3102)$$

Table A.2: (continued)

$$+ \frac{\mu_{xJ_1}^{\beta_3} \mu_{J_1 J_2}^{\beta_2} \mu_{J_2 J_3}^{\beta_0} \mu_{J_3 x}^{\beta_1}}{(\omega_{J_1 x} + \omega_3 + i\Gamma_{J_1 x}) (\omega_{J_2 x} + \omega_3 + \omega_2 + i\Gamma_{J_2 x}) (\omega_{J_3 x} - \omega_1 - i\Gamma_{J_3 x})} \quad (3201)$$

$$+ \frac{\mu_{xJ_1}^{\beta_1} \mu_{J_1 J_2}^{\beta_2} \mu_{J_2 J_3}^{\beta_3} \mu_{J_3 x}^{\beta_0}}{(\omega_{J_1 x} + \omega_1 + i\Gamma_{J_1 x}) (\omega_{J_2 x} + \omega_1 + \omega_2 + i\Gamma_{J_2 x}) (\omega_{J_3 x} + \omega_1 + \omega_2 + \omega_3 + i\Gamma_{J_3 x})} \quad (1230)$$

$$+ \frac{\mu_{xJ_1}^{\beta_1} \mu_{J_1 J_2}^{\beta_3} \mu_{J_2 J_3}^{\beta_2} \mu_{J_3 x}^{\beta_0}}{(\omega_{J_1 x} + \omega_1 + i\Gamma_{J_1 x}) (\omega_{J_2 x} + \omega_1 + \omega_3 + i\Gamma_{J_2 x}) (\omega_{J_3 x} + \omega_1 + \omega_3 + \omega_2 + i\Gamma_{J_3 x})} \quad (1320)$$

$$+ \frac{\mu_{xJ_1}^{\beta_2} \mu_{J_1 J_2}^{\beta_1} \mu_{J_2 J_3}^{\beta_3} \mu_{J_3 x}^{\beta_0}}{(\omega_{J_1 x} + \omega_2 + i\Gamma_{J_1 x}) (\omega_{J_2 x} + \omega_2 + \omega_1 + i\Gamma_{J_2 x}) (\omega_{J_3 x} + \omega_2 + \omega_1 + \omega_3 + i\Gamma_{J_3 x})} \quad (2130)$$

$$+ \frac{\mu_{xJ_1}^{\beta_2} \mu_{J_1 J_2}^{\beta_3} \mu_{J_2 J_3}^{\beta_1} \mu_{J_3 x}^{\beta_0}}{(\omega_{J_1 x} + \omega_2 + i\Gamma_{J_1 x}) (\omega_{J_2 x} + \omega_2 + \omega_3 + i\Gamma_{J_2 x}) (\omega_{J_3 x} + \omega_2 + \omega_3 + \omega_1 + i\Gamma_{J_3 x})} \quad (2310)$$

$$+ \frac{\mu_{xJ_1}^{\beta_3} \mu_{J_1 J_2}^{\beta_1} \mu_{J_2 J_3}^{\beta_2} \mu_{J_3 x}^{\beta_0}}{(\omega_{J_1 x} + \omega_3 + i\Gamma_{J_1 x}) (\omega_{J_2 x} + \omega_3 + \omega_1 + i\Gamma_{J_2 x}) (\omega_{J_3 x} + \omega_3 + \omega_1 + \omega_2 + i\Gamma_{J_3 x})} \quad (3120)$$

$$+ \frac{\mu_{xJ_1}^{\beta_3} \mu_{J_1 J_2}^{\beta_2} \mu_{J_2 J_3}^{\beta_1} \mu_{J_3 x}^{\beta_0}}{(\omega_{J_1 x} + \omega_3 + i\Gamma_{J_1 x}) (\omega_{J_2 x} + \omega_3 + \omega_2 + i\Gamma_{J_2 x}) (\omega_{J_3 x} + \omega_3 + \omega_2 + \omega_1 + i\Gamma_{J_3 x})} \quad (3210) \Bigg\}$$

A.1.4 Determination of DFWM Resonant Terms

Table A.3 lists all the terms for the DFWM $\overleftrightarrow{\chi}^{(3)}$ process showing which are resonant, along with the nature of the level needed for resonance (single, double, or ground state). This supplements the partial expansion shown in Table 2.1 (page 34) of Chapter 2.

Table A.3: Determination of resonant terms, in the degenerate case, of the full 24 term expansion of the $\chi^{(3)}$ expression.

Term	J_1	J_2	J_3	Type
$\chi_{\beta_0 \beta_1 \beta_2 \beta_3}^{(3)} (-\omega; \omega, \omega, -\omega) = \dfrac{N}{\epsilon_o \, n! \, \hbar^3 \, 2\pi} \rho_o(g)$ $\times \Bigg\{ \dfrac{\mu_{gJ_1}^{\beta_0} \mu_{J_1 J_2}^{\beta_1} \mu_{J_2 J_3}^{\beta_2} \mu_{J_3 g}^{\beta_3} \quad (0123)}{(\omega_{J_1 g} - \omega) (\omega_{J_2 g}) (\omega_{J_3 g} + \omega)}$	Single	Ground	—	—

Table A.3: (continued)

Term	J_1	J_2	J_3	Type
$+\dfrac{\mu_{gJ_1}^{\beta_0}\mu_{J_1J_2}^{\beta_2}\mu_{J_2J_3}^{\beta_1}\mu_{J_3g}^{\beta_3}\quad(0213)}{(\omega_{J_1g}-\omega)(\omega_{J_2g})(\omega_{J_3g}+\omega)}$	Single	Ground	—	—
$+\dfrac{\mu_{gJ_1}^{\beta_0}\mu_{J_1J_2}^{\beta_1}\mu_{J_2J_3}^{\beta_3}\mu_{J_3g}^{\beta_2}\quad(0132)}{(\omega_{J_1g}-\omega)(\omega_{J_2g})(\omega_{J_3g}-\omega)}$	Single	Ground	Single	Single
$+\dfrac{\mu_{gJ_1}^{\beta_0}\mu_{J_1J_2}^{\beta_2}\mu_{J_2J_3}^{\beta_3}\mu_{J_3g}^{\beta_1}\quad(0231)}{(\omega_{J_1g}-\omega)(\omega_{J_2g})(\omega_{J_3g}-\omega)}$	Single	Ground	Single	Single
$+\dfrac{\mu_{gJ_1}^{\beta_0}\mu_{J_1J_2}^{\beta_3}\mu_{J_2J_3}^{\beta_1}\mu_{J_3g}^{\beta_2}\quad(0312)}{(\omega_{J_1g}-\omega)(\omega_{J_2g}-2\omega)(\omega_{J_3g}-\omega)}$	Single	Double	Single	Double
$+\dfrac{\mu_{gJ_1}^{\beta_0}\mu_{J_1J_2}^{\beta_3}\mu_{J_2J_3}^{\beta_2}\mu_{J_3g}^{\beta_1}\quad(0321)}{(\omega_{J_1g}-\omega)(\omega_{J_2g}-2\omega)(\omega_{J_3g}-\omega)}$	Single	Double	Single	Double
$+\dfrac{\mu_{gJ_1}^{\beta_1}\mu_{J_1J_2}^{\beta_0}\mu_{J_2J_3}^{\beta_2}\mu_{J_3g}^{\beta_3}\quad(1023)}{(\omega_{J_1g}+\omega)(\omega_{J_2g})(\omega_{J_3g}+\omega)}$	—	Ground	—	—
$+\dfrac{\mu_{gJ_1}^{\beta_1}\mu_{J_1J_2}^{\beta_0}\mu_{J_2J_3}^{\beta_3}\mu_{J_3g}^{\beta_2}\quad(1032)}{(\omega_{J_1g}+\omega)(\omega_{J_2g})(\omega_{J_3g}-\omega)}$	—	Ground	Single	—
$+\dfrac{\mu_{gJ_1}^{\beta_2}\mu_{J_1J_2}^{\beta_0}\mu_{J_2J_3}^{\beta_1}\mu_{J_3g}^{\beta_3}\quad(2013)}{(\omega_{J_1g}+\omega)(\omega_{J_2g})(\omega_{J_3g}+\omega)}$	—	Ground	—	—
$+\dfrac{\mu_{gJ_1}^{\beta_2}\mu_{J_1J_2}^{\beta_0}\mu_{J_2J_3}^{\beta_3}\mu_{J_3g}^{\beta_1}\quad(2031)}{(\omega_{J_1g}+\omega)(\omega_{J_2g})(\omega_{J_3g}-\omega)}$	—	Ground	Single	—
$+\dfrac{\mu_{gJ_1}^{\beta_3}\mu_{J_1J_2}^{\beta_0}\mu_{J_2J_3}^{\beta_1}\mu_{J_3g}^{\beta_2}\quad(3012)}{(\omega_{J_1g}-\omega)(\omega_{J_2g}-2\omega)(\omega_{J_3g}-\omega)}$	Single	Double	Single	Double
$+\dfrac{\mu_{gJ_1}^{\beta_3}\mu_{J_1J_2}^{\beta_0}\mu_{J_2J_3}^{\beta_2}\mu_{J_3g}^{\beta_1}\quad(3021)}{(\omega_{J_1g}-\omega)(\omega_{J_2g}-2\omega)(\omega_{J_3g}-\omega)}$	Single	Double	Single	Double
$+\dfrac{\mu_{gJ_1}^{\beta_1}\mu_{J_1J_2}^{\beta_2}\mu_{J_2J_3}^{\beta_0}\mu_{J_3g}^{\beta_3}\quad(1203)}{(\omega_{J_1g}+\omega)(\omega_{J_2g}+2\omega)(\omega_{J_3g}+\omega)}$	—	—	—	—
$+\dfrac{\mu_{gJ_1}^{\beta_1}\mu_{J_1J_2}^{\beta_3}\mu_{J_2J_3}^{\beta_0}\mu_{J_3g}^{\beta_2}\quad(1302)}{(\omega_{J_1g}+\omega)(\omega_{J_2g})(\omega_{J_3g}-\omega)}$	—	Ground	Single	—
$+\dfrac{\mu_{gJ_1}^{\beta_2}\mu_{J_1J_2}^{\beta_1}\mu_{J_2J_3}^{\beta_0}\mu_{J_3g}^{\beta_3}\quad(2103)}{(\omega_{J_1g}+\omega)(\omega_{J_2g}+2\omega)(\omega_{J_3g}+\omega)}$	—	—	—	—

Table A.3: (continued)

Term	J_1	J_2	J_3	Type
$+\dfrac{\mu_{gJ_1}^{\beta_2}\mu_{J_1J_2}^{\beta_3}\mu_{J_2J_3}^{\beta_0}\mu_{J_3g}^{\beta_1}\quad(2301)}{(\omega_{J_1g}+\omega)(\omega_{J_2g})(\omega_{J_3g}-\omega)}$	—	Ground	Single	—
$+\dfrac{\mu_{gJ_1}^{\beta_3}\mu_{J_1J_2}^{\beta_1}\mu_{J_2J_3}^{\beta_0}\mu_{J_3g}^{\beta_2}\quad(3102)}{(\omega_{J_1g}-\omega)(\omega_{J_2g})(\omega_{J_3g}-\omega)}$	Single	Ground	Single	Single
$+\dfrac{\mu_{gJ_1}^{\beta_3}\mu_{J_1J_2}^{\beta_2}\mu_{J_2J_3}^{\beta_0}\mu_{J_3g}^{\beta_1}\quad(3201)}{(\omega_{J_1g}-\omega)(\omega_{J_2g})(\omega_{J_3g}-\omega)}$	Single	Ground	Single	Single
$+\dfrac{\mu_{gJ_1}^{\beta_1}\mu_{J_1J_2}^{\beta_2}\mu_{J_2J_3}^{\beta_3}\mu_{J_3g}^{\beta_0}\quad(1230)}{(\omega_{J_1g}+\omega)(\omega_{J_2g}+2\omega)(\omega_{J_3g}+\omega)}$	—	—	—	—
$+\dfrac{\mu_{gJ_1}^{\beta_1}\mu_{J_1J_2}^{\beta_3}\mu_{J_2J_3}^{\beta_2}\mu_{J_3g}^{\beta_0}\quad(1320)}{(\omega_{J_1g}+\omega)(\omega_{J_2g})(\omega_{J_3g}+\omega)}$	—	Ground	—	—
$+\dfrac{\mu_{gJ_1}^{\beta_2}\mu_{J_1J_2}^{\beta_1}\mu_{J_2J_3}^{\beta_3}\mu_{J_3g}^{\beta_0}\quad(2130)}{(\omega_{J_1g}+\omega)(\omega_{J_2g}+2\omega)(\omega_{J_3g}+\omega)}$	—	—	—	—
$+\dfrac{\mu_{gJ_1}^{\beta_2}\mu_{J_1J_2}^{\beta_3}\mu_{J_2J_3}^{\beta_1}\mu_{J_3g}^{\beta_0}\quad(2310)}{(\omega_{J_1g}+\omega)(\omega_{J_2g})(\omega_{J_3g}+\omega)}$	—	Ground	—	—
$+\dfrac{\mu_{gJ_1}^{\beta_3}\mu_{J_1J_2}^{\beta_1}\mu_{J_2J_3}^{\beta_2}\mu_{J_3g}^{\beta_0}\quad(3120)}{(\omega_{J_1g}-\omega)(\omega_{J_2g})(\omega_{J_3g}+\omega)}$	Single	Ground	—	—
$+\dfrac{\mu_{gJ_1}^{\beta_3}\mu_{J_1J_2}^{\beta_2}\mu_{J_2J_3}^{\beta_1}\mu_{J_3g}^{\beta_0}\quad(3210)}{(\omega_{J_1g}-\omega)(\omega_{J_2g})(\omega_{J_3g}+\omega)}$	Single	Ground	—	—

A.1.5   Inhomogeneous Linear Susceptibility Solution

The inhomogeneous solution involves integrating the homogeneous linear susceptibility (Equation (2.24))

$$\frac{1}{(\omega_{ag}-\omega-i\Gamma_{ag})^{\alpha_{ag}}}, \quad \text{where} \quad \Gamma_{ag}>0 \quad \text{and} \quad 0<\alpha_{ag}\leq 1 \qquad (A.3)$$

over the level energy ω_{ag}, weighted by an inhomogeneous broadening function (as discussed in Chapter 2). Taking the inhomogeneous broadening function to be a normalized Gaussian, this gives the following solution for the inhomogeneously broadened linear

susceptibility:

$$
\chi^{(1)}_{\beta_0,\beta_1,\text{inhom}} = \frac{N}{\epsilon_o\hbar}\rho_o(g)\sum_{a^c}\mu^{\beta_0}_{ga}\,\mu^{\beta_1}_{ag}\frac{\sqrt{4\ln(2)}}{\sqrt{\pi}\Gamma_{a,\text{inh}}}\int\limits_{-\infty}^{+\infty}d\omega_{ag}\,\frac{e^{-\dfrac{4\ln(2)}{\Gamma^2_{a,\text{inh}}}\left(\omega_{ag}-\omega^c_{ag}\right)^2}}{(\omega_{ag}-\omega-i\Gamma_{ag})^{\alpha_{ag}}}
$$

$$
= \frac{N}{\epsilon_o\hbar}\rho_o(g)\sum_{a^c}\mu^{\beta_0}_{ga}\,\mu^{\beta_1}_{ag}\frac{\sqrt{4\ln(2)}}{\sqrt{\pi}\Gamma_{a,\text{inh}}}\int\limits_{-\infty}^{+\infty}dx\,\frac{e^{-\dfrac{4\ln(2)}{\Gamma^2_{a,\text{inh}}}x^2}}{(-x+\Delta_{a^c\omega}-i\Gamma_{ag})^{\alpha_{ag}}}
$$

(A.4)

where $\Delta_{ag^c\omega}=\omega_{ag^c}-\omega$, and $-x=\omega_{ag}-\omega_{ag^c}$. The Fourier transform of the susceptibility denominator is given by Equation (2.18),

$$
R_i(t_i) = \frac{(\mp i)^\alpha\sqrt{2\pi}}{\Upsilon(\alpha_i)}\,H(t_i)\,t_i^{\alpha_i-1}\,e^{\pm i\,(\Delta_{a^c\omega}\pm i\Gamma_i)\,t_i}\,.
$$

(A.5)

In time, Equation (A.4) becomes a convolution integral, giving

$$
\chi^{(1)}_{\beta_0,\beta_1,\text{inhom}} = \sqrt{2\pi}\frac{N}{\epsilon_o\hbar}\rho_o(g)\sum_{a^c}\mu^{\beta_0}_{ga}\,\mu^{\beta_1}_{ag}\frac{\sqrt{4\ln(2)}}{\sqrt{\pi}\Gamma_{a,\text{inh}}}\lim_{\tau\to0}\frac{1}{\sqrt{2\pi}}\int\limits_{-\infty}^{+\infty}dx\,\frac{e^{-\dfrac{4\ln(2)}{\Gamma^2_{a,\text{inh}}}x^2}}{(-x+\Delta_{a^c\omega}-i\Gamma_{ag})^{\alpha_{ag}}}e^{-ix\tau}
$$

$$
= \sqrt{2\pi}\frac{N}{\epsilon_o\hbar}\rho_o(g)\sum_{a^c}\mu^{\beta_0}_{ga}\,\mu^{\beta_1}_{ag}\frac{(+i)^{\alpha_{ag}}}{\Upsilon(\alpha_{ag})}\lim_{\tau\to0}\int\limits_{0}^{+\infty}dt\,t^{\alpha_{ag}-1}\,e^{-\left(i\Delta_{a^c\omega}+\Gamma_{ag}\right)t}
$$

$$
\times\,e^{-\dfrac{\Gamma^2_{a,\text{inh}}}{16\ln(2)}(\tau-t)^2}\,.
$$

(A.6)

Taking the limit of $\tau\to0$ this can be solved by noting, from [47, Page 382, Equation 3.462, #1], that

$$
\int\limits_{0}^{+\infty}dx\,x^{\alpha-1}\,e^{-\beta x^2-\gamma x} = (2\beta)^{-\alpha/2}\,\Upsilon(\alpha)\,e^{\frac{1}{4}\frac{\gamma^2}{2\beta}}\,D_{-\alpha}\left(\frac{\gamma}{\sqrt{2\beta}}\right)
$$

(A.7)

subject to the restrictions $\mathbb{R}e\{\beta\}>0$ and $\mathbb{R}e\{\alpha\}>0$, and where D is the Parabolic Cylinder function (see Section A.2.1). Note that in our case the first condition is always satisfied as long as the inhomogeneous broadening parameter is greater than zero, which is a physically reasonable assumption to make. From this we get the final answer, that

the inhomogeneous linear susceptibility is equal to

$$
\chi^{(1)}_{\beta_0,\beta_1,\text{inhom}} = \sqrt{2\pi}\,\frac{N}{\epsilon_o \hbar}\rho_o(g)\sum_{a^c}\mu^{\beta_0}_{ga}\,\mu^{\beta_1}_{ag}\,(+i)^{\alpha_{ag}}\left(\frac{\sqrt{8\ln(2)}}{\Gamma_{a,\text{inh}}}\right)^{\alpha_{ag}}
$$
$$
\times\ e^{+\frac{1}{4}\frac{8\ln(2)}{\Gamma^2_{a,\text{inh}}}\left(i\Delta_{a^c\omega}+\Gamma_{ag}\right)^2}\ D_{-\alpha_{ag}}\left(\frac{\sqrt{8\ln(2)}}{\Gamma_{a,\text{inh}}}\left(i\Delta_{a^c\omega}+\Gamma_{ag}\right)\right)
$$

$$(A.8)$$

A.1.6 The Relationship Between $\overleftrightarrow{\chi}^{(1)}$, $\overleftrightarrow{\epsilon}$, and $\vec{n}$

To outline the relationships between the susceptibility, permittivity, and the refractive index the linear regime of wave propagation needs to be considered. Starting with Maxwell's equations for non-magnetic media and eliminating the magnetic field term the wave equation, containing only the electric field term, is [see, for example, Butcher and Cotter ([8, Chapter 7]]:

$$
\vec{\nabla}\times\vec{\nabla}\times\vec{\mathbf{E}}(t) = -\frac{1}{c^2}\frac{\partial^2}{\partial t^2}\vec{\mathbf{E}}(t) - \mu_o\frac{\partial^2}{\partial t^2}\vec{\mathbf{P}}(t)
$$
$$
\vec{\nabla}\times\vec{\nabla}\times\vec{\mathbf{E}}(\omega) = \frac{\omega^2}{c^2}\vec{\mathbf{E}}(\omega) + \omega^2\mu_o\vec{\mathbf{P}}(\omega)\ .
$$

$$(A.9)$$

Considering only the linear polarization term and inserting $\vec{\mathbf{P}}^{(1)}(\omega) = \epsilon_o\overleftrightarrow{\chi}^{(1)}(-\omega;\omega)\cdot\vec{\mathbf{E}}(\omega)$ (Equation (2.23)) into the latter equation along with the definition $\mu_o = 1/(\epsilon_o c^2)$, the wave equation becomes

$$
\vec{\nabla}\times\vec{\nabla}\times\vec{\mathbf{E}}(\omega) = \frac{\omega^2}{c^2}\left(1+\overleftrightarrow{\chi}^{(1)}\right)\cdot\vec{\mathbf{E}}(\omega) = \frac{\omega^2}{c^2}\overleftrightarrow{\epsilon}^{(1)}\cdot\vec{\mathbf{E}}(\omega)\ ,
$$

$$(A.10)$$

which provides the definition of $\overleftrightarrow{\epsilon}^{(1)}$ in terms of $\overleftrightarrow{\chi}^{(1)}$. The net contribution of non-resonant terms to the behaviour of $\overleftrightarrow{\chi}^{(1)}$ is included here as a constant as we are interested in absorption, for which only the resonant terms dominate. In GaAs, this constant is $\epsilon_r = 12.40$ [49].

The permittivity now needs to be related to the refractive index, $n(\omega)$. To do this, consider the solution to Equation (A.10). One such solution are the waves

$$
\vec{\mathbf{E}}(\omega) = \hat{E}(\omega)\,e^{i\vec{\mathbf{k}}\cdot\vec{\mathbf{r}}}\quad\text{with}\quad\vec{\mathbf{k}} = \frac{\omega}{c}\,n(\omega)\hat{k} = \frac{\omega}{c}\,[n_{\mathbb{Re}}(\omega)+in_{\mathbb{Im}}(\omega)]\,\hat{k}
$$

$$(A.11)$$

where the unit vector $\hat{k}$ is a real unit vector in the direction of propagation ($\hat{k}\cdot\hat{k} = 1$). The two orthogonal electric field unit vectors can be separated out of $\hat{E}$, by writing it as $\hat{E} = \hat{e}\hat{E}(\omega)$. The complex orthogonal unit vector $\hat{e}$ is in the direction of polarization of the field ($\hat{e}\cdot\hat{e}^* = 1$). The envelope function $\hat{E}(\omega)$ is, in general, a function of the spatial

coordinates as well. Note that there are two independent, orthogonal directions of $\hat{e}$ for each direction $\hat{k}$. Inserting the vector identity (see, for example, page 118 of [58])

$$\vec{v} \times (\vec{v} \times \vec{e}) = (\vec{v} \cdot \vec{e})\vec{v} - (\vec{v} \cdot \vec{v})\vec{e} \tag{A.12}$$

into Equation (A.10), the result is *Fresnel's equation*,

$$\left[(\hat{k} \cdot \hat{e})\hat{k} - \hat{e} \right] [n_{\mathbb{Re}} + in_{\mathbb{Im}}]^2 + \overleftrightarrow{\epsilon} \cdot \hat{e} = 0 . \tag{A.13}$$

Fresnel's equation connects the direction of propagation ($\hat{k}$) with the refractive index in that direction. Equation (A.13) represents a system of three homogeneous, linear equations for the components of $\hat{e}$, and the determinant of their coefficients must thus vanish if this system of equations is to be consistent. Re-writing this equation in the form $\overleftrightarrow{\mathbf{K}} \cdot \hat{e} = 0$ we get the general determinential equation $|\overleftrightarrow{\mathbf{K}}| = 0$, or

$$\left| [n_{\mathbb{Re}} + in_{\mathbb{Im}}]^2 [\overleftrightarrow{\mathbf{K}} - \overleftrightarrow{\mathbf{1}}] + \overleftrightarrow{\epsilon} \right| = 0 , \tag{A.14}$$

where the components of $\overleftrightarrow{\mathbf{K}}$, derived from $\hat{k}$, are $k_i k_j$ ($i, j = \{x, y, z\}$).

For GaAs, since $\overleftrightarrow{\mathcal{X}}^{(1)}$ is a symmetrical tensor, so is $\overleftrightarrow{\epsilon}^{(1)}$ [8, Chapter 5 & Appendix 3]. This means that principal axes can be found where $\overleftrightarrow{\epsilon}^{(1)}$ is diagonal. For cubic (GaAs) or isotropic materials the components ϵ_{ii} are along the principal axes and the determinant reduces to the more familiar equation

$$n = \sqrt{\epsilon} . \tag{A.15}$$

A.1.7 Inhomogeneous Broadening

In Chapter 2, it was mentioned that the Gaussian inhomogeneous broadening weight function is

$$g_{inh} = \left(\frac{4 \ln 2}{\pi} \right)^{n/2} |\mathbf{\Gamma} \, \mathbf{\Lambda} \, \mathbf{\Gamma}|^{-1/2} e^{-4 \ln 2 \left((\vec{\omega} - \vec{\omega}^c) \mathbf{\Gamma}^{-1} \, \mathbf{\Lambda}^{-1} \, \mathbf{\Gamma}^{-1} (\vec{\omega} - \vec{\omega}^c) \right)} . \tag{A.16}$$

$\mathbf{\Gamma}^{-1}$ is a 2-D matrix with diagonal elements $\Gamma_{ii}^{-1} = 1/\Gamma_{J_i x, \text{inh}}$ and off-diagonal elements zero. The correlation matrix $\mathbf{\Lambda}$ is a symmetric 2-D matrix with diagonal elements $\Lambda_{ii} = 1$ and off-diagonal elements $\Lambda_{ij} = \Lambda_{ji}) = \lambda_{J_i J_j}$, where $-1 \leq \lambda_{J_i J_j} \leq 1$. $|\mathbf{\Gamma} \, \mathbf{\Lambda} \, \mathbf{\Gamma}|$ is the determinant of the multiplied matrices. In this section, the forms of this matrix and derivation of the partially correlated and fully-correlated polarization is given.

The correlation matrix, $\mathbf{\Gamma} \mathbf{\Lambda} \mathbf{\Gamma}$ described above looks like

$$\begin{pmatrix} \Gamma_{inh,1} & 0 & \cdots & 0 \\ 0 & \Gamma_{inh,2} & \cdots & 0 \\ \vdots & \vdots & \ddots & \vdots \\ 0 & 0 & \cdots & \Gamma_{inh,n} \end{pmatrix} \begin{pmatrix} 1 & \lambda_{1,2} & \cdots & \lambda_{1,n} \\ \lambda_{2,1} & 1 & \cdots & \lambda_{2,n} \\ \vdots & \vdots & \ddots & \vdots \\ \lambda_{n,1} & \lambda_{n,2} & \cdots & 1 \end{pmatrix} \begin{pmatrix} \Gamma_{inh,1} & 0 & \cdots & 0 \\ 0 & \Gamma_{inh,2} & \cdots & 0 \\ \vdots & \vdots & \ddots & \vdots \\ 0 & 0 & \cdots & \Gamma_{inh,n} \end{pmatrix} .$$

$$\tag{A.17}$$

The correlation matrix is real, Hermitian ($\mathbf{\Lambda} = \mathbf{\Lambda}^\dagger$, or $\Lambda_{n,m} = \Lambda_{m,n}$), and all the inhomogeneous FWHM parameters ($\Gamma_{inh,m}$) are real and greater than (inhomogeneous) or equal to (homogeneous) zero. Additionally, the correlation parameters $\lambda_{n,m}$ lie in the range -1 (anticorrelated) to 0 (uncorrelated) to $+1$ (correlated). By making the appropriate changes of variables and taking the limits as the correlation parameters approach $+1$, we get the fully correlated case ($\lambda_{n,m} = +1$).

A.1.7.1 Two-Dimensional Gaussian Broadening

This case is used in both the single ($a \neq c$) and double ($a = c$) level DFWM terms. It includes a correlation parameter, λ The correlation matrix for this case is

$$
\begin{pmatrix} \Gamma_a & 0 \\ 0 & \Gamma_c \end{pmatrix} \begin{pmatrix} 1 & \lambda \\ \lambda & 1 \end{pmatrix} \begin{pmatrix} \Gamma_a & 0 \\ 0 & \Gamma_c \end{pmatrix} = \begin{pmatrix} \Gamma_a^2 & \lambda\Gamma_a\Gamma_c \\ \lambda\Gamma_a\Gamma_c & \Gamma_c^2 \end{pmatrix} . \tag{A.18}
$$

Inverting this gives

$$
\begin{pmatrix} \dfrac{1}{\Gamma_a} & 0 \\ 0 & \dfrac{1}{\Gamma_c} \end{pmatrix} \dfrac{1}{(1-\lambda^2)} \begin{pmatrix} 1 & -\lambda \\ -\lambda & 1 \end{pmatrix} \begin{pmatrix} \dfrac{1}{\Gamma_a} & 0 \\ 0 & \dfrac{1}{\Gamma_c} \end{pmatrix} = \dfrac{1}{(1-\lambda^2)} \begin{pmatrix} \dfrac{1}{\Gamma_a^2} & -\dfrac{\lambda}{\Gamma_a\Gamma_c} \\ -\dfrac{\lambda}{\Gamma_a\Gamma_c} & \dfrac{1}{\Gamma_c^2} \end{pmatrix} \tag{A.19}
$$

Multiplying by the appropriate frequency terms gives the 2-D inhomogeneous polarization

$$
\vec{\mathbf{P}}_{\text{inh}}(\Delta_{ap}^c; \Delta_{cp}^c) = \frac{4\ln 2}{\pi\Gamma_a\Gamma_c\sqrt{1-\lambda^2}} \int\limits_{-\infty}^{+\infty} d\,\Delta_{ap} \int\limits_{-\infty}^{+\infty} d\,\Delta_{cp} \ \vec{\mathbf{P}}_{\text{hom}}(\Delta_{ap}\,;\,\Delta_{cp})
$$

$$
\times \ e^{-\dfrac{4\ln 2}{(1-\lambda^2)} \left(\dfrac{(\Delta_{ap} - \Delta_{ap}^c)^2}{\Gamma_a^2} - \dfrac{2\lambda(\Delta_{ap} - \Delta_{ap}^c)(\Delta_{cp} - \Delta_{cp}^c)}{\Gamma_a\Gamma_c} + \dfrac{(\Delta_{cp} - \Delta_{cp}^c)^2}{\Gamma_c^2} \right)} . \tag{A.20}
$$

Note that $\Delta_{ip}^c = \omega_i^c - \omega^p$.

Making the variable substitutions

$$
x_c = \frac{\sqrt{4\ln 2}}{\Gamma_c}(\Delta_{cp} - \Delta_{cp}^c)\,,\ \text{then}\ x_a = \frac{\sqrt{4\ln 2}}{\Gamma_a\sqrt{1-\lambda^2}}(\Delta_{ap} - \Delta_{ap}^c) - \frac{\lambda}{\sqrt{1-\lambda^2}}x_c\,, \tag{A.21}
$$

the above polarization expression becomes

$$
\vec{\mathbf{P}}_{\text{inh}}(\Delta_{ap}\,;\,\Delta_{cp}) = \frac{1}{\pi} \int\limits_{-\infty}^{+\infty} d\,x_a\ e^{-x_a^2} \int\limits_{-\infty}^{+\infty} d\,x_c\ e^{-x_c^2}
$$

$$
\times \ \vec{\mathbf{P}}_{\text{hom}}\left(\frac{\Gamma_a}{\sqrt{4\ln 2}}\left[\sqrt{1-\lambda^2}x_a + \lambda x_c\right] + \Delta_{ap}^c\,;\,\frac{\Gamma_c}{\sqrt{4\ln 2}}x_c + \Delta_{ap}^c \right) \tag{A.22}
$$

Taking the limit as $\lambda \to +1^-$, the homogeneous polarization becomes independent of the x_a variable and it can be integrated out, reducing the expression to the one dimensional case, with the distinguishing characteristic that each of our original variables is now replaced by a term that contains the inhomogeneous broadening FWHM for the corresponding term. This expression can replace the 1-D inhomogeneous broadening integral in the case that $a = c$, but only for the correlated expression below.

$$\vec{P}_{inh}(\Delta^c_{ap}; '\Delta^c_{cp}) = \frac{1}{\sqrt{\pi}} \int\limits_{-\infty}^{+\infty} dx \, e^{-x^2} \, \vec{P}_{hom}\left(\frac{\Gamma_a}{\sqrt{4\ln 2}}x + \Delta^c_{ap}; \frac{\Gamma_c}{\sqrt{4\ln 2}}x + \Delta^c_{cp}\right) \quad \text{(A.23)}$$

A.1.7.2 Three-Dimensional Gaussian Broadening

The 3-D case is, in general, used in double level $a \neq c$ FWM terms. It includes three correlation parameters linking the three combinations of two variables. The correlation matrix for this case is

$$\begin{pmatrix} \Gamma_a & 0 & 0 \\ 0 & \Gamma_b & 0 \\ 0 & 0 & \Gamma_c \end{pmatrix} \begin{pmatrix} 1 & \lambda_{a,b} & \lambda_{a,c} \\ \lambda_{a,b} & 1 & \lambda_{c,b} \\ \lambda_{a,c} & \lambda_{c,b} & 1 \end{pmatrix} \begin{pmatrix} \Gamma_a & 0 & 0 \\ 0 & \Gamma_b & 0 \\ 0 & 0 & \Gamma_c \end{pmatrix} = \begin{pmatrix} \Gamma_a^2 & \lambda_{a,b}\Gamma_a\Gamma_b & \lambda_{a,c}\Gamma_a\Gamma_c \\ \lambda_{a,b}\Gamma_a\Gamma_b & \Gamma_b^2 & \lambda_{c,b}\Gamma_c\Gamma_b \\ \lambda_{a,c}\Gamma_a\Gamma_c & \lambda_{c,b}\Gamma_c\Gamma_b & \Gamma_c^2 \end{pmatrix}.$$
$$\text{(A.24)}$$

The determinant of this matrix is $|\Lambda| = 1 - \lambda_{a,b}^2 - \lambda_{a,c}^2 - \lambda_{c,b}^2 + 2\lambda_{a,b}\lambda_{a,c}\lambda_{c,b}$, and the inverse of the matrix is

$$\begin{pmatrix} \frac{1}{\Gamma_a} & 0 & 0 \\ 0 & \frac{1}{\Gamma_b} & 0 \\ 0 & 0 & \frac{1}{\Gamma_c} \end{pmatrix} \frac{1}{|\Lambda|} \begin{pmatrix} (1-\lambda_{c,b}^2) & \lambda_{c,b}\lambda_{a,c} - \lambda_{a,b} & \lambda_{a,b}\lambda_{c,b} - \lambda_{a,c} \\ \lambda_{a,c}\lambda_{c,b} - \lambda_{a,b} & (1-\lambda_{a,c}^2) & \lambda_{a,b}\lambda_{a,c} - \lambda_{c,b} \\ \lambda_{a,b}\lambda_{c,b} - \lambda_{a,c} & \lambda_{a,b}\lambda_{a,c} - \lambda_{c,b} & (1-\lambda_{a,b}^2) \end{pmatrix} \begin{pmatrix} \frac{1}{\Gamma_a} & 0 & 0 \\ 0 & \frac{1}{\Gamma_b} & 0 \\ 0 & 0 & \frac{1}{\Gamma_c} \end{pmatrix}$$

$$= \frac{1}{|\Lambda|} \begin{pmatrix} \dfrac{(1-\lambda_{c,b}^2)}{\Gamma_a^2} & \dfrac{\lambda_{c,b}\lambda_{a,c} - \lambda_{a,b}}{\Gamma_a\Gamma_b} & \dfrac{\lambda_{a,b}\lambda_{c,b} - \lambda_{a,c}}{\Gamma_a\Gamma_c} \\[3mm] \dfrac{\lambda_{a,c}\lambda_{c,b} - \lambda_{a,b}}{\Gamma_a\Gamma_b} & \dfrac{(1-\lambda_{a,c}^2)}{\Gamma_b^2} & \dfrac{\lambda_{a,b}\lambda_{a,c} - \lambda_{c,b}}{\Gamma_c\Gamma_b} \\[3mm] \dfrac{\lambda_{a,b}\lambda_{c,b} - \lambda_{a,c}}{\Gamma_a\Gamma_c} & \dfrac{\lambda_{a,b}\lambda_{a,c} - \lambda_{c,b}}{\Gamma_c\Gamma_b} & \dfrac{(1-\lambda_{a,b}^2)}{\Gamma_c^2} \end{pmatrix}$$

$$\text{(A.25)}$$

Putting this into the inhomogeneous broadening integral gives the 3-D inhomogeneous

expression

$$\vec{P}_{\text{inh}}(\Delta_{ap}^c; \Delta_{b,2p}^c; \Delta_{cp}^c) = \left(\frac{4\ln 2}{\pi}\right)^{3/2} \frac{1}{\Gamma_a \Gamma_b \Gamma_c \sqrt{|\Lambda|}} \int\limits_{-\infty}^{+\infty} d\Delta_{ap} \int\limits_{-\infty}^{+\infty} d\Delta_{b,2p} \int\limits_{-\infty}^{+\infty} d\Delta_{cp}$$

$$\times\, e^{-\frac{4\ln 2}{|\Lambda|}\left(\frac{(1-\lambda_{c,b}^2)(\Delta_{ap}-\Delta_{ap}^c)^2}{\Gamma_a^2} - \frac{2(\lambda_{a,c}\lambda_{c,b}-\lambda_{a,b})(\Delta_{ap}-\Delta_{ap}^c)(\Delta_{b,2p}-\Delta_{b,2p}^c)}{\Gamma_a\Gamma_b}\right.}$$

$$\left.+\frac{(1-\lambda_{a,c}^2)(\Delta_{b,2p}-\Delta_{b,2p}^c)^2}{\Gamma_b^2} - \frac{2(\lambda_{a,b}\lambda_{c,b}-\lambda_{a,c})(\Delta_{ap}-\Delta_{ap}^c)(\Delta_{cp}-\Delta_{cp}^c)}{\Gamma_a\Gamma_c}\right.$$

$$\left.+\frac{(1-\lambda_{a,b}^2)(\Delta_{cp}-\Delta_{cp}^c)^2}{\Gamma_c^2} - \frac{2(\lambda_{a,b}\lambda_{a,c}-\lambda_{c,b})(\Delta_{cp}-\Delta_{cp}^c)(\Delta_{b,2p}-\Delta_{b,2p}^c)}{\Gamma_b\Gamma_c}\right)$$

$$\times\quad \vec{P}_{\text{hom}}(\Delta_{ap}; \Delta_{b,2p}; \Delta_{cp}) \tag{A.26}$$

Making the variable substitutions

$$x_b = \frac{\sqrt{4\ln 2}}{\Gamma_b}\left(\Delta_{b,2p} - \Delta_{b,2p}^c\right), \text{ then } x_a = \frac{\sqrt{4\ln 2}}{\Gamma_a\sqrt{1-\lambda_{a,b}^2}}\left(\Delta_{ap} - \Delta_{ap}^c\right) - \frac{\lambda_{a,b}}{\sqrt{1-\lambda_{a,b}^2}} x_b , \tag{A.27}$$

and, finally,

$$x_c = \frac{\sqrt{4\ln 2}\sqrt{1-\lambda_{a,b}^2}}{\Gamma_c\sqrt{|\Lambda|}}\left(\Delta_{cp} - \Delta_{cp}^c\right) - \frac{\lambda_{a,c} - \lambda_{a,b}\lambda_{c,b}}{\sqrt{|\Lambda|}} x_a - \frac{\lambda_{c,b}\sqrt{1-\lambda_{a,b}^2}}{\sqrt{|\Lambda|}} x_b , \tag{A.28}$$

the inhomogeneous polarization expression becomes

$$\vec{P}_{\text{inh}}(\Delta_{ap}^c; \Delta_{b,2p}^c; \Delta_{cp}^c) = \frac{1}{\pi^{3/2}} \int\limits_{-\infty}^{+\infty} dx_a\, e^{-x_a^2} \int\limits_{-\infty}^{+\infty} dx_b\, e^{-x_b^2} \int\limits_{-\infty}^{+\infty} dx_c\, e^{-x_c^2}$$

$$\times\, \vec{P}_{\text{hom}}\left(\frac{\Gamma_a}{\sqrt{4\ln 2}}\left[\sqrt{1-\lambda_{a,b}^2}x_a + \lambda_{a,b}x_b\right] + \Delta_{ap}^c;\, \frac{\Gamma_b}{\sqrt{4\ln 2}} x_b + \Delta_{b,2p}^c;\right.$$

$$\left.\frac{\Gamma_c}{\sqrt{4\ln 2}}\left[\frac{\sqrt{|\Lambda|}}{\sqrt{1-\lambda_{a,b}^2}} x_c + \frac{(\lambda_{a,c} - \lambda_{a,b}\lambda_{c,b})}{\sqrt{1-\lambda_{a,b}^2}} x_a + \lambda_{c,b} x_b\right] + x_c\right) \tag{A.29}$$

Taking the limit $\lambda_{n,m} \to +1^-$, the above expression is independent of $\lambda_{a,c}$ (except for the determinant). Setting both this and $\lambda_{c,b}$ to one, two of the terms in the third part of the homogeneous expression are of the form $0/0$. Using L'Hospital's rule to take the limits, these terms both vanish in the limit $\lambda_{a,b} \to +1^-$. The expression thus becomes independent of both the x_a and x_c variables and they can be integrated out,

again reducing the expression to one dimension. As with the 2–D case, the integral has the property that each of the original variables is now replaced by a term that contains the inhomogeneous broadening FWHM for the corresponding term.

$$
\vec{\mathbf{P}}_{\text{inh}} = \frac{1}{\sqrt{\pi}} \int\limits_{-\infty}^{+\infty} d\,x\, e^{-x^2}\, \vec{\mathbf{P}}_{\text{hom}} \left(\frac{\Gamma_a}{\sqrt{4\ln 2}}\, x + \Delta^c_{ap}\,;\; \frac{\Gamma_b}{\sqrt{4\ln 2}}\, x + \Delta^c_{b,2p}\,;\; \frac{\Gamma_c}{\sqrt{4\ln 2}}\, x + \Delta^c_{cp} \right)
\tag{A.30}
$$

A.2 Numerical Methods

This section outlines the evaluation of the integrals in the power law singularity method, which are of the form

$$
G(\omega) = \int\limits_a^b dt\, f(t) e^{i\omega t}\,,
\tag{A.31}
$$

where, in general, ω, a, and b could all vary in the entire range of $\pm\infty$. For this work, $a = 0$ and $b = +\infty$ and $f(t)$ is a smoothly varying (pulse shape) function times an exponential decay and a power law singularity at $t = 0$. For the special case of a Gaussian pulse shape the integral can be evaluated analytically as a parabolic cylinder function, discussed next. Following this, a general method of calculating these types of integrals using a modified Gaussian integration method will be described.

A.2.1 The Parabolic Cylinder Function $D_\nu(z)$

The parabolic cylinder function, $D_\nu(z)$, is useful in evaluating the inhomogeneous linear absorption expression. As well, it can be used as a test of the numerical method for the DFWM simulations, comparing the results of the single 'A' term integrations for the special case of Gaussian pulses. The parabolic cylinder functions can be defined by [47, page 382]

$$
D_{-\alpha}\left(\frac{\gamma}{\sqrt{2\beta}} \right) = \frac{(2\beta)^{\alpha/2}}{\Upsilon(\alpha)} e^{\frac{1}{4}\frac{\gamma^2}{2\beta}} \int\limits_0^{+\infty} dx\, x^{\alpha-1}\, e^{-\beta x^2 - \gamma x}
\tag{A.32}
$$

subject to the restrictions $\mathbb{R}e\,\{\beta\} > 0$ and $\mathbb{R}e\,\{\alpha\} > 0$. It is related to the confluent hypergeometric function, $_1\mathrm{F}_1(z)$, by the expression

$$
D_p(z) = 2^{p/2} e^{-z^2/4} \left\{ \frac{\sqrt{\pi}}{\Gamma\left(\frac{1-p}{2}\right)} {}_1\mathrm{F}_1\left(\frac{-p}{2}\,;\, \frac{1}{2}\,;\, \frac{z^2}{2} \right) - \frac{\sqrt{2\pi}\,z}{\Gamma\left(\frac{-p}{2}\right)} {}_1\mathrm{F}_1\left(\frac{1-p}{2}\,;\, \frac{3}{2}\,;\, \frac{z^2}{2} \right) \right\}\,,
\tag{A.33}
$$

and it is related to the error function by

$$D_{-1}(z) = e^{z^2/4} \sqrt{\frac{\pi}{2}} \, \text{erfc} \left(\frac{z}{\sqrt{2}} \right) . \qquad (A.34)$$

For p an integer with values greater than or equal to zero, it forms a set of orthogonal polynomials on $\pm\infty$, with weight 1. The formulae for evaluating $D_p(z)$ are given in [47], with numerical algorithms and routines given in [76]. These routines were adapted and modified for use in this work. Note that due to the complex arguement z inherent in this work, this function shows its full range of oscillatory and non-oscillatory exponential behaviour (increasing, decreasing, and asymptotically approaching limits).

A.2.2 Singular/Oscillatory Function Integration using Orthogonal Polynomials

The method used to integrate oscillatory/singular integrals is based on the calculation of Fourier transforms of orthogonal polynomials [77-84]. The integral

$$G(\omega) = \int_a^b dt \, w(t) \, f(t) e^{i\omega t} , \qquad (A.35)$$

is evaluated by first expanding $f(t)$ in terms of the orthogonal polynomials $p_k(t)$, as

$$f(t) = \sum_{k=0}^{+\infty} c_k p_k(t) , \qquad (A.36)$$

where the $p_k(t)$ are orthogonal in the space from $t = a$ to b with weight function $w(t)$. The orthogonality constant is given by

$$\int_a^b dt \, w(t) p_k(t) p_m(t) = \begin{cases} 0, & k \neq m \\ |p_k|^2, & k = m \end{cases} . \qquad (A.37)$$

The coefficients c_k are then defined by

$$c_k = |p_k|^{-2} \int_a^b dt \, w(t) p_k(t) f(t) . \qquad (A.38)$$

Putting the $f(t)$ expansion (A.36) back into the original integral (A.35) gives

$$
\begin{aligned}
G(\omega) &= \int_a^b dt\, w(t)\, f(t) e^{i\omega t} \\
&= \int_a^b dt\, w(t) \sum_{k=0}^{+\infty} c_k p_k(t) e^{i\omega t} \\
&= \sum_{k=0}^{+\infty} c_k \int_a^b dt\, w(t)\, p_k(t) e^{i\omega t} \\
&= \sum_{k=0}^{+\infty} c_k |p_k| b_k(\omega) \ ,
\end{aligned}
\tag{A.39}
$$

where

$$
b_k(\omega) = |p_k|^{-2} \int_a^b dt\, w(t)\, p_k(t) e^{i\omega t} \ .
\tag{A.40}
$$

Providing the integrals for $b_k(\omega)$ can be evaluated, this method has the advantage that the oscillatory terms are contained entirely within $b_k(\omega)$, with the function $f(t)$ being inside the c_k coefficients. In practice the series is not taken to $+\infty$, but is truncated at some value N. The function $f(t)$ is then approximated by an Nth order value $f_N(t)$, with the coefficients c_k evaluated by an $(N+1)$th order Gaussian quadrature method. $G_N(\omega)$ is then an Nth order approximation to $G(\omega)$, with the error in the approximation being dependent on how closely $f_N(t)$ approximates $f(t)$.

A.2.2.1 Orthogonal Polynomial Choices

There are three main polynomial choices used in this work, the Jacobi, Laguerre, and Hermite polynomials. The integration limits, weights, and usual symbols for these polynomials are listed in Table A.4, while further properties will be deferred to the sections on evaluating the $b_k(\omega)$ and c_k terms.

A.2.2.2 Modifications to Handle Convolution Integrals

The convolution integrals evaluated in this work are modifications of the above form,

$$
G(\omega) = \int_0^{+\infty} dt\, t^{\beta_j} \mu(t)\, f(\tau - t) e^{(i\Delta_j - \Gamma_j)t} \ .
\tag{A.41}
$$

Evaluation of these integrals is slightly more complex than the above method would indicate, and two general considerations need to be addressed to evaluate these integrals.

Polynomial		Weight	a	b
Jacobi	$P_k^{(\alpha,\beta)}(t)$	$(t-1)^\alpha (t+1)^\beta$, $\alpha, \beta > -1$	-1	$+1$
Laguerre	$L_k^{(\beta)}(t)$	$t^\beta e^{-t}$, $\beta > -1$	0	$+\infty$
Hermite	$H_k(t)$	e^{-t^2}	$-\infty$	$+\infty$

Table A.4: Integration limits and weights of Jacobi, Laguerre, and Hermite polynomials. These Laguerre polynomials are often called the *Generalized-Laguerre* polynomials, where the non-generalized version has $\beta = 0$ and the integrals then correspond to Laplace Transform integrals.

The first has to do with the slowness of convergence of the Laguerre polynomial method, while the second has to do with the change in delay value, τ, with the sharply peaked pulse shapes $f(\tau - t)$.

Early tests using only Laguerre polynomials indicated a highly oscillatory component. Figure A.2 shows the results of using the integral method with only the Laguerre polynomials as well as a combined Laguerre-Jacobi method (described below) with a varying switch-over point, a_{split}. Although the behaviour of the Laguerre polynomial method improves as the order (N) increases, it still retained the oscillatory component even at the largest values $(N = 125)$ possible with the routines currently used to calculate weights and zeros. For the combined methods, the integral is split into two. The range from 0 to a_{split} is calculated with the Jacobi method, while the remainder of the integral (a_{split} to $+\infty$) uses Laguerre polynomials. a_{split} depends on the pulse detuning,

$$a_{\text{split}} = \begin{cases} a_{\text{switch}}, & a_{\text{switch}} \geq \tau \\ \tau, & a_{\text{switch}} < \tau \end{cases} \tag{A.42}$$

With a large value of a_{switch}, the Jacobi portion of the signal starts to oscillate as well (solid line in the figure). A small switch-over value, approximately 10-20 times the pulse width, was found to be an optimal choice that worked consistently under a wide variety of test conditions.

The general integral method used to numerically evaluate equations such as Equation (A.41) is

$$I(\tau) = I_{\text{Jacobi}}(\tau) + I_{\text{Laguerre}}(\tau) = \int_0^{+\infty} dt\, t^{\beta_j}\, \mu(t)\, f(\tau - t) e^{(i\Delta_j - \Gamma_j)t} \quad (\beta_j > -1), \tag{A.43}$$

where

$$I_{\text{Jacobi}}(\tau) = \int_0^{a_{\text{split}}} dt\, t^{\beta_j}\, \mu(t)\, f(\tau - t) e^{(i\Delta_j - \Gamma_j)t} \quad (\beta_j > -1), \tag{A.44}$$
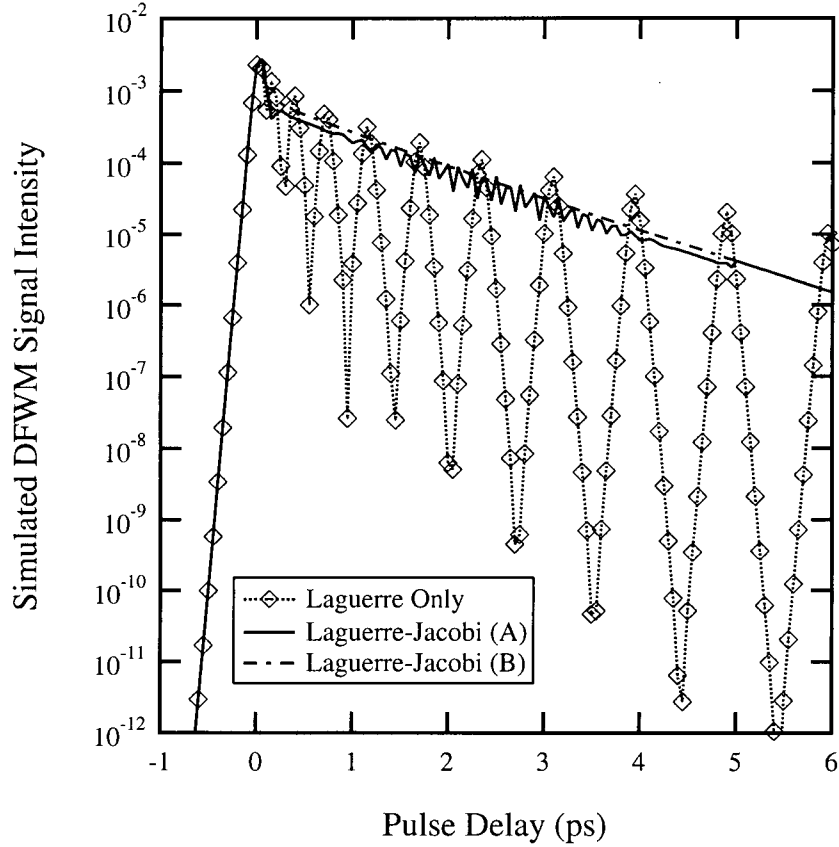
Figure A.2: Comparison of various Laguerre and Jacobi integral components, with 100 fs pulse widths. For the combined Laguerre-Jacobi method, (A) is the signal that results with the switch-over point $a_{\text{switch}} = 5\,\text{ps}$, while (B) results from $a_{\text{switch}} = 3\,\text{ps}$.

and

$$\text{I}_{\text{Laguerre}}(\tau) = \int\limits_{a_{\text{split}}}^{+\infty} dt\, t^{\beta_j}\, \mu(t)\, f(\tau - t)e^{(i\Delta_j - \Gamma_j)t} \quad (\beta_j > -1). \tag{A.45}$$

The first equation (A.44) is put into the standard Jacobi form by making the substitution $t' = 2t/a_{\text{split}} - 1$, or $t = a_{\text{split}}(t' + 1)/2$. Making these substitutions gives the following form, where the terms in the curly braces are the new function "$f(t)$" that is to be evaluated,

$$\text{I}_{\text{Jacobi}}(\tau) = \left(\frac{a_{\text{split}}}{2}\right)^{\beta_j + 1} e^{ia_{\text{split}}/2\,\Delta_j} \int\limits_{-1}^{+1} dt\, (t+1)^{\beta_j}\, e^{(ia_{\text{split}}/2\,\Delta_j t}$$

$$\left\{ \mu\left(a_{\text{split}}/2\,(t+1)\right) f\left(\tau - a_{\text{split}}/2\,(t+1)\right) e^{(-\Gamma_j a_{\text{split}}/2\,(t+1)} \right\}. \tag{A.46}$$

The Laguerre term (Equation (A.45)) is evaluated in a similar form, by making the substitution $t' = t - a_{\text{split}}$, resulting in

$$
I_{\text{Laguerre}}(\tau) = \frac{e^{(i\Delta_j a_{\text{split}} - \Gamma_j a_{\text{split}})}}{\Gamma_j} \int\limits_0^{+\infty} dt\, e^{(i\Delta_j/\Gamma_j - 1)t}
$$

$$
\left\{ (t/\Gamma_j + a_{\text{split}})^{\beta_j}\, \mu\, (t/\Gamma_j + a_{\text{split}})\, f\, (\tau - (t/\Gamma_j + a_{\text{split}})) \right\} \ . \quad \text{(A.47)}
$$

The point at which the integrals are split, a_{split}, is taken far enough away from the origin such that the Laguerre solution's singularity does not cause the large oscillatory component that was visible in the solution with only Laguerre terms. This was confirmed using Gaussian pulses and a constant μ term, which results in parabolic cylinder solutions for the integral. Experiments showed that the Jacobi term followed the 'exact' solution at short times, while the Laguerre terms dominated at longer times and that the choice of $a_{\text{switch}} = 10\text{-}20$ times the pulse width was the optimal point. This switch-over method of evaluating the integral has the effect that a magnitude and phase shift occur at the switch-over point where the convolution factor, τ, becomes the point at which the integral evaluation switches over. This is shown in Figure A.3, which shows the magnitude and phase of the complex integral, both uncorrected and corrected. The correction factor is applied to all the convolution delay values greater than the switch-over point as a multiplicative constant.

The inhomogeneous broadening integral uses the integral form

$$
\overrightarrow{\mathbf{P}}_{\text{inh}}^{(n)}(\omega_{J_1 x}^c; \omega_{J_2 x}^c; \cdots; \omega_{J_n x}^c) = \int\limits_{-\infty}^{+\infty} dx \quad e^{-x^2}
$$

$$
\times\ \overrightarrow{\mathbf{P}}_{\text{hom}}^{(n)} \left(\frac{\Gamma_{J_1 x,\ \text{inh}}}{\sqrt{4\ln(2)}}\, x + \omega_{J_1 x}^c;\ \frac{\Gamma_{J_2 x,\ \text{inh}}}{\sqrt{4\ln(2)}}\, x + \omega_{J_2 x}^c; \cdots \frac{\Gamma_{J_n x,\ \text{inh}}}{\sqrt{4\ln(2)}}\, x + \omega_{J_n x}^c \right) \ , \quad \text{(A.48)}
$$

from Equation (2.22) on page 25 and the Hermite polynomials. Since there is no singularity here, the integral is a Gaussian integration method. Several methods were implemented to calculate the inhomogeneous integral, as illustrated by the TI- and TR-DFWM simulated signal tests in Figures A.4 and A.5, using a system with two-excited single-level states .

The figures illustrate several points. First, the delta-function pulse solutions have deeper, more visible beats than the corresponding full-pulse shape method. Secondly, the inhomogeneous Hermite solution still has significant signals at times away from $t = 2\tau$, which depend on the number of Hermite terms and the size of the inhomogeneous broadening. As a result, a Hermite-Window method was implemented that uses the Hermite method to calculate the signal around $t = 2\tau$ and multiplies by a Gaussian outside the window, which is centered on the $t = 2\tau$ line, to remove the slowly converging portion. A faster method uses the homogeneous solution and multiplies by the same
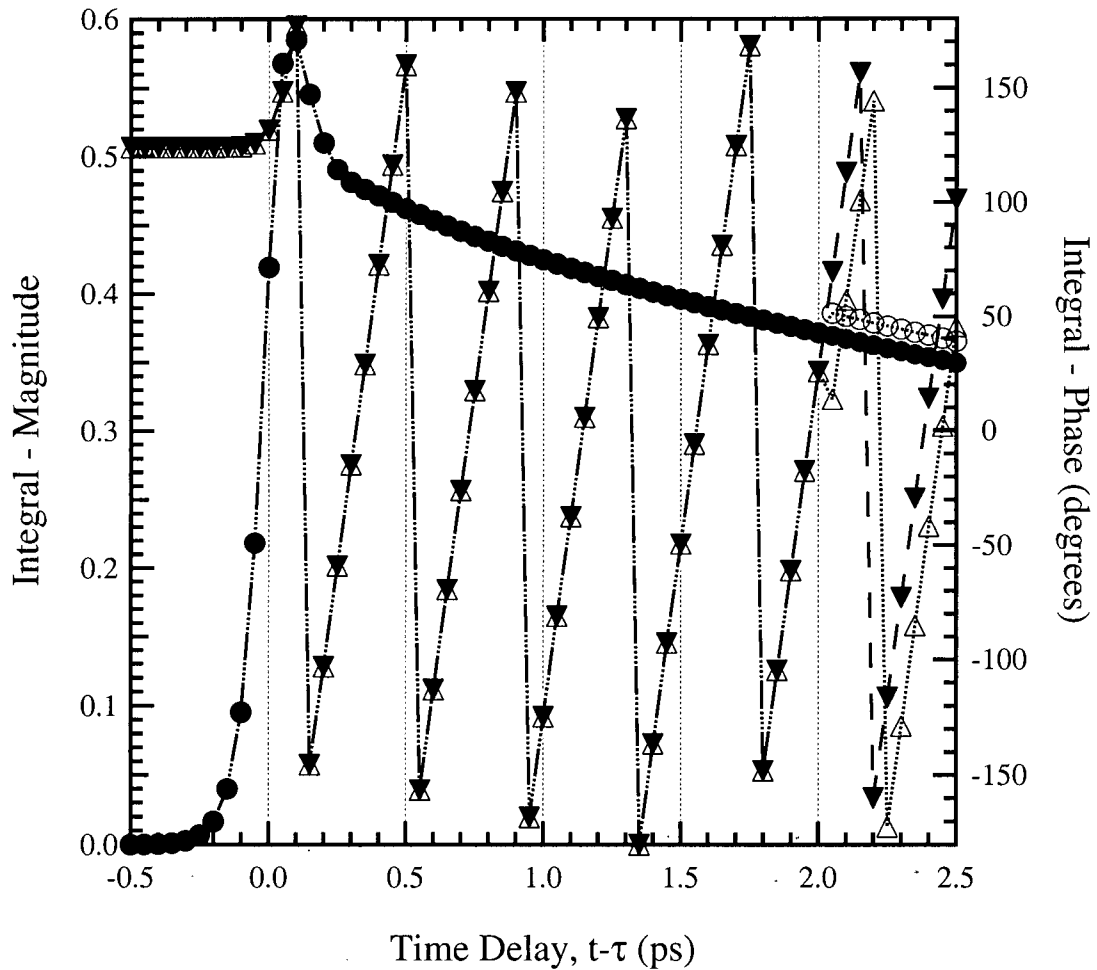
Figure A.3: Illustration of convolution integral method and integral correction factor. Amplitudes are the circles, phases are the triangles, uncorrected terms are empty symbols, and corrected terms are the filled symbols. ($a_{\text{switch}} = 2\,\text{ps}$.)
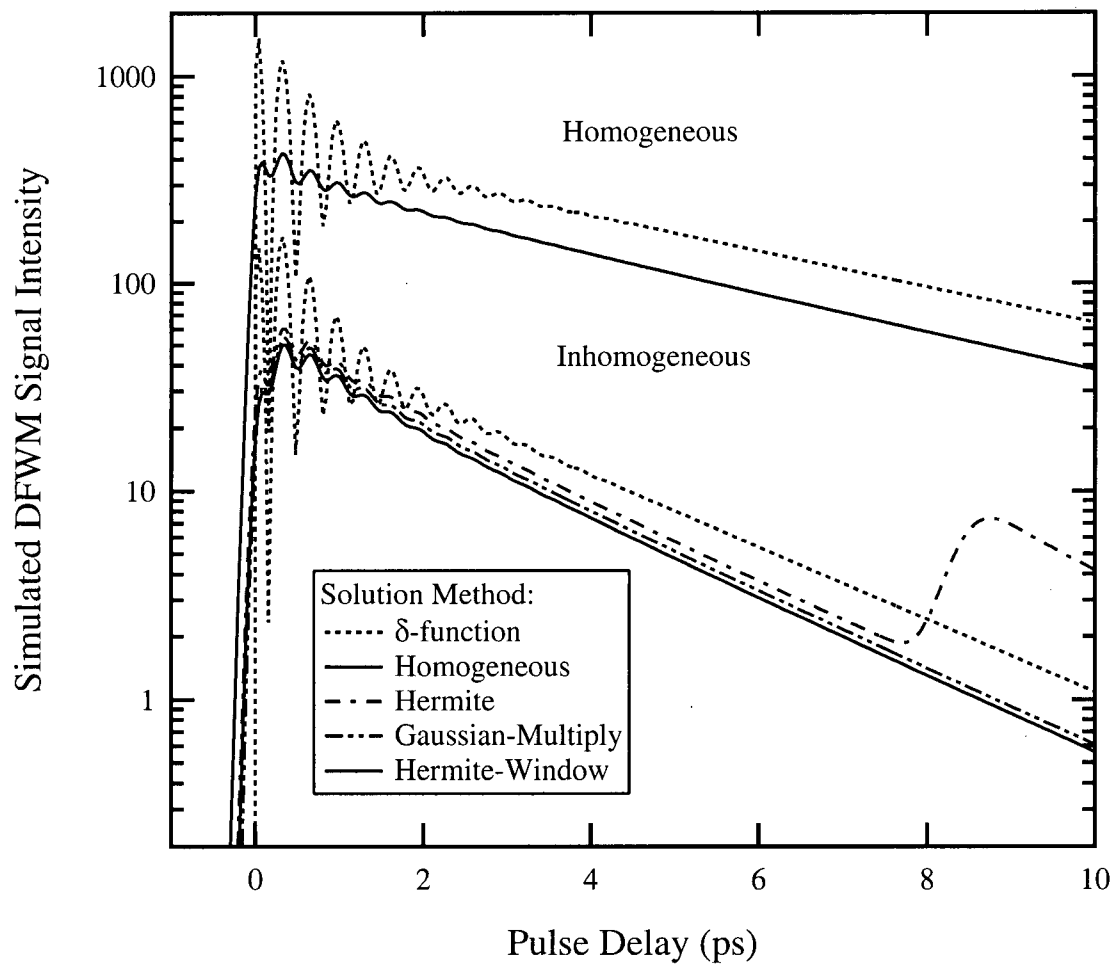
Figure A.4: Comparison of integral method types, both homogeneous and inhomogeneous, for TI-DFWM signal simulations of a two level system.
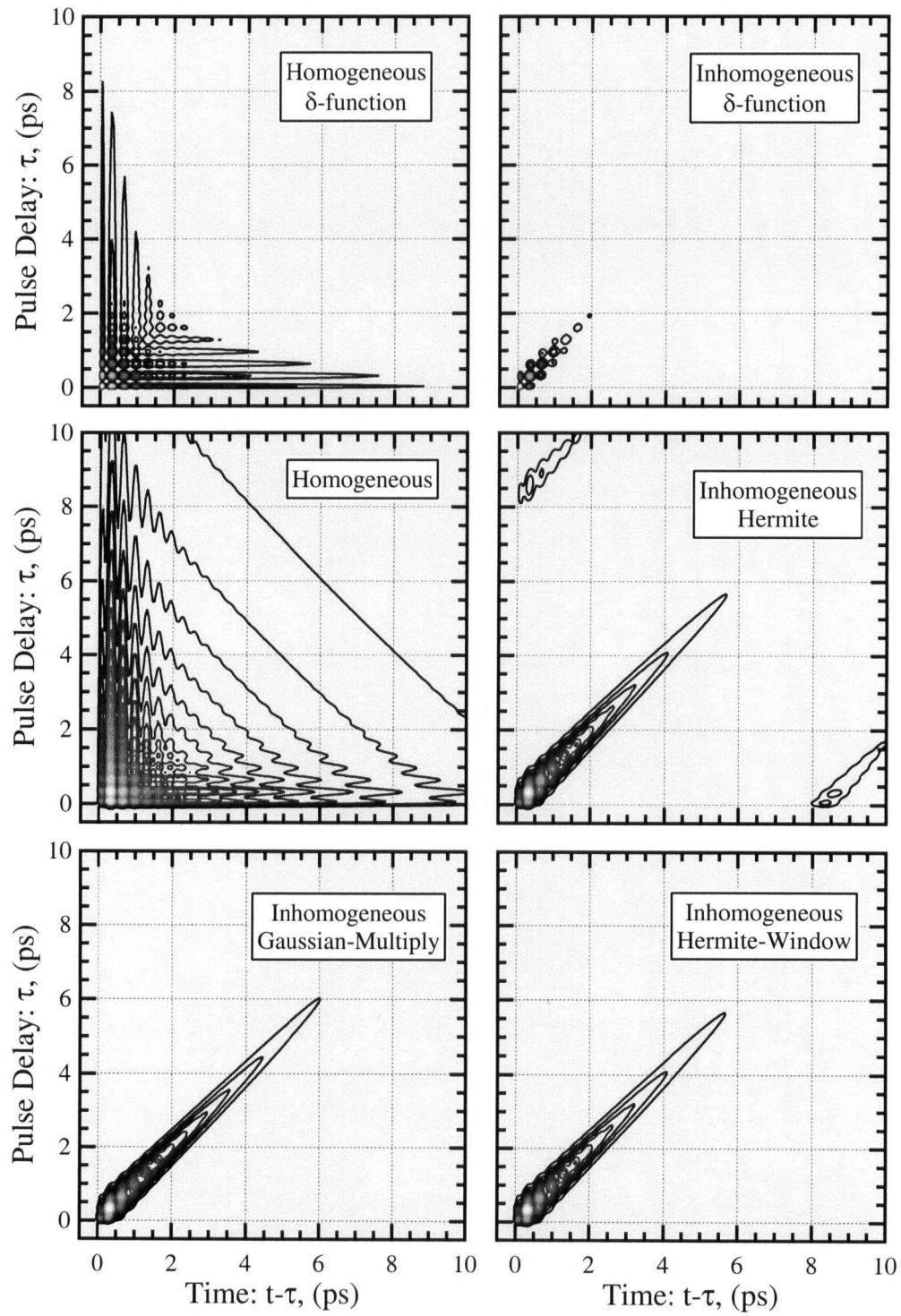
Figure A.5: Comparison of integral method types, both homogeneous and inhomogeneous, for TR-DFWM signal simulations of a two level system.

Gaussian used in the delta-function case to allow faster tests of the simulations. It does, however, suffer from the same problems as the delta-function case under some integration conditions (larger beat signals), although they are not as large as in the delta-function case.

A.2.3 Tests of Singular/Oscillatory Convolution Integral Method

A comprehensive test of the dependence of an inhomogeneous, two excited level system was conducted as a function of the number of terms used to perform the integration (N_{Jacobi}, N_{Laguerre}, and N_{Hermite}). Evaluation of these simulations to determine convergence was conducted by calculating convergence as both differences and relative differences in the solutions, as a function of the delay. The absolute convergence assumes that $I_{N_{\max}}(\tau)$ is correct, where $N_{\max}$ is the 125 term solution. The convergence for each delay term is then added using the sum of the squares of the individual differences to arrive at a convergence factor for the entire simulation, given by the formula

$$\sigma^2_{\text{Absolute, } (N,N_{\max})} = \frac{1}{N_\tau} \sum_\tau \left(I_N^{\text{DFWM}}(\tau) - I_{N_{\max}}^{\text{DFWM}}(\tau) \right)^2 \tag{A.49}$$

and

$$\sigma^2_{\text{Relative, } (N,N_{\max})} = \frac{1}{N_\tau} \sum_\tau \left(\frac{I_N^{\text{DFWM}}(\tau) - I_{N_{\max}}^{\text{DFWM}}(\tau)}{I_{N_{\max}}^{\text{DFWM}}(\tau)} \right)^2 . \tag{A.50}$$

The same process is then conducted for the incremental convergence factors, which compare how much the integral $I_{(N-1)_{\text{terms}}}$ changes when compared to $I_{N_{\text{terms}}}$. These are given by

$$\sigma^2_{\text{Absolute, } (N-1,N)} = \frac{1}{N_\tau} \sum_\tau \left(I_{N_{\text{terms}}}^{\text{DFWM}}(\tau) - I_{(N-1)_{\text{terms}}}^{\text{DFWM}}(\tau) \right)^2 \tag{A.51}$$

and

$$\sigma^2_{\text{Relative, } (N-1,N)} = \frac{1}{N_\tau} \sum_\tau \left(\frac{I_{N_{\text{terms}}}^{\text{DFWM}}(\tau) - I_{(N-1)_{\text{terms}}}^{\text{DFWM}}(\tau)}{I_{N_{\text{terms}}}^{\text{DFWM}}(\tau)} \right)^2 . \tag{A.52}$$

The results of these studies are illustrated in Figures A.6 and A.7. The Jacobi terms converge in an oscillatory manner with dips approximately one order of magnitude below their peaks. The Jacobi terms have a short oscillation (4-5 points), but converge in a monotonic manner by 6 orders of magnitude over the range from 10 to 125 points. In contrast, the Laguerre terms convergence is only about 2 orders of magnitude over the same range of terms. In contrast to the Jacobi terms, the Laguerre terms have a much longer oscillatory component with troughs about 2 orders of magnitude lower than the corresponding peaks.

For the combined Laguerre-Jacobi study, the terms follow the Jacobi solution out to about 80 terms and then the convergence difference estimates start to level out, consistent with the Laguerre terms starting to have a larger effect when more terms are used. The
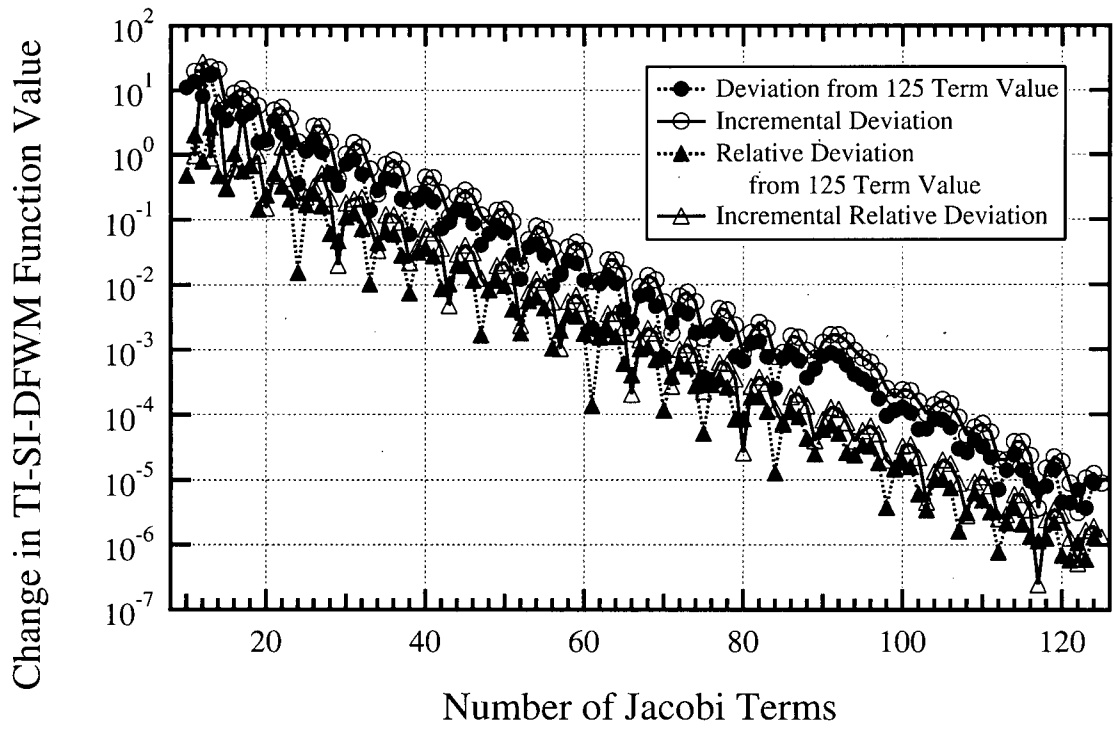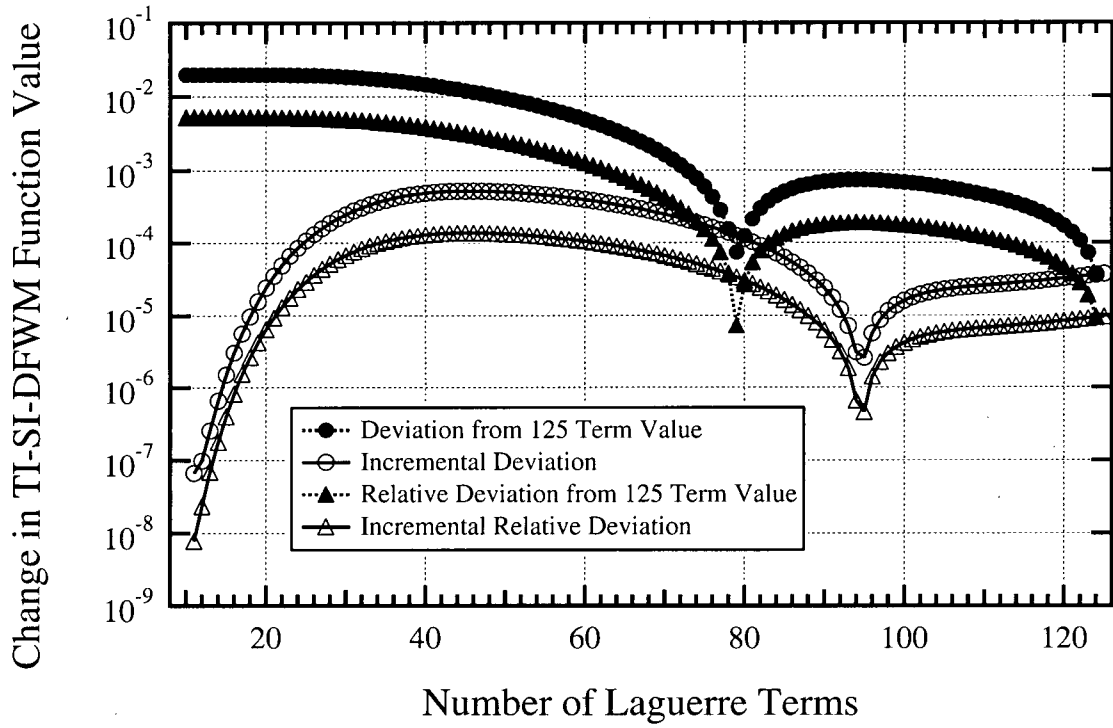
Figure A.6: Error in DFWM simulations with varying number of Laguerre (upper plot) or Jacobi (lower plot) terms. Number of Jacobi (upper), Laguerre (lower), and Hermite (both plots) terms are fixed at 125.

Hermite terms used for the inhomogeneous broadening integral also have an oscillatory component, after a initial fast decay, as the number of terms increases. These terms converge faster than the Laguerre terms, and are comparable to the convergence of the Jacobi terms.

The residuals for the absolute difference case comparing N terms to 125 terms is shown in Figures A.8 and A.9. They show an oscillatory component at small numbers of Jacobi and Hermite values that becomes smoother and dies off at larger values of N. In contrast, the Laguerre component appears as a single smooth peak. In all cases, there is a noticeable shift in the residual behaviour as the delay becomes equal to the switch-over point. For the Jacobi terms, the signal dies out, while the others are small before this point and die out more slowly afterwards.

An examination of the time-integrated signal simulations (Figure A.10) shows that these oscillatory components correspond to the beat signals in the two level system, shifted in phase from their large N values. The beat strengths are also larger, closer to the delta-function behaviour. The long term behaviour is also not exponential. By the time $N = 50$, the visible portions of this behaviour have disappeared in the simulation.

A.2.4   Calculation of $b_k(\omega)$ Coefficients

Use of the Gauss-Oscillatory integral method requires the ability to evaluate the $b_k(\omega)$ coefficients. These are the Fourier transforms of the orthogonal polynomials over their orthogonal integration limits, multiplied by their corresponding weights. From [81], the Laguerre polynomial integral

$$
b_k^{\text{Laguerre}}(\omega) = |L_k^{(\beta)}(t)|^{-2} \int\limits_{-\infty}^{+\infty} dt\, t^\beta e^{-t} L_k^{(\beta)}(t) e^{i\omega t} = i^{1+\beta}\, \omega^k \left(\frac{\omega - i}{1 + \omega^2} \right)^{k+1+\beta},
$$

(A.53)

where

$$
b_0^{\text{Laguerre}}(\omega) = \left(\frac{1 + i\omega}{1 + \omega^2} \right)^{1+\beta}
$$

(A.54)

and

$$
b_k^{\text{Laguerre}}(\omega) = \omega \left(\frac{\omega - i}{1 + \omega^2} \right)^k b_{k-1}(\omega) \qquad (k \neq 0) .
$$

(A.55)

The orthogonal normalization of the Laguerre polynomials is given by

$$
|L_k^{(\beta)}(t)|^2 = \Upsilon\, (k + 1 + \beta) \,/\, k! .
$$

(A.56)
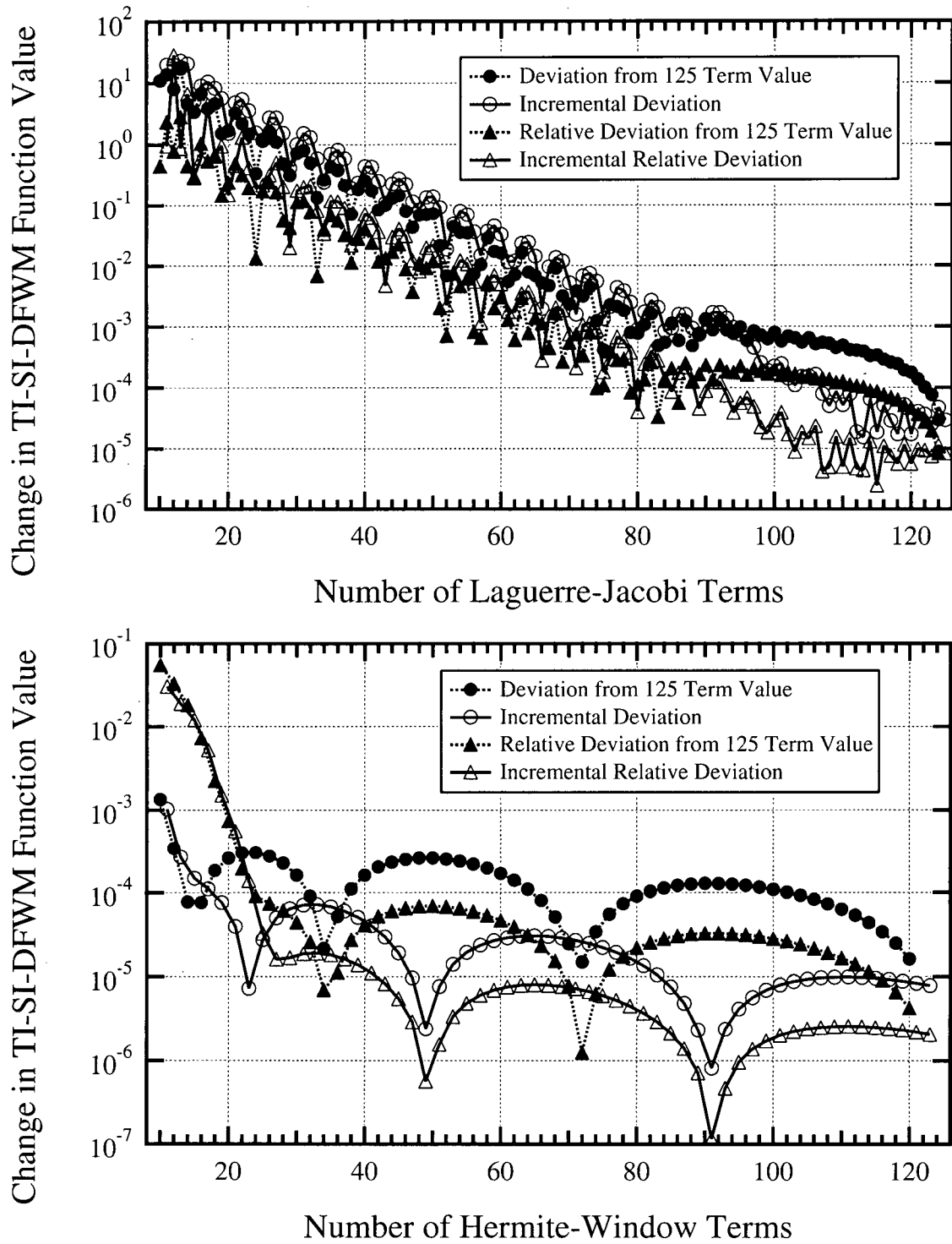
Figure A.7: Error in DFWM simulations with varying number of Laguerre and Jacobi (upper plot) or Hermite (lower plot) terms. Number of Hermite (upper) or Laguerre and Jacobi (lower) terms is fixed at 125.
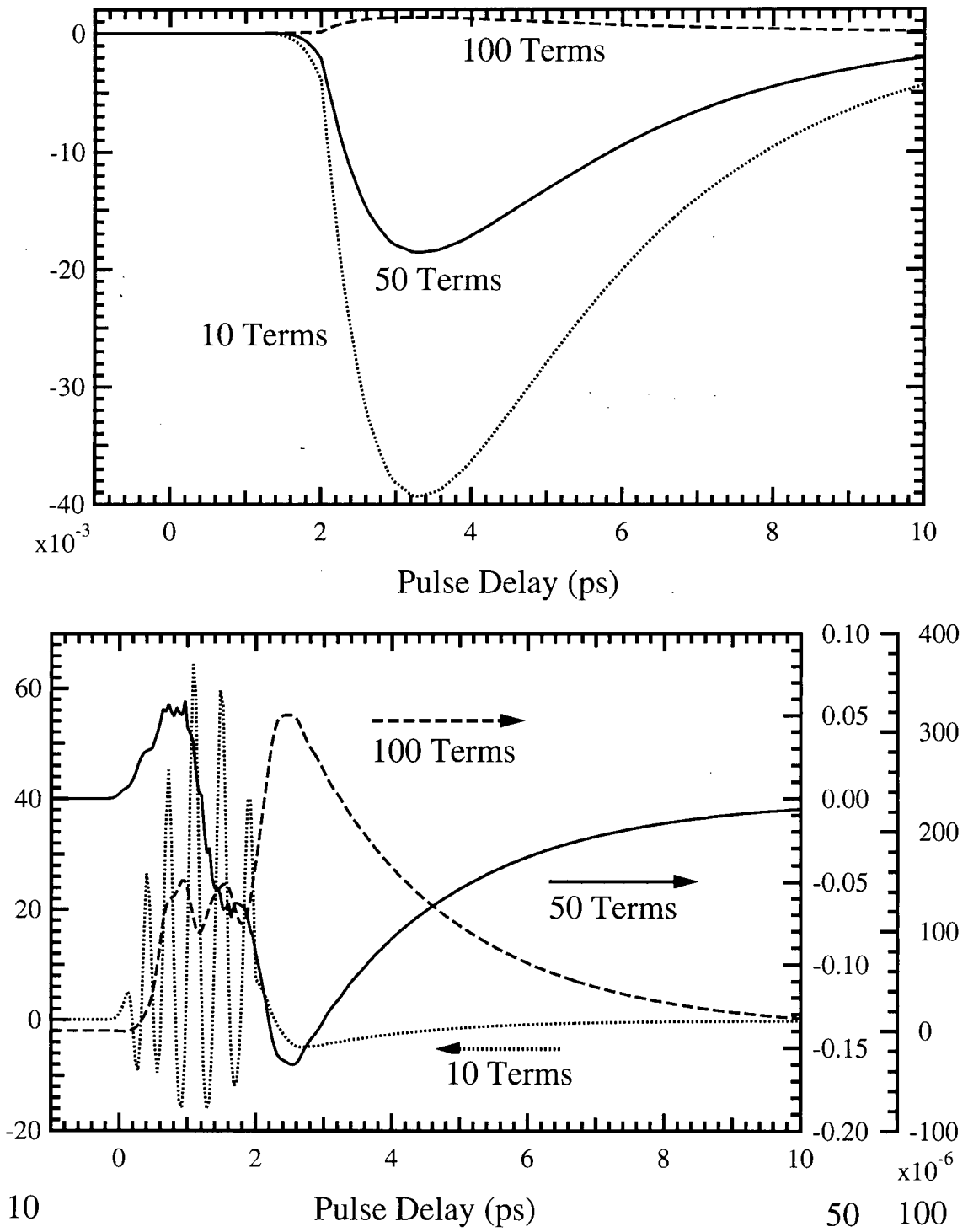
Figure A.8: Residuals for DFWM simulations with varying number of Laguerre (upper plot) or Jacobi (lower plot) terms. Number of Hermite, Jacobi (upper), and Laguerre (lower) terms are fixed at 125.
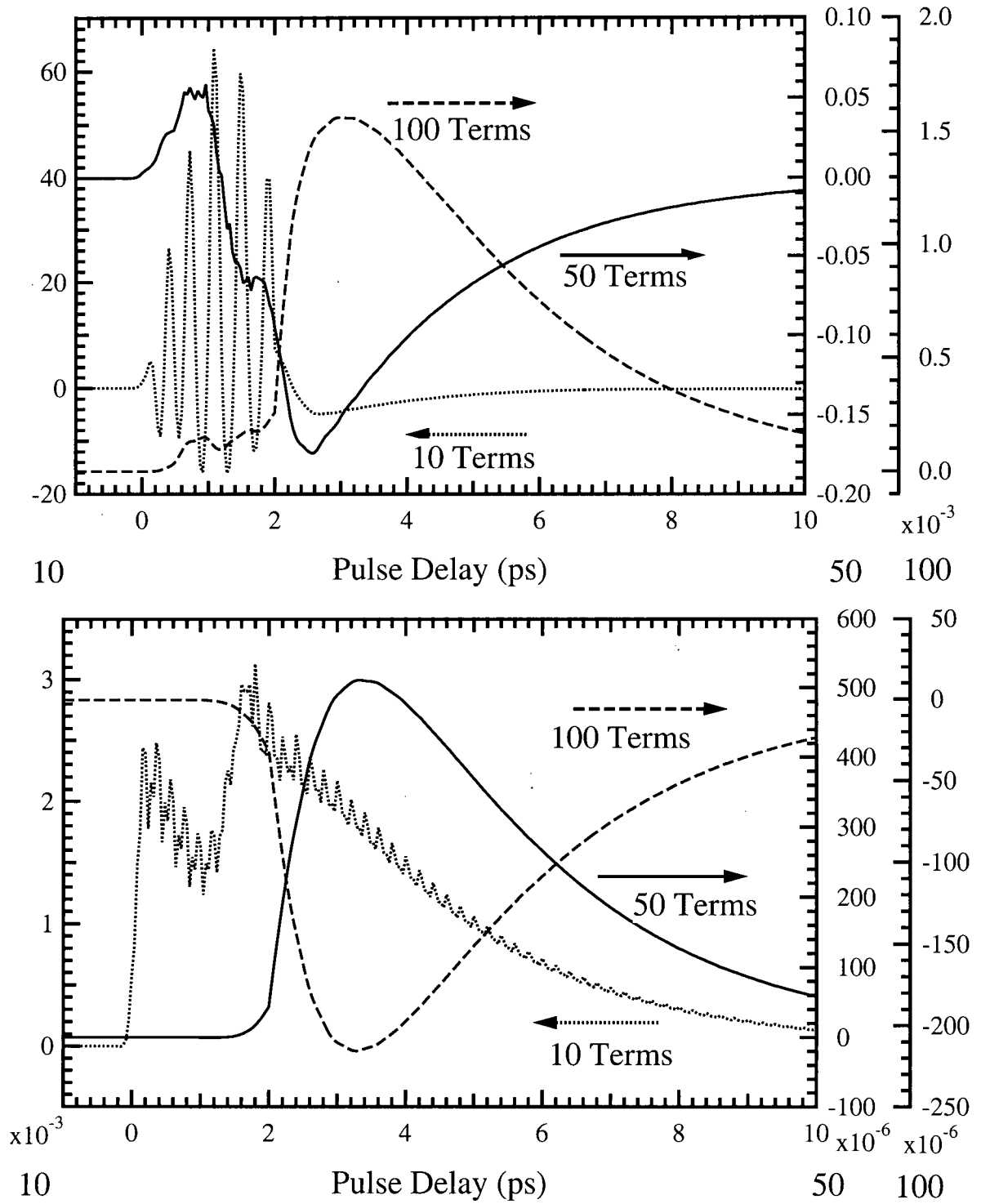
Figure A.9: Residuals for DFWM simulations with varying number of Laguerre-Jacobi (upper plot) or Hermite (lower plot) terms. Number of Hermite (upper) or Laguerre and Jacobi (lower) terms are fixed at 125.
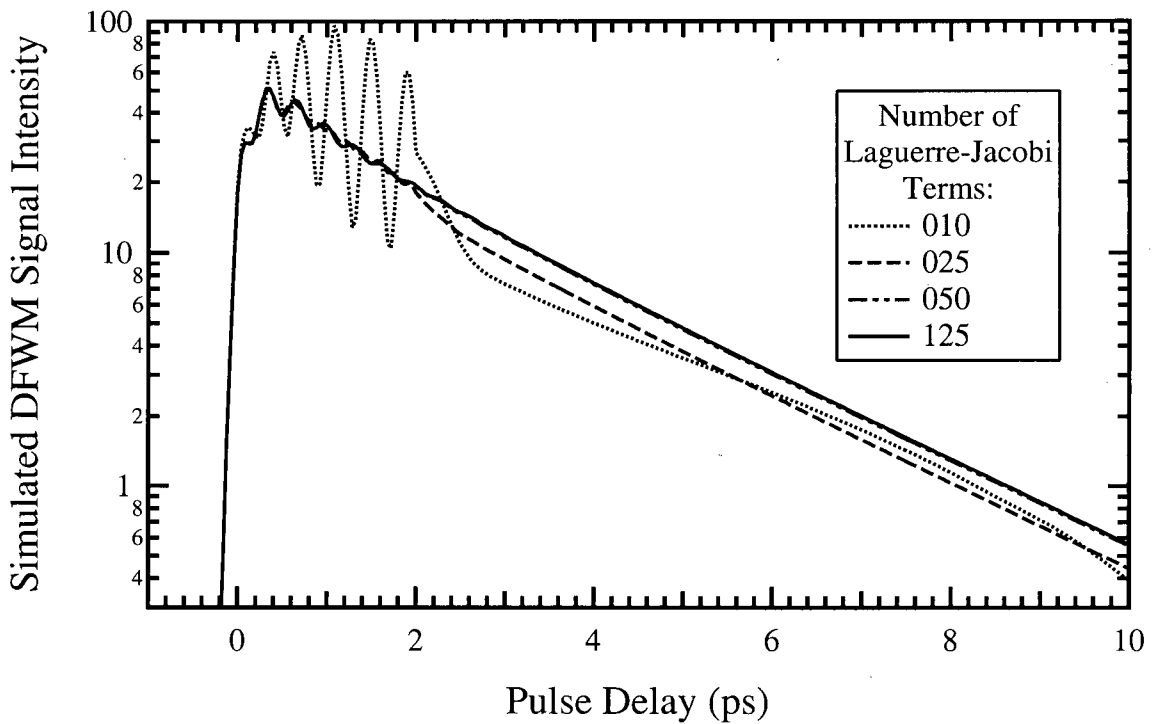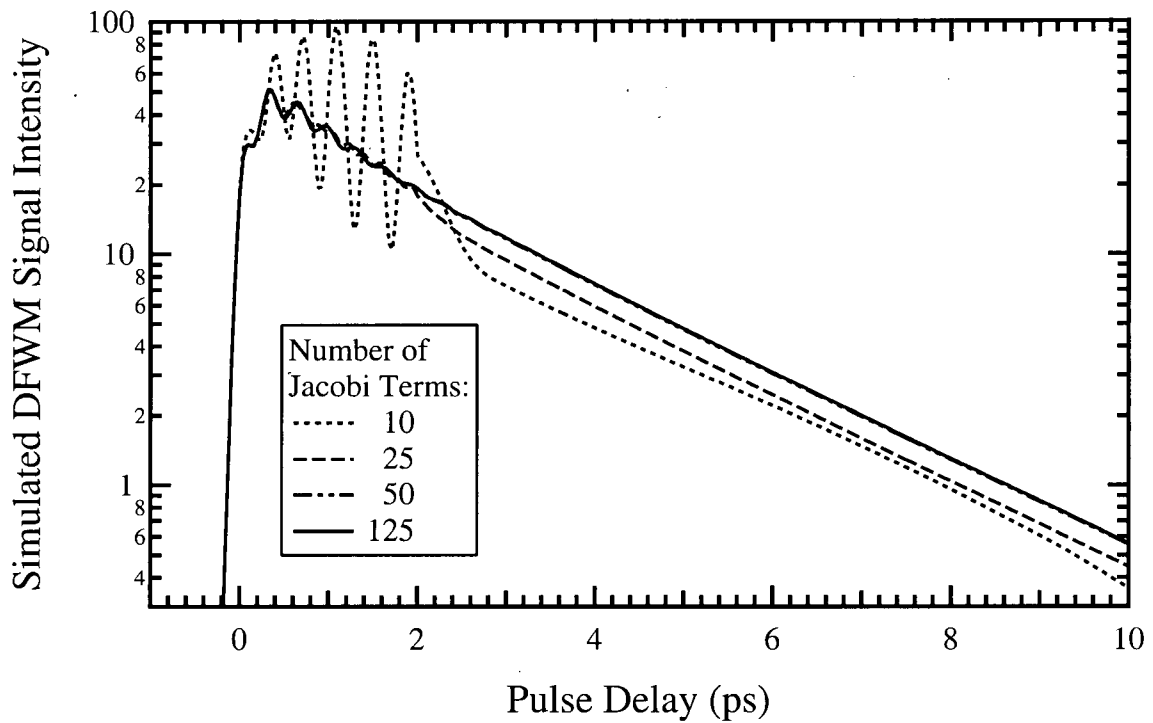
Figure A.10: DFWM simulations as a function of the number of Jacobi (upper plot) or Laguerre-Jacobi (lower plot) terms. Number of Hermite (both plots) and Laguerre (lower plot) terms are fixed at 125.

For the Jacobi polynomials, the relevant integral and numerical evaluation of the result was outlined by Ting [78,82]. The result is that $b_k(\omega)$ is given by

$$b_k^{\text{Jacobi}}(\omega) = |P_k^{(\alpha,\beta)}(t)|^2 \int\limits_{-1}^{+1} dt\,(t-1)^\alpha (t+1)^\beta P_k^{(\alpha,\beta)}(t) e^{i\omega t}$$

$$= \frac{e^{-i\omega}(2i\omega)^k}{(k+\lambda)_k} {}_1F_1\left(k+\beta+1; 2k+\lambda+1; 2i\omega\right)\,, \tag{A.57}$$

where $\lambda = \alpha + \beta + 1$ and $(n)_k = \Upsilon(n+k)/\Upsilon(n)$. Since $b_k^{\text{Jacobi}}(\omega)$ is related to the confluent hypergeometric function ${}_1F_1$ which has three-term recurrence relations, $b_k^{\text{Jacobi}}(\omega)$ also has a three-term recurrence relation,

$$b_{k+1}^{\text{Jacobi}}(\omega) = \frac{(k+\lambda)(2k+\lambda+2)}{(k+\alpha+1)(k+\beta+1)(2k+\lambda-1)}$$
$$\times \left[(\alpha-\beta) + \frac{i(2k+\lambda-1)(2k+\lambda+1)}{2\omega}\right] b_k^{\text{Jacobi}}(\omega)$$
$$+ \frac{(k+2\alpha)(k+2\alpha+1)(2k+\lambda+1)(2k+\lambda+2)}{(k+\alpha)(k+\alpha+1)(2k+\lambda-2)(2k+\lambda-1)} b_{k-1}^{\text{Jacobi}}(\omega) \quad (\text{A.58})$$

which can be used to evaluate the function. Ting shows that the backward recursion process is convergent and also points out that the $b_k(\omega)$ are the coefficients of $p_k(t)$ in the general orthogonal polynomial expansion

$$e^{i\omega t} = \sum_{k=0}^{+\infty} b_k(\omega) p_k(t)\,. \tag{A.59}$$

Setting $t = \pm 1$ in the above equation results in

$$e^{\pm i\omega} = \sum_{k=0}^{+\infty} \frac{(\pm)^k}{k!} \binom{\alpha}{\beta}+1_k b_k^{\text{Jacobi}}(\omega)\,. \tag{A.60}$$

For 'large' ω, the three term recurrence relation can be used to evaluate the $b_k^{\text{Jacobi}}(\omega)$. Examining the hypergeometric function more closely indicates that it oscillates in value until $k \approx \omega$ and then decays exponentially above that value. To gain more accurate values for $b_k^{\text{Jacobi}}(\omega)$ by the backward recursion method, Ting's procedure was modified to start by setting $b_{k+n+1}^{\text{Jacobi}}(\omega) = 0$ (instead of the $k+1$ term being set to 0) and $b_{k+n}^{\text{Jacobi}}(\omega) = 1$ (instead of k term being set to 1). Backward recursion was done to the $k = 0$ term, and then the sum in Equation (A.60) was evaluated and set equal to the exponential. This provided a 'normalization' constant with which the $b_k^{\text{Jacobi}}(\omega)$ were multiplied. This procedure was used for $\omega \geq 0.1$, with n set to 50. Tests against the hypergeometric function (evaluated using Maple V, Release 6) indicated exact agreement to all 15 decimal places.

For smaller ω Ting [78, page 40] provides a series expansion in $2i\omega$, which was used for $\omega < 0.1$. The series expansion is given by

$$b_k^{\text{Jacobi}}(\omega) = \frac{(2i\omega)^k \exp\{(\beta - \alpha)i\omega/(2k + \lambda + 1)\}}{(k + \lambda)_k} \sum_{r=0}^{+\infty} g_r (2i\omega)^r \qquad (A.61)$$

with

$$g_0 = 1, \; g_1 = 0, \; g_2 = \frac{(k + \alpha + 1)(k + \beta + 1)}{2(2k + \lambda + 1)^2(2k + \lambda + 2)}$$

$$g_3 = \frac{(\alpha - \beta)(k + \alpha + 1)(k + \beta + 1)}{3(2k + \lambda + 1)^3(2k + \lambda + 2)(2k + \lambda + 3)} \qquad (A.62)$$

$$g_{r+1} = \frac{(k + \alpha + 1)(k + \beta + 1)g_{r-1} + r(\alpha - \beta)(2k + \lambda + 1)g_r}{(r + 1)(2k + \lambda + 1)^2(2k + \lambda + r + 1)} .$$

A.2.5 Calculation of c_k Coefficients

A.2.5.1 Gaussian Quadrature (Integration) Method

The simplest methods used for integration, such as Simpson's method, interpolate the function at fixed points and gain more accuracy by breaking the integral into successively smaller sections. Each section is then evaluated in a similar manner. The Gaussian integration method [77, 79] extends these methods by finding 'optimal' points in the integral to evaluate the function at, evaluating the integral more efficiently. The discussion here initially follows that in [79].

The Gaussian quadrature method evaluates integrals using

$$\int_a^b dt \, w(t) f(t) \simeq \sum_{j=1}^n W_j f(x_j) , \qquad (A.63)$$

where $w(t)$ is called a *weight* function and it has the finite, defined moments

$$d_n = \int_a^b dt \, w(t) t^n \qquad n \geq 0, \text{ and } d_0 \geq 0. \qquad (A.64)$$

The x_j are the usually called *points* or *nodes* of the formula, while the W_j are usually called *coefficients* or *weights*. With a non-negative weight, n sets of nodes and weights can be found such that the formula is exact for all polynomials of degree $\leq 2n - 1$ (the polynomial of degree $2n - 1$ includes powers of t up to t^{2n-1}). These formulae are called *Gaussian quadrature formulas* and have the property that they have the highest degree of precision which can be obtained using n points. Note that not all of the properties of these formulae depend on the weight function being positive — see [79] for further details. Gaussian quadrature formulas are closely related to orthogonal polynomials and, consequently, orthogonal polynomials and their relationship to these quadrature methods will be discussed next.

A.2.5.2 Orthogonal Polynomials & Gaussian Quadrature

The evaluation of the c_k terms in the oscillatory-singular method involves evaluating the N orthogonal polynomials as well as the function at the $(N + 1)$ zeros of $p_{(N+1)}(t)$. As such, the orthogonal polynomials need to be evaluated as well as the weights and zeros for each Gaussian integration method needed (Laguerre, Jacobi, and Hermite). More details on the method can be found in [79].

A monomial orthogonal polynomial $p_n(t)$ (so called because the coefficient $a_{n,n} = 1$) is defined by

$$p_n(t) = \sum_{j=0}^{n} a_{n,j}\, t^j \ . \tag{A.65}$$

Orthogonal polynomials have the property that any three consecutive polynomials are related by a recursion relation, of the form:

$$\begin{aligned} p_n(t) &= (x - b_n)p_{n-1}(t) - c_n p_{n-2}(t), \ \ (n \geq 2) \\ p_1(t) &= t - b_1, \quad p_0(t) = 1 \end{aligned} \tag{A.66}$$

where b_n and c_n can be defined by

$$\begin{aligned} b_n &= \frac{I_{n,n-1}}{I_{n-1,n-1}} + a_{n-1,n-2} \\ c_n &= \frac{I_{n-1,n-1}}{I_{n-2,n-2}} \end{aligned} \tag{A.67}$$

with

$$I_{n,m} = \int_{a}^{b} w(t)t^n p_m(t)dt \ . \tag{A.68}$$

This can be shown by substituting the recursion relation into the orthogonality relation, which will be zero for all p_k where $0 \leq k < n$.

For the Gaussian quadrature method,

$$\int_{a}^{b} w(t)f(t)dt = \sum_{i=1}^{k} W_i f(t_i) \ , \tag{A.69}$$

where t_i are the k zeros of the kth orthogonal polynomial $p_k(t)$ which, with positive weight $w(t)$, are all real and lie in the range of integration $[a, b]$. This method is exact for polynomials of degree $2k - 1$. The zeros of the polynomials can be found by the methods pointed out in [73, 74, 79].

The weights W_i are all greater than zero and can also be evaluated by the methods outlined in these references. Note that the weights are given by

$$\begin{aligned} W_i &= \frac{1}{|p_{n-1}|^2 p_n'(t_i)p_{n-1}(t_i)} \\ &= -\frac{1}{|p_n|^2 p_n'(t_i)p_{n+1}(t_i)} \ , \end{aligned} \tag{A.70}$$

Polynomial	Weight	a	b	Series Expansion[†]
$P_k^{(\alpha,\beta)}(t)$	$(t-1)^\alpha (t+1)^\beta$ $\alpha,\beta > -1$	-1	$+1$	$\dfrac{1}{2^k} \sum\limits_{n=0}^{k} \binom{k+\alpha}{n}\binom{k+\beta}{k-n}(t-1)^{k-n}(t+1)^n$
$L_k^{(\beta)}(t)$	$t^\beta e^{-t},\ \beta > -1$	0	$+\infty$	$\sum\limits_{n=0}^{k} \binom{k+\beta}{k-n}(-t)^n/n!$
$H_k(t)$	e^{-t^2}	$-\infty$	$+\infty$	$k! \sum\limits_{n=0}^{[k/2]} (-1)^n (2t)^{k-2m}/\{n!(k-2n)!\}$

Table A.5: Jacobi, Laguerre, and Hermite polynomial definitions and series expansions. [†]Jacobi expansion is from [47, page 1059], while the Laguerre and Hermite series expansions are from [85]. The Hermite expansion terminates at the truncated integer part of [k/2].

where the prime (′) indicates differentiation. The derivative terms also have recurrence relations, derived from the orthogonal polynomial three term recurrence relations.

The recurrence relations and orthogonality constants $|p_k|^2$ are given below, while the integration ranges $[a, b]$, weights $w(t)$, and series definitions for the Jacobi, Laguerre, and Hermite polynomials are given in Table A.5.

Jacobi:

$$d_j P_{n+1}^{(\alpha,\beta)}(t) = (a_j + b_j t)P_n^{(\alpha,\beta)}(t) - c_j P_{n-1}^{(\alpha,\beta)}(t) \tag{A.71}$$

where

$$
\begin{aligned}
a_j &= (2n + \alpha + \beta + 1)(\alpha^2 - \beta^2)\\
b_j &= (2n + \alpha + \beta)(2n + \alpha + \beta + 1)(2n + \alpha + \beta + 2)\\
c_j &= 2(n + \alpha)(n + \beta)(2n + \alpha + \beta + 2\\
d_j &= 2(n + 1)(n + \alpha + \beta + 1)(2n + \alpha + \beta)
\end{aligned}
\tag{A.72}
$$

$$\int_{+1}^{-1} dt\,(1-t)^\alpha (1+t)^\beta P_n^{(\alpha,\beta)} P_m^{(\alpha,\beta)}$$

$$
= \begin{cases}
0, & n \neq m\\[2mm]
\dfrac{2^{\alpha+\beta+1}\Upsilon(1+\alpha+n)\,\Upsilon(1+\beta+n)}{\Upsilon(n+1)\,\Upsilon(\alpha+\beta+1+n)(\alpha+\beta+1+n)}, & n = m
\end{cases}
\tag{A.73}
$$

Laguerre:

$$(n+1)L_{n+1}^{(\beta)}(t) = (-t + 2n + \beta + 1)L_n^{(\beta)}(t) - (n+\beta)L_{n-1}^{(\beta)}(t) \tag{A.74}$$

$$\int\limits_{+\infty}^{0} dt\, t^\beta e^{-t}L_n^{(\beta)}(t)L_m^{(\beta)}(t) = \begin{cases} 0, & n \neq m \\ \Upsilon(1+\beta)\binom{n+\beta}{n}, & n = m \end{cases} \tag{A.75}$$

Hermite:

$$H_{n+1}(t) = 2tH_n(t) - 2nH_{n-1} \tag{A.76}$$

$$\int\limits_{+\infty}^{-\infty} dt\, e^{-t^2}H_n(t)H_m(t) = \begin{cases} 0, & n \neq m \\ \pi^{1/2}\, 2^n\, n!, & n = m \end{cases} \tag{A.77}$$

A.2.5.3 Testing of Weights and Zeros

The weights and zeros can be tested by noting [79] that

$$-a_{n,n-1} = \sum_{i=1}^{N} b_i = \sum_{i=1}^{N} t_i, \tag{A.78}$$

where the t_i are the N zeros of the polynomial $p_N(t)$, and

$$\int\limits_{a}^{b} w(t)\, t^k dt = \sum_{i=1}^{N} W_i t_i^k, \qquad (0 \leq k \leq 2N - 1). \tag{A.79}$$

The analytic expressions for the Jacobi, Laguerre, and Hermite polynomials are given in Table A.6. Expressions for the Laguerre and Hermite polynomials can be found in [85]. Tables A.7, A.8, & A.9 contain the test results from the log files of the $N = 125$ term simulation runs shown earlier in the appendix. The tests all use the Gamma, or Generalized-Factorial function, $\Upsilon(x)$, in their evaluation. The routine for $\Upsilon(x)$ is based on the ones in Numerical Recipes [73,74], which uses an algorithm by C. Lanczos (SIAM Journal on Numerical Analysis, Ser. B, Vol. 1, 1964, pages 86-96). This algorithm reports an error over the entire complex plane of $\epsilon \leq 2.0 \times 10^{-10}$.

The Laguerre tests, Table A.7, all show a relative error between the analytic and numerically calculated functions, based on the generated weights and zeros, less than the estimated error in the Gamma function. The Jacobi results are similar, except for near $\beta = -1$. Here, the results indicate that the errors are larger. That the sum of

	Hermite	Laguerre	Jacobi
$\sum_i t_i$	0	$(N+\beta)N$	$\dfrac{N(\beta-\alpha)}{(2N+\alpha+\beta)}$
$\prod_i t_i$	—	$\dfrac{\Upsilon(N+\beta+1)}{\Upsilon(\beta+1)}$	—
$\sum_i W_i t_i^k$	$\Upsilon\left(\dfrac{k+1}{2}\right)$, k even 0, k odd	$\Upsilon(\beta+k+1)$	$(-1)^k \, 2^{(\alpha+\beta)} \dfrac{\Upsilon(\alpha+1)\,\Upsilon(\beta+1)}{\Upsilon(\alpha+\beta+2)}$ $\times \, {}_2F_1(-k,\alpha+1;\alpha+\beta+2;2)^\dagger$

Table A.6: Quadrature weight-zero test formulae. †This hypergeometric function is a finite polynomial whose value depends on k.

p	α	Relative Error	Numerical Result	Theoretical Result
			N = 10	
†	0.0	0.000(15)	121.000000000000E+000	121.000000000000E+000
‡	0.0	+1.401(12)	39.916800000000E+006	39.916800000056E+006
0	0.0	-2.220(15)	1.000000000000E+000	1.000000000000E+000
1	0.0	+1.998(15)	999.999999999997E−003	999.999999999999E−003
3	0.0	+36.415(15)	6.000000000000E+000	6.000000000000E+000
5	0.0	+104.213(15)	119.999999999988E+000	120.000000000000E+000
7	0.0	+223.945(15)	5.039999999999E+003	5.040000000000E+003
			N = 125	
†	0.0	0.000(15)	15.876000000000E+003	15.876000000000E+003
‡	0.0	+118.135(12)	23.721732428804E+210	23.721732431607E+210
0	0.0	-137.446(15)	1.000000000000E+000	1.000000000000E+000
1	0.0	-560.552(15)	1.000000000001E+000	999.999999999999E−003
3	0.0	-258.164(15)	6.000000000002E+000	6.000000000000E+000
5	0.0	-102.437(15)	120.000000000012E+000	120.000000000000E+000
7	0.0	-202.651(15)	5.040000000001E+003	5.040000000000E+003

Table A.7: Results of Laguerre zero and weight tests, for N = 10 and N = 125 terms. The error is relative, equal to (Numerical − Theoretical)/Theoretical. The error is given in the form $x.xx(y) \equiv x.xx \times 10^{-y}$. †Sum of zeros (t_i) test. ‡Product of zeros (t_i) test. The other tests are the sum of the product $(W_i t_i^k)$.

zeros tests is within the numerical precision (≈ 15 digits) available from the calculations while the weight-zero product sum test is not seems to indicate that this may be due to inaccuracies in the generation of the Gaussian quadrature weights, W_i, which use those available in [74]. It could also be due to problems with the evaluation of the hypergeometric function in the theoretical expression, which may have problems such as round-off error in its evaluation. Further investigation of these two sources will be needed to confirm whether this region presents a problem with the weight generation or if it is the analytical test that is generating more erroneous results.

The Hermite weight/zero tests indicate excellent agreement for all the tests to greater than 12 decimal places. The sum of weight times zero tests were multiplied by $\sqrt{\pi}$ due to the use of orthonormal Hermite polynomials in the generation of the weights [74]. A good indication of accuracy is given by the odd power tests since these should be zero regardless of whether orthonormal polynomials are used as the base or not.

k	$-\beta$	Error ($\times 10^{-15}$)	Numerical Result	Theoretical Result
			N = 10	
†	0.050	−0.271(15)	−25.056947608200E−003	−25.056947608200E−003
0	0.050	+1.096(12)	2.033550166155E+000	2.033550166158E+000
1	0.050	−54.075(15)	−52.142311952704E−003	−52.142311952758E−003
2	0.050	+1.113(12)	690.222807373879E−003	690.222807374647E−003
3	0.050	−39.073(15)	−35.138168170657E−003	−35.138168170696E−003
4	0.050	+1.120(12)	418.671783945486E−003	418.671783945955E−003
†	0.001	−0.317(15)	−500.022728305516E−006	−500.022728305833E−006
0	0.001	+1.100(12)	2.000614800779E+000	2.000614800782E+000
1	0.001	−0.544(15)	−1.000807804293E−003	−1.000807804293E−003
2	0.001	+1.117(12)	667.094298628629E−003	667.094298629374E−003
3	0.001	−0.899(15)	−667.344312882005E−006	−667.344312882904E−006
4	0.001	+1.126(12)	400.336780002038E−003	400.336780002489E−003
			N = 125	
†	0.050	−16.466(15)	−25.004961301829E−003	−25.004961301846E−003
0	0.050	+2.863(12)	2.033550166152E+000	2.033550166158E+000
1	0.050	−418.485(15)	−52.142311952340E−003	−52.142311952758E−003
2	0.050	+6.172(12)	690.222807370387E−003	690.222807374647E−003
3	0.050	−392.457(15)	−35.138168170303E−003	−35.138168170696E−003
4	0.050	+9.521(12)	418.671783941969E−003	418.671783945955E−003
†	0.001	−10.826(15)	−500.001984124032E−006	−500.001984134858E−006
0	0.001	+2.809(12)	2.000614800776E+000	2.000614800782E+000
1	0.001	−24.370(15)	−1.000807804269E−003	−1.000807804293E−003
2	0.001	+6.095(12)	667.094298625308E−003	667.094298629374E−003
3	0.001	−24.792(15)	−667.344312858112E−006	−667.344312882904E−006
4	0.001	+9.445(12)	400.336779998708E−003	400.336780002489E−003
†	0.938	−34.195(15)	−470.757836014225E−003	−470.757836014259E−003
0	0.938	+422.849(09)	16.840167421088E+000	16.840174541950E+000
1	0.938	−7.121(06)	−14.874226165711E+000	−14.874233286512E+000
2	0.938	+476.836(09)	14.933327616744E+000	14.933334737490E+000
3	0.938	−7.121(06)	−14.290083975597E+000	−14.290091096282E+000
4	0.938	+496.938(09)	14.329000100634E+000	14.329007221264E+000

Table A.8: Results of Jacobi zero and weight tests, for N = 10 and N = 125 terms. $\alpha = 0.0$ for all of these tests. The error is relative, equal to (Numerical − Theoretical)/Theoretical. The error is given in the form $x.xx(y) \equiv x.xx \times 10^{-y}$. †Sum of zeros ($t_i$) test. The other tests are the sum of the product ($W_i t_i^k$).

k	Relative Error	Numerical Result	Theoretical Result
N = 10			
†	+444.089(18)	444.089209850063E−018	0.000000000000E+000
0	−274.052(15)	1.772453850906E+000	1.772453850906E+000
1	+23.006(18)	23.006332024254E−018	0.000000000000E+000
2	+15.401(18)	886.226925452758E−003	886.226925452754E−003
3	−31.444(18)	−31.443788691984E−018	0.000000000000E+000
4	−103.073(15)	1.329340388179E+000	1.329340388179E+000
N = 125			
†	+79.936(15)	79.936057773011E−015	0.000000000000E+000
0	−273.053(15)	1.772453850906E+000	1.772453850906E+000
1	−38.082(18)	−67.497728501461E−018	0.000000000000E+000
2	+4.529(15)	886.226925452758E−003	886.226925452754E−003

Table A.9: Results of Hermite zero and weight tests, for N = 10 and N = 125 terms. The error is relative, equal to (Numerical − Theoretical)/Theoretical. The error is given in the form $x.xx(y) \equiv x.xx \times 10^{-y}$. †Sum of zeros ($t_i$) test. The other tests are the sum of the product ($W_i t_i^k$). All numerical results of the sum of products of weights and zeros are multiplied by $\sqrt{\pi}$ to account for the weights and zeros being calculated with orthonormal Hermite polynomials.

Appendix B

Laser Pulse Autocorrelation

In this Appendix the autocorrelation process used to characterize the laser pulses — second harmonic generation (SHG) is described. The autocorrelated pulse results (Table B.1) are listed for the three most common pulses: Gaussian, Lorentzian, and Hyperbolic Secant. The relevant time and frequency profiles for these pulses can be found in Table 3.3, on page 81.

The nonlinear crystal used for upconverting the autocorrelation pulses is used far from its resonance frequencies. Under these conditions, dephasing terms can be neglected. Additionally, crystals used for these purposes are usually used at frequencies well below the resonant frequencies, as is the case here. This condition makes the second order susceptibility approximately a constant, simplifying the polarization solution dramatically. From this point, the second order polarization can be solved in either the time or frequency domains. Since the general time dependent second order polarization is of the following form

$$P_{\beta_0}^{(2)}(t) = \epsilon_o \int\limits_{-\infty}^{+\infty} d\omega_1 \int\limits_{-\infty}^{+\infty} d\omega_2 \; \chi_{\beta_0\beta_1\beta_2}^{(2)}(-\omega_\sigma;\omega_1,\omega_2) \; E^{\beta_1}(\omega_1) \; E^{\beta_2}(\omega_2)e^{-i\omega_\sigma t} \;, \qquad \text{(B.1)}$$

the above simplifying assumptions give

$$P_{\beta_0}^{(2)}(t) = \epsilon_o \; \chi_{\beta_0\beta_1\beta_2}^{(2)}(-2\omega) \int\limits_{-\infty}^{+\infty} d\omega_1 \; E^{\beta_1}(\omega_1)e^{-i\omega_1(t-\tau_1)} \int\limits_{-\infty}^{+\infty} d\omega_2 \; E^{\beta_2}(\omega_2)e^{-i\omega_2(t-\tau_2)} \;,$$

$$\text{(B.2)}$$

where summation over the repeated β_i indices is again implied. The integrals over the pulse shapes are thus just Fourier transforms of the pulse shapes and can be immediately evaluated using those definitions (Table 3.3) to give

$$P_{\beta_0}^{(2)}(t) = \epsilon_o \chi_{\beta_0\beta_1\beta_2}^{(2)}(-2\omega)E_{\beta_1}(t-\tau_1)E_{\beta_2}(t-\tau_2) \;. \qquad \text{(B.3)}$$

The detector generates a signal proportional to the time integrated intensity of the field generated by $P_{\beta_0}^{(2)}(t)$. This field is proportional to $P_{\beta_0}^{(2)}(t)$, so the time averaged

detected signal, $I_{\beta_0}(\tau_2)$, is [59]

$$I_{\beta_0}(\tau_2) = \int\limits_{-\infty}^{+\infty} dt \, |P_{\beta_0}^{(2)}(t)|^2 = \epsilon_o^2 \, |\chi_{\beta_0\beta_1\beta_2}^{(2)}(-2\omega)|^2 \int\limits_{-\infty}^{+\infty} dt \, |E^{\beta_1}(t-\tau_1)|^2 |E^{\beta_2}(t-\tau_2)|^2 \, , \quad \text{(B.4)}$$

where one of the two τ_i values is taken to be zero for convenience.

The normalization is chosen so that the integral over the field pulse shape equals one, while some references [59] normalize such that the function is one when $\tau = 0$. This choice was influenced by the desire to have the correct delta-function limits as the pulse width goes to zero, for comparison to time delta-function published results. The pulse autocorrelations for various pulse shapes considered in this thesis are presented in Table B.1. These are called the 'background-free' intensity autocorrelation functions because the directions of the two pulses and the autocorrelation SHG signals are different. The pulse autocorrelation formulas (called the first order, background free correlation function) are also presented in the table, due to their usefulness elsewhere in this work. This table is the same as Table 3.4 on page 82, and is presented here for reference. Table B.2 presents the values of the ratios of the full-width half maximum values for the pulse correlations, in units of the pulse intensity FWHM, σ_t.

Although the Gaussian and Lorentzian expressions in Table B.1 can be implemented directly, the denominators of the hyperbolic secant ones approach zero as their arguments approach zero. The expressions themselves are finite, however, and a Taylor series expansion around zero was conducted to evaluate these expressions for arguments $x \leq 0.1$. These two expansions are given by

$$\frac{x}{\sinh(x)} = 1 - \frac{1}{6}x^2 + \frac{7}{360}x^4 - \frac{31}{15\,120}x^6 + \frac{127}{604\,800}x^8 - \frac{73}{3\,421\,440}x^{10}$$
$$+ \frac{1\,414\,477}{653\,837\,184\,000}x^{12} - \frac{8191}{37\,362\,124\,800}x^{14} + O\left(x^{16}\right)$$

$$\text{(B.5)}$$

and

$$\frac{x\cosh(x) - \sinh(x)}{\sinh^3(x)} = \frac{1}{3} - \frac{2}{15}x^2 + \frac{2}{63}x^4 - \frac{4}{675}x^6 + \frac{2}{2079}x^8 - \frac{2764}{19\,348\,875}x^{10}$$
$$+ \frac{4}{200475}x^{12} - \frac{28936}{10\,854\,718\,875}x^{14} + O\left(x^{16}\right) \, , \quad \text{(B.6)}$$

and both accurate to within 15 decimal places for $x \leq 0.1$.

Table B.1: 1st (pulse autocorrelation – G_0^1), & 2nd (intensity autocorrelation – G_0^2) correlation profiles for various pulse shapes. These are the "background free" correlations [59]. The term a_t is specified in Table 3.3 (page 81) for each pulse shape and τ is the time delay between the pulses.

	G_0^1	G_0^2
General	$\int\limits_{-\infty}^{+\infty} dt\; g(t)g(t-\tau)$	$\int\limits_{-\infty}^{+\infty} dt\; g^2(t)g^2(t-\tau)$
Gaussian	$\dfrac{a_t}{\sqrt{2\pi}}\, \exp\left\{-\dfrac{a_t^2\tau^2}{2}\right\}$	$\dfrac{\sqrt{2}a_t^3}{(2\pi)^{3/2}}\, \exp\left\{-a_t^2\tau^2\right\}$
Sech	$\dfrac{2a_t}{\pi^2}\dfrac{(a_t\tau)}{\sinh(a_t\tau)}$	$\dfrac{4a_t^3}{\pi^4}\dfrac{(a_t\tau)\cosh(a_t\tau)-\sinh(a_t\tau)}{\sinh^3(a_t\tau)}$
Lorentzian	$\dfrac{a_t}{2\pi}\dfrac{1}{1+\left(\dfrac{a_t\tau}{2}\right)^2}$	$\dfrac{a_t^3}{(4\pi)^3}\dfrac{(20+a_t^2\tau^2)}{\left(1+\left(\dfrac{a_t\tau}{2}\right)^2\right)^3}$

Table B.2: Ratios of the full-width half maximums (FWHM) of the pulse correlation profiles ($(G_0^1)^2$ & G_0^2) with respect to that of the field intensity profiles $g(t)^2$. The profiles are defined in Tables 3.3 & 3.4. Also shown is the ratio $\sigma_{G_0^2}/\sigma_{(G_0^1)^2}$.

	$\sigma_{(G_0^1)^2}/\sigma_t$	$\sigma_{G_0^2}/\sigma_t$	$\sigma_{G_0^2}/\sigma_{(G_0^1)^2}$
Gaussian	$\sqrt{2}$	$\sqrt{2}$	1
Sech	1.69217	1.54281	0.91174
Lorentzian	2	1.65396	0.82698